frontiers | Research Topics

Programmable elastic metamaterials for wave control and device applications

Edited by
Hui Chen, Zhenhua Tian, Lingyun Yao,
Feng Zhou and Xiaopeng Li

Published in
Frontiers in Physics

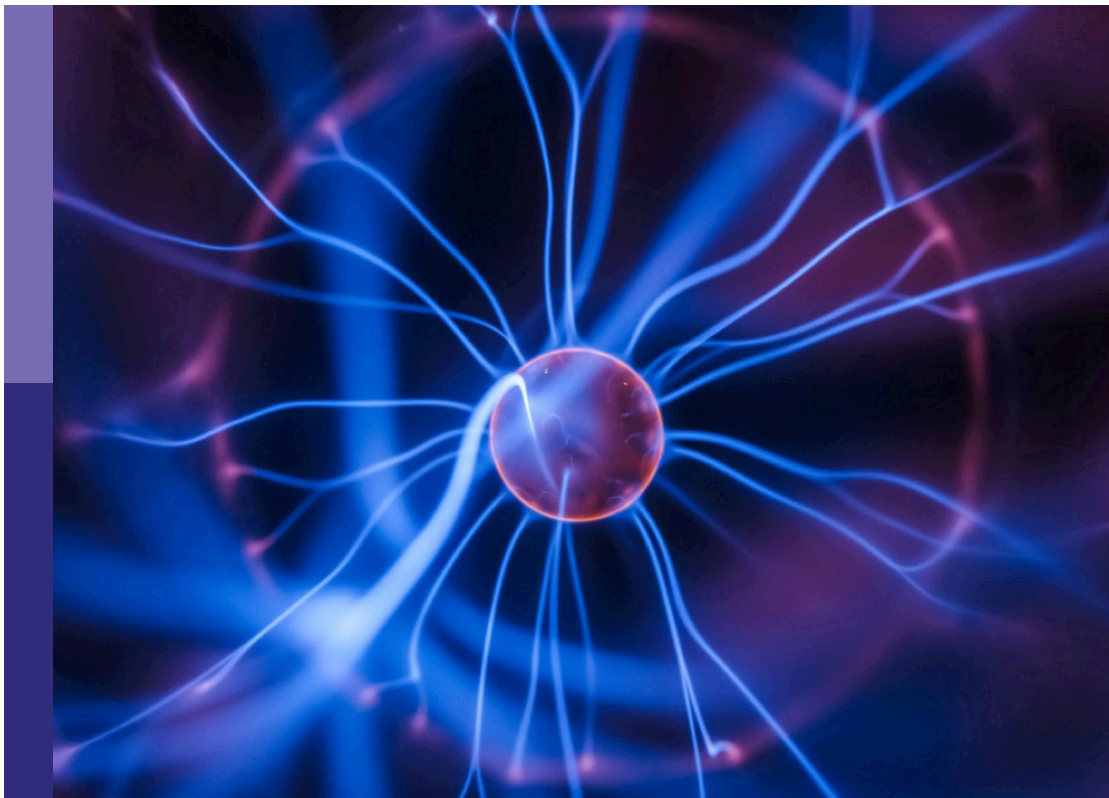

ISSN 1664-8714
ISBN 978-2-8325-3714-5
DOI 10.3389/978-2-8325-3714-5

About Frontiers

Frontiers is more than just an open access publisher of scholarly articles: it is a pioneering approach to the world of academia, radically improving the way scholarly research is managed. The grand vision of Frontiers is a world where all people have an equal opportunity to seek, share and generate knowledge. Frontiers provides immediate and permanent online open access to all its publications, but this alone is not enough to realize our grand goals.

Frontiers journal series

The Frontiers journal series is a multi-tier and interdisciplinary set of open-access, online journals, promising a paradigm shift from the current review, selection and dissemination processes in academic publishing. All Frontiers journals are driven by researchers for researchers; therefore, they constitute a service to the scholarly community. At the same time, the *Frontiers journal series* operates on a revolutionary invention, the tiered publishing system, initially addressing specific communities of scholars, and gradually climbing up to broader public understanding, thus serving the interests of the lay society, too.

Dedication to quality

Each Frontiers article is a landmark of the highest quality, thanks to genuinely collaborative interactions between authors and review editors, who include some of the world's best academicians. Research must be certified by peers before entering a stream of knowledge that may eventually reach the public - and shape society; therefore, Frontiers only applies the most rigorous and unbiased reviews. Frontiers revolutionizes research publishing by freely delivering the most outstanding research, evaluated with no bias from both the academic and social point of view. By applying the most advanced information technologies, Frontiers is catapulting scholarly publishing into a new generation.

What are Frontiers Research Topics?

Frontiers Research Topics are very popular trademarks of the *Frontiers journals series*: they are collections of at least ten articles, all centered on a particular subject. With their unique mix of varied contributions from Original Research to Review Articles, Frontiers Research Topics unify the most influential researchers, the latest key findings and historical advances in a hot research area.

Find out more on how to host your own Frontiers Research Topic or contribute to one as an author by contacting the Frontiers editorial office: frontiersin.org/about/contact

Programmable elastic metamaterials for wave control and device applications

Topic editors

Hui Chen — Ningbo University, China
Zhenhua Tian — Virginia Tech, United States
Lingyun Yao — Southwest University, China
Feng Zhou — Toyota Research Institute of North America, United States
Xiaopeng Li — Toyota Research Institute of North America, United States

Citation

Chen, H., Tian, Z., Yao, L., Zhou, F., Li, X., eds. (2023). *Programmable elastic metamaterials for wave control and device applications*.
Lausanne: Frontiers Media SA. doi: 10.3389/978-2-8325-3714-5

Table of contents

frontiers | Frontiers in Physics

ORIGINAL RESEARCH
published: 04 July 2022
doi: 10.3389/fphy.2022.909536

Continuous and Discrete Deformation Modes of Mechanical Metamaterials With Ring-Like Unit Cells

Nan Yang, Juncheng Zhuang, Shichuan Wei and Ying Yu**

Intelligent Manufacturing Key Laboratory of the Ministry of Education, Shantou University, Shantou, China

Structures with multiple deformation paths provide a promising platform for robotics and reprogrammable mechanical and thermal deformation materials. Reconfigurations with a multi-path can fulfill many tasks (e.g., walking and grasping) and possess multiple properties (e.g., targeted Poisson's ratio and thermal expansion coefficient). Here, we proposed a new ring-like kirigami structure and theoretically and experimentally found that for a basic unit, there are four discrete deformation patterns and a continuous shearing deformation pattern; thus, there are a large number of discrete deformation patterns for a multi-unit combination with geometrical compatibility coupled with a shearing deformation mode. Moreover, targeted Poisson's ratios (either + or -) in the x- and y-directions can be realized by inversely designing the geometrical parameters for a certain deformation path. Additionally, we showed the capability of constructing 2D and 3D cellular structures in various patterns with the proposed ring-like units. The multiple deformation modes demonstrated here open up avenues to design new reprogrammable materials and robots across various scales.

Keywords: mechanical metamaterials, origami, kirigami, deformation paths, Poisson's ratio

OPEN ACCESS

Edited by:
Yangyang Chen,
Hong Kong University of Science and Technology, Hong Kong SAR, China

Reviewed by:
Zongliang Du,
Dalian University of Technology, China
Chen Shen,
Rowan University, United States

****Correspondence:***
Nan Yang
nyang@stu.edu.cn
Ying Yu
yuying@stu.edu.cn

Specialty section:
This article was submitted to Physical Acoustics and Ultrasonics, a section of the journal Frontiers in Physics

Received: *31 March 2022*
Accepted: *26 May 2022*
Published: *04 July 2022*

Citation:
Yang N, Zhuang J, Wei S and Yu Y (2022) Continuous and Discrete Deformation Modes of Mechanical Metamaterials With Ring-Like Unit Cells. Front. Phys. 10:909536. doi: 10.3389/fphy.2022.909536

INTRODUCTION

Material deformation can provide motion, function, and power for diverse applications. For robotics, the deformation of a material enables the realization of gripping motions, walking motions, sensing capabilities, and muscle-like actuating forces [1–3]. Material deformation also provides a platform to realize a negative Poisson's ratio [4], negative thermal expansion [5], negative compressibility [6], and negative stiffness [7–9]. The design of multiple deformation modes provides a flexible way to create mechanical metamaterial switching between soft and stiff states [10], the mechanical properties of which depend more on their own architectures but less on molecular or chemical compositions [11]. These metamaterials have been studied for their potential applications in vibration isolation [12–15], biomedical devices [16], protective systems [17], energy absorption [18, 19], and wave attenuation [20]. Recently, origami has been used to create deployable mechanical metamaterials with unusual "negative" properties coded in the inherent architecture [21–30]. For example, negative Poisson's ratio and negative stiffness are easily realized in a reentrant origami-based structure [31] compared to traditional design methods.

Generally, materials with a positive Poisson's ratio undergo a transverse contraction when stretched, while materials with a negative Poisson's ratio experience a transverse expansion when stretched [32]. Although the deformation mechanism of mechanical metamaterials with either positive and negative Poisson's ratios has been investigated in previous studies [7, 10, 17, 20, 22, 31–33], critical aspects have been overlooked: 1) whether any combinations of Poisson's ratio can be

realized in different directions, 2) how the targeted Poisson's ratios are structurally realized, and 3) how the number of deformation patterns of a cellular structure increases with the configurations of unit cells in different deformation paths. This mechanism may result in more applications. For example, in a recent study, we found that there is a relation between Poisson's ratio and the thermal expansion coefficient in kirigami-based materials [34]; thus if any combinations of Poisson's ratio can be realized, then that of the thermal expansion coefficient can be realized in a designed material. Also, this auxetic design has some merit for the biomedical application. When the structure is used as implant in the intervertebral disc, the uniaxial compression would not cause a cross-section expansion, and thus, it would not squeeze the surrounding tissues and can avoid aching.

Here, our proposed ring-like kirigami structure can be easily transformed into a concave shape in one direction for a negative Poisson's ratio and a convex shape in another direction for a positive Poisson's ratio. Compared to the origami-based designs [35, 36], our kirigami-based design enables us to straightforwardly generate a convex and concave pattern for the same structural unit. In this way, we can obtain any combinations of Poisson's ratios along two orthometric directions in the 2D Poisson's ratio space due to the different planar design angles and deformation modes in the two directions. In this sense, the Poisson's ratios can be independently tuned and inversely designed [37]. Additionally, in theory and experiment, we find that a basic ring-like unit has four discrete deformation patterns and a continuous shearing deformation pattern, and a structure with four basic units has 16 discrete deformation patterns. Furthermore, additional potential deformation patterns can be realized by plenty of multi-unit combinations (with 8, 16, or 32 ... basic units). Finally, we showed that a 3D cellular structure with multiple deformation modes can be built by stacking 2D cellular structures layer by layer.

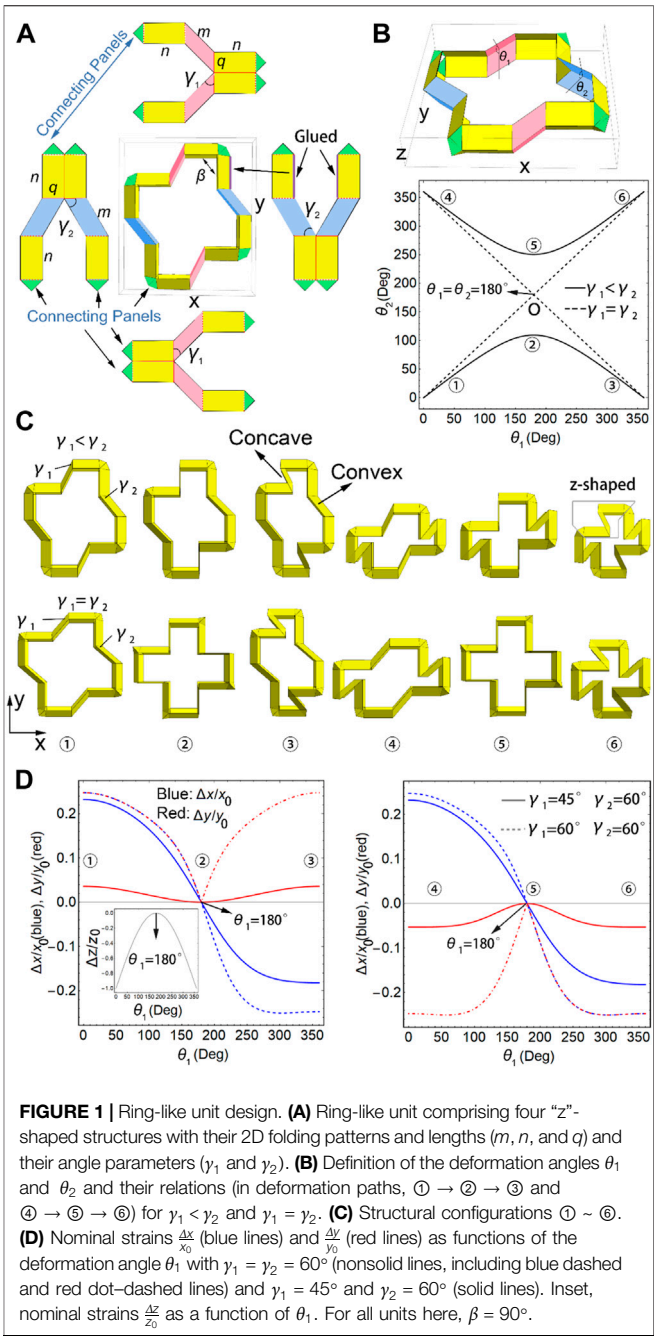

FIGURE 1 | Ring-like unit design. **(A)** Ring-like unit comprising four "z"-shaped structures with their 2D folding patterns and lengths (m, n, and q) and their angle parameters (γ_1 and γ_2). **(B)** Definition of the deformation angles θ_1 and θ_2 and their relations (in deformation paths, ① → ② → ③ and ④ → ⑤ → ⑥) for $\gamma_1 < \gamma_2$ and $\gamma_1 = \gamma_2$. **(C)** Structural configurations ① ~ ⑥. **(D)** Nominal strains $\frac{\Delta x}{x_0}$ (blue lines) and $\frac{\Delta y}{y_0}$ (red lines) as functions of the deformation angle θ_1 with $\gamma_1 = \gamma_2 = 60°$ (nonsolid lines, including blue dashed and red dot–dashed lines) and $\gamma_1 = 45°$ and $\gamma_2 = 60°$ (solid lines). Inset, nominal strains $\frac{\Delta z}{z_0}$ as a function of θ_1. For all units here, $\beta = 90°$.

MATERIALS AND METHODS

Unit Design

Here, we designed a ring-like unit cell with multiple deformation modes. In **Figure 1A**, the ring-like unit cell comprises four "z"-shaped structures (also in the gray frame in **Figure 1C**), which are folded with mountain (solid line) and valley (dashed line) creases and formed into 3D configurations from the 2D patterns by taping the edges (see purple edges in **Figure 1A** and see also **Supplementary Figure S1**), where the opposite "z"-shaped structures are centrosymmetric. γ_1 and γ_2 are important planar design angles on the facets of the opposite "z"-shaped structures, as shown in **Figure 1A**. For a regular unit, the "z"-shaped structure with γ_1 is perpendicular to that with γ_2, that is, $\beta = 90°$. The length parameters m, n, and q are identical for the four "z"-shaped structures (in this study, $m = n = 2q$), and only the angle parameters γ_1 and γ_2 are different. Deformation angles θ_1 and θ_2 are defined as the dihedral angles between two facets, corresponding to the "z"-shaped structures with γ_1 and γ_2, respectively (**Figure 1B** top, pink, and blue dihedrals). Based on the requirement of geometrical compatibility (the same height in z-direction), there is a relation between θ_1 and θ_2 (**Figure 1B** bottom; see Eq. 11). The panels of the kirigami structure are assumed to be rigid. The Miura origami is a specific case of our kirigami design, which is shown in Section 8 of SI.

Sample Fabrication

The ring-like unit samples were fabricated using the Strathmore 500 Series 3-ply Bristol card stock that was laser cut based on a design pattern generated using Mathematica 11.2. The edges of

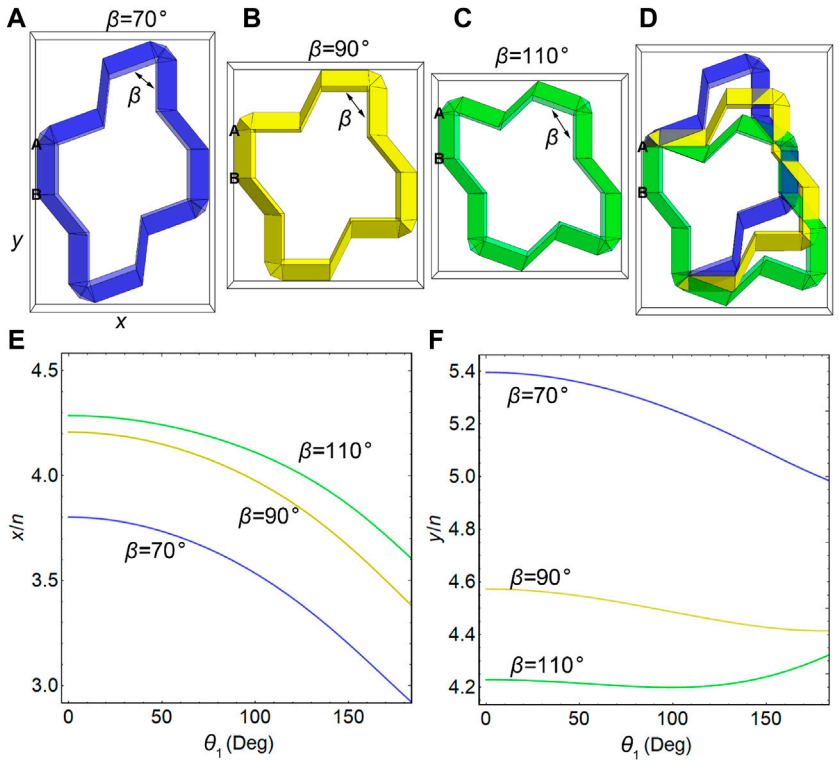

FIGURE 2 | Shearing deformation modes of the ring-like unit. Configurations of the ring-like unit with **(A)** β = 70°, **(B)** 90°, and **(C)** 110°. **(D)** Overlapped configurations of **(A–C)**. The dimensionless size, **(E)** x/n and **(F)** y/n, as functions of the deformation angle θ_1 with **(A)** β = 70°, **(B)** 90°, and **(C)** 110°. Here, γ_1 = 45° andγ_2 = 60°.

the given panels were glued to be connected (**Figure 1A**) to build 3D units for flexible foldability. See SI **Section 6** for details.

Calculation Methods

The calculation methods for the sizes of a ring-like unit and four-unit combination comprising four ring-like units and the design method for targeted Poisson's ratios are given in SI Sections 1–4.

Sample Size Measurement

The top box, camera, and bottom box were connected and moved together with the test head under the control of a universal testing machine. The sample was put on a motionless substrate. When the bottom box touched the sample, it was deformed and captured using a camera. Then, the binary images of the sample at different times were obtained, and the sample in each image was enclosed within a minimum enclosed rectangle, and then, the x- and y-sizes were obtained. Finally, the real size of the sample was obtained by using a conversion factor of 0.4167 mm/pixel. The experimental setup is shown in **Figure 3F**.

RESULTS AND DISCUSSION

Here, we used Mathematica 11.2 software to simulate the deformation using geometrical relation equations (see SI) to obtain the vertex coordinates and then the facets of the structures at different deformation angles.

Unit Cell Deformation

Once θ_1 is fixed, the height in the z-direction of the whole ring-like structure is determined, and then, θ_2 is determined. With different initial settings of $\theta_1 = \theta_2 = 0$ and $\theta_1 = 360° - \theta_2 = 0$, there are two deformation paths, that is, ① → ② → ③ and ④ → ⑤ → ⑥, in the $\theta_1 - \theta_2$ space (see **Figure 1B** for the plot and **Figure 1C** for the configurations of ① ~ ⑥). For $\gamma_1 < \gamma_2$, the two paths are disconnected. However, for $\gamma_1 = \gamma_2$, the two paths are connected at point O, and points ② and ⑤ overlap, resulting in the connected "X"-shaped paths (**Figure 1B** plot). **Figure 1C** shows the discrete configuration examples ① ~ ⑥ of a unit with $\gamma_1 < \gamma_2$ and $\gamma_1 = \gamma_2$ and the convex ($\theta_2 < 180°$) and concave ($\theta_1 > 180°$) parts in a unit cell. **Figures 1B,C** show that these discrete configurations are realized by continuously changing θ_1. In fact, for $\gamma_1 < \gamma_2$, configuration ② can be switched to ⑤ with panel bending, and vice versa. Here, we study only the case of $\gamma_1 \leq \gamma_2$, as the case of $\gamma_1 \geq \gamma_2$ can be known by swapping the current γ_1 and γ_2, which means that the unit is rotated by 90°. See SI Sections 1 and 2 for the detailed geometric model.

Here, the ring-like units possess various deformation behaviors in the x- and y-directions. **Figure 1D** shows the isotropic deformations for $\gamma_1 = \gamma_2 = 60°$ along paths ① → ② and ⑤ → ⑥, where the nominal x- and y-strains are equal

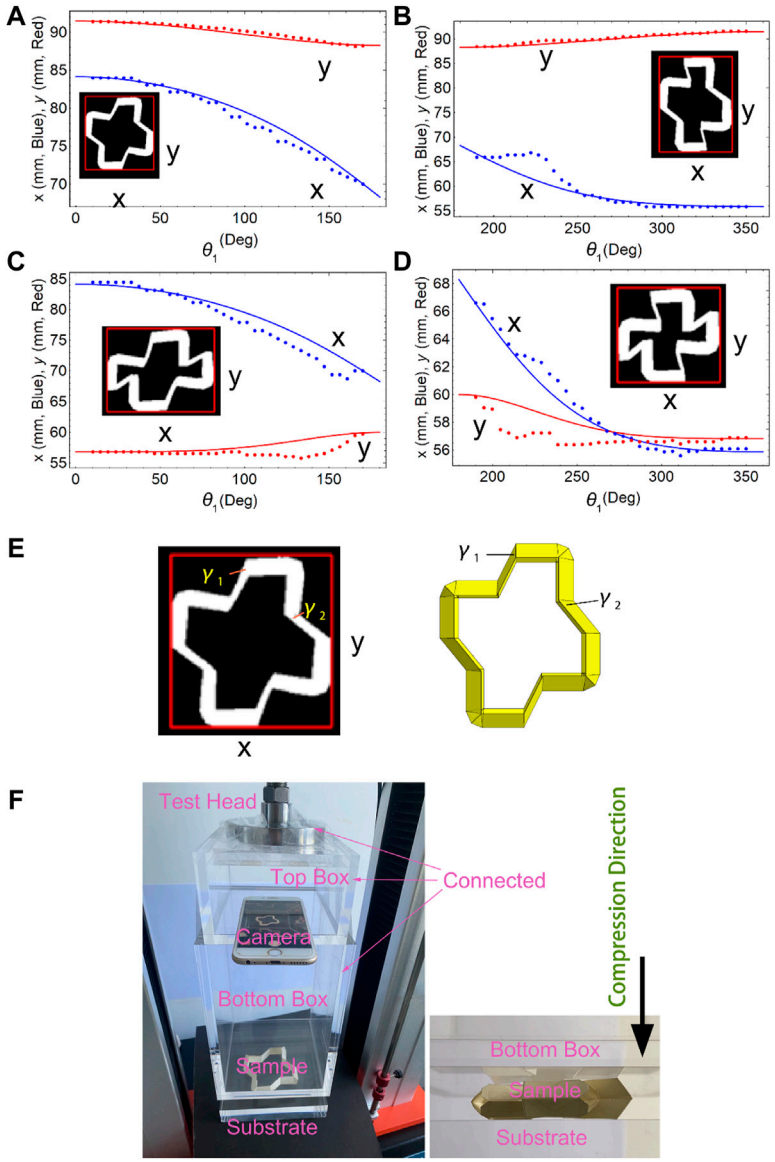

FIGURE 3 | Experimental verification. Dimensions of a unit with $\gamma_1 = 45°$, $\gamma_2 = 60°$, and $\beta = 90°$ under compression in the *z*-direction for four patterns: **(A)** ①, **(B)** ③, **(C)** ④, and **(D)** ⑥ (curves, analytical model; points, measured data). **(E)** γ_1 and γ_2 in the binary image and structural model. **(F)** Experimental setup.

($\frac{\Delta x}{x_0} = \frac{\Delta y}{y_0}$, see the overlapped blue and red nonsolid lines, where the nonsolid lines are pertaining to $\gamma_1 = \gamma_2 = 60°$, and the solid lines are pertaining to $\gamma_1 = 45°$ and $\gamma_2 = 60°$), and the anisotropic deformations ($\frac{\Delta x}{x_0} \neq \frac{\Delta y}{y_0}$) for $\gamma_1 = \gamma_2 = 60°$ along paths ② → ③ and ④ → ⑤ and for $\gamma_1 = 45°$ and $\gamma_2 = 60°$ along all paths. The nominal z-strain is always symmetrical about $\theta_1 = 180°$ (see **Figure 1D** inset). Here, the nominal strain is defined as $\frac{\Delta s}{s_0} = \frac{s}{s_0} - 1$, where $s = x, y, z$ denotes the dimension and $s_0 = s|_{\theta_1=180°}$ denotes the initial dimension. **Figure 1D** implies that we may obtain arbitrary combinations of different Poisson's ratios along the x- and y-directions. The relations between the nominal z-strain and the nominal x- and y-strains are shown in **Supplementary Figure S3**, which is a variant of **Figure 1D**.

There are two degrees of freedom (DOFs) of the ring-like unit, that is, θ_1 and β. To explain the two DOFs, **Figures 2**a and c show that the ring-like unit can be skewed by $\beta \neq 90°$ with fixed θ_1 compared to that with $\beta = 90°$ (**Figure 2B**), with the opposite "z"-shaped structures remain parallel. We defined the dimensions of the units by aligning the AB side in the *y*-direction, as shown in **Figure 2A**, and found that with the continuous change of β, the ring-like unit shows a continuous shearing deformation mode. The size changes in the x- and *y*-directions under different values of β are shown in **Figures 2E, F**, respectively. This shows that θ_1 controls the opening and closing mode of the structure, while β controls the shearing mode.

To demonstrate the analytical geometrical model with experimental data, we compressed a paper-made ring-like unit

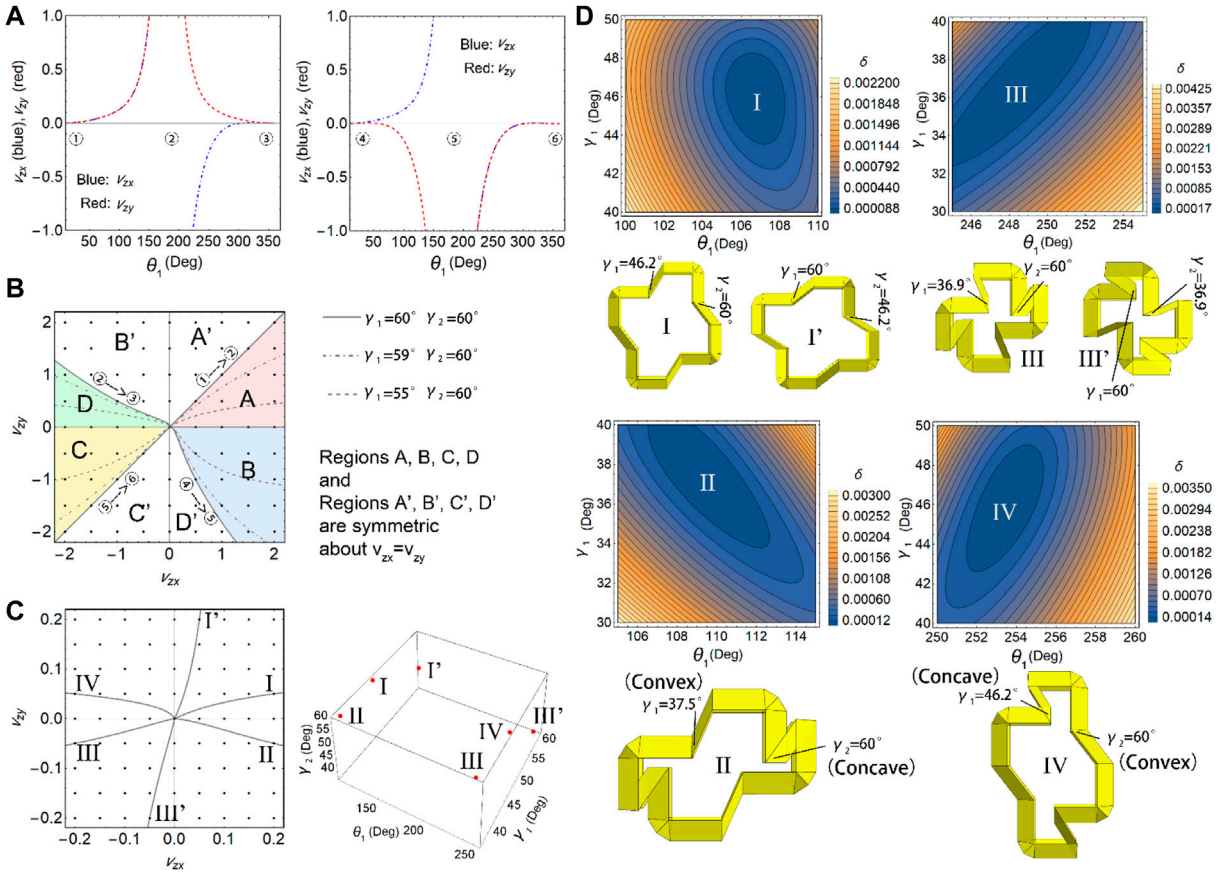

FIGURE 4 | Optimal design for the targeted Poisson's ratios in the x- and y-directions. **(A)** Poisson's ratios along different deformation paths with $\gamma_1 = \gamma_2 = 60°$. **(B)** With $\gamma_1 < \gamma_2 = 60°$, the region in the 2D Poisson's ratio space where the curve (ν_{zx}, ν_{zy}) can reach are plotted. Pink region, deformation from ① → ②; green region, ② → ③; blue region, ④ → ⑤; and yellow region, ⑤ → ⑥. **(C)** Optimal design for selected Poisson's ratios (ν_x, ν_y) = (0.2, 0.05), (0.05, 0.2), (0.2, −0.05), (−0.2, −0.05), (−0.05, −0.2), and (−0.2, 0.05) at points I, I′, II, III, III′, and IV in the Poisson's ratio space, respectively, and the corresponding optimal parameters (red points) in the design space. **(D)** Searching for the optimal parameters in the design space with $\gamma_2 = 60°$. Top: contour plots of δ; bottom, configurations. For I, $\theta_1 = 106.8°$, $\theta_2 = 84°$, $\gamma_1 = 46.2°$, and $\gamma_2 = 60°$. For I′, $\theta_2 = 106.8°$, $\theta_1 = 84°$, $\gamma_2 = 46.2°$, and $\gamma_1 = 60°$. For II, $\theta_1 = 109.3°$, $\theta_2 = 290.0°$, $\gamma_1 = 37.5°$, and $\gamma_2 = 60°$. For III, $\theta_1 = 248.8°$, $\theta_2 = 290.2°$, $\gamma_1 = 36.9°$, and $\gamma_2 = 60°$. For III′, $\theta_2 = 248.8°$, $\theta_1 = 290.2°$, $\gamma_2 = 36.9°$, and $\gamma_1 = 60°$. For IV, $\theta_1 = 253.6°$, $\theta_2 = 83.7°$, $\gamma_1 = 46.2°$, and $\gamma_2 = 60°$.

(**Figure 3**) in the z-direction using a universal testing machine. Here, the unit with $\gamma_1 = 45°$ and $\gamma_2 = 60°$ is programmed into four discrete patterns (①, ③, ④, and⑥ corresponding to **Figure 1C**; the sample cannot stay at $\theta_1 = 180°$, i.e., transitional patterns ② and ⑤) and compressed in the z-direction. From the top, a camera is used to obtain a video of the unit deformation process to calculate the x- and y-dimensions (see **Figure 3F** for the experimental setup and **Supplementary Videos S1–4**). The measured x- and y-dimensions are shown in **Figures 3A–D** and compared to the analytical curves. When the unit is shrunk in a given direction under compression, the scraping and friction between the unit and substrate become apparent; thus, the measured dimensions oscillate around the analytical values (see **Figures 3B–D**). **Figure 3E** is used to show the sample layout direction compared with the model. The results of the model and experiment agree with each other well. The experimental setup is shown in **Figure 3F**.

Inverse Design for the Desired Poisson's Ratio

After validating the analytical model, we focused on the inverse design of a unit with $\beta = 90°$ for targeted Poisson's ratios as the x- and y-dimensions can be clearly defined with $\beta = 90°$ (see **Figure 2B**). Poisson's ratios in the x- and y-directions under compression in the z-direction are calculated by $\nu_{zx} = -\frac{dx/x}{dz/z}$ and $\nu_{zy} = -\frac{dy/y}{dz/z}$ [31] based on the definition in **Figure 1B**. Even with $\gamma_1 = \gamma_2$, the ring-like unit shows various Poisson's ratios in different paths. In **Figure 4A**, with $\gamma_1 = \gamma_2 = 60°$ for deformation path ① → ②, we have $\nu_{zx} > 0$ and $\nu_{zy} > 0$; for ② → ③, $\nu_{zx} < 0$ and $\nu_{zy} > 0$; for ④ → ⑤, $\nu_{zx} > 0$ and $\nu_{zy} < 0$; and for ⑤ → ⑥, $\nu_{zx} < 0$ and $\nu_{zy} < 0$. Therefore, we can expect more various Poisson's ratios of a unit cell with $\gamma_1 \neq \gamma_2$. Taking $\gamma_2 = 60°$ as example, we plotted Poisson's ratio curves ($\nu_{zx} - \nu_{zy}$ relations) with $\gamma_1 = 60°$, 59°, and 55° for paths ① → ②, ② → ③, ④ → ⑤, and ⑤ → ⑥ as shown in **Figure 4B**. If we plot the $\nu_{zx} - \nu_{zy}$ curves within $\gamma_1 \leq \gamma_2 = 60°$, the curves

would fill the regions A (pink), B (blue), C (yellow), and D (green), which are the half of $\nu_{zx} - \nu_{zy}$ space (i.e., regions A, B, C, and D and regions A′, B′, C′, and D′ are symmetric about $\nu_{zx} = \nu_{zy}$, see **Figure 4B**). Also, this does not limit to $\gamma_2 = 60°$, which implies that the curves would fill the other half of $\nu_{zx} - \nu_{zy}$ space (i.e., regions A'+B'+C'+D′) by swapping the x-size and y-size (or swapping γ_1 and γ_2), which means that a unit cell is rotated by 90°. For example, if the design parameters $\gamma_1 = \tau$ and $\gamma_2 = \omega$ obtain the point $(\nu_{zx}, \nu_{zy}) = (\nu_\tau, \nu_\omega)$ in the Poisson's ratio space, then the point $(\nu_{zx}, \nu_{zy}) = (\nu_\omega, \nu_\tau)$ can be obtained by $\gamma_1 = \omega$ and $\gamma_2 = \tau$.

The optimization of the structures for given Poisson's ratios in the x- and y-directions can be achieved by minimizing the error, $\delta = (\nu_{zx} - \nu_x)^2 + (\nu_{zy} - \nu_y)^2$, subjected to $0 < \theta_1$, $\theta_2 < 360°$, and $0 < \gamma_1 \le \gamma_2 < 90°$ (see SI for details), where (ν_x, ν_y) are the targeted Poisson's ratios. To test this method, we chose six points, I, I′, II, III, III′, and IV, in the Poisson's ratio space to represent the six targeted pairs of Poisson's ratios, as shown in **Figure 4C**, where points I, II, III, and IV are four vertices of a rectangle, and I′ and III′ are the symmetrical points of I and III about $\nu_{zx} = \nu_{zy}$. As a result, we obtained$\theta_1 = 106.8°$, $\theta_2 = 84°$, $\gamma_1 = 46.2°$, and $\gamma_2 = 60°$ for point I with $(\nu_x, \nu_y) = (0.2, 0.05)$. At point I′ with $(\nu_x, \nu_y) = (0.05, 0.2)$, we have the structure with $\theta_2 = 106.8°$, $\theta_1 = 84°$, $\gamma_2 = 46.2°$, and $\gamma_1 = 60°$, which is shown as the structure I′ in **Figure 4D**. Other optimal design results for points II, III, III′, and IV are also shown in **Figures 4C,D** (with the resulting parameters listed in the caption of **Figure 4**), where **Figure 4C** shows the $\nu_{zx} - \nu_{zy}$ curves passing through the six targeted points (left) and the corresponding parameters in the 3D design space $(\theta_1, \gamma_1, \gamma_2)$ (right), and **Figure 4D** presents the contour plots and minima of δ and the corresponding structural configurations. Taking configurations II and IV as examples, the convex and concave parts result in positive and negative Poisson's ratios, respectively, but the specific values are determined by the design angles γ_1 and γ_2. This optimization method provides an effective tool to design a ring-like unit with targeted Poisson's ratios, and the minimum value of δ can be less than 10^{-12} for each case.

Multiple Deformation Patterns of 2D Cellular Structures

After understanding the deformation mechanism of one ring-like unit, here we focus on that with multiple units. Four identical ring-like units can be combined to form a four-unit combination, which can be periodically replicated to construct a 2D cellular structure, as shown in **Figure 5A** (in the gray shade, the four-unit combination is displayed with a yellow–pink–yellow–pink pattern because the diagonal ring-like units are with the same configuration). Although the four ring-like units are identically designed with $\gamma_1 = 45°$, $\gamma_2 = 60°$, and $\beta = 90°$, four deformation patterns of each ring-like unit (see **Figure 1C**, ①, ③, ④, and ⑥) make $4 \times 4 = 16$ discrete patterns for the four-unit combination. **Figure 5B** introduces one pattern of four-unit combinations in detail, and the other 15 patterns are shown in **Figure 5C**. **Figure 5B** shows the relation between the dimensionless sizes x_c/n and y_c/n (where x_c and y_c are defined as the sizes of the four-unit combination in the x- and y-directions, see also **Supplementary Figure S2** and Eq. (14)). The four-unit combination is with two ring-like units in pattern ① (yellow) and the other two in pattern ③ (pink) (see **Figure 5B**). Here, the four ring-like units have the same value of θ_1 within $0 \le \theta_1 \le 180°$ to maintain the same height in the z-direction, which is necessary given the geometrical compatibility requirements for building 3D cellular structures. In the plot of **Figure 5B**, there is a sharp corner in the $x_c/n - y_c/n$ curve since, before the corner (stage 1), the yellow unit dominates the x_c value, and then, the pink unit dominates the x_c value (stage 2). Similar sharp corners, as well as smooth $x_c/n - y_c/n$ curves, can be found in the other 15 patterns in **Figure 5C**. In fact, the 16 patterns can be divided into four groups based on the pattern of the diagonal ring-like units in yellow (groups #1, #2, #3, and #4 in **Figure 5C**, where the symbol "#a, b" means No. b in group #a), and within each group, the pattern of the yellow unit remains unchanged. Some size ranges related to the x- and y-dimensions of the four-unit combination are identical. For example, in group #2, the first two plots and last two plots individually have the same x_c range, while the first and fourth plots and the second and third plots individually have the same y_c range. This implies that different four-unit combinations may be again connected through the side with identical sizes to create a new unit (comprising $4n$ ($n = 2, 3, 4, \ldots$) basic ring-like units), then the number of deformation patterns of the resulting structure is greatly increased. This operation can be recursively implemented within a group (see the combination of #3.1 and #3.4 in **Figure 5D**) or across groups (see the combination of #3.1 and #2.1 in **Figure 5D**).

The shearing deformation of the 2D cellular structures with $\beta \neq 90°$ compared to the non-shearing case with $\beta = 90°$ is shown in **Figure 6**. Three representatives of the 16 discrete patterns are chosen, as shown in **Figures 6A–C**, and the top edges of the upper-left-most yellow structures are aligned with the y-direction (**Figure 6A**). This is to show a rotation-like effect of the 2D cellular structures with shearing deformations, although the directions of key sides are fixed. This figure shows the potential ability to control mechanical waves in the shearing directions (see the possible shearing forces in **Figure 6B**), which is beyond the topic of this work but will be an interesting further work. The structures in **Figure 6** (column 1–3) are shown on the x–y plane, and they can be stacked in the z-direction layer by layer to build 3D cellular structures (see **Figure 6**, column 4).

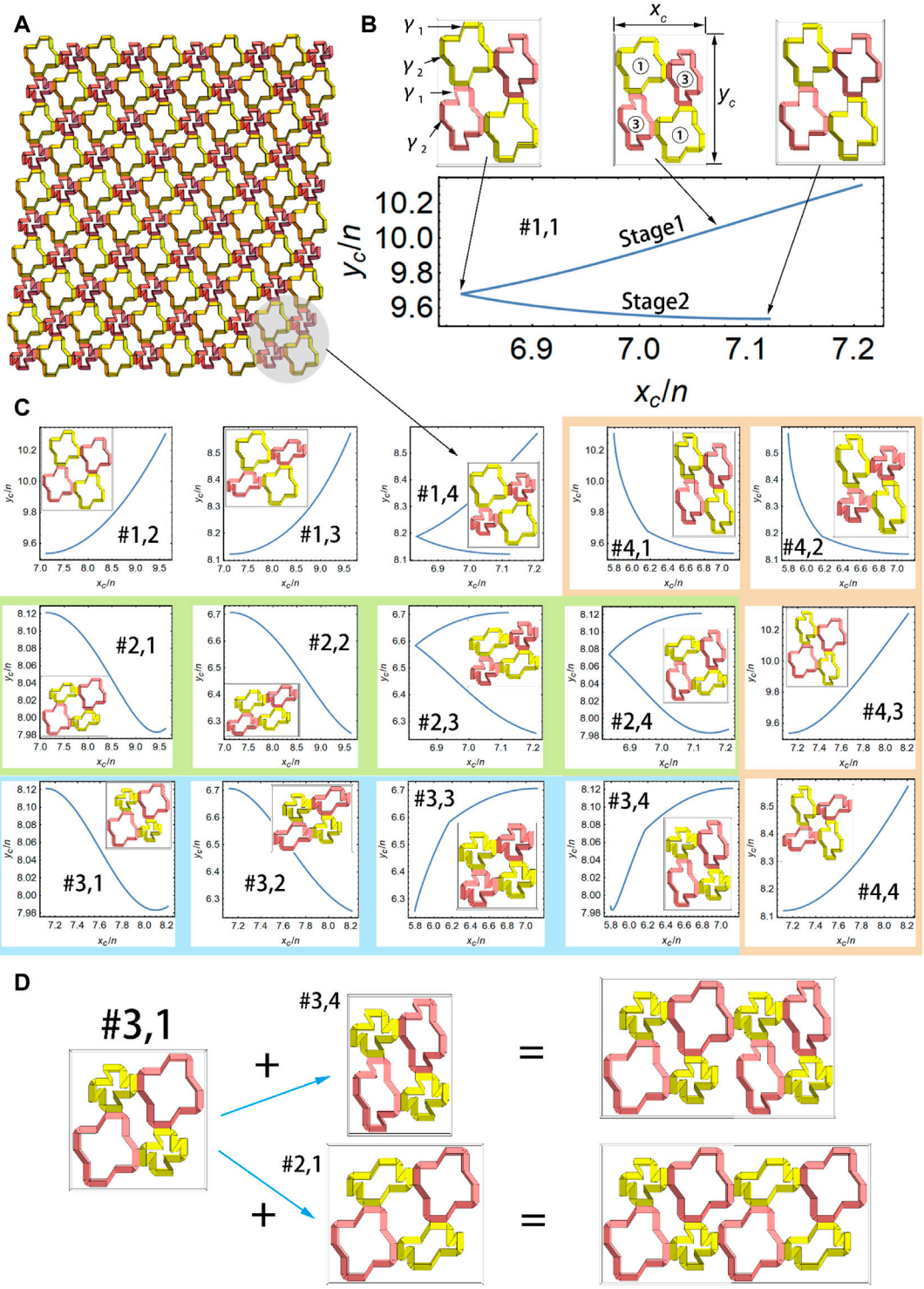

FIGURE 5 | Multiple deformation patterns of 2D cellular structures. **(A)** 2D cellular structures comprising 5 × 5 four-unit combinations. **(B)** One deformation pattern of a four-unit combination comprising four ring-like units. **(C)** Other 15 deformation patterns of the four-unit combination. Each deformation pattern is represented by a $x_c/n - y_c/n$ curve. For all units, the value of θ_1 is the same, and $0 \leq \theta_1 \leq 180°$. The 16 patterns can be divided into four groups, shown against white (group #1), green (group #2), blue (group #3), and orange (group #4) backgrounds. **(D)** Combination within a group: #3.1 and #3.4; combination across groups: #3.1 and #2.1.

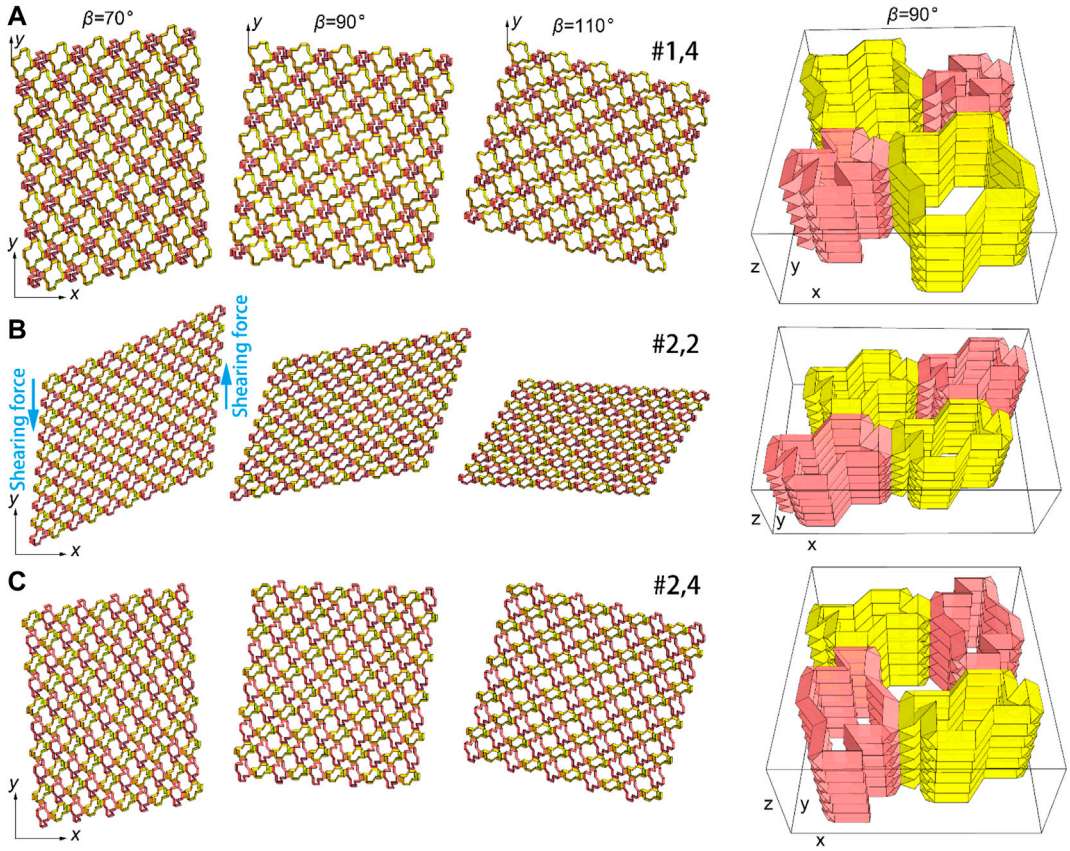

FIGURE 6 | Shearing deformation modes of the 2D cellular structure. Three of the 16 discrete patterns in **Figure 5C**, **(A)** #1.4 **(B)** #2.2 **(C)** #2.4; column 1–3, 2D cellular structures with β = 70°, 90°, and 110°; column 4, 3D cellular structures with β = 90°.

Another Method for Building 2D and 3D Cellular Structures

Finally, we explore another design of cellular structures consisting of multiple ring-like units with $\beta = 90°$ (see **Figure 7**). Different from the manner in **Figure 6**, the 2D cellular structure is constructed by symmetrically connecting the ring-like units with the same pattern in the x- and *y*-direction, and the 3D cellular structure is also built by stacking 2D structures. Similar to the units discussed earlier, both the 2D and 3D structures are flat-foldable. By taking advantage of our analysis of a unit cell, we can design new 2D and 3D cellular structures exhibiting anisotropic and isotropic deformation in the x–y plane under uniaxial compression/tension in the *z*-direction. Similar to a ring-like unit with $\gamma_1 = 45°$ and $\gamma_2 = 60°$ (**Figure 1D**, solid lines), a 3D cellular structure comprising the same units shows two anisotropic deformation behaviors: for ② → ①, we have $\nu_{zx} > 0$ and $\nu_{zy} > 0$ but $\nu_{zx} \neq \nu_{zy}$; and for ② → ③, $\nu_{zx} < 0$ and $\nu_{zy} > 0$ (**Figure 7A**); likewise, the 3D cellular structure shows two other anisotropic deformation behaviors: for ⑤ → ④, $\nu_{zx} > 0$, and $\nu_{zy} < 0$; and for ⑤ → ⑥, $\nu_{zx} < 0$ and $\nu_{zy} < 0$ but $\nu_{zx} \neq \nu_{zy}$ (**Figure 7B**). Although ν_{zx} and ν_{zy} have the same sign, their values are different because of $\gamma_1 \neq \gamma_2$ (see also a ring-like unit in **Figure 1D** with $\gamma_1 = 45°$ and $\gamma_2 = 60°$, solid lines). Moreover, isotropic behaviors can be realized with the same value of γ_1 and γ_2. **Figure 7C** shows two isotropic deformation behaviors with $\gamma_1 = \gamma_2 = 60°$: for ② → ①, $\nu_{zx} > 0$ and $\nu_{zy} > 0$; for ② → ⑥, $\nu_{zx} < 0$, and $\nu_{zy} < 0$ (see also a ring-like unit in paths ② → ① and ⑤ → ⑥ in **Figure 1D** with $\gamma_1 = \gamma_2 = 60°$, nonsolid lines, notice that configurations ② and ⑤ are identical, as shown in **Figures 1B,C**). These cellular structures also have only one DOF with $\beta = 90°$ (folding and unfolding by manipulating one parameter, i.e., the deformation angle θ_1; see **Figure 1B**), which can be easily controlled as an origami robot. Using this construction method, we can realize the deformation behavior of a 3D cellular structure only based on that of a single unit.

The cellular structures in **Figure 7** with 6 × 6 × 6 units look like 2.5D because for each unit, the height is less than the length or the width. But in essence, the structures are 3D since the layers can be continuously stacked along the *z*-direction, such as with 6 × 6 × 12 units. Here, we used 6 × 6 × 6 units for clear visualization.

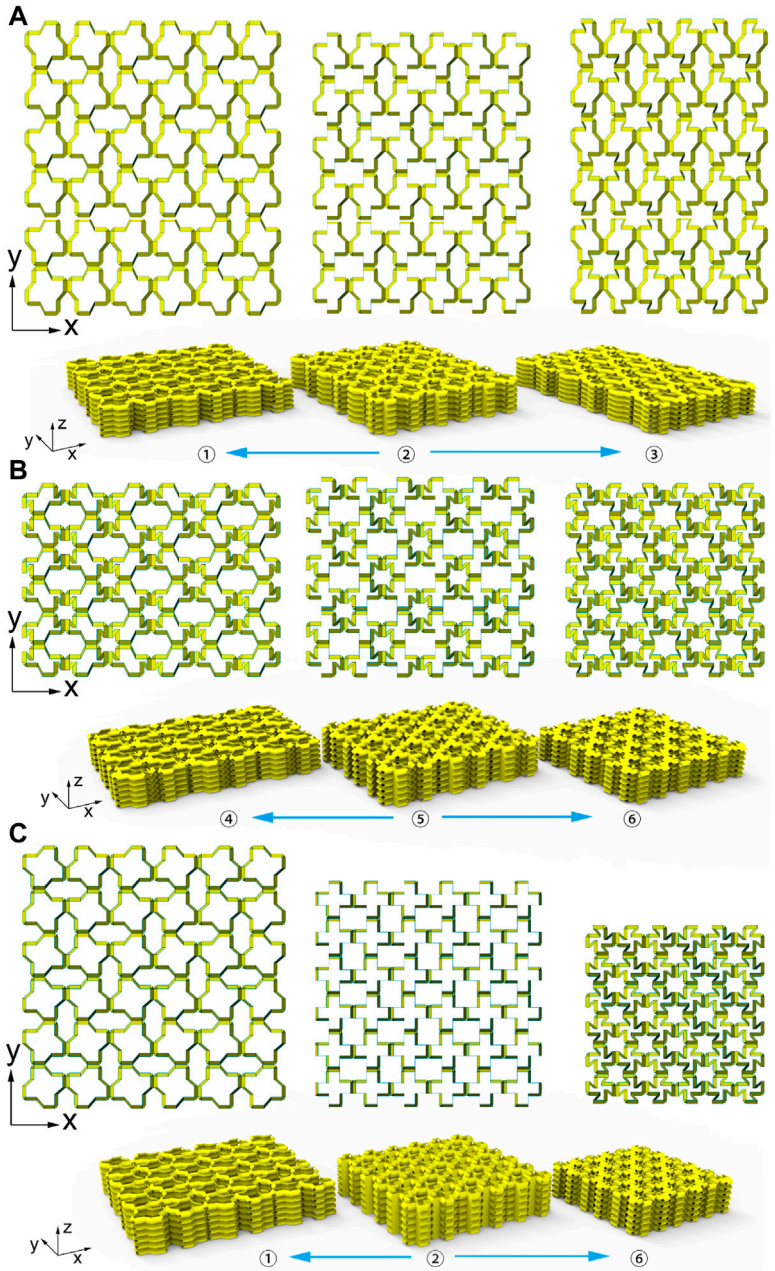

FIGURE 7 | Three patterns of 3D cellular structures. **(A)** Deformation paths ② → ① *and* ② → ③ with $\gamma_1 = 45°$ and $\gamma_2 = 60°$. **(B)** Deformation paths ⑤ → ④ *and* ⑤ → ⑥ with $\gamma_1 = 45°$ and $\gamma_2 = 60°$. **(C)** Deformation paths ② → ① *and* ② → ⑥ with $\gamma_1 = \gamma_2 = 60°$. Anisotropic pattern: **(A)** and **(B)**; isotropic pattern: **(C)**. Top: 2D metamaterials with 6 × 6 units. Bottom: 3D metamaterials with 6 × 6 × 6 units.

CONCLUSION

We have investigated the unique kinematics of kirigami-based 3D metamaterials with ring-like units. We foundd that the various combinations of Poisson's ratios (values and signs) can be obtained with different combinations of the design angles γ_1 and γ_2 and targeted Poisson's ratios can be realized by choosing the proper deformation paths. Additionally, we numerically and experimentally verified the analytical geometrical model of the ring-like unit cell. Interestingly, we showed multiple continuous and discrete deformation patterns for a ring-like unit and a multi-unit combination. These 2D and 3D cellular structures, offering multiple deformation patterns, show great potential for various engineering applications, from robotics, and impact absorbers to biomedical implants.

DATA AVAILABILITY STATEMENT

The original contributions presented in the study are included in the article/**Supplementary Material**; further inquiries can be directed to the corresponding authors.

AUTHOR CONTRIBUTIONS

NY designed and performed the research; JZ and SW processed the data; NY and YY analyzed the data and wrote the manuscript.

FUNDING

This work was supported by the National Natural Science Foundation of China (11872046), the Scientific Research Funding of Shantou University (NTF19012), the 2020 LKSF Cross-Disciplinary Research Projects (2020LKSFG01D), the Natural Science Foundation of Guangdong, China (2021A1515010318, 2022A1515011024, and 2018A030307030), the Key Project of Guangdong Provincial Department of Education (2021ZDZX2007), and the Science and Technology Project of Guangdong, China (180917114960497).

SUPPLEMENTARY MATERIAL

The Supplementary Material for this article can be found online at: https://www.frontiersin.org/articles/10.3389/fphy.2022.909536/full#supplementary-material

REFERENCES

1. Lee K, Wang Y, Zheng C. Twister Hand: Underactuated Robotic Gripper Inspired by Origami Twisted tower. *IEEE Trans Robot* (2020) 36:488–500. doi:10.1109/tro.2019.2956870
2. Hu W, Lum GZ, Mastrangeli M, Sitti M. Small-scale Soft-Bodied Robot with Multimodal Locomotion. *Nature* (2018) 554:81–5. doi:10.1038/nature25443
3. Kanik M, Orguc S, Varnavides G, Kim J, Benavides T, Gonzalez D, et al. Strain-programmable Fiber-Based Artificial Muscle. *Science* (2019) 365:145–50. doi:10.1126/science.aaw2502
4. Wu W, Hu W, Qian G, Liao H, Xu X, Berto F. Mechanical Design and Multifunctional Applications of Chiral Mechanical Metamaterials: a Review. *Mater Des* (2019) 180:107–950. doi:10.1016/j.matdes.2019.107950
5. Boatti E, Vasios N, Bertoldi K. Origami Metamaterials for Tunable thermal Expansion. *Adv Mater* (2017) 29:1700360. doi:10.1002/adma.201700360
6. Mirzaali MJ, Pahlavani H, Zadpoor AA. Auxeticity and Stiffness of Random Networks: Lessons for the Rational Design of 3D Printed Mechanical Metamaterials. *Appl Phys Lett* (2019) 115:021901. doi:10.1063/1.5096590
7. Dudek KK, Gatt R, Dudek MR, Grima JN. Negative and Positive Stiffness in Auxetic Magneto-Mechanical Metamaterials. *Proc R Soc A* (2018) 474: 20180003. doi:10.1098/rspa.2018.0003
8. Yang H, Ma L. Multi-stable Mechanical Metamaterials with Shape-Reconfiguration and Zero Poisson's Ratio. *Mater Des* (2018) 152:181–90. doi:10.1016/j.matdes.2018.04.064
9. Tan X, Wang B, Zhu S, Chen S, Yao K, Xu P, et al. Novel Multidirectional Negative Stiffness Mechanical Metamaterials. *Smart Mater Struct* (2019) 29: 015037. doi:10.1088/1361-665x/ab47d9
10. Yang N, Chen C-W, Yang J, Silverberg JL. Emergent Reconfigurable Mechanical Metamaterial Tessellations with an Exponentially Large Number of Discrete Configurations. *Mater Des* (2020) 196:109143. doi:10.1016/j.matdes.2020.109143
11. Dudek KK, Gatt R, Grima JN. 3D Composite Metamaterial with Magnetic Inclusions Exhibiting Negative Stiffness and Auxetic Behaviour. *Mater Des* (2020) 187:108403. doi:10.1016/j.matdes.2019.108403
12. Sui N, Yan X, Huang TH, Xu J, Yuan FG, Jing Y. A Lightweight yet Sound-Proof Honeycomb Acoustic Metamaterial. *Appl Phys Lett* (2015) 106:171–905. doi:10.1063/1.4919235
13. Lee C-M, Goverdovskiy VN. A Multi-Stage High-Speed railroad Vibration Isolation System with "negative" Stiffness. *J Sound Vibration* (2012) 331: 914–21. doi:10.1016/j.jsv.2011.09.014
14. Le TD, Ahn KK. Experimental Investigation of a Vibration Isolation System Using Negative Stiffness Structure. *Int J Mech Sci* (2013) 70:99–112. doi:10.1016/j.ijmecsci.2013.02.009
15. Nagarajaiah S, Pasala DTR, Reinhorn A, Constantinou M, Sirilis AA, Taylor D. Adaptive Negative Stiffness: a New Structural Modification Approach for Seismic protection. *Amr* (2013) 639-640:54–66. doi:10.4028/www.scientific.net/amr.639-640.54
16. Kuribayashi K, Tsuchiya K, You Z, Tomus D, Umemoto M, Ito T, et al. Self-deployable Origami Stent Grafts as a Biomedical Application of Ni-Rich TiNi Shape Memory alloy Foil. *Mater Sci Eng A* (2006) 419:131–7. doi:10.1016/j.msea.2005.12.016
17. Imbalzano G, Linforth S, Ngo TD, Lee PVS, Tran P. Blast Resistance of Auxetic and Honeycomb sandwich Panels: Comparisons and Parametric Designs. *Compos Structures* (2018) 183:242–61. doi:10.1016/j.compstruct.2017.03.018
18. Dudek KK, Wolak W, Gatt R, Grima JN. Impact Resistance of Composite Magnetic Metamaterials. *Sci Rep* (2019) 9:3963. doi:10.1038/s41598-019-40610-w
19. Zhang L, Feih S, Daynes S, Chang S, Wang MY, Wei J, et al. Energy Absorption Characteristics of Metallic Triply Periodic Minimal Surface Sheet Structures under Compressive Loading. *Additive Manufacturing* (2018) 23:505–15. doi:10.1016/j.addma.2018.08.007
20. Scarpa F, Yates JR, Ciffo LG, Patsias S. Dynamic Crushing of Auxetic Open-Cell Polyurethane Foam. *Proc Inst Mech Eng C: J Mech Eng Sci* (2002) 216: 1153–6. doi:10.1243/095440602321029382
21. Li M, Shen L, Jing L, Xu S, Zheng B, Lin X, et al. Origami Metawall: Mechanically Controlled Absorption and Deflection of Lightflection of Light. *Adv Sci* (2019) 6:1901434. doi:10.1002/advs.201901434
22. Wang H, Zhao D, Jin Y, Wang M, Mukhopadhyay T, You Z. Modulation of Multi-Directional Auxeticity in Hybrid Origami Metamaterials. *Appl Mater Today* (2020) 20:100715. doi:10.1016/j.apmt.2020.100715
23. Reis PM, Jaeger HM, Van Hecke M. Designer Matter: A Perspective. *Extreme Mech Lett* (2015) 5:25–9. doi:10.1016/j.eml.2015.09.004
24. Fang H, Wang KW, Li S. Asymmetric Energy Barrier and Mechanical Diode Effect from Folding Multi-Stable Stacked-Origami. *Extreme Mech Lett* (2017) 17:7–15. doi:10.1016/j.eml.2017.09.008
25. He YL, Zhang PW, You Z, Li ZQ, Wang ZH, Shu XF. Programming Mechanical Metamaterials Using Origami Tessellations. *Composites Sci Tech* (2020) 189:108015. doi:10.1016/j.compscitech.2020.108015
26. Zhai Z, Wang Y, Jiang H. Origami-inspired, On-Demand Deployable and Collapsible Mechanical Metamaterials with Tunable Stiffness. *Proc Natl Acad Sci U.S.A* (2018) 115:2032–7. doi:10.1073/pnas.1720171115
27. Liu B, Silverberg JL, Evans AA, Santangelo CD, Lang RJ, Hull TC, et al. Topological Kinematics of Origami Metamaterials. *Nat Phys* (2018) 14:811–5. doi:10.1038/s41567-018-0150-8
28. Zhang J, Karagiozova D, You Z, Chen Y, Lu G. Quasi-static Large Deformation Compressive Behaviour of Origami-Based Metamaterials. *Int J Mech Sci* (2019) 153-154:194–207. doi:10.1016/j.ijmecsci.2019.01.044
29. Brunck V, Lechenault F, Reid A, Adda-Bedia M. Elastic Theory of Origami-Based Metamaterials. *Phys Rev E* (2016) 93:033005. doi:10.1103/PhysRevE.93.033005

30. Yang N, Silverberg JL. Decoupling Local Mechanics from Large-Scale Structure in Modular Metamaterials. *Proc Natl Acad Sci U.S.A* (2017) 114: 3590–5. doi:10.1073/pnas.1620714114
31. Yasuda H, Yang J. Reentrant Origami-Based Metamaterials with Negative Poisson's Ratio and Bistability. *Phys Rev Lett* (2015) 114:185502. doi:10.1103/physrevlett.114.185502
32. Ruzzene M, Scarpa F, Soranna F. Wave Beaming Effects in Two-Dimensional Cellular Structures. *Smart Mater Struct* (2003) 12:363–72. doi:10.1088/0964-1726/12/3/307
33. Qin G, Qin Z. Negative Poisson's Ratio in Two-Dimensional Honeycomb Structures. *Npj Comput Mater* (2020) 6:51. doi:10.1038/s41524-020-0313-x
34. Yang N, Zhang M, Zhu R. 3D Kirigami Metamaterials with Coded thermal Expansion Properties. *Extreme Mech Lett* (2020) 40:100912. doi:10.1016/j.eml.2020.100912
35. Wang H, Zhao D, Jin Y, Wang M, Mukhopadhyay T, You Z. Modulation of Multi-Directional Auxeticity in Hybrid Origami Metamaterials. *Appl Mater Today* (2020) 20:100715. doi:10.1016/j.apmt.2020.100715
36. Pratapa PP, Liu K, Paulino GH. Geometric Mechanics of Origami Patterns Exhibiting Poisson's Ratio Switch by Breaking Mountain and valley Assignment. *Phys Rev Lett* (2019) 122:155501. doi:10.1103/physrevlett.122.155501
37. Xue R, Li R, Du Z, Zhang W, Zhu Y, Sun Z, et al. Kirigami Pattern Design of Mechanically Driven Formation of Complex 3D Structures through Topology Optimization. *Extreme Mech Lett* (2017) 15:139–44. doi:10.1016/j.eml.2017.03.004

Conflict of Interest: The authors declare that the research was conducted in the absence of any commercial or financial relationships that could be construed as a potential conflict of interest.

frontiers | Frontiers in Physics

TYPE Original Research
PUBLISHED 13 October 2022
DOI 10.3389/fphy.2022.1046781

OPEN ACCESS

EDITED BY
Yifan Zhu,
Southeast University, China

REVIEWED BY
Shi-Wang Fan,
Shijiazhuang Tiedao University, China
Xudong Fan,
Nanjing University of Science and Technology, China

*CORRESPONDENCE
Fengbao Yang,
yfengb@163.com

SPECIALTY SECTION
This article was submitted to Physical Acoustics and Ultrasonics, a section of the journal Frontiers in Physics

RECEIVED 17 September 2022
ACCEPTED 03 October 2022
PUBLISHED 13 October 2022

CITATION
Wang R and Yang F (2022), Acoustic wavefront manipulation via transmission-type labyrinth structure. *Front. Phys.* 10:1046781. doi: 10.3389/fphy.2022.1046781

Acoustic wavefront manipulation *via* transmission-type labyrinth structure

Rui Wang and Fengbao Yang*

School of Information and Communication Engineering, North University of China, Taiyuan, Shanxi, China

In this work, a transmission-type labyrinth structure (LS) is proposed to construct subwavelength acoustic functional metasurfaces, through which various desirable acoustic wavefront manipulation can be achieved in a broadband from 2,700 Hz to 3,900 Hz. By utilizing the excellent guiding property of LS, an invisibility cloak is designed to shield the target scattering body in the transmitted field. In addition, gradient metasurfaces composed of several LSs with different phase responses are constructed to obtain broadband beam deflection and focusing. Moreover, binary coding approach is adopted to further simplify the design philosophy of the metasurfaces by taking advantage of only two kinds of LS with opposite phase responses. Numerous wavefront manipulations including acoustic splitting beam and self-bending beam can be realized by using corresponding coding sequences. Our work provides a solution for multifunctional acoustic wavefront manipulation in a broadband, which may have potential applications in acoustic communication, detection and holography.

KEYWORDS

acoustic focusing, acoustic waveguide, broadband response, periodic structure, binary design

1 Introduction

Acoustic wavefront manipulation is desirable in numerous engineering applications such as acoustic communication, detection, holography and bioimaging. Three wavefront categories including reflection wave, absorption wave and transmission wave are essential for target pattern of the acoustic field. It is easy to manipulate the reflection wave by groove structures with different depths [1–4]. To achieve tunable and broadband reflected wavefront modulation, Fan et al. [5] proposed a helical metasurface, through which many interesting acoustic phenomena including anomalous reflection, arbitrary focusing and self-bending beams were realized. They also designed a tunable lossy metsurface to achieve multi-plane acoustic holograms [6]. Weng et al. [7] adopted multiple resonant elements to construct an ultrathin planar metasurface with wavelength-dependent manipulation. Meanwhile, porous materials are investigated to achieve perfect absorption [8, 9]. For transmission wave, although using phased array transducers is an effective approach to generate arbitrary transmission wavefront, it has disadvantages in large scale, complex circuit and high cost.

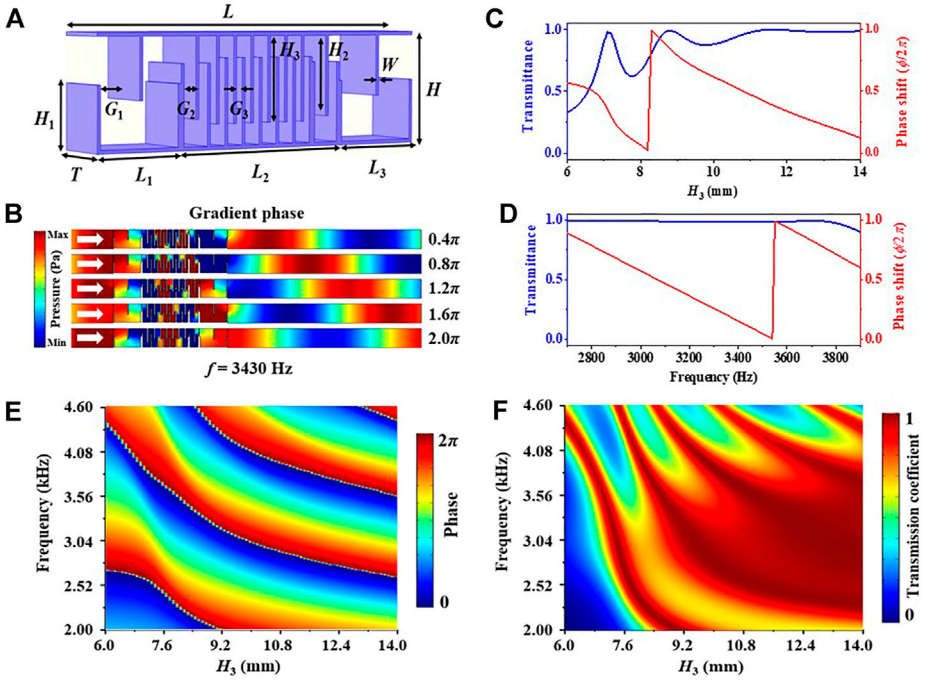

FIGURE 1
(A) The three-dimensional schematic of LS. **(B)** The acoustic pressure distributions of the LS with different interdigital length (H_3 = 13.30 mm, 11.53 mm, 10.12 mm, 8.97 mm, 8.30 mm) at 3,430 Hz. **(C)** The relation between the interdigital length and transmission information (transmittance and phase shift) for LS. **(D)** The relation between the operating frequency and transmission information (transmittance and phase shift) for LS. **(E)** The relation between phase shift and incident frequency with the increase of parameter H_3. **(F)** The relation between transmission coefficient and incident frequency with the increase of parameter H_3.

In past decade, the development of acoustic metamaterial and metasurface provides another method to manipulate the transmission wavefront by artificial passive structures [10–17]. By utilizing the band characteristics of the phononic crystals, some abnormal acoustic phenomena for instance negative refraction [18], beam focusing [19] and topological energy transport [20] have been widely reported. Meanwhile, multiple fascinating acoustic wavefront modulations including splitting beam [21], vortex beam [22], Airy beam [23], focusing beam [24], and acoustic illusion [25] have been realized by taking advantage of the Helmholtz resonators [26], spiral cavities [27] and coiling waveguides [28]. For example, Zhu et al. [29] reported an investigation of multiplexed acoustic holograms at both audio and ultrasonic frequencies *via* a rationally designed transmission-type metamaterial. Wang et al. [30] proposed a tunable flat acoustic metasurface composed of fan-shaped annular resonator arrays. However, both the phononic crystals and resonant cavities are suffering from the limitation of bandwidth. In addition, the structure designed by phononic crystals has a large size, while that by resonant cavities needs a complicated configuration. Therefore, a simple design method for the realization of broadband acoustic wavefront manipulation is needed to be sought.

In this work, we propose a transmission-type labyrinth structure (LS) with sub-wavelength scale to achieve various acoustic wavefront manipulations. By changing the interdigital length of the LS, the phase response of the transmission wave can cover a full range from 0 to 2π under a high transmittance. Thanks to the excellent guiding property of LS to the transmission acoustic waves, a stealth structure is constructed to shield target scattering body. Meanwhile, a metasurface composed of several LSs with gradient phase responses is designed to achieve broadband beam deflection and beam focusing. Owing to the linear relation between operating frequency and phase shift, the metasurface showing a low dispersion feature for wavefront manipulation. Moreover, by taking advantage of the binary design, broadband splitting beam and self-bending beam are realized as well, which further simplify the design philosophy of the metasurface. Our work provides a solution for multifunctional acoustic wavefront manipulation in a broadband, which may have potential applications in acoustic communication, detection and holography.

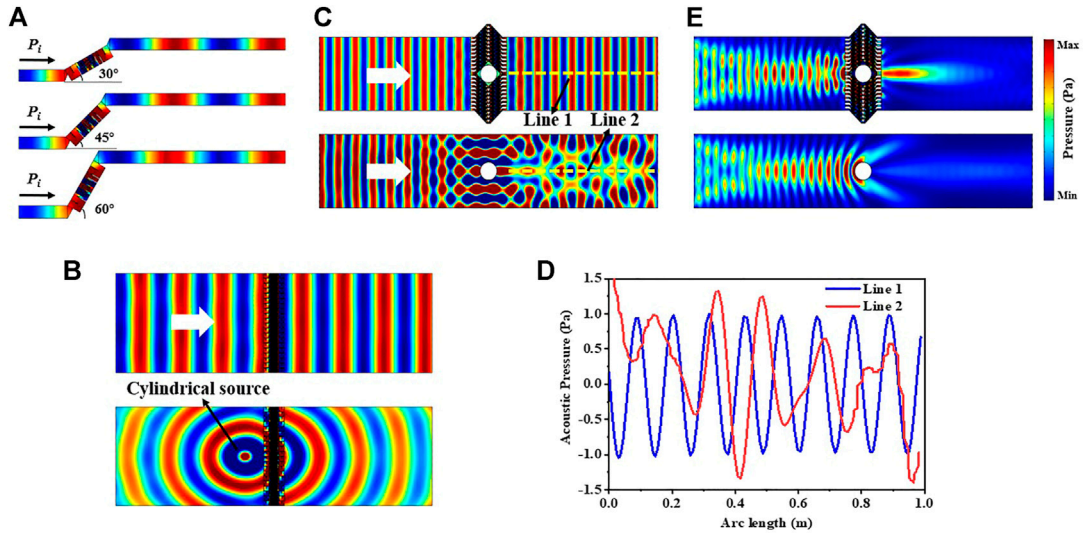

FIGURE 2
Acoustic pressure distributions of **(A)** the waveguide designed by LS with different rotation angles, **(B)** the array of LS stimulated by plane and cylindrical sources, and **(C)** the circular scattering body surrounded by LS array and without LS array at 3,430 Hz. **(D)** Acoustic pressure distributions along Lines one and 2 marked by yellow dashed lines in Panel 2C. **(E)** Acoustic intensity distributions of the circular scattering body surrounded by LS array and without LS array at 3,430 Hz.

2 Model design and analysis

As shown in Figure 1A, the LS designed in our work is a rectangular cavity with several interdigital plates. The length, height, and thickness of the LS are L = 55.5 mm, H = 15.5 mm, and T = 10 mm. The air gaps between two adjacent interdigital plates are G_1 = 6.4 mm, G_2 = 2 mm, and G_3 = 1 mm. The thickness and heights of interdigital plate at different positions are w = 0.5 mm and H_1 = 8.6 mm, H_2 = 11.3 mm, H_3 = 12 mm, respectively. The LS is a mirror symmetrical structure, and the lengths of each composing cavity are L_1 = L_3 = 14 mm, L_2 = 27.5 mm. Here, we adopt finite element software COMSOL Multiphysics to calculate the transmission information of the LS. The acoustic velocity and density of the air are c = 343 m/s and ρ = 1.29 kg/m^3. Hard acoustic field conditions are set along the upper and lower boundaries of the LS, and plane wave radiation conditions are used in left and right boundaries of the LS to avoid unwanted echo interference. When we adjust the height of middle interdigital plate (H_3), as shown in Figure 1C, the transmission information including transmittance and phase responses of the LS can be modulated correspondingly at 3,430 Hz. The phase shift can nearly cover a full range from 0 to 2π under a high transmittance when H_3 changes from 8.3 mm to 14 mm, exhibiting an excellent performance for wavefront modulation by LS with subwavelength scale. The high transmittance steams from resonance effect of the LS and the phase shift originates from the change of equivalent acoustic velocity (or propagation length) caused by different shield heights. According to the acoustic pressure distributions shown in Figures 1A,B gradient phase response (ϕ = 0.4π, 0.8π, 1.2π, 1.6π, 2.0π) is generated by five LSs with different parameters (H_3 = 13.30 mm, 11.53 mm, 10.12 mm, 8.97 mm, 8.30 mm) for plane wave incidence at 3,430 Hz, which verifies the ability of phase modulation for transmission wave. In addition, as illustrated in Figure 1D, the phase shift is linear with the operating frequency in a broadband of 2,700 Hz–3900 Hz, and the transmittance of the LS is relatively high (near unity) within this band. Therefore, as shown in Figures 1E,F), the gradient of the phase delay can be linear in a frequency range of 2,700 Hz–3900 Hz under a high transmission coefficient when H_3 > 7.6 mm, providing an opportunity to achieve broadband acoustic wavefront manipulation.

3 Results and discussions

The LS proposed here is flexible, which can control the acoustic propagation path of the transmission wavefront by rotating different angles. As shown in Figure 2A, the LSs with rotation angles of 30°, 45°, and 60° have identical transmission wavefront under the same incident condition (normal incidence at 3,430 Hz). With the increase of rotation angle, the acoustic propagation path moves up gradually, making it is suitable for LS to construct invisibility cloak. As shown in Figure 2B, when the plane acoustic wave normally incident on the LS array, the shape of wavefront in the transmission field is the same as that in the incident field. The result is applicable to both plane wave incidence and spherical wave incidence, indicating a zero refractive property of the LS array. Taking a circular scattering

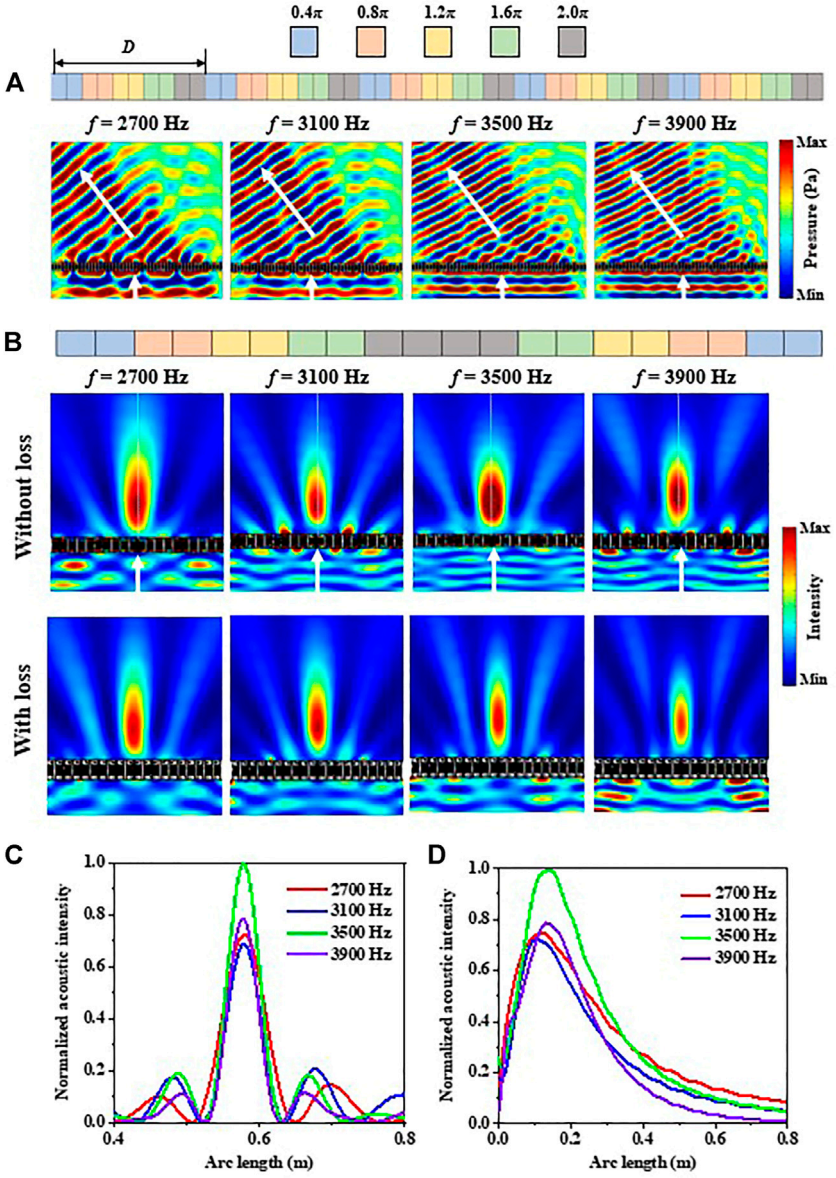

FIGURE 3
(A) Acoustic pressure distributions and **(B)** intensity distributions of the metasurface composed of LS with different interdigital length at 2,700 Hz, 3,100 Hz, 3,500 Hz and 3,900 Hz. Normalized acoustic intensities along **(C)** horizontal and **(D)** vertical cut-lines in Panel 3B.

body as an example, as shown in Figure 2C, the transmission wavefront is damaged and disorderly when the scattering body is placed in a free air space for normal incidence, making it is easy to be detected under this circumstance. As a comparison, when the scattering body is surrounded by LS array, the incident acoustic waves propagate along the designed path and bypass the scattering body. In this case, the shape of transmission wavefront remains unchanged, and the scattering body is invisible. To further verify the stealth performance of the LS array, as shown in Figure 2D, the acoustic amplitude and pressure distribution along the cut-line 1 marked in Figure 1C is periodic and uniform. The target scattering body is hardly to be detected since the waveform in the transmission field is identical to that in the incident field. For acoustic amplitude and pressure distributions along the cut-line 2 marked in Figure 1C, it is uneven and visible owing to the strong scattering by rigid body. Therefore, the acoustic cloak designed by LS array can extremely improve the security of the acoustic target.

Next, we construct a gradient metasurface composed of periodic LS arrays to achieve desirable acoustic beam shaping. Similar to the generalized Snell's law in optics [31], if the acoustic wave with a frequency f is incident from one medium to another, the generalized Snell's law in acoustics can be expressed as follows:

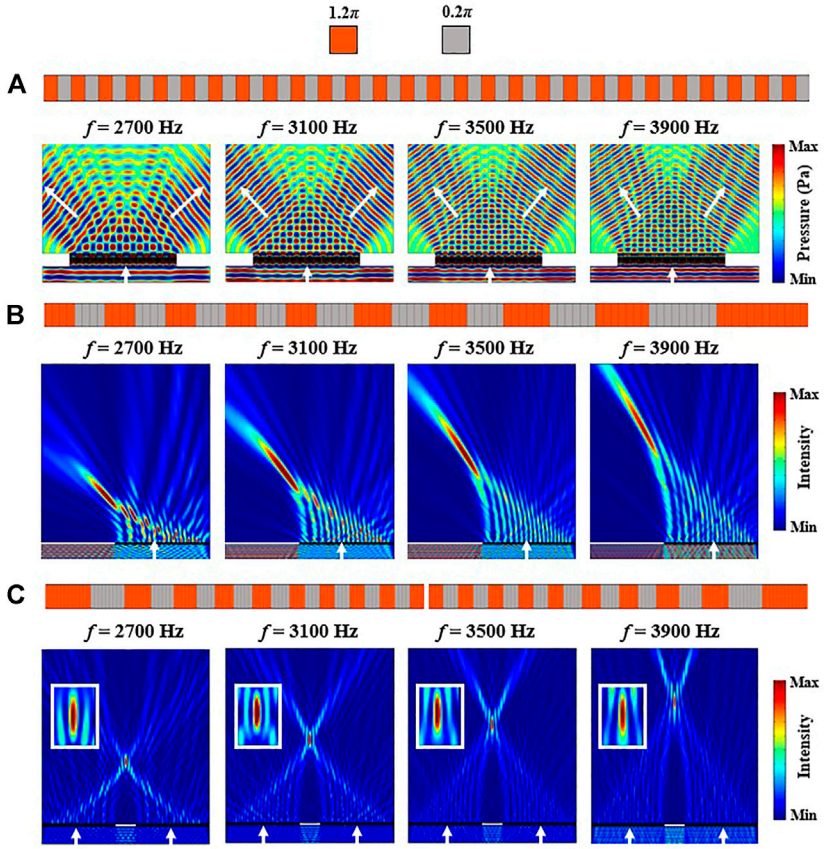

FIGURE 4
(A) Acoustic pressure distributions and **(B)**, **(C)** intensity distributions of the binary metasurfaces at 2,700 Hz, 3,100 Hz, 3,500 Hz and 3,900 Hz.

$$k_t \sin\theta_t - k_i \sin\theta_i = d\phi(x)/dx \quad (1)$$

$$k_i = 2\pi f/c_i \quad (2)$$

$$k_t = 2\pi f/c_t \quad (3)$$

where θ_i and θ_t represent the incident angle and refraction angle; c_i and c_t represent the acoustic velocities of the incident medium and transmitted medium, respectively; $d\phi(x)/dx$ represents the phase gradient along the metasurface. To be simplified, we consider the case of $\theta_i = 0$, and Eq. 1 is rewritten as

$$k_t \sin\theta_t = d\phi(x)/dx \quad (4)$$

Following Eq. 4, the refraction property of the metasurface is closely related to the phase gradient along the metasurface. As shown in Figures 3A supercell composed of ten LSs is constructed as a periodic unit. The rectangular blocks with different colors correspond to distinct phase responses. The phase shifts from left to right are 0.4π, 0.4π, 0.8π, 0.8π, 1.2π, 1.2π, 1.6π, 1.6π, 2.0π, 2.0π. The design principle of the period length should be longer than incident wavelength, otherwise the surface acoustic wave will appear [32]. In Figure 3A, the period length is set as D = 155 mm, and it can be adjusted by altering the number of LS. When plane acoustic waves are normally incident on the metasurface, the propagation direction of the transmission wavefront is changed. The simulated acoustic pressure distributions verify that the desirable acoustic beam deflection is generated by a gradient metasurface. Meanwhile, the metasurface can work well in a broadband within 2,700 Hz–3900 Hz, showing an excellent wavelength tolerance.

The function of the metasurface can be changed if we adopt other arrangements of LS. As shown in Figures 3A,B mirror symmetrical structure composed of 20 LSs is constructed to serve as an acoustic lens. From left to right, the phase responses of 20 LSs are 0.4π, 0.4π, 0.8π, 0.8π, 1.2π, 1.2π, 1.6π, 1.6π, 2.0π, 2.0π, 2.0π, 2.0π, 1.6π, 1.6π, 1.2π, 1.2π, 0.8π, 0.8π, 0.4π, 0.4π. Owing to the symmetrical distributions of the phase response, interference superposition of acoustic intensity is generated in the transmitted field. The acoustic intensity distributions of the metasurface shown in Figure 3B confirms that the incident plane acoustic waves are converted into focusing beams after passing through the designed lens, and the metasurface can work in a broadband from 2,700 Hz to 3900 Hz. Figure 3B also illustrates the acoustic intensity distribution of the metasurface with thermal viscosity loss, it can be seen that although the intensity of the focus is reduced compared with that in lossless case, the ability of beam focusing exists. In addition, note that the refraction angle of the transmission wave shown in Figure 3A and the focal length of the focus shown in Figure 3B are independent of incident frequencies.

Following the linear relation between transmitted phase response and incident frequency shown in Figure 1D, the change of incident wavelength and gradient phase response along the metasurface can be offset, exhibiting a low dispersion feature for gradient metasurface. Figure 3C shows the normalized acoustic intensity distributions along the cut-line of $y = 0.15$ m marked in Figure 3B, apparent acoustic wave convergence can be observed at this position. The peak intensity value of the focus is at 3,500 Hz, which near the center frequency (3,430 Hz) of the LS. Moreover, the performance of the beam focusing can also be verified by plotting the normalized acoustic intensity distributions along the cut-line of $x = 0$ m marked in Figure 3B. From Figure 3D it can be seen that the beam focusing for different incident frequencies from 2,700 Hz to 3,900 Hz is generated at the position of $y = 0.15$ m, and the high intensity value of the focus is at 3,500 Hz, which agrees well with the results shown in Figure 3C. Therefore, the gradient metasurfaces designed by LSs not only can work in a broadband, but also have a low dispersion feature for acoustic wavefront manipulation [33].

As another feasible approach to realize broadband acoustic wavefront manipulation, binary design for functional metasurface can further simplify the design philosophy since only two kinds of coding units with high transmittance and opposite phase responses are needed [34–39]. We define LS with parameters of $H_3 = 10$ mm and $H_3 = 14$ mm as coding bits '0' and '1', respectively. Following the relation between phase shift of the LS and parameter H_3 shown in Figure 1C, coding bit '0' has a phase response of 1.2π and coding bit '1' has a phase response of 0.2π, which meets the requirement of opposite phase response for the design of binary metasurface. As shown in Figure 4A, an acoustic beam splitter is composed of two coding bits '0' and '1' with a periodic coding sequence of 01/01/01 . . . 01/01/01, and the cycle length is set as $D = 160$ mm. According to the generalized Snell's law, the diffraction orders of $n = 0, 1, -1$ are all open for normal incidence when the reciprocal lattice vector ($G = 2\pi/D$) is smaller than the wavenumber in air background. However, the diffraction orders of $n = 1, -1$ is preferential to the $n = 0$ order, leading to a beam splitting stemming from the transmission channel of the $n = 1, -1$ orders for normal incidence. The simulated acoustic pressure distributions display apparent beam splitting at four different frequencies (2,700 Hz, 3,100 Hz, 3,500 Hz and 3,900 Hz), verifying the broadband performance of the beam splitter.

Meanwhile, the function of the metasurface can be customized by adopting different coding sequences. Taking acoustic self-bending beam as an example, as shown in Figure 4B, the coding sequence of the metasurface is a staggered arrangement composed of coding bits '0' (orange blocks) and '1' (grey blocks). From left to right, the numbers of the coding bit are 4, 4, 4, 4,4,4,4,4,4,5,5,5,5,5,5,6,6,7,9,12. The incident plane acoustic wave can be converted into self-bending beam at this time. The intensity of the transmitted wave is localized in the main lobe, and the trajectory of transmission wave is curved. Similar to the beam splitter, the acoustic self-bending beam generator can work in a broadband of 2,700 Hz–3900 Hz as well. Moreover, if we place two self-bending beam generators in a mirror symmetrical manner, as shown in Figure 4C, acoustic beam focusing can be obtained owing to the interference superposition from two identical self-bending beams with opposite radiation directions, which further expends the function of binary metasurface designed by LSs.

4 Conclusion

In summary, a labyrinth structure (LS) is proposed in this work for transmitted acoustic wavefront manipulation. Owing to the excellent guiding property of LS, an invisibility cloak is designed to achieve acoustic stealth for scattering body. The transmission information including phase response and transmittance of the LS can be modulated by the height of interdigital plate, and there exists a linear relation between phase shift and incident wavelength, which can be adopted to construct gradient acoustic metasurfaces to achieve beam deflection and focusing in a broadband from 2,700 Hz to 3,900 Hz. Moreover, a binary design for acoustic metasurface is utilized to further simplify the design philosophy by using only two kinds of LS with opposite phase responses. Two binary metasurfaces with different coding sequences are constructed to play the roles of acoustic beam splitter and self-bending beam generator, through which the broadband wavefront manipulation has been obtained. The acoustic metasurface constructed by LS has the advantages of simple design, subwavelength scale and broadband response, which may have potential applications in acoustic communication, detection and holography.

Data availability statement

The original contributions presented in the study are included in the article/supplementary material, further inquiries can be directed to the corresponding author.

Author contributions

RW conceived the presented idea, performed the calculations and simulations and drafted the manuscript. All authors discussed the results and contributed to the final manuscript.

Funding

This work was supported by the National Natural Science Foundation of China (61972363).

Conflict of interest

The authors declare that the research was conducted in the absence of any commercial or financial relationships that could be construed as a potential conflict of interest.

Publisher's note

References

1. Zhang Y, Cheng H, Tian J, Chen S. Frequency-Selected bifunctional coding acoustic metasurfaces. *Phys Rev Appl* (2020) 14:064057. doi:10.1103/physrevapplied.14.064057

2. Zhu Y, Assouar B. Multifunctional acoustic metasurface based on an array of Helmholtz resonators. *Phy Rev B* (2019) 99:174109. doi:10.1103/physrevb.99.174109

3. Zhang Y, Xie B, Liu W, Cheng H, Chen S, Tian J. Anomalous reflection and vortex beam generation by multi-bit coding acoustic metasurfaces. *Appl Phys Lett* (2019) 114:091905. doi:10.1063/1.5087636

4. Song X, Chen T, Huang W, Chen C. Frequency-selective modulation of reflected wave fronts using a four-mode coding acoustic metasurface. *Phys Lett A* (2021) 394:127145. doi:10.1016/j.physleta.2021.127145

5. Fan S, Zhao S, Chen A, Wang Y, Assouar B, Wang Y. Tunable broadband reflective acoustic metasurface. *Phys Rev Appl* (2019) 11:044038. doi:10.1103/physrevapplied.11.044038

6. Fan S, Zhu Y, Cao L, Wang Y, Chen A, Merkel A, et al. Broadband tunable lossy metasurface with independent amplitude and phase modulations for acoustic holography. *Smart Mater Struct* (2020) 29:105038. doi:10.1088/1361-665x/abaa98

7. Weng J, Zhu Y, Liang B, Yang J, Cheng J. Wavelength-dependent multi-functional wavefront manipulation for reflected acoustic waves. *Appl Phys Express* (2020) 13:094003. doi:10.35848/1882-0786/abb062

8. Gao N, Zhang Z, Tang L, Hou H, Chen K. Optimal design of broadband quasi-perfect sound absorption of composite hybrid porous metamaterial using TLBO algorithm. *Appl Acoust* (2021) 183:108296. doi:10.1016/j.apacoust.2021.108296

9. Gao N, Wu J, Lu K, Zhong H. Hybrid composite meta-porous structure for improving and broadening sound absorption. *Mech Syst Signal Process* (2021) 154:107504. doi:10.1016/j.ymssp.2020.107504

10. Ju F, Xiong W, Liu C, Cheng Y, Liu X. Acoustic accelerating beam based on a curved metasurface. *Appl Phys Lett* (2019) 114:113507. doi:10.1063/1.5087544

11. Li X, Zhou H, Wang Y, Wang Y. Modulation of acoustic self-accelerating beams with tunable curved metasurfaces. *Appl Phys Lett* (2021) 118:023503. doi:10.1063/5.0035286

12. Tang S, Ren B, Feng Y, Song J, Jiang Y. The generation of acoustic Airy beam with selective band based on binary metasurfaces: Customized on demand. *Appl Phys Lett* (2021) 119:071907. doi:10.1063/5.0060032

13. Li Y, Shen C, Xie Y, Li J, Wang W, Cummer S, et al. Tunable asymmetric transmission via lossy acoustic metasurfaces. *Phys Rev Lett* (2017) 119:035501. doi:10.1103/physrevlett.119.035501

14. Xia J, Zhang X, Sun H, Yuan S, Qian J, Ge Y. Broadband tunable acoustic asymmetric focusing lens from dual-layer metasurfaces. *Phys Rev Appl* (2018) 10:014016. doi:10.1103/physrevapplied.10.014016

15. Zhang C, Cao W, Wu L, Ke J, Jing Y, Cui T, et al. A reconfigurable active acoustic metalens. *Appl Phys Lett* (2021) 118:133502. doi:10.1063/5.0045024

16. Tang S, Ren B, Feng Y, Song J, Jiang Y. Asymmetric acoustic beam shaping based on monolayer binary metasurfaces. *Appl Phys Express* (2021) 14:085504. doi:10.35848/1882-0786/ac15bf

17. Zhao J, Ye H, Huang K, Chen Z, Li B, Qiu C. Manipulation of acoustic focusing with an active and configurable planar metasurface transducer. *Sci Rep* (2014) 4:6257. doi:10.1038/srep06257

18. Li X, Gao J, Liu S, Zhou K, Huang B. *Acta Phys Sin* (2010) 59:376.

19. Tang S, Wang R, Han J. Acoustic focusing imaging characteristics based on double negative locally resonant phononic crystal. *IEEE Access* (2019) 7:112598–604. doi:10.1109/access.2019.2932419

20. Fleury R, Khanikaev A, Alu A. Floquet topological insulators for sound. *Nat Commun* (2016) 7:11744. doi:10.1038/ncomms11744

21. Li W, Meng F, Huang X. Coding metalens with helical-structured units for acoustic focusing and splitting. *Appl Phys Lett* (2020) 117:021901. doi:10.1063/5.0012784

22. Jiang X, Li Y, Liang B, Cheng J, Zhang L. Convert acoustic resonances to orbital angular momentum. *Phys Rev Lett* (2016) 117:034301. doi:10.1103/physrevlett.117.034301

23. Fan X, Huang X, Kang Y, Li C, Li N, Weng C. Ultra-broadband bending beam and bottle beam based on acoustic metamaterials. *Appl Sci (Basel)* (2022) 12:3025. doi:10.3390/app12063025

24. Fan X, Zhu Y, Liang B, Yang J, Cheng J. Broadband convergence of acoustic energy with binary reflected phases on planar surface. *Appl Phys Lett* (2016) 109:243501. doi:10.1063/1.4971795

25. Fan X, Liang B, Yang J, Cheng J. Illusion for airborne sound source by a closed layer with subwavelength thickness. *Sci Rep* (2019) 9:1750. doi:10.1038/s41598-018-38424-3

26. Li Y, Jiang X, Liang B, Cheng J, Zhang L. Metascreen-Based acoustic passive phased array. *Phys Rev Appl* (2015) 4:024003. doi:10.1103/physrevapplied.4.024003

27. Li K, Liang B, Yang J, Cheng J. Broadband transmission-type coding metamaterial for wavefront manipulation for airborne sound. *Appl Phys Express* (2018) 11:077301. doi:10.7567/apex.11.077301

28. Ghaffarivardavagh R, Nikolajczyk J, Holt R, Anderson S, Zhang X. Horn-like space-coiling metamaterials toward simultaneous phase and amplitude modulation. *Nat Commun* (2018) 9:1349. doi:10.1038/s41467-018-03839-z

29. Zhu Y, Gerard N, Xia X, Stevenson G, Cao L, Fan S, et al. Systematic design and experimental demonstration of transmission-type multiplexed acoustic metaholograms. *Adv Funct Mater* (2021) 31:2101947. doi:10.1002/adfm.202101947

30. Wang X, Yang J, Liang B, Cheng J. Tunable annular acoustic metasurface for transmitted wavefront modulation. *Appl Phys Express* (2020) 13:014002. doi:10.7567/1882-0786/ab59a5

31. Yu N, Genevet P, Kats M, Aieta F, Tetienne J, Capasso F, et al. Light propagation with phase discontinuities: Generalized laws of reflection and refraction. *Science* (2011) 334:333–7. doi:10.1126/science.1210713

32. Mei J, Wu Y. Controllable transmission and total reflection through an impedance-matched acoustic metasurface. *New J Phys* (2014) 16:123007. doi:10.1088/1367-2630/16/12/123007

33. Dong H, Shen C, Zhao S, Qiu W, Zheng H, Zhang C, et al. *Natl Sci Rev Nwac030* (2022).

34. Tang S, Wu J, Lü C, Song J, Jiang Y. Functional acoustic metamaterial using shortcut to adiabatic passage in acoustic waveguide couplers. *Phys Rev Appl* (2022) 18:014038. doi:10.1103/physrevapplied.18.014038

35. Xie B, Cheng H, Tang K, Liu Z, Chen S, Tian J. Multiband Asymmetric transmission of airborne sound by coded metasurfaces. *Phys Rev Appl* (2017) 7:024010. doi:10.1103/physrevapplied.7.024010

36. Tang S, Lü C, Wu J, Song J, Jiang Y. Wavelength-selected bifunctional beam shaping for transmitted acoustic waves via coding metasurface. *Appl Acoust* (2022) 194:108786. doi:10.1016/j.apacoust.2022.108786

37. Tang S, Ren B, Feng Y, Song J, Jiang Y. Broadband acoustic focusing via binary rectangular cavity/Helmholtz resonator metasurface. *J Appl Phys* (2021) 129:155307. doi:10.1063/5.0049407

38. Fu Y, Tao J, Song A, Liu Y, Xu Y. Controllably asymmetric beam splitting via gap-induced diffraction channel transition in dual-layer binary metagratings. *Front Phys (Beijing)* (2020) 15:52502. doi:10.1007/s11467-020-0968-2

39. Tang S, Wu J, Lü C, Wang X, Song J, Jiang Y. Acoustic wavelength-selected metamaterials designed by reversed fractional stimulated Raman adiabatic passage. *Phys Rev B* (2022) 105:104107. doi:10.1103/physrevb.105.104107

frontiers | Frontiers in Physics

TYPE Brief Research Report
PUBLISHED 31 October 2022
DOI 10.3389/fphy.2022.1041053

OPEN ACCESS

EDITED BY
Lingyun Yao,
Southwest University, China

REVIEWED BY
Lixia Li,
Xi'an University of Architecture and Technology, China
Yan-Feng Wang,
Tianjin University, China

*CORRESPONDENCE
Gang Wang,
wanggang@hebut.edu.cn

SPECIALTY SECTION
This article was submitted to Physical Acoustics and Ultrasonics, a section of the journal Frontiers in Physics

RECEIVED 10 September 2022
ACCEPTED 04 October 2022
PUBLISHED 31 October 2022

CITATION
Yang H and Wang G (2022), Polynomial eigenvalue solution for elastic wave prediction of piezoelectric shunting arrays.
Front. Phys. 10:1041053.
doi: 10.3389/fphy.2022.1041053

Polynomial eigenvalue solution for elastic wave prediction of piezoelectric shunting arrays

Huisong Yang and Gang Wang*

School of Mechanical Engineering, Hebei University of Technology, Tianjin, China

This paper presents a polynomial eigenvalue solution to predict the propagation behaviors of elastic wave in piezoelectric shunting arrays. Based on the Bloch theorem, one independent unit cell is selected to conduct the dynamic characteristic analysis instead of infinity. The reduced form of the discretized governing equations is first derived by the standard finite element procedures. To facilitate the subsequent acquisition of dispersion relationship, the dynamic stiffness matrix is then partitioned into a block matrix. Through applying the periodic boundary conditions, a polynomial eigenvalue equation concerning complex propagation constant is finally obtained. The wave propagation and attenuation characteristics in arbitrary directions are investigated using the above methodology. The results demonstrate that the present method can provide very accurate and reliable solutions for wave propagation prediction of piezoelectric shunting arrays.

KEYWORDS

polynomial eigenvalue solution, complex propagation constants, wave propagation and attenuation, arbitrary directions, piezoelectric shunting arrays

1 Introduction

Over the past several decades, the propagation of elastic waves including bulk waves [1] and surface waves [2] in phononic crystals (PCs) has attracted a great deal of interest [3, 4]. Due to the existence of band gaps, PCs have many potential applications, such as elastic wave filters and vibration isolation. There are two main mechanisms for the formation of band gaps, namely, Bragg scattering (BS) [5] and locally resonant (LR) [6]. Compared with the BS mechanism, the LR one allows the acquisition of low-frequency band gaps with the structure of small dimensions. Hence, researchers prefer to use the LR PCs for the reduction of vibration noise in practical engineering [7]. However, for the traditional PCs, the non-adjustable characteristics of band gaps restrict their practical application, especially for structures with variable working conditions. By combining the piezoelectric shunt damping technology [8, 9] with PCs theory, piezoelectric shunt arrays (PSA) which belong to a new type of PCs emerged. The tunable characteristics of shunt circuits allow the band gaps to be adjusted over desired frequency range. However, due to the existence of complex wave vectors caused by the piezoelectric shunt damping, it is not an easy work to predict the band structures of PSA using the traditional numerical approaches.

The transfer matrix method [10, 11] is the first numerical algorithm used in band structures simulation of PSA. Based on this approach, Thorp [12] et al. studied the attenuation and localization of elastic wave propagation in a piezoelectric resistive-inductive-shunted rod. Airoldi and Ruzzene [13] investigated the wave propagation characteristics of a periodic beam with shunted piezoelectric patches. Wang [14] et al. analyzed the vibration attenuation effects of piezoelectric beams connected by an enhanced resonant shunting circuit. However, this algorithm is restricted to one-dimensional system, which is not suitable for practical engineering applications. In order to obtain the two-dimensional band structures of PSA, the enhanced plane wave expansion (PWE) method [15] emerged. Lian [16] et al. analyzed the effect of circuit parameters on the LR band gaps in a piezoelectric PC plate with resonant shunting circuits. Chen [17] et al. studied the band gap characteristics of piezoelectric metamaterial plate with interface circuits. Compared with the conventional PWE, the enhanced PWE can provide more accurate results and has a good convergence. But it is difficult to predict the attenuation degree of elastic waves due to the neglect of information on amplitude attenuation in the wave vectors. With the rapid development of computational mechanics, researchers have gradually applied the finite element method for the prediction of wave propagation and attenuation in PSA. Spadoni [18] et al. analyzed the wave propagation and subsequent vibrations in plates with periodic shunted piezoelectric patches. Gardonio [19] et al. realized the effective control of bending vibration in thin plate by self-tuning PSA. Although the propagation properties can be obtained in some specific directions, these studies rarely concern the arbitrarily oriented ones. By using the '*fsolve*' function in Matlab, Chen [20] et al. predicted the propagation behaviors of elastic wave in arbitrary directions in PSA. However, several numerical defects still exist, for example, initial value sensitivity and tendency to converge to wrong results. Later, Wen [21] et al. proposed a wave field transformation method to analyze the directionality of dispersion relationships when elastic waves propagate in PSA. But this method suffers from the complication formulations and the low computational efficiency, which limits its practical application.

In order to facilitate the prediction of propagation characteristics in arbitrary directions, developing a new algorithm which can cure the above mentioned drawbacks seems more feasible. In this work, we further present a polynomial eigenvalue solution (PES) to predict the propagation behaviors of elastic wave in PSA. As the structure is periodic in the *x-y* plane, one independent unit cell is selected for the dynamic characteristic analysis instead of infinity. Based on the classic Kirchhoff hypothesis and standard finite element procedures, rectangular element with corner nodes is first employed to obtain the discretized system equations [22]. To acquire the dispersion relationship conveniently, the dynamic stiffness matrix is then partitioned into a block matrix. By implementing the Bloch theorem, a polynomial eigenvalue equation concerning complex propagation constants is further obtained. Through a simple transformation, a linear eigenvalue equation is finally derived, from which the dispersion relationships of PSA can be easily derived. In order to examine the performance of the proposed algorithm, the wave propagation behaviors of a semi-covered piezoelectric periodic plate connecting with a inductance-resistance circuit are in detail studied. The results reveal that the present PES can provide very accurate and reliable numerical predictions for the wave propagation characteristics in arbitrary directions in PSA.

2 Methods

2.1 Theoretical basis

Consider a piezoelectric shunt system consisting of a host plate and arrays of shunted piezoelectric patches, the periodic plate behaves as a two-dimensional infinite waveguide propagating transverse waves. Based on the Bloch theorem, one independent unit cell is selected to conduct the dynamic characteristic analysis, as illustrated in Figure 1A. The divided regions of the unit cell contain two different structural types, i.e., one is the single-layer plate without piezoelectric patches attached, the other is a composite plate consisting of a host plate and piezoelectric patches connecting with a circuit. Noteworthy, the polarization directions of the piezoelectric patches are same.

As the existence of piezoelectric patches, the electromechanical coupling effect needs to be considered for the dynamic analysis of the unit cell. The stress-charge form of the constitutive equations for a piezoelectric material can be written as [23].

$$\begin{bmatrix} \boldsymbol{\sigma}_p \\ \mathbf{D}_e \end{bmatrix} = \begin{bmatrix} \mathbf{c}^E & -\mathbf{e} \\ \mathbf{e}^{\mathbf{T}} & \varepsilon^s \end{bmatrix} \begin{bmatrix} \boldsymbol{\varepsilon}_p \\ \mathbf{E} \end{bmatrix} \tag{1}$$

where, $\boldsymbol{\sigma}_p$ and $\boldsymbol{\varepsilon}_p$ are the mechanical stress vector and the mechanical strain vector, respectively; $\mathbf{D}_e$ and $\mathbf{E}$ represent the electric displacement vector and the electric field vector on the piezoelectric patches electrode, separately; ε^s is the permittivity matrix; $\mathbf{e}$ denotes the matrix of piezoelectric stress constants; $\mathbf{c}^E$ is the stiffness matrix of piezoelectric material.

In order to obtain the subsequent discretized governing equations, the energy functional of the whole unit cell is presented. Here, only the energy functional of the composite plate with piezoelectric patches attached is discussed. According to the Lagrange's equations, the energy functional L of the composite plate can be described as

$$L = T - U + U_e \tag{2}$$

where, T is the kinetic energy, U is the potential energy and U_e is the electric energy, which can be expressed as

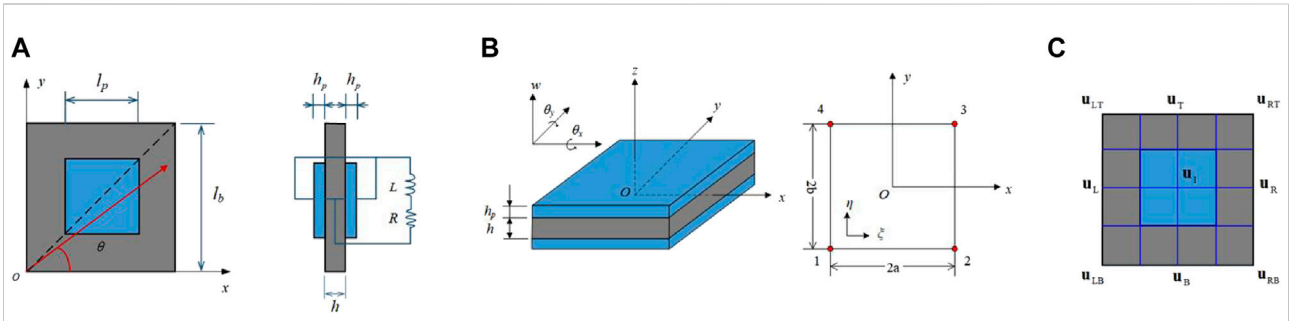

FIGURE 1
(A) The square unit cell; **(B)** Composite plate structure and rectangular element in *x*-*y* plane; **(C)** A typical mesh arrangement for the domain discretization.

$$T = \frac{1}{2}\int_{\Omega_b} \rho_b \dot{w}^2 d\Omega_b + \frac{1}{2}\int_{\Omega_p} \rho_p \dot{w}^2 d\Omega_p \tag{3}$$

$$U = \frac{1}{2}\int_{\Omega_b} \boldsymbol{\varepsilon}_b^{\mathrm{T}} \boldsymbol{\sigma}_b d\Omega_b + \frac{1}{2}\int_{\Omega_p} \boldsymbol{\varepsilon}_p^{\mathrm{T}} \boldsymbol{\sigma}_p d\Omega_p \tag{4}$$

$$U_e = \frac{1}{2}\int_{\Omega_p} \mathbf{E}^{\mathrm{T}} \mathbf{D}_e d\Omega_p \tag{5}$$

where, ρ is the density; w denotes the element displacement. Note that, the subscript 'b' and 'p' represent the quantities corresponding to host plate and piezoelectric shunting, respectively.

To gain the wave propagation characteristics in the whole PSA, the periodic boundary conditions need to be imposed. The Bloch theorem explains this behavior, which can be described in what follows. According to the lattice theory, the whole two-dimensional lattice structure can be seen as the result of translating the unit cell along the basis vectors $\boldsymbol{\alpha}_1$ and $\boldsymbol{\alpha}_2$ [24]. Let $\mathbf{R}(\mathbf{r})$ represent the displacement of a lattice point located at the position $\mathbf{r}(x, y)$, which can be expressed as

$$\mathbf{R}(\mathbf{r}) = \mathbf{R}e^{(i\omega t - \mathbf{k}\cdot\mathbf{r})} \tag{6}$$

in which, $\mathbf{R}$ is the amplitude of displacement vector and $\mathbf{k}$ is the wave vector. The position of other ones based on this lattice point can be given by

$$\mathbf{r}^{n_1,n_2} = \mathbf{r} + n_1\boldsymbol{\alpha}_1 + n_2\boldsymbol{\alpha}_2 \tag{7}$$

where, the n_1 and n_2 are integers related to periodicity. Putting $\mu_x = -\mathbf{k}\cdot\boldsymbol{\alpha}_1$ and $\mu_y = -\mathbf{k}\cdot\boldsymbol{\alpha}_2$, the displacement of lattice points located at the position r^{n_1,n_2} can be given by

$$\mathbf{R}(\mathbf{r}^{n_1,n_2}) = \mathbf{R}(\mathbf{r})\mathbf{e}^{n_1\mu_x + n_2\mu_y} \tag{8}$$

2.2 Basic formulations of the PES

This section presents the basic formulations of PES for wave propagation prediction of PSA in detail. To perform the numerical investigation, both the finite element discretization and the Bloch theorem are utilized, which will be detailedly discussed in the following.

2.2.1 Finite element discretization

Based on the Bloch theorem, only one unit cell is selected for the dynamic analysis. The composite plate structure, which is used to represent the wave propagation characteristics, is shown in Figure 1B. In order to implement the investigation, a set of four-node rectangular elements with corner nodes [22] are first adopted to discrete the problem domain. According to the Kirchhoff hypothesis, the relationship between the vertical deflection w and the rotation θ_x about x-axis, as well as the rotation θ_y about y-axis, can be defined as

$$\begin{cases} \theta_x = \dfrac{\partial w}{\partial y} \\ \theta_y = -\dfrac{\partial w}{\partial x} \end{cases} \tag{9}$$

Using the standard finite element procedure, the generalized deflection w within an element can be interpolated using

$$w = \mathbf{N}\mathbf{u}^e \tag{10}$$

where, N is the element shape function; u^e is the element displacement vector that can be written as

$$\mathbf{u}^e = \begin{bmatrix} \mathbf{u}_1 & \mathbf{u}_2 & \mathbf{u}_3 & \mathbf{u}_4 \end{bmatrix}^{\mathrm{T}} \tag{11}$$

in which, $\mathrm{u}_i = \{w_i, \theta_{xi}, \theta_{yi}\}\,(i = 1, 2, 3, 4)$ is the nodal displacement vector.

To clearly illustrate Eq.10, $\mathbf{N}$ can be explicitly expressed using

$$\mathbf{N} = \begin{bmatrix} \mathbf{N}_1 & \mathbf{N}_2 & \mathbf{N}_3 & \mathbf{N}_4 \end{bmatrix} \tag{12}$$

in which

$$\mathbf{N}_i = \frac{1}{8}(1+\xi_0)(1+\eta_0)\begin{bmatrix} 2+\xi_0+\eta_0-\xi^2-\eta^2 \\ b\eta_i(1-\eta^2) \\ -a\xi_i(1-\xi^2) \end{bmatrix}^{\mathrm{T}} \quad (i = 1, 2, 3, 4) \tag{13}$$

with

$$\begin{cases} \xi_0 = \xi\xi_i,\ \xi = (x - x_c)/a \\ \eta_0 = \eta\eta_i,\ \eta = (y - y_c)/b \end{cases} \tag{14}$$

where, ξ and η are the normalized coordinates; x_c and y_c are the coordinates of the centroid O; a and b are the half lengths of side; the values of ξ_i and η_i can be found in Ref. [22].

Based on the relationship between stain and displacement, the relevant strain vector related to the host plate and the piezoelectric patches can be written as

$$\boldsymbol{\varepsilon} = \left\{ \varepsilon_x \ \ \varepsilon_y \ \ \gamma_{xy} \right\}^{\mathrm{T}} = z\mathbf{L}w \tag{15}$$

in which, $\mathbf{L}$ denotes the differential operator with the form of

$$\mathbf{L} = \left\{ -\frac{\partial^2}{\partial x^2}, -\frac{\partial^2}{\partial y^2}, -2\frac{\partial^2}{\partial x \partial y} \right\}^{\mathrm{T}} \tag{16}$$

The stress-strain relationship for the host plate of PSA can be written as

$$\boldsymbol{\sigma}_b = \mathbf{D}\boldsymbol{\varepsilon}_b \tag{17}$$

where, the matrix D is the constitutive coefficient that can be found in Ref. [22].

In order to represent the electromechanical coupling effect of the piezoelectric shunt system, the potential degree of freedom (DOF) should also be included in the kinetic analysis. Consider the fact that the potential on the electrode of piezoelectric patch is equal everywhere, a potential DOF φ namely the electric potential difference is introduced for the whole unit cell, which can be expressed as

$$\varphi = Eh_p \tag{18}$$

in which, E is the electric field intensity in z-axis direction; h_p denotes the thickness of piezoelectric patch.

According to the Hamilton principle, the energy functional L in Eq. 2 should be at a minimum to reach equilibrium-stability state. Substituting Eqs 1 and 10, 15, 17 and 18 into Eq. 2, the discretized system equations for the dynamic characteristics of unit cell corresponding to the PSA can then be derived as follows [15, 25]

$$\mathbf{M}_{uu}\ddot{\mathbf{u}} + \mathbf{K}_{uu}\mathbf{u} + \mathbf{K}_{u\varphi}\,\varphi = \mathbf{f} \tag{19}$$

$$\mathbf{K}_{\varphi u}\mathbf{u} + \mathrm{K}_{\varphi\varphi}\,\varphi = q \tag{20}$$

in which, $\mathbf{u}$ is the nodal displacements vector of the whole unit cell; $\mathbf{f}$ is the system forces vector; q is the total charge; $\mathbf{M}_{uu}$, $\mathbf{K}_{uu}$ and $\mathbf{K}_{u\varphi}$ are the assembled mass, stiffness and coupling matrices, respectively. $\mathbf{K}_{\varphi u}$ is the transpose matrix of $\mathbf{K}_{u\varphi}$. Note that, $\mathrm{K}_{\varphi\varphi}$ is a scalar, which is opposite to the total capacitance of the piezoelectric patches at constant strain.

Assuming that the displacement $\mathbf{u}$ is a small harmonic perturbation which satisfies

$$\mathbf{u} = \mathrm{u}e^{i\omega t} \tag{21}$$

where, ω denotes the angular frequency; u represents the amplitude of the displacement. Under the same hypothesis, the relationship between the total charge $q(\omega)$ and the electric potential difference $\varphi(\omega)$ can then be written as

$$q(\omega) = \frac{\varphi(\omega)}{i\omega Z(\omega)} \tag{22}$$

in which, $Z(\omega)$ is the complex impedance and $i = \sqrt{-1}$. On its substitution into Eq. 20, $\varphi(\omega)$ can be rewritten as

$$\varphi(\omega) = \left[\frac{1}{i\omega Z(\omega)} - K_{\varphi\varphi} \right]^{-1} \mathbf{K}_{\varphi u}\mathbf{u} \tag{23}$$

Substituting Eqs 21, 23 into Eq. 19, we can finally obtain

$$\mathbf{K}_D(\omega)\,\mathbf{u} = \mathbf{f} \tag{24}$$

where, $\mathbf{K}_D(\omega)$ is the dynamic stiffness matrix with the form of

$$\mathbf{K}_D(\omega) = \mathbf{K}_{uu} - \omega^2\mathbf{M}_{uu} + \mathbf{K}_{u\varphi}\left[\frac{1}{i\omega Z(\omega)} - K_{\varphi\varphi} \right]^{-1} \mathbf{K}_{\varphi u} \tag{25}$$

2.2.2 Bloch analysis

To study the wave propagation behaviors of the whole PSA, the periodic boundary conditions are introduced in this subsection. As shown in Figure 1C, the nodal displacements u and forces f have been divided according to their relative positions in the unit cell, which can be expressed using

$$\mathbf{u} = \left[\mathbf{u}_I \ \ \mathbf{u}_B \ \ \mathbf{u}_T \ \ \mathbf{u}_L \ \ \mathbf{u}_R \ \ \mathbf{u}_{LB} \ \ \mathbf{u}_{RB} \ \ \mathbf{u}_{LT} \ \ \mathbf{u}_{RT} \right]^T \tag{26}$$

$$\mathbf{f} = \left[\mathbf{0} \ \ \mathbf{f}_B \ \ \mathbf{f}_T \ \ \mathbf{f}_L \ \ \mathbf{f}_R \ \ \mathbf{f}_{LB} \ \ \mathbf{f}_{RB} \ \ \mathbf{f}_{LT} \ \ \mathbf{f}_{RT} \right]^{\mathrm{T}} \tag{27}$$

Based on the periodic conditions and equilibrium conditions [24], the Bloch boundary conditions can be written as

$$\begin{cases} \mathbf{u}_T = \mathrm{e}^{\mu_y}\mathbf{u}_B, \mathbf{u}_R = \mathrm{e}^{\mu_x}\mathbf{u}_L \\ \mathbf{u}_{LT} = \mathrm{e}^{\mu_y}\mathbf{u}_{LB}, \mathbf{u}_{RB} = \mathrm{e}^{\mu_x}\mathbf{u}_{LB}, \mathbf{u}_{RT} = \mathrm{e}^{\mu_x+\mu_y}\mathbf{u}_{LB} \end{cases} \tag{28}$$

$$\begin{cases} \mathbf{f}_B + \mathrm{e}^{-\mu_y}\mathbf{f}_T = 0, \mathbf{f}_L + \mathrm{e}^{-\mu_x}\mathbf{f}_R = 0 \\ \mathbf{f}_{LB} + \mathrm{e}^{-\mu_x}\mathbf{f}_{RB} + \mathrm{e}^{-\mu_y}\mathbf{f}_{LT} + \mathrm{e}^{-\mu_x-\mu_y}\mathbf{f}_{RT} = 0 \end{cases} \tag{29}$$

in which, (μ_x, μ_y) are propagation constants that are normally complex numbers, i.e., $\mu_j = \alpha_j + \mathrm{i}\beta_j$ (j = x, y). The real part α_j is attenuation constant which indicates the amplitude decay of elastic wave propagating from one unit cell to the next. The imaginary part β_j is phase constant which denotes the phase change of elastic waves propagation.

Putting $\mathrm{e}^{\mu_x} = \lambda_x$ and $\mathrm{e}^{\mu_y} = \lambda_y$, the matrix form of Eqs 28, 29 can be further expressed by

$$\begin{cases} \mathbf{u} = \mathbf{T}\left(\lambda_x, \lambda_y\right)\hat{\mathbf{u}} \\ \mathbf{T}^{\mathrm{T}}\left(1/\lambda_x, 1/\lambda_y\right)\mathbf{f} = 0 \end{cases} \tag{30}$$

in which

$$\hat{\mathbf{u}} = \left[\mathbf{u}_I \ \ \mathbf{u}_B \ \ \mathbf{u}_L \ \ \mathbf{u}_{LB} \right]^{\mathrm{T}} \tag{31}$$

$$\mathbf{T}(\lambda_x, \lambda_y) = \begin{bmatrix} \mathbf{I} & 0 & 0 & 0 & 0 & 0 & 0 & 0 & 0 \\ 0 & \mathbf{I} & \mathbf{I}\lambda_y & 0 & 0 & 0 & 0 & 0 & 0 \\ 0 & 0 & 0 & \mathbf{I} & \mathbf{I}\lambda_x & 0 & 0 & 0 & 0 \\ 0 & 0 & 0 & 0 & 0 & \mathbf{I} & \mathbf{I}\lambda_x & \mathbf{I}\lambda_y & \mathbf{I}\lambda_x\lambda_y \end{bmatrix}^{\mathrm{T}} \tag{32}$$

2.2.3 The acquirement of propagation constant

This subsection formulates a polynomial eigenvalue equation to obtain the propagation constant on the basis of periodic boundary conditions and dynamic equilibrium equation. To facilitate the subsequent acquisition of propagation constant, $\mathbf{K}_D(\omega)$ can be rewritten in the form of block matrix

$$\mathbf{K}_D(\omega) = \begin{bmatrix} \mathbf{K}_{II} & \mathbf{K}_{IB} & \mathbf{K}_{IT} & \mathbf{K}_{IL} & \mathbf{K}_{IR} & \mathbf{K}_{ILB} & \mathbf{K}_{IRB} & \mathbf{K}_{ILT} & \mathbf{K}_{IRT} \\ \mathbf{K}_{BI} & \mathbf{K}_{BB} & \mathbf{K}_{BT} & \mathbf{K}_{BL} & \mathbf{K}_{BR} & \mathbf{K}_{BLB} & \mathbf{K}_{BRB} & \mathbf{K}_{BLT} & \mathbf{K}_{BRT} \\ \mathbf{K}_{TI} & \mathbf{K}_{TB} & \mathbf{K}_{TT} & \mathbf{K}_{TL} & \mathbf{K}_{TR} & \mathbf{K}_{TLB} & \mathbf{K}_{TRB} & \mathbf{K}_{TLT} & \mathbf{K}_{TRT} \\ \mathbf{K}_{LI} & \mathbf{K}_{LB} & \mathbf{K}_{LT} & \mathbf{K}_{LL} & \mathbf{K}_{LR} & \mathbf{K}_{LLB} & \mathbf{K}_{LRB} & \mathbf{K}_{LLT} & \mathbf{K}_{LRT} \\ \mathbf{K}_{RI} & \mathbf{K}_{RB} & \mathbf{K}_{RT} & \mathbf{K}_{RL} & \mathbf{K}_{RR} & \mathbf{K}_{RLB} & \mathbf{K}_{RRB} & \mathbf{K}_{RLT} & \mathbf{K}_{RRT} \\ \mathbf{K}_{LBI} & \mathbf{K}_{LBB} & \mathbf{K}_{LBT} & \mathbf{K}_{LBL} & \mathbf{K}_{LBR} & \mathbf{K}_{LBLB} & \mathbf{K}_{LBRB} & \mathbf{K}_{LBLT} & \mathbf{K}_{LBRT} \\ \mathbf{K}_{RBI} & \mathbf{K}_{RBB} & \mathbf{K}_{RBT} & \mathbf{K}_{RBL} & \mathbf{K}_{RBR} & \mathbf{K}_{RBLB} & \mathbf{K}_{RBRB} & \mathbf{K}_{RBLT} & \mathbf{K}_{RBRT} \\ \mathbf{K}_{LTI} & \mathbf{K}_{LTB} & \mathbf{K}_{LTT} & \mathbf{K}_{LTL} & \mathbf{K}_{LTR} & \mathbf{K}_{LTLB} & \mathbf{K}_{LTRB} & \mathbf{K}_{LTLT} & \mathbf{K}_{LTRT} \\ \mathbf{K}_{RTI} & \mathbf{K}_{RTB} & \mathbf{K}_{RTT} & \mathbf{K}_{RTL} & \mathbf{K}_{RTR} & \mathbf{K}_{RTLB} & \mathbf{K}_{RTRB} & \mathbf{K}_{RTLT} & \mathbf{K}_{RTRT} \end{bmatrix} \tag{33}$$

Substituting Eqs. 30, 33 into Eq.24, a polynomial eigenvalue equation, depending on ω, λ_x and λ_y, can be obtained and expressed in the following form

$$\left[\mathbf{K}_{D0} + \mathbf{K}_{D1}\lambda_x + \mathbf{K}_{D2}\lambda_y + \mathbf{K}_{D3}\lambda_x^2 + \mathbf{K}_{D4}\lambda_y^2 + \mathbf{K}_{D5}\lambda_x\lambda_y + \mathbf{K}_{D6}\lambda_x^2\lambda_y + \mathbf{K}_{D7}\lambda_x\lambda_y^2 + \mathbf{K}_{D8}\lambda_x^2\lambda_y^2\right]\hat{\mathbf{u}} = 0 \tag{34}$$

in which, the coefficient matrices are shown in Appendix A. It is difficult to directly obtain λ_x and λ_y through a given ω as the solution conditions of polynomial eigenvalue equation are not satisfied [26]. Consider the fact that μ_x and μ_y can be represented by wave vector k in x and y directions [27, 28], then we can get

$$\frac{\mu_y}{\mu_x} = \tan(\theta) \tag{35}$$

in which, θ is the wave propagation angle.

To make Eq. 34 solvable, the following two requirements need to be satisfied: 1) the ratio $\mu_y/\mu_x = m_2/m_1$ is rational; 2) m_2 and m_1 are integers with no common divisor. Hence, the propagation constants can be further expressed using $\mu_x = m_1\delta$ and $\mu_y = m_2\delta$ where δ is the quantity without practical meaning. By introducing $\tau = e^{\delta}$, Eq. 34 can be rewritten as

$$\left[\mathbf{K}_{D0} + \mathbf{K}_{D1}\tau^{m_1} + \mathbf{K}_{D2}\tau^{m_2} + \mathbf{K}_{D3}\tau^{2m_1} + \mathbf{K}_{D4}\tau^{2m_2} + \mathbf{K}_{D5}\tau^{m_1+m_2} + \mathbf{K}_{D6}\tau^{2m_1+m_2} + \mathbf{K}_{D7}\tau^{m_1+2m_2} + \mathbf{K}_{D8}\tau^{2m_1+2m_2}\right]\hat{\mathbf{u}} = 0 \tag{36}$$

Through a simple transformation process, Eq. 36 can be further expressed using

$$[\mathbf{Q} - \tau\mathbf{I}]\hat{\mathbf{U}} = \mathbf{0} \tag{37}$$

with

$$\mathbf{Q} = \begin{bmatrix} -\mathbf{K}_{Dm}^{-1}\mathbf{K}_{D(m-1)} & \cdots & -\mathbf{K}_{Dm}^{-1}\mathbf{K}_{D1} & -\mathbf{K}_{Dm}^{-1}\mathbf{K}_{D0} \\ \mathbf{I} & & & \vdots \\ & \ddots & & \\ & & \mathbf{I} & 0 \end{bmatrix} \tag{38}$$

$$\hat{\mathbf{U}} = \begin{Bmatrix} \tau^{m-1}\hat{\mathbf{u}} \\ \vdots \\ \tau\hat{\mathbf{u}} \\ \hat{\mathbf{u}} \end{Bmatrix} \tag{39}$$

in which, $\mathbf{K}_{Dm} \neq 0$ and $m = 2m_1 + 2m_2$

Obviously, Eq. 37 is a linear eigenvalue problem which is easier to solve. When the propagation angular frequency ω and the tangent value $\tan(\theta)$ are given, δ can be easily derived. The propagation constant μ_θ in arbitrary direction θ can be finally calculated using

$$\mu_\theta = \delta\sqrt{m_1^2 + m_2^2} \tag{40}$$

It can be seen from Eq. 40 that μ_θ varies with the changes of δ, m_1 and m_2. Therefore, when θ is determined, the relationship between μ_θ and ω can be easily obtained to represent the propagation behaviors of elastic wave.

3 Results

The present formulation has been coded using MATLAB program. In what follows, a typical numerical example is carefully studied to illustrate the accuracy and reliability of our PES. In addition, the wave propagation and attenuation in arbitrary directions are also investigated using the above methodology.

The host plate is epoxy with Young's modulus $E = 4.35$GPa, Poisson's ratio $\upsilon = 0.37$ and mass density $\rho_b = 1180$kg/m^3. The piezoelectric patch is PZT-5H. Table 1 and Table 2 list the related material and geometric parameters used in this study.

Moreover, the shunt circuit is a serial resistive-inductive network, hence the complex impedance Z becomes

$$Z(\omega) = R + i\omega L \tag{41}$$

where, the shunt resistance and inductance value are selected to be 100Ω and 0.2H [20], respectively.

3.1 Accuracy of the PES

To implement this investigation, the problem domain is first discretized using 16 four-node rectangular elements. As the elastic wave can propagate in arbitrary directions, two representative wave propagation angle, namely $\theta = 0$ and $\theta = \pi/4$, are selected to study the wave propagation and attenuation characteristics. Because the exact solutions are unknown for this case, the numerical results verified by commercial software ANSYS and experiment [20] are taken as the reference.

TABLE 1 Material parameters of the PZT-5H.

Density ρ_p (kg/m^3)	s_{11}^E (m^2/N)	s_{12}^E (m^2/N)	d_{31} (C/N)	ε_{33}^T (F/m)
7500	16.5×10^{-12}	-4.78×10^{-12}	-2.74×10^{-10}	3.01×10^{-8}

TABLE 2 Geometric parameters of the unit cell.

Length of side l_b (mm)	Thickness h (mm)	Lenth of side l_p (mm)	Thickness h_p (mm)
80	5	40	0.2

The attenuation constant a and phase constant $ß$ obtained using both algorithms by varying the frequency from 0 Hz to 1,500 Hz are plotted in Figure 2. It can be observed that 1) For $\theta = 0$, there are two band gaps in the considered frequency range. The first band gap named the locally resonant gap is about 525 Hz–580 Hz, while the second one called the Bragg gap is about 750 Hz–985 Hz. 2) For $\theta = \pi/4$, only one band gap exists which is about 527 Hz–582 Hz. 3) Whatever the wave propagation angle is, the attenuation constant in the band gap increases with the growth of frequency. However, it decreases gradually after reaching the maximum at the center of frequency range. 4) The maximum value of phase constant can only be π in the considered frequency range. The Bloch theorem contributes to this phenomenon. 5) For the ranges and widths of the band gaps, together with the amplitude of the central band structures, the PES can always give very accurate numerical predictions compared with the reference. Therefore, the effectiveness and accuracy of the present method is confirmed.

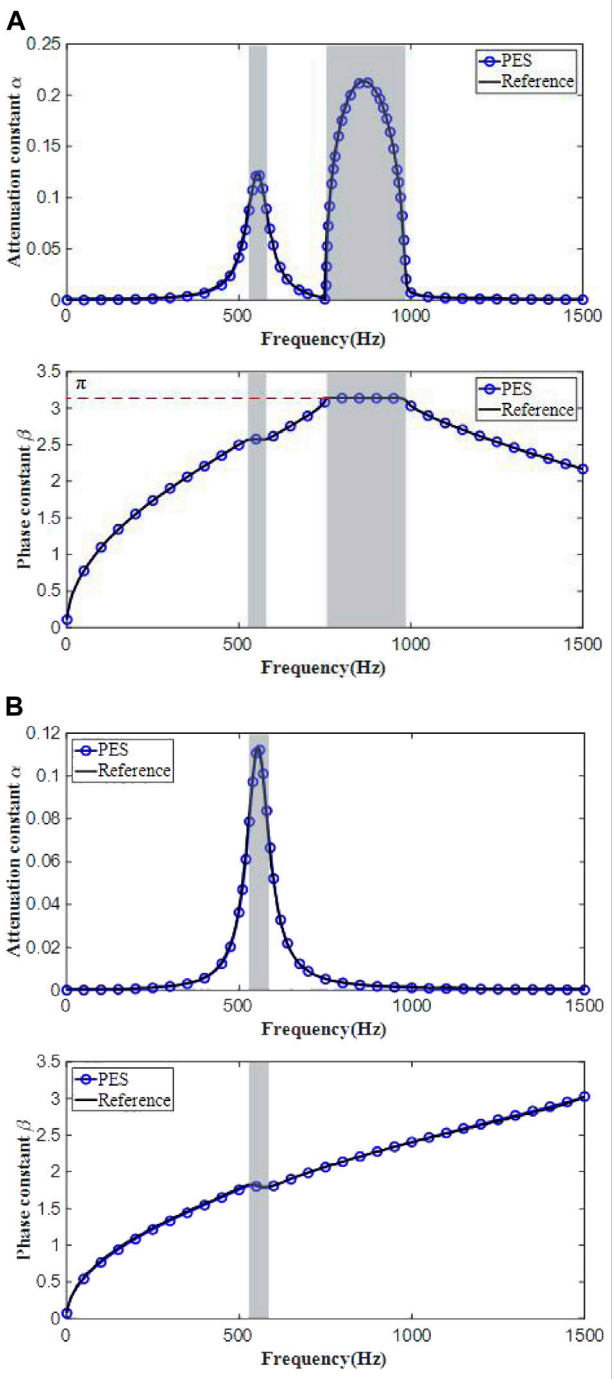

FIGURE 2
Variations in propagation constant with frequency at: **(A)** θ = 0; **(B)** θ = π/4.

3.2 Convergence study

In order to further verify the reliability of our PES, the convergence property of the present method is investigated in this package. Differ from the previous subsection, two representative directions, namely $\tan(\theta) = 0.2$ and $\tan(\theta) = 1$, are studied in this part. The attenuation constants and phase constants *versus* the increase of element number N are plotted in Figure 3. It can be observed from these figures that 1) With the increase of element number, the range and width of the band gaps change very little. However, the attenuation constant near the center of band gaps decreases continuously. 2) In the direction of $\tan(\theta) = 0.2$, the phase constants obtained using 16, 64 and 144 elements are almost the same. Hence, very accurate results can be obtained with few number of elements. 3) In the direction of $\tan(\theta) = 1$, the phase constants obtained using 64 and 144 elements are slightly smaller than that obtained using 16 elements. 4) The numerical results calculated using 64 and 144 elements are almost overlapped, which means that the present model could give very stable numerical predictions with a coarse mesh discretization. Therefore, the convergence of the present method is confirmed.

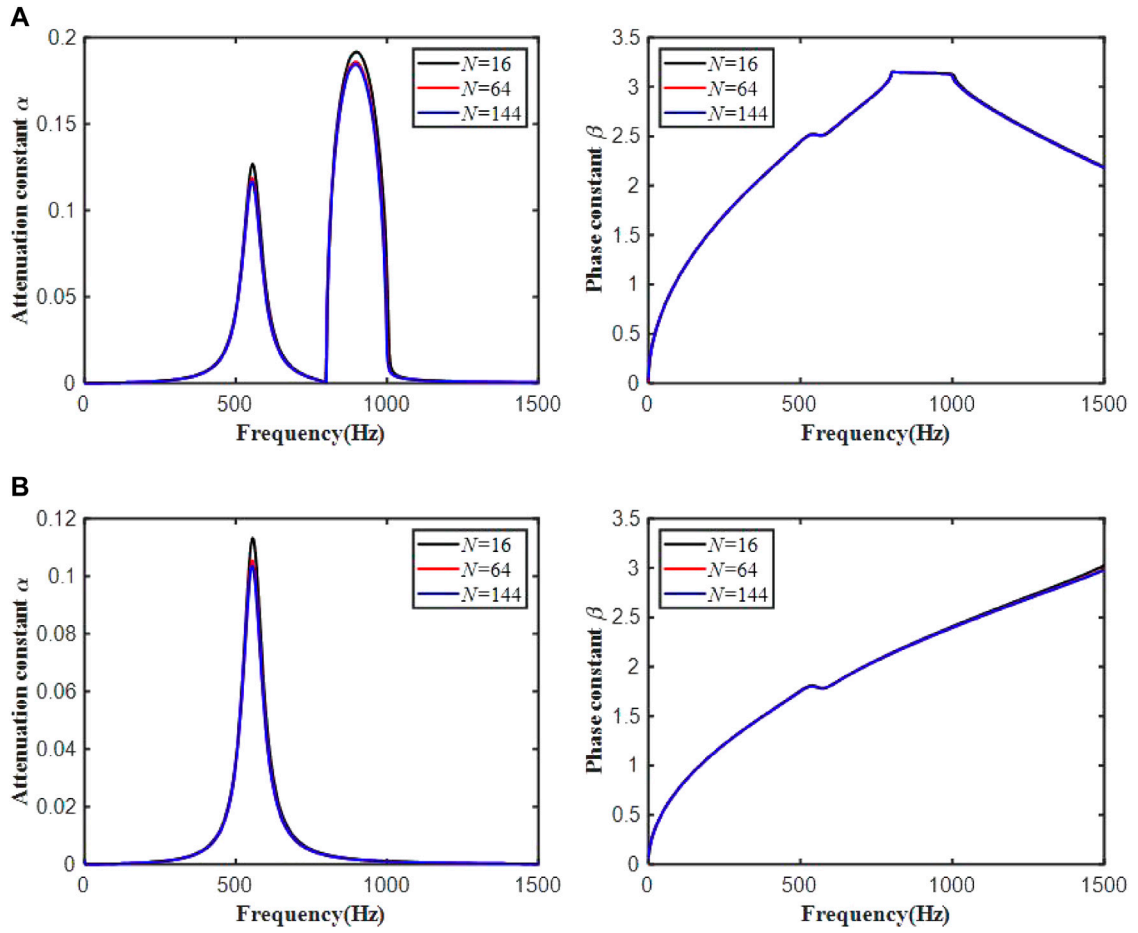

FIGURE 3
Convergence of propagation constants with different amount of elements: **(A)** tan(θ) = 0.2; **(B)** tan(θ) = 1.

3.3 Directionality of the wave propagation and attenuation

Based on the previous findings and discussion, it can be found that the Bragg gap and the locally resonant gap differ from each other greatly with the change of direction. In order to clearly reveal the evolution of band gaps, the directionality of the wave propagation and attenuation are further studied in this part.

According to the symmetry of square unit cell as shown in Figure 1A, the propagation constant in arbitrary direction can be obtained by sweeping θ from 0 to $\pi/4$, i. e

$$\mu_\theta = \begin{cases} \mu_\theta & 0 \le \theta \le \pi/4 \\ \mu_{\pi/2-\theta} & \pi/4 < \theta \le \pi/2 \end{cases} \tag{42}$$

Therefore, the tangent value is taken from 0 to 1.

Figure 4A depicts the band gaps vary with tangent values, in which the color spectra represents the magnitude of attenuation constant. It can be seen from the figure that (1) A complete band gap is first observed in the frequency range of 525–580 Hz. As locally resonant gap is strongly related to the resonance of shunting circuits, the band width changes very little with direction. In other words, it is a typically full band gap in all directions. 2) The frequency range of Bragg gap increases with the growth of tangent value. However, due to the frequency of lower boundary increases faster than that of upper boundary, the band width decreases until it vanishes. The Bragg gap is mainly induced by the impedance mismatch between the piezoelectric patches and the substrate plate. With the wave propagation angle θ increases, it gradually reaches impedance matching. Hence, the Bragg gap is distinctly directional.

To further investigate the attenuation degree of elastic waves in different directions, the attenuation constant obtained using the present algorithm is also outlined in Figure 4B. Here, nine different tangent values are considered, namely tan(θ) = 0, 0.125, 0.25, 0.375, 0.5, 0.625, 0.75, 0.875 and 1.0. It can be found that 1) The amplitude of attenuation constant near the center of locally

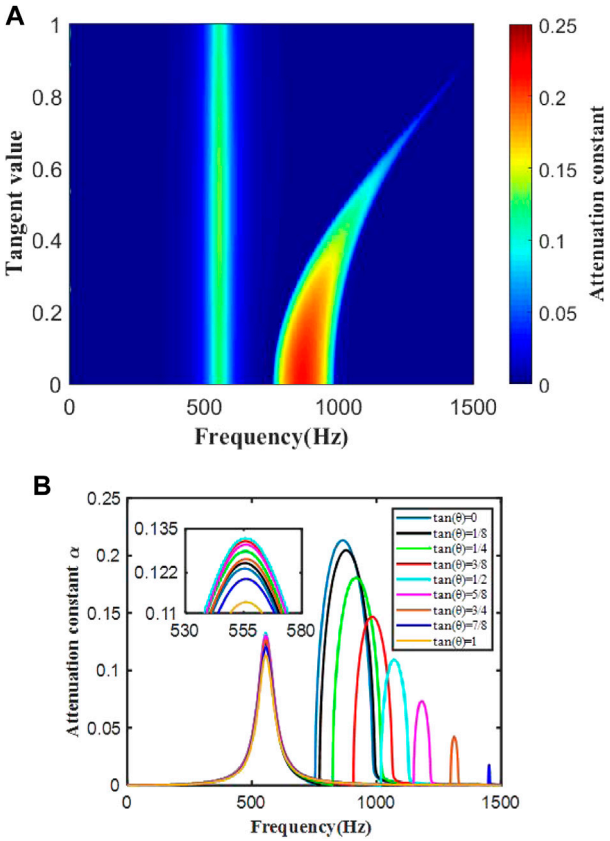

FIGURE 4
(A) Variation in band gaps with different tangent values; **(B)** Variations in attenuation constant with different tangent values.

resonant gap increases with the growth of tangent value. However, it decreases quickly after reaching the maximum when the tangent value is about 0.5. 2) The maximum of attenuation constant within Bragg gap decreases with the increase of tangent value. Combing with Figure 4A, when the tangent value is about 0.9, it eventually equals zero.

Based on these preliminary findings, we can further conclude that the PES can be seen a good choice for the prediction of wave propagation and attenuation in arbitrary direction.

4 Conclusion

In this work, a polynomial eigenvalue solution is formulated for predicting the propagation behaviors of elastic wave in arbitrary directions in piezoelectric shunting arrays. Based on the Bloch theorem, the wave propagation in PSA is evaluated through the dynamic analysis of one unit cell. A typical square plate with shunted piezoelectric patches is investigated in detail to study the accuracy, convergence and effectiveness of PES. The results show that the present method can provide very accurate numerical solutions compared with the reference. Besides, the proposed formulation can give very stable and convergent numerical predictions with a coarse mesh discretization. The variations of band gaps and attenuation constant with the wave propagation angle are finally investigated, which can verify the effectiveness of PES. Through the obtained results, the present algorithm is thus a strong competitor to other solutions in the analysis of wave propagation and attenuation in arbitrary directions in PSA.

Data availability statement

The original contributions presented in the study are included in the article/supplementary material, further inquiries can be directed to the corresponding author.

Author contributions

HY implemented the research, analyzed the data and wrote the manuscript. GW conceptualized the idea, discussed all the results and conducted the proof reading. All authors have read and agreed the published version of the manuscript.

Funding

This work was supported by the National Natural Science Foundation of China (12072099, 11832011) and the Natural Science Foundation of Hebei Province of China (A2021202023).

Conflict of interest

The authors declare that the research was conducted in the absence of any commercial or financial relationships that could be construed as a potential conflict of interest.

Publisher's note

All claims expressed in this article are solely those of the authors and do not necessarily represent those of their affiliated organizations, or those of the publisher, the editors and the reviewers. Any product that may be evaluated in this article, or claim that may be made by its manufacturer, is not guaranteed or endorsed by the publisher.

References

1. Wang YF, Wang YS, Laude V. Wave propagation in two-dimensional viscoelastic metamaterials. *Phys Rev B* (2015) 92:104110. doi:10.1103/PhysRevB.92.104110

2. Zhang SY, Wang YF, Wang YS. Evanescent surface acoustic waves in 1D viscoelastic phononic crystals. *J Appl Phys* (2021) 129:245111. doi:10.1063/5.0046004

3. Kushwaha MS, Halevi P, Dobrzynski L, Djafari-Rouhani B. Acoustic band structure of periodic elastic composites. *Phys Rev Lett* (1993) 71(13):2022–2025. doi:10.1103/PhysRevLett.71.2022

4. Martínez-Sala R, Sancho J, Sánchez JV, Gómez V, Llinares J, Meseguer F. Sound attenuation by sculpture. *Nature* (1995) 378(6554):241. doi:10.1038/378241a0

5. Foehr A, Bilal OR, Huber SD, Daraio C. Spiral-based phononic plates: From wave beaming to topological insulators. *Phys Rev Lett* (2018) 120 (20):205501. doi:10.1103/PhysRevLett.120.205501

6. Liu ZY, Zhang XX, Mao YW, Zhu YY, Yang ZY, Chan CT, et al. Locally resonant sonic materials. *Science* (2000) 289(5485):1734–1736. doi:10.1126/science.289.5485.1734

7. He ZC, Hu JY, Li E. An uncertainty model of acoustic metamaterials with random parameters. *Comput Mech* (2018) 62(5):1023–1036. doi:10.1007/s00466-018-1548-y

8. Forward RL. Electronic damping of vibrations in optical structures. *Appl Opt* (1979) 18(5):690–697. doi:10.1364/AO.18.000690

9. Hagood NW, Flotow von A. Damping of structural vibrations with piezoelectric materials and passive electrical networks. *J Sound Vibration* (1991) 146 (2):243–268. doi:10.1016/0022-460x(91)90762-9

10. Guo X, Liu H, Zhang K, Duan HL. Dispersion relations of elastic waves in two-dimensional tessellated piezoelectric phononic crystals. *Appl Math Model* (2018) 56:65–82. doi:10.1016/j.apm.2017.11.037

11. Hou ZL, Fu XJ, Liu YY. Calculational method to study the transmission properties of phononic crystals. *Phys Rev B* (2004) 70(1):014304. doi:10.1103/PhysRevB.70.014304

12. Thorp O, Ruzzene M, Baz A. Attenuation and localization of wave propagation in rods with periodic shunted piezoelectric patches. *Smart Mater Struct* (2001) 10(5):979–989. doi:10.1088/0964-1726/10/5/314

13. Airoldi L, Ruzzene M. Design of tunable acoustic metamaterials through periodic arrays of resonant shunted piezos. *New J Phys* (2011) 13 (11):113010. doi:10.1088/1367-2630/13/11/113010

14. Wang G, Wang JW, Chen SB, Wen JH. Vibration attenuations induced by periodic arrays of piezoelectric patches connected by enhanced resonant shunting circuits. *Smart Mater Struct* (2011) 20(12):125019. doi:10.1088/0964-1726/20/12/125019

15. Sugino C, Ruzzene M, Erturk A. An analytical framework for locally resonant piezoelectric metamaterial plates. *Int J Sol Structures* (2020) 182:281–294. doi:10.1016/j.ijsolstr.2019.08.011

16. Lian ZY, Jiang S, Hu HP, Dai LX, Chen XD, Jiang W. An enhanced plane wave expansion method to solve piezoelectric phononic crystal with resonant shunting circuits. *Shock and Vibration* (2016) 2016: 4015363. doi:10.1155/2016/4015363

17. Chen ZS, Xiong YP, Wei YX. Binary-Like topology optimization of piezoelectric metamaterial plate with interface circuits using extended plane wave expansion method. *Appl Sci* (2021) 11(11):5191. doi:10.3390/app11115191

18. Spadoni A, Ruzzene M, Cunefare K. Vibration and wave propagation control of plates with periodic arrays of shunted piezoelectric patches. *J Intell Mater Syst Structures* (2019) 20(8):979–990. doi:10.1177/1045389x08100041

19. Gardonio P, Zientek M, Dal Bo L. Panel with self-tuning shunted piezoelectric patches for broadband flexural vibration control. *Mech Syst Signal Process* (2019) 134:106299. doi:10.1016/j.ymssp.2019.106299

20. Chen SB, Wang G, Wen JH, Wen XS. Wave propagation and attenuation in plates with periodic arrays of shunted piezo-patches. *J Sound Vibration* (2013) 332:1520–1532. doi:10.1016/j.jsv.2012.11.005

21. Wen JH, Chen SB, Wang G, Yu DL, Wen XS. Directionality of wave propagation and attenuation in plates with resonant shunting arrays. *J Intell Mater Syst Structures* (2016) 27(1):28–38. doi:10.1177/1045389X14560361

22. Zienkiewicz OC, Taylor RL, Fox DD. *The finite element method for solid and structural mechanics*. 7th ed. Oxford: Butterworth-Heinemann (2014).

23. Airoldi L, Ruzzene M. Wave propagation control in beams through periodic multi-Branch shunts. *J Intell Mater Syst Structures* (2011) 22 (14):1567–1579. doi:10.1177/1045389X11408372

24. Farzbod F, Leamy MJ. The treatment of forces in Bloch analysis. *J Sound Vib* (2009) 325:545–551. doi:10.1016/j.jsv.2009.03.035

25. Casadei F, Ruzzene M, Dozio L, Cunefare KA. Broadband vibration control through periodic arrays of resonant shunts: Experimental investigation on plates. *Smart Mater Struct* (2010) 19:015002. doi:10.1088/0964-1726/19/1/015002

26. Dedieu JP, Tisseur F. Perturbation theory for homogeneous polynomial eigenvalue problems. *Linear Algebra Its Appl* (2003) 358:71–94. doi:10.1016/s0024-3795(01)00423-2

27. Mace BR, Manconi E. Modelling wave propagation in two-dimensional structures using finite element analysis. *J Sound Vibration* (2008) 318:884–902. doi:10.1016/j.jsv.2008.04.039

28. Langley RS. Wave motion and energy flow in cylindrical shells. *J Sound Vibration* (1994) 169(1):29–42. doi:10.1006/j.svi.1994.1004

Appendix A

The coefficient matrices for any combination of λ_x and λ_y in Eq. 34 are elaborated below.

$$\mathbf{K}_{\mathrm{D0}} = \begin{bmatrix} 0 & 0 & 0 & 0 \\ 0 & 0 & 0 & 0 \\ 0 & 0 & 0 & 0 \\ \mathbf{K}_{\mathrm{RTI}} & \mathbf{K}_{\mathrm{RTB}} & \mathbf{K}_{\mathrm{RTL}} & \mathbf{K}_{\mathrm{RTLB}} \end{bmatrix} \tag{A.1}$$

$$\mathbf{K}_{\mathrm{D1}} = \begin{bmatrix} 0 & 0 & 0 & 0 \\ \mathbf{K}_{\mathrm{TI}} & \mathbf{K}_{\mathrm{TB}} & \mathbf{K}_{\mathrm{TL}} & \mathbf{K}_{\mathrm{TLB}} \\ 0 & 0 & 0 & 0 \\ \mathbf{K}_{\mathrm{LTI}} & \mathbf{K}_{\mathrm{LTB}} & \mathbf{K}_{\mathrm{RTR}} + \mathbf{K}_{\mathrm{LTL}} & \mathbf{K}_{\mathrm{LTLB}} + \mathbf{K}_{\mathrm{RTRB}} \end{bmatrix} \tag{A.2}$$

$$\mathbf{K}_{\mathrm{D2}} = \begin{bmatrix} 0 & 0 & 0 & 0 \\ 0 & 0 & 0 & 0 \\ \mathbf{K}_{\mathrm{RI}} & \mathbf{K}_{\mathrm{RB}} & \mathbf{K}_{\mathrm{RL}} & \mathbf{K}_{\mathrm{RLB}} \\ \mathbf{K}_{\mathrm{RBI}} & \mathbf{K}_{\mathrm{RBB}} + \mathbf{K}_{\mathrm{RTT}} & \mathbf{K}_{\mathrm{RBL}} & \mathbf{K}_{\mathrm{RBLB}} + \mathbf{K}_{\mathrm{RTLT}} \end{bmatrix} \tag{A.3}$$

$$\mathbf{K}_{\mathrm{D3}} = \begin{bmatrix} 0 & 0 & 0 & 0 \\ 0 & 0 & \mathbf{K}_{\mathrm{TR}} & \mathbf{K}_{\mathrm{TRB}} \\ 0 & 0 & 0 & 0 \\ 0 & 0 & \mathbf{K}_{\mathrm{LTR}} & \mathbf{K}_{\mathrm{LTRB}} \end{bmatrix} \tag{A.4}$$

$$\mathbf{K}_{\mathrm{D4}} = \begin{bmatrix} 0 & 0 & 0 & 0 \\ 0 & 0 & 0 & 0 \\ 0 & \mathbf{K}_{\mathrm{RT}} & 0 & \mathbf{K}_{\mathrm{RLT}} \\ 0 & \mathbf{K}_{\mathrm{RBT}} & 0 & \mathbf{K}_{\mathrm{RBLT}} \end{bmatrix} \tag{A.5}$$

$$\mathbf{K}_{\mathrm{D5}} = \begin{bmatrix} \mathbf{K}_{\mathrm{II}} & \mathbf{K}_{\mathrm{IB}} & \mathbf{K}_{\mathrm{IL}} & \mathbf{K}_{\mathrm{ILB}} \\ \mathbf{K}_{\mathrm{BI}} & \mathbf{K}_{\mathrm{BB}} + \mathbf{K}_{\mathrm{TT}} & \mathbf{K}_{\mathrm{BL}} & \mathbf{K}_{\mathrm{BLB}} + \mathbf{K}_{\mathrm{TLT}} \\ \mathbf{K}_{\mathrm{LI}} & \mathbf{K}_{\mathrm{LB}} & \mathbf{K}_{\mathrm{LL}} + \mathbf{K}_{\mathrm{RR}} & \mathbf{K}_{\mathrm{LLB}} + \mathbf{K}_{\mathrm{RRB}} \\ \mathbf{K}_{\mathrm{LBI}} & \mathbf{K}_{\mathrm{LBB}} + \mathbf{K}_{\mathrm{LTT}} & \mathbf{K}_{\mathrm{LBL}} + \mathbf{K}_{\mathrm{RBR}} & \mathbf{K}_{\mathrm{LBLB}} + \mathbf{K}_{\mathrm{RBRB}} + \mathbf{K}_{\mathrm{LTLT}} + \mathbf{K}_{\mathrm{RTRT}} \end{bmatrix} \tag{A.6}$$

$$\mathbf{K}_{\mathrm{D6}} = \begin{bmatrix} 0 & 0 & \mathbf{K}_{\mathrm{IR}} & \mathbf{K}_{\mathrm{IRB}} \\ 0 & 0 & \mathbf{K}_{\mathrm{BR}} & \mathbf{K}_{\mathrm{TRT}} + \mathbf{K}_{\mathrm{BRB}} \\ 0 & 0 & \mathbf{K}_{\mathrm{LR}} & \mathbf{K}_{\mathrm{LRB}} \\ 0 & 0 & \mathbf{K}_{\mathrm{LBR}} & \mathbf{K}_{\mathrm{LBRB}} + \mathbf{K}_{\mathrm{LTRT}} \end{bmatrix} \tag{A.7}$$

$$\mathbf{K}_{\mathrm{D7}} = \begin{bmatrix} 0 & \mathbf{K}_{\mathrm{IT}} & 0 & \mathbf{K}_{\mathrm{ILT}} \\ 0 & \mathbf{K}_{\mathrm{BT}} & 0 & \mathbf{K}_{\mathrm{BLT}} \\ 0 & \mathbf{K}_{\mathrm{LT}} & 0 & \mathbf{K}_{\mathrm{LLT}} + \mathbf{K}_{\mathrm{RRT}} \\ 0 & \mathbf{K}_{\mathrm{LBT}} & 0 & \mathbf{K}_{\mathrm{LBLT}} + \mathbf{K}_{\mathrm{RBRT}} \end{bmatrix} \tag{A.8}$$

$$\mathbf{K}_{\mathrm{D8}} = \begin{bmatrix} 0 & 0 & 0 & \mathbf{K}_{\mathrm{IRT}} \\ 0 & 0 & 0 & \mathbf{K}_{\mathrm{BRT}} \\ 0 & 0 & 0 & \mathbf{K}_{\mathrm{LRT}} \\ 0 & 0 & 0 & \mathbf{K}_{\mathrm{LBRT}} \end{bmatrix} \tag{A.9}$$

frontiers | Frontiers in Physics

TYPE Mini Review
PUBLISHED 18 November 2022
DOI 10.3389/fphy.2022.1069454

OPEN ACCESS

EDITED BY
Lingyun Yao,
Southwest University, China

REVIEWED BY
Mostafa Ranjbar,
Ankara Yıldırım Beyazıt University, Turkey

*CORRESPONDENCE
Xueting Zhang,
zxt@hdu.edu.cn
Rougang Zhou,
42141@hdu.edu.cn
Youping Gong,
joany0204@163.com

SPECIALTY SECTION
This article was submitted to Physical Acoustics and Ultrasonics, a section of the journal Frontiers in Physics

RECEIVED 13 October 2022
ACCEPTED 03 November 2022
PUBLISHED 18 November 2022

CITATION
Dai H, Zhang X, Zheng Y, Pei W, Zhou R, Liu R and Gong Y (2022), Review and prospects of metamaterials used to control elastic waves and vibrations. *Front. Phys.* 10:1069454. doi: 10.3389/fphy.2022.1069454

Review and prospects of metamaterials used to control elastic waves and vibrations

Huajie Dai[1,2], Xueting Zhang[1]*, Yongju Zheng[1,2], Wanrong Pei[1], Rougang Zhou[1]*, Rong Liu and Youping Gong[1]*

[1]School of Mechanical Engineering, Hangzhou Dianzi University, Hangzhou, China, [2]School of Aerospace Engineering and Applied Mechanics, Tongji University, Shanghai, China

Acoustic metamaterials, artificial composite structures with exotic material properties used to control elastic waves, have become a new frontier in physics, materials science, engineering and chemistry. In this paper, the research progress and development prospect of acoustic metamaterials are reviewed. Related studies on passive acoustic metamaterials and active acoustic metamaterials are introduced and compared. Additionally, we discuss approaches to material structure design, including topology optimization approaches, as well as bio-inspired and fractal geometry-based approaches to structure design. Finally, we summarize and look forward to the prospects and directions of acoustic metamaterial research. With the development of additive manufacturing technology, the research potential of acoustic metamaterials is huge.

KEYWORDS

acoustic metamaterial, elastic wave control, material structure design, fractal geometry-based approaches, bio-inspired approaches

1 Introduction

Metamaterial is a material that obtains extraordinary physical properties that conventional materials do not possess by designing special artificial structures. Veselago, a Soviet physicist, demonstrated the feasibility of negative refractive index materials and named them in 1967 [1]. After that, the concept of electromagnetic metamaterials began to formally enter people's sight. The researchs related to the application of electromagnetic metamaterials in various fields quickly attracted the interest of researchers [2, 3]. With the continuous deepening of research, it has been found that elastic waves will have elastic wave band gaps similar to the photonic band gaps of electromagnetic metamaterials when they propagate in periodic elastic composite media. As a result, the concept of acoustic metamaterials was proposed, and related researches continued [4–6]. Different crystal compositions and periodic structures lead to different band gap properties of elastic waves. This makes it adaptable to different situations and makes it applicable to various fields [7–10]. In particular, it provides a simple, low-cost, and easy-to-apply solution to engineering problems for the solution of vibration and noise [11–13].

One of the earliest and more popular acoustic metamaterials is phononic crystals, which is a new type of functional material formed by the periodic arrangement of elastic solids in another solid or fluid medium. The Bragg type of phononic crystals was proposed earlier and is relatively mature. But the lattice constant of Bragg diffraction-based phononic crystals is of the same order of magnitude as the band gap frequency. As a result, it cannot be used to control low frequency problems. Liu et al. [14] first proposed the concept of locally resonant phononic crystals (LRPCs). the band gap frequency of LRPCs with the same lattice size is much lower than the Bragg's, which can be used to solve low-frequency problems. With the deepening of research, the potential of phononic crystals in various fields has gradually emerged, and related research has become more abundant [15–20]. Topology optimization is the most commonly used optimization design of phononic crystals. Among them, Ranjbar and Hosseinkhani [21–23] have made remarkable research achievements in this regard.

It is worth noting that metamaterials that combine mechanics and biology have emerged in recent years and have begun to attract the attention of researchers [24, 25], such as DNA-inspired chiral metamaterials [26], microtubules composed of Biological nanonetworks [27], layered cellular materials [28]. These biological systems-inspired materials offer a completely new approach to the structural design of acoustic metamaterials. In addition, many researchers have introduced fractal geometry into phononic crystals to obtain better dynamic properties, such as Hilbert fractal [29, 30], Koch fractal [31, 32]. However, the related acoustic metamaterials mentioned above are all passive metamaterials, and the structural invariance of passive metamaterials limits their performance, function, and tunability. An increasing number of researchers are beginning to incorporate active elements, tunable and/or programmable devices into metamaterial designs, enabling active control of materials [30–32]. However, there are few studies reported in related fields, mainly not showing the characteristics of active feedback control. It is expected that there will be more related studies in the future.

In this paper, the related researches on acoustic metamaterials in recent years are collected and analyzed. And the future prospects of acoustic metamaterials are prospected. The rest of this paper is organized as follows. In Section 2, the current related research on passive acoustic metamaterials is mainly introduced, and it is divided into three parts for comparative analysis of phononic crystals topology optimization, bioinspired acoustic metamaterials and acoustic metamaterials based on fractal geometry. In Section 3, the related research on active acoustic metamaterials is mainly introduced. Finally, the research progress of acoustic metamaterials is summarized and its prospects are prospected. It can be seen that with the promotion of additive manufacturing methods, acoustic metamaterials have great application prospects in the fields of vibration and noise control.

2 Passive metamaterials

2.1 Phononic crystals

Bragg scattering crystals [33–35] is an earlier phononic crystal type. In order to generate the Bragg band gap in the phononic crystal, the size of the lattice should be at least equal to 1/2 of the wavelength of the elastic wave. It can be seen that the center frequency of the band gap is limited by the lattice constant, and the elastic wave at low frequencies cannot be controlled. Liu et al. [14] proposed the local resonance theory. By using this theory, they made acoustic crystals based on local resonance structures. Its lattice constant is two orders of magnitude smaller than the spectral gap of the relevant wavelength, breaking through the predicament of Bragg scattering crystals at low frequencies.

Figure 1 shows the local resonance structure and its frequency characteristics of a kind of phononic crystal. The materials have a simple microstructural unit consisting of a relatively high-density solid material and a coating of elastically soft material. And using a centimeter-sized lead ball as the core material, a 2.5 mm thick layer of silicone rubber was applied (Figure 1A). The coated spheres are arranged in an 8 × 8 × 8 simple cubic crystal with a lattice constant of 1.55 cm (Figure 1B) and the hard matrix is epoxy resin. Disordered composites made from such locally resonant structures possess effective negative elastic constants and full-wave reflectors over a certain tunable range of acoustic frequencies.

The local resonance mechanism is different from the Bragg scattering mechanism, which emphasizes the influence of the periodic structure on the wave propagation [36–38]. It emphasizes the interaction between the resonance characteristics of a single scatterer and the long-wave traveling waves in the matrix. For the phononic crystal of the single-sided column type, the band gap of the phononic crystal can be transformed from Bragg scattering type to local resonance type by adjusting the quality of the additional column, which belongs to the composite phononic crystal. Zhang et al. [39] designed a novel hybrid phononic crystal composed of a rubber plate with periodic holes and lead pillars to obtain a wide low frequency band gap, as shown in Figure 2. Compared with the phononic crystals without periodic holes, the newly designed phononic crystals have wider band gaps and better vibration damping properties. The wider band gap can be attributed to the interaction of local resonance and Bragg scattering.

Nowadays, the three more traditional and mature types of phononic crystals are Bragg type, local scattering type and composite type. The three types of levels are progressive. A common problem in all three types of phononic crystals is the

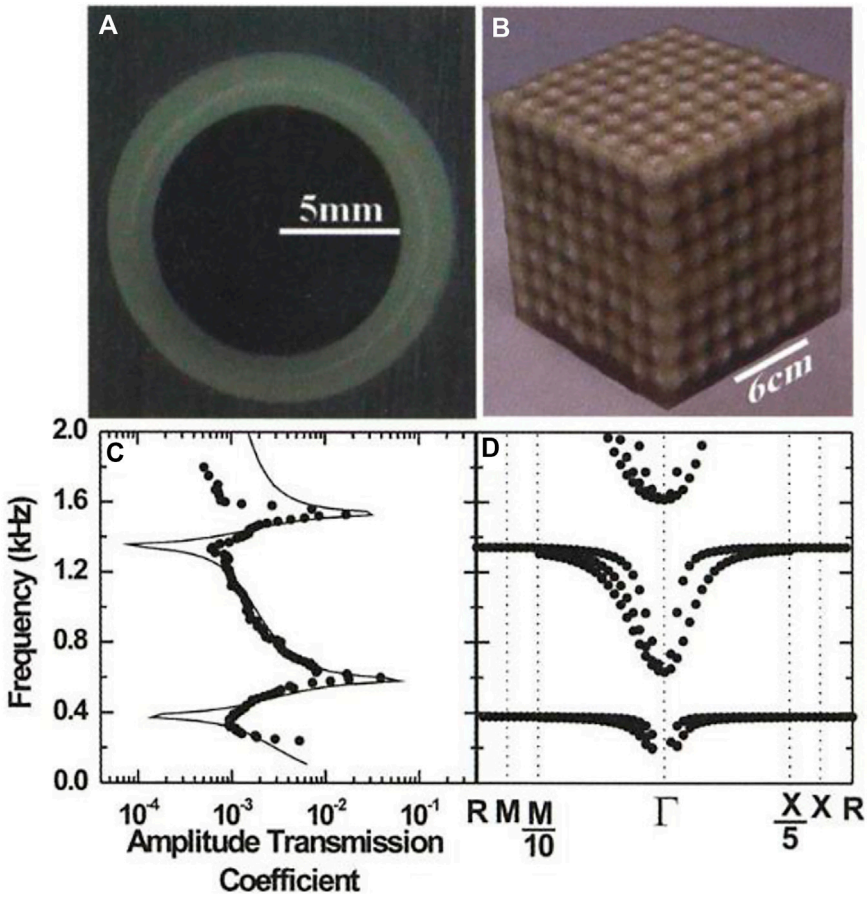

FIGURE 1
(A) The cross-section of the coated lead ball of the basic structural unit; **(B)** is an 8 × 8 × 8 sonic crystal; **(C)** Calculated (solid line) and measured (circle) amplitude transfer coefficients as a function of frequency; **(D)** Comparison of the observed transmission properties with the calculated band structure. Reprinted from [14] with permission.

optimal design of the crystal structure. The most commonly used for the optimal design of phononic crystals is topology optimization, a method for calculating material distributions that creates structural layouts without prior shape information [40]. It is used to iteratively search for innovative material distributions within a prescribed design domain for optimal structural performance [41, 42]. Over the past decade, topology optimization methods have made great strides. These methods include density-based [43], level sets [44], phase fields [45, 46], topological derivatives [47], evolutionary methods [48], topology and geometry optimization [21–23, 49], etc. However, due to the high dimensionality of the engineering design space, topology optimization cannot solve the problem of precise manipulation of acoustic waves [50].

Hosseinkhani, Younesian, Krushynska, et. al [21]. studied the structural noise and vibration response of concave hexagonal honeycomb core plates by using topological optimization method and full gradient two-dimensional geometric optimization method. The results shown in Figure 3 indicate that the interaction between structural vibration and induced noise is more complex in the low frequency range, and the best noise reduction effect can be obtained by properly combining the enhanced and non-enhanced characteristics of a single structure. Under various random loads, the sound power level can be reduced by about 20%, but the total mass increases slightly (<5%). In addition, the structural eigenfrequency is transferred to a lower value, which is ideal for applications in the aerospace industry.

Mazloomi, Ranjbar and Hosseinkhani [22, 23] optimized the parameters of the distribution by identifying local internal resonators to enhance the vibration-acoustic performance of the sandwich panels with four-chiral resistance. The sandwich panel and its reinforced core were simulated using the full-scale finite element method. The equivalent homogenization model is

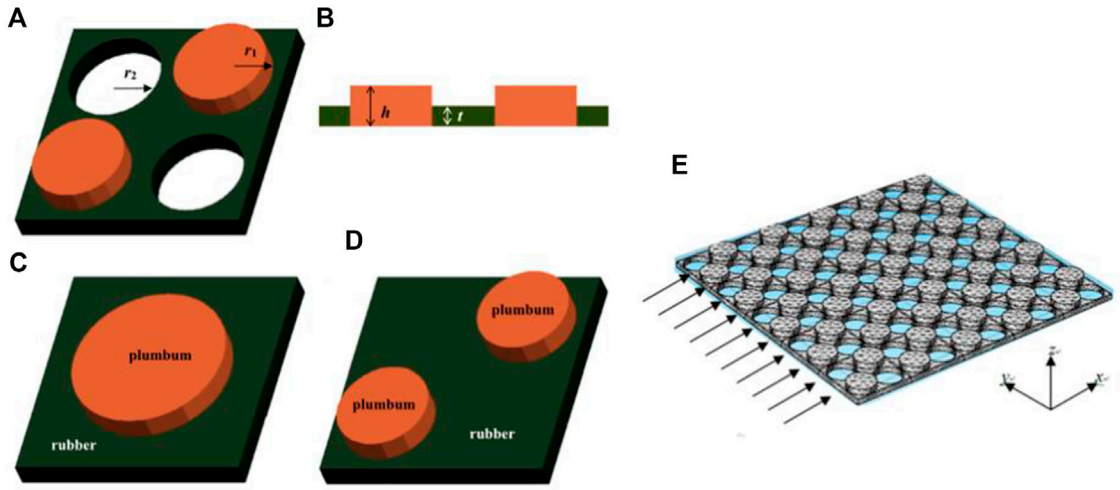

FIGURE 2
Unit cell of phononic crystal: **(A)** Novel PC plate; **(B)** Section of new PC plate; **(C)** Single short plate; **(D)** Thick plate with double short piles; **(E)** Incident situation of PCS. Reprinted from [39] with permission.

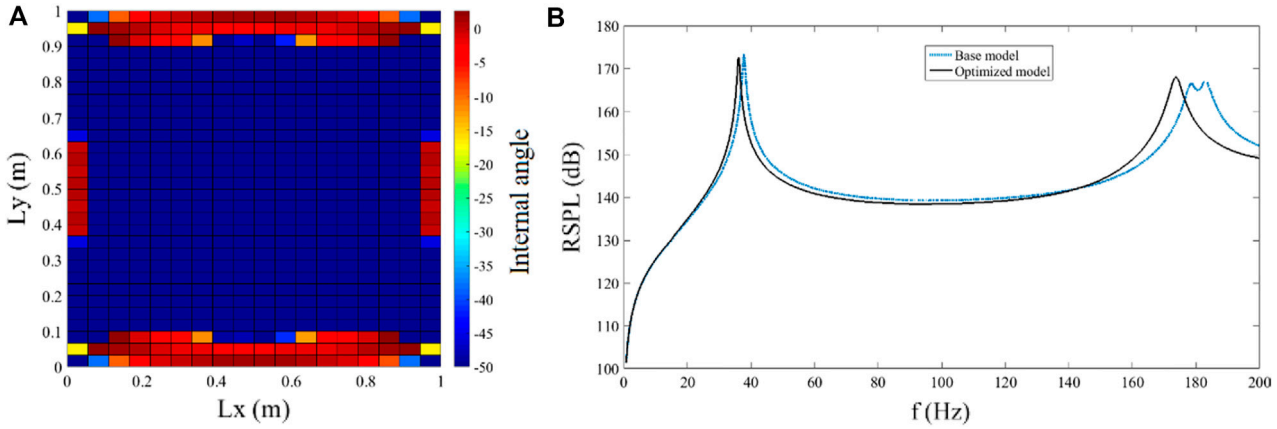

FIGURE 3
(A) Structure of the optimum core for the Violet noise excitation; **(B)** The RSPL of the optimized configuration in comparison with the base model. Reprinted from [21] with permission.

used to reduce the calculation time of the optimization problem. The results shown in Figure 4 indicate compared with the calculated results of the accurate full size sandwich structure finite element model, and the radiated sound power levels of different geometric parameters of the sandwich structure and the minimized sandwich structure in the 0–200 Hz band are calculated. A hybrid optimization design method combining moving asymptote method and genetic algorithm is adopted. Compared with the baseline sandwich panel configuration, the optimized 2D gradient configuration significantly reduces the standardized radiated sound power level by 78% and increases the fundamental frequency by 15%.

Aided by image-based finite element analysis and deep learning, Li et al. [51] proposed a data-driven phononic crystal design method in this study, and the workflow is shown in Figure 5. Train an autoencoder to extract topological features from sample images. The band gap of the samples was studied by finite element analysis. A multilayer perceptron is trained to establish the intrinsic relationship between the band gap and topological features. The trained

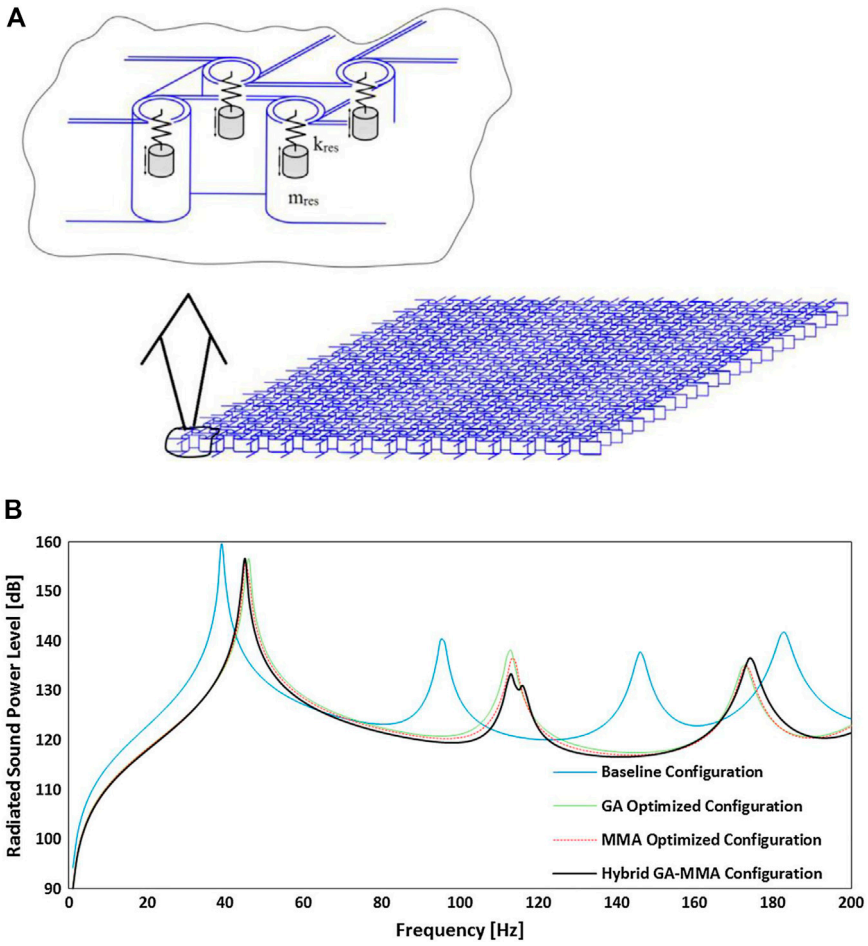

FIGURE 4
(A) Schematic of localized resonators in the auxetic core structure. Reprinted from [23] with permission. **(B)** RSPL vs. frequency, different anti-tetrachiral configurations. Reprinted from [22] with permission.

model was finally used to design phononic crystals with the expected band gaps.

In contrast to topology optimization methods, this method does not require real-time computations for specific optimization applications. The deep learning model in this method learns the implicit relationship between the input and output data. To a certain extent, the learned knowledge can accurately handle data outside the training set. In addition, deep learning models are able to self-evolve in the background by continuously providing training data. The method is not only applicable to this material, but can be further applied to design various structured mechanical materials with specific functions.

2.2 Bioinspired acoustic metamaterials

In addition to the design methods mentioned above, it is worth noting recently that many studies have begun to combine biology with mechanics, taking inspiration from biological systems to create new knots [24–28]. These new structural metamaterials have superior mechanical properties, better designability and tunability, and are new ideas for future structural design of acoustic metamaterials.

Microtubules are biopolymer hollow tubes that form an entangled radial network from the nucleus to the cell membrane. They are a major component of the cytoskeleton, providing mechanical stiffness, organization, and shape to the cytoplasm of eukaryotic cells. It plays an important role in the processes of division, intercellular transport, and internal organization of cellular components. Jafari et al. [27] investigated the propagation of elastic waves in periodic networks of various 2D microtubule bio-nanostructures, and analyzed their dynamic properties, providing the possibility for further applications. Figure 6 depicts a single microtubule and the method by which it builds its architectural structure. Microtubules themselves

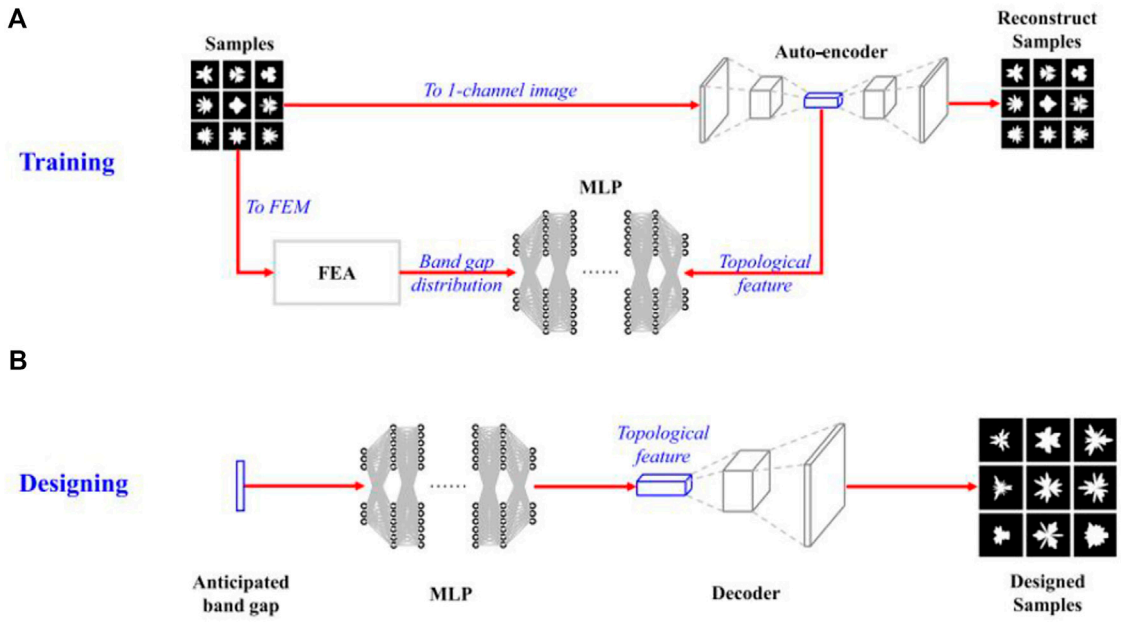

FIGURE 5
Workflow for designing a prospective bandgap phononic crystal. Reprinted from [51] with permission. **(A)** phononic crystal training, **(B)** Phononic crystal design.

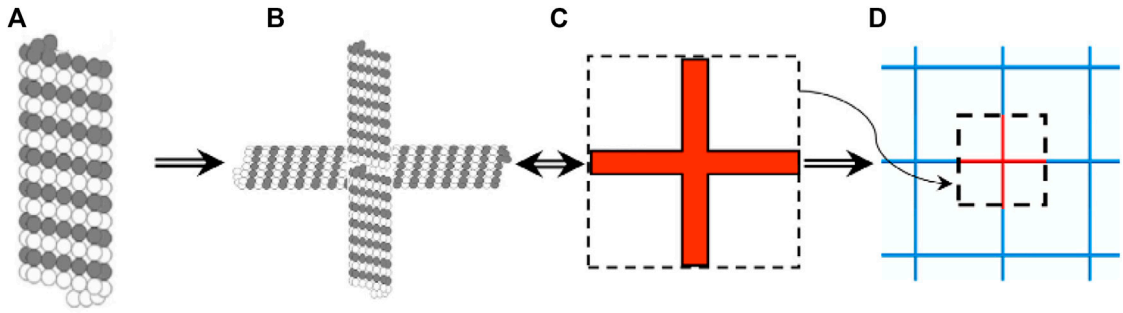

FIGURE 6
From single microtubule to periodic architected structure. Reprinted from [27] with permission. **(A)** Microtubule structure, **(B)** Two perpendicular microtubule structure, **(C)** Square unit cell microtubule, **(D)** 2-D periodic architected structure.

are composed of α-tubulin and β-tubulin (a), and a square unit cell composed of two vertical microtubules is shown in (b, c). By repeating cells in the *x* and *y* directions, two-dimensional periodic architectures can be formed (d).

The research starts with the selection of a suitable single-microtubule beam model and experimentally demonstrates that ten widely used periodic structures are established. The finite element models of individual microtubules and network microtubules are established respectively, and the phonon band structure is calculated according to Bloch's theorem. The results show that depending on the chosen topology of the unit cell and the periodicity considered, the low and high frequency band gaps of the biological filter can be designed within a specific range. This application could help researchers use architectural periodic structures to control some unwanted or harmful vibrations, and the network could be applied to next-generation nanobiomechanical instruments due to its higher biocompatibility due to its biomaterial origin, such as implantable biosensors.

Panahi, Hosseinkhani, Khansanami et al. [49] carried out numerical and experimental studies on the dispersion characteristics of elastic waves of a new Maltese cross shaped

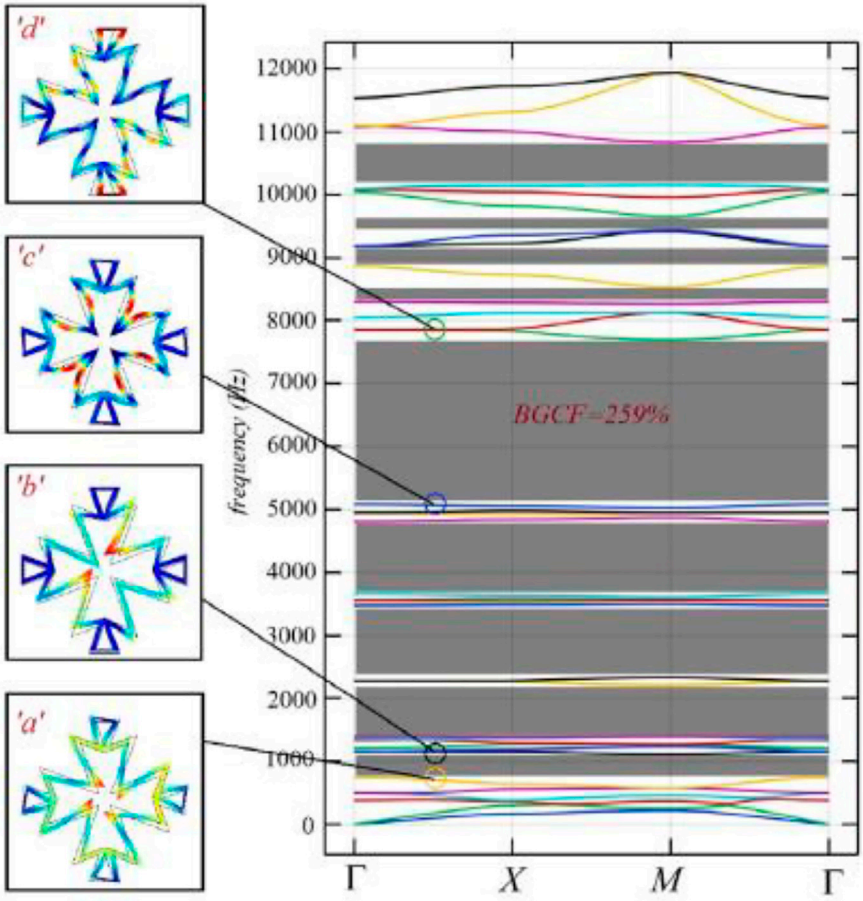

FIGURE 7
The dispersion curves along the borderline of the first irreducible Brillouin zone and vibration mode shapes. Reprinted from [49] with permission.

element and a triangular element instead of a lateral ligament element. Based on Bloch theorem of infinite element structure, the eigenfrequency problem of element is solved by finite element method. The results as shown in Figure 7 indicate that these new cells can provide more than 200% phonon band gap coverage factor (BGCF) in the low frequency range of 0–12 kHz. The results are compared with the band gap obtained from the periodic Bloch theorem. This study provides a practical application of a new phononic crystal as a frequency tool to prevent the propagation of elastic waves and adjust the position of the band gap according to the topology of the unit cell.

2.3 Acoustic metamaterials based on fractal geometry

There are also many researchers using fractal structures to realize elastic wave band gaps. It has been demonstrated that optimized fractal techniques can be used to create wider band gaps and that fractal geometries have significant advantages in band gap generation [51–53]. The most commonly used fractal technique is the Hilbert fractal. Man et al. [29, 30] designed the topology of Hilbert fractal acoustic metamaterials (HFAMs) with negative mass density and bulk modulus at the subwavelength scale by introducing the Hilbert curve channel. As shown in Figure 6. HFAM can enable applications ranging from acoustic blocking, quarter-bending, acoustic stealth to acoustic tunneling, and may further offer the possibility of engineering guidance for exotic properties at subwavelength scales.

Figure 8 shows the first-order, second-order, and third-order two-dimensional cells of HFAM, respectively. In the design of HFAM, a square with side length a/2 is divided into 2^1-by-2^1 sections. The centers of the 2^1-by-2^1 sections are connected in a clockwise direction from the lower left and lower right to form the K-Hilbert curve channel width, as shown in Figure 6A. As the fractal order increases, the square of a/2 is divided into sections of 2^2-by-2^2 and 2^3-by-2^3, respectively, as shown in Figures 8B,C. Figures 8D–F represent the first to third order cells of HFAM.

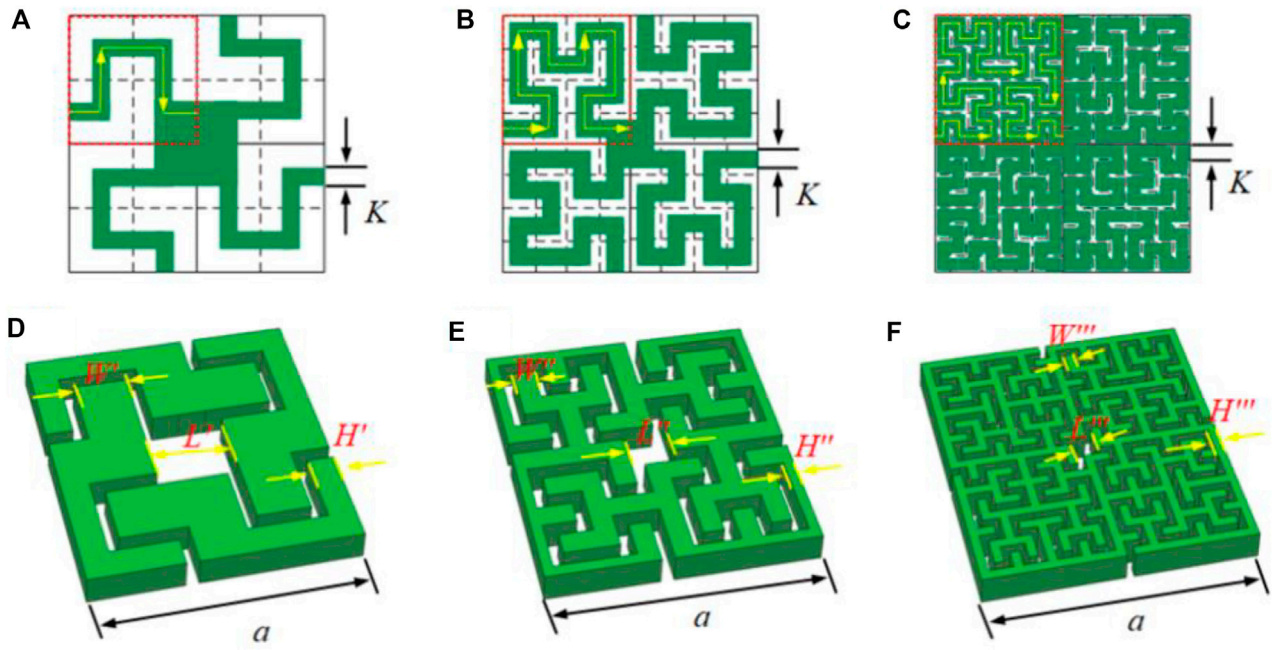

FIGURE 8
Schematic cross-sectional illustrations of three types of unit cells of HFAM: **(A–C)** The Hilbert curve channel of the first to third order HFAM with fluid. **(D–F)** The oblique drawing of unit cells of the first to third order HFAM. The material of HFAM applied is epoxy resin. The geometric and property parameters of HFAM are listed: a = 105 mm, K = 5 mm; H' = 10.625 mm, H'' = 4.0625 mm, H''' = 0.7812 mm: W' = 21.25 mm, W'' = 8.125 mm, W''' = 1.5625 mm: p = 1,050 kg/m, c = 2,500 m/s and p_o = 1.25 kg/m, c_o = 343 m/s. Reprinted from [29] with permission.

The proposed structure consists of a square frame and is divided into four sectors with independent curved channels connected in the center. The total Euclidean length of a fractal waveguide can be simply calculated as $L = 2^{N-1}a - 1 (N = 1, 2, 3)$. In addition, the propagation length of sound waves within a unit cell is related to the Hilbert curve. From the above discussion, we can conclude that the low frequency acoustic wave propagation between monopole and dipole resonances can be effectively blocked by simply arranging HFAM units in an array. Furthermore, the resonant frequencies of monopoles and dipoles can vary with the width K, so the elastic wave bandgap of HFAM is easy to tune in the subwavelength range. Furthermore, the third-order HFAM can effectively block sound waves with longer wavelengths compared to the first two. Therefore, arranging subwavelength-thick, lightweight high-order HFMs in a sparse array provides an efficient method for designing acoustic impedance.

What's more, Zhao et al. [32] found that there are multiple low energy band gaps in lattice materials with different Koch fractal geometric parameters, and the position of the lowest energy band gap decreases with the increase of the number of iterations. Lattice metamaterials with Koch fractals have potential applications in vibration isolation and multifunctional design.

3 Active metamaterials and metadevices

The mechanism of active control is the introduction of loads from electrical and/or mechanical devices. It reduces vibration amplitudes and absorbs energy associated with dynamic structures. Active control actions have superior characteristics and engineering applications due to the ability to receive external information and respond in a timely manner. Huang et al. [54] changed the effective stiffness of metamaterials by applying normal initial stress and bias electric field, so that the position of the band gap was shifted. And they calculated the band structure under the initial shear normal stress and the initial electric field by using the theory of the small field superimposed on the bias field and the plane wave expansion method. But the application of this method is difficult because large values are required to show its impact. Malinovsky and Donskoy [35] proposed and discussed the design of an actively controlled metamaterial consisting of layers of charged nano- or micro-particles exposed to an external magnetic field. As shown in Figure 9, the particles are attached to the mechanically compliant layer. These particles are in a magnetic field created by a permanent magnet. Such structures can be used to reduce acoustic radiation from structures (due to structural support vibrations) or to protect structures from incident acoustic waves.

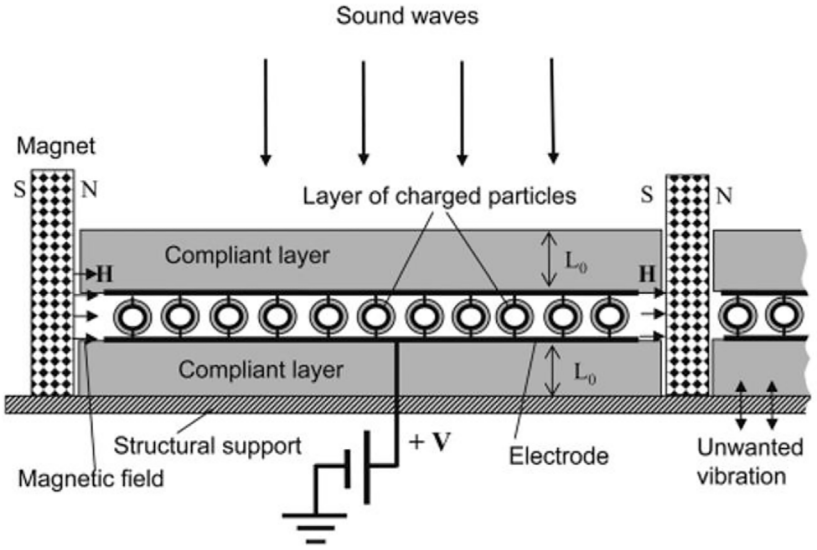

FIGURE 9
Schematic diagram of the implementation example. Reprinted from [35] with permission.

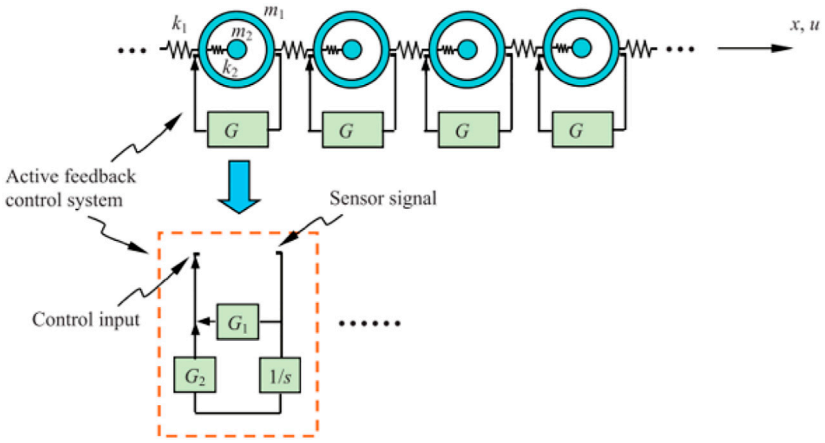

FIGURE 10
Elastic wave metamaterials with active feedback control system. Reprinted from [55] with permission.

This study highlights that the proposed method of combining electromagnetic cyclotron resonance with mechanical resonance offers many opportunities for innovative design of acoustic metamaterials. It acts as a superior sound and vibration suppressor over a very wide frequency range. Applied voltages and magnetic fields may enable more advanced capabilities such as reprogrammable material acoustic properties, metalens and stealth. In addition, Wang [55] et al. proposed a novel elastic wave metamaterial and its automatic control system, as shown in Figure 10. The propagation properties of elastic waves are discussed. To verify the effectiveness of active feedback control, the stop-band characteristics of the system, the tunability of negative effective mass and the stability of the control system are considered.

Numerical results in the study show that positive acceleration and velocity feedback control actions can reduce the stopping bandwidth. The frequency region of the negative effective mass

increases as the negative acceleration control effect increases, which is the opposite of the positive case. In addition, stable characteristics can be achieved by both positive and negative feedback control actions. This will provide a possible approach for the application of elastic wave metamaterials.

4 Conclusion and research prospect

In this paper, the related literatures on acoustic metamaterials are sorted and analyzed, and the acoustic metamaterials are divided into passive acoustic metamaterials and active acoustic metamaterials according to the response mode and compared and analyzed.

Passive acoustic metamaterial is an early and relatively mature metamaterial, which can achieve the required elastic wave gap through a specially designed material structure. The most well-known passive acoustic metamaterials are phononic crystals, which are a new type of functional material formed by periodic arrangement of elastic solids in another solid or fluid medium. In this paper, Bragg scattering and local resonance phononic crystals are introduced. The former is mainly because the periodicity of the structure plays a leading role, so the central frequency of the band gap is limited by the lattice constant, and the low-frequency elastic wave cannot be controlled. The latter is mainly dominated by the resonance characteristics of a single scatterer, whose lattice constant is several orders of magnitude smaller than the spectral gap of the relevant wavelength, which can effectively solve the predicament of Bragg scattering crystals at low frequencies. The structural design of phononic crystals mainly adopts topological structure. Mazloomi, Ranjbar and Hosseinkhani et. al. have solved the problem of precise control of sound waves in topological optimization design. The research on crystal structure design based on machine learning can also effectively solve these problems. Also noteworthy for structural design methods of passive acoustic metamaterials are bio-inspired and fractal geometry-based structural design methods. Acoustic metamaterials based on bio-inspired designs combine biology and mechanics to create new structures inspired by biological systems. The designed metamaterials have better mechanical properties, better designability and tunability. There are multiple low-energy band gaps in the acoustic metamaterial based on fractal geometry design, and the position of the lowest energy band gap decreases with the increase of fractal iterations, which has potential applications in vibration isolation and multi-functional design. Both of these design methods have great research potential.

However, the structural immutability of passive metamaterials limits their performance, functionality, and tunability. To address this conundrum, researchers have begun to incorporate active elements, tunable and/or programmable devices into metamaterial designs, making it possible to control the function of active acoustic metamaterials by external stimuli. Compared with passive acoustic metamaterials, active acoustic metamaterials can control external stimuli more freely and conveniently, and there are fewer related studies, so they have great research potential. The method of applying initial stress and bias electric field to change the material properties is feasible, but it is less practical due to the large value of the applied field. Other methods, such as magnetic field-based control, are also enumerated in this paper. Some researchers have also established automatic control systems to analyze actively controlled metamaterials more comprehensively and systematically. Active metamaterials are still less researched so far and more research is needed.

In addition, with the continuous development of additive manufacturing technology, the development process of metamaterials has been accelerated. Additive manufacturing techniques can create custom polymer, metal, ceramic and composite structures. Therefore, designing and fabricating programmable metamaterials with additive manufacturing techniques could enable a large number of metamaterial devices for practical applications. It can be seen that the manufacturing potential and application prospects of acoustic metamaterials in the future are huge.

Author contributions

Conceptualization, HD and YZ; methodology, XZ and YZ; formal analysis, WP and RZ; investigation, YZ and YG; data curation, HD; writing—original draft preparation, HD and YZ; writing—review and editing, XZ and YZ; supervision, XZ and RL; project administration, RZ; funding acquisition, RZ All authors have read and agreed to the published version of the manuscript.

Funding

This research was funded by the Sichuan Science and Technology Program (No.2022YFG0274), the Key Research and Development Program of Zhejiang Province (Grant No.2021C01399), National Natural Science Foundation of China (Grant No.51875146).

Acknowledgments

We thank Junyi Wu for many helpful conversations and meetings, and Wenxin Li for highly fruitful discussions and comments.

Conflict of interest

The authors declare that the research was conducted in the absence of any commercial or financial relationships that could be construed as a potential conflict of interest.

Publisher's note

References

1. Veselago VG. Electrodynamics of substances with simultaneously negative and. *Usp fiz nauk* (1967) 92(7):790. doi:10.3367/ufnr.0173.200307m.0790

2. Bliokh KY, Bliokh YP. What are the left-handed media and what is interesting about them? *Phys -Usp* (2004) 47(4):393–400. doi:10.1070/pu2004v047n04abeh001728

3. Vendik I, Vendik O. Metamaterials and their application in microwaves: A review. *Tech Phys* (2013) 58(1):1–24. doi:10.1134/s1063784213010234

4. Sellami K, Ketata H, Ben Ghozlen MH. Locally resonant phononic crystals band-gap analysis on a two dimensional phononic crystal with a square and a triangular lattice. *Opt Quan Electron* (2019) 51(9):311–4. doi:10.1007/s11082-019-2028-0

5. Miniaci M, Gliozzi AS, Morvan B, Krushynska A, Bosia F, Scalerandi M, et al. Proof of concept for an ultrasensitive technique to detect and localize sources of elastic nonlinearity using phononic crystals. *Phys Rev Lett* (2017) 118(21):214301. doi:10.1103/physrevlett.118.214301

6. Darinskii A, Shuvalov A. Surface acoustic waves on one-dimensional phononic crystals of general anisotropy: Existence considerations. *Phys Rev B* (2018) 98(2): 024309. doi:10.1103/physrevb.98.024309

7. Liu Y, Chang Z, Feng XQ. Stable elastic wave band-gaps of phononic crystals with hyperelastic transformation materials. *Extreme Mech Lett* (2017) 11:37–41. doi:10.1016/j.eml.2016.11.007

8. Fomenko S, Golub M, Zhang C, Bui T, Wang Y-S. In-plane elastic wave propagation and band-gaps in layered functionally graded phononic crystals. *Int J Sol Structures* (2014) 51(13):2491–503. doi:10.1016/j.ijsolstr.2014.03.017

9. Zheng M, Wei PJ. Band gaps of elastic waves in 1-D phononic crystals with imperfect interfaces. *Int J Minerals, Metall Mater* (2009) 16(5):608–14. doi:10.1016/s1674-4799(09)60105-9

10. Li F-L, Wang Y-S, Zhang C. A BEM for band structure and elastic wave transmission analysis of 2D phononic crystals with different interface conditions. *Int J Mech Sci* (2018) 144:110–7. doi:10.1016/j.ijmecsci.2018.05.042

11. Sun Y, Yu Y, Zuo Y, Qiu L, Dong M, Ye J, et al. Band gap and experimental study in phononic crystals with super-cell structure. *Results Phys* (2019) 13:102200. doi:10.1016/j.rinp.2019.102200

12. Engheta N, Ziolkowski RW. *Metamaterials: Physics and engineering explorations*. New York: John Wiley & Sons (2006).

13. Marqués R, Martin F, Sorolla M. *Metamaterials with negative parameters: Theory, design, and microwave applications*. New York: John Wiley & Sons (2011).

14. Liu Z, Zhang X, Mao Y, Zhu Y, Yang Z, Chan CT, et al. Locally resonant sonic materials. *science* (2000) 289(5485):1734–6. doi:10.1126/science.289.5485.1734

15. Wang P, Casadei F, Kang SH, Bertoldi K. Locally resonant band gaps in periodic beam lattices by tuning connectivity. *Phys Rev B* (2015) 91(2):020103. doi:10.1103/physrevb.91.020103

16. Chen Y, Li T, Scarpa F, Wang L. Lattice metamaterials with mechanically tunable Poisson's ratio for vibration control. *Phys Rev Appl* (2017) 7(2):024012. doi:10.1103/physrevapplied.7.024012

17. Hosseinkhani A, Younesian D, Ranjbar M. Vibro-acoustic analysis and topology optimization of anti-tetra chiral auxetic lattices driven by different colored noises. *Int J Str Stab Dyn* (2020) 20:2050113. doi:10.1142/s0219455420501138

18. Trainiti G, Rimoli JJ, Ruzzene M. Wave propagation in undulated structural lattices. *Int J Sol Structures* (2016) 97:431–44. doi:10.1016/j.ijsolstr.2016.07.006

19. Fan H, Xia B, Tong L, Zheng S, Yu D. Elastic higher-order topological insulator with topologically protected corner states. *Phys Rev Lett* (2019) 122(20): 204301. doi:10.1103/physrevlett.122.204301

20. Xia B, Wang G, Zheng S. Robust edge states of planar phononic crystals beyond high-symmetry points of Brillouin zones. *J Mech Phys Sol* (2019) 124: 471–88. doi:10.1016/j.jmps.2018.11.001

21. Hosseinkhani A, Younesian D, Krushynska AO, Ranjbar M, Scarpa F. Full-gradient optimization of the vibroacoustic performance of (Non-)auxetic sandwich panels. *Transp Porous Media* (2022) 142:139–56. doi:10.1007/s11242-021-01693-0

22. Mazloomi MS, Ranjbar M. Hybrid design optimization of sandwich panels with gradient shape anti-tetrachiral auxetic core for vibroacoustic applications. *Transp Porous Media* (2022) 142:5–22. doi:10.1007/s11242-021-01646-7

23. Hosseinkhani A, Younesian D, Ranjbar M, Scarpa F. Enhancement of the vibro-acoustic performance of anti-tetra-chiral auxetic sandwich panels using topologically optimized local resonators. *Appl Acoust* (2021) 177:107930. doi:10.1016/j.apacoust.2021.107930

24. Chen Y, Wang L. Bio-inspired heterogeneous composites for broadband vibration mitigation. *Sci Rep* (2015) 5(1):17865–11. doi:10.1038/srep17865

25. Miniaci M, Krushynska A, Movchan AB, Bosia F, Pugno NM. Spider web-inspired acoustic metamaterials. *Appl Phys Lett* (2016) 109(7):071905. doi:10.1063/1.4961307

26. Zheng B, Xu J. Mechanical logic switches based on DNA-inspired acoustic metamaterials with ultrabroad low-frequency band gaps. *J Phys D Appl Phys* (2017) 50(46):465601. doi:10.1088/1361-6463/aa8b08

27. Jafari H, Yazdi MRH, Fakhrabadi MMS. Wave propagation in microtubule-based bio-nano-architected networks: A lesson from nature. *Int J Mech Sci* (2019) 164:105175. doi:10.1016/j.ijmecsci.2019.105175

28. Zhu Z, Deng Z, Du J. Elastic wave propagation in hierarchical honeycombs with woodpile-like vertexes. *J Vibration Acoust* (2019) 141(4). doi:10.1115/1.4043352

29. Man X, Luo Z, Liu J, Xia B. Hilbert fractal acoustic metamaterials with negative mass density and bulk modulus on subwavelength scale. *Mater Des* (2019) 180:107911. doi:10.1016/j.matdes.2019.107911

30. Man XF, Xia BZ, Luo Z, Liu J. 3D Hilbert fractal acoustic metamaterials: Low-frequency and multi-band sound insulation. *J Phys D Appl Phys* (2019) 52(19): 195302. doi:10.1088/1361-6463/ab092a

31. Khoshhesab MM, Li Y. Mechanical behavior of 3D printed biomimetic Koch fractal contact and interlocking. *Extreme Mech Lett* (2018) 24:58–65. doi:10.1016/j.eml.2018.09.003

32. Zhao P, Zhang K, Deng Z. Elastic wave propagation in lattice metamaterials with Koch fractal. *Acta Mech Solida Sin* (2020) 33(5):600–11. doi:10.1007/s10338-020-00177-w

33. Asiri S, Baz A, Pines D. Active periodic struts for a gearbox support system. *Smart Mater Struct* (2006) 15(6):1707–14. doi:10.1088/0964-1726/15/6/024

34. Chen Y, Hu J, Huang G. A design of active elastic metamaterials for control of flexural waves using the transformation method. *J Intell Mater Syst Structures* (2016) 27(10):1337–47. doi:10.1177/1045389x15590273

35. Malinovsky VS, Donskoy DM. Electro-magnetically controlled acoustic metamaterials with adaptive properties. *The J Acoust Soc America* (2012) 132(4): 2866–72. doi:10.1121/1.4744943

36. Zhang Z, Han X. A new hybrid phononic crystal in low frequencies. *Phys Lett A* (2016) 380(45):3766–72. doi:10.1016/j.physleta.2016.09.019

37. Sigalas MM, Economou EN. Elastic and acoustic wave band structure. *J sound vibration* (1992) 158(2):377–82. doi:10.1016/0022-460x(92)90059-7

38. Kushwaha MS, Halevi P, Dobrzynski L, Djafari-Rouhani B. Acoustic band structure of periodic elastic composites. *Phys Rev Lett* (1993) 71(13):2022–5. doi:10.1103/physrevlett.71.2022

39. Martínez-Sala R, Sancho J, Sánchez JV, Gómez V, Llinares J, Meseguer F. Sound attenuation by sculpture. *nature* (1995) 378(6554):241. doi:10.1038/378241a0

40. Liu K, Tovar A. An efficient 3D topology optimization code written in Matlab. *Struct Multidiscipl Optim* (2014) 50(6):1175–96. doi:10.1007/s00158-014-1107-x

41. Bendsøe MP. Optimal shape design as a material distribution problem. *Struct optimization* (1989) 1(4):193–202. doi:10.1007/bf01650949

42. Sigmund O, Maute K. Topology optimization approaches. *Struct Multidiscipl Optim* (2013) 48(6):1031–55. doi:10.1007/s00158-013-0978-6

43. Andreassen E, Clausen A, Schevenels M, Lazarov BS, Sigmund O. Efficient topology optimization in MATLAB using 88 lines of code. *Struct Multidiscipl Optim* (2011) 43(1):1–16. doi:10.1007/s00158-010-0594-7

44. Allaire G, Jouve F, Toader A-M. Structural optimization using sensitivity analysis and a level-set method. *J Comput Phys* (2004) 194(1):363–93. doi:10.1016/j.jcp.2003.09.032

45. Bourdin B, Chambolle A. Design-dependent loads in topology optimization. *ESAIM: Control, Optimisation and Calculus of Variations* (2003) 9:19–48. doi:10.1051/cocv:2002070

46. Takezawa A, Nishiwaki S, Kitamura M. Shape and topology optimization based on the phase field method and sensitivity analysis. *J Comput Phys* (2010) 229(7):2697–718. doi:10.1016/j.jcp.2009.12.017

47. Norato JA, Bendsøe MP, Haber RB, Tortorelli DA. A topological derivative method for topology optimization. *Struct Multidiscipl Optim* (2007) 33(4):375–86. doi:10.1007/s00158-007-0094-6

48. Mattheck C, Burkhardt S. A new method of structural shape optimization based on biological growth. *Int J Fatigue* (1990) 12(3):185–90. doi:10.1016/0142-1123(90)90094-u

49. Panahi E, Hosseinkhani A, Khansanami MF, Younesian D, Ranjbar M. Novel cross shape phononic crystals with broadband vibration wave attenuation characteristic: Design, modeling and testing. *Thin-Walled Structures* (2021) 163:107665. doi:10.1016/j.tws.2021.107665

50. Bessa MA, Bostanabad R, Liu Z, Hu A, Apley DW, Brinson C, et al. A framework for data-driven analysis of materials under uncertainty: Countering the curse of dimensionality. *Comp Methods Appl Mech Eng* (2017) 320:633–67. doi:10.1016/j.cma.2017.03.037

51. Li X, Ning S, Liu Z, Yan Z, Luo C, Zhuang Z. Designing phononic crystal with anticipated band gap through a deep learning based data-driven method. *Comp Methods Appl Mech Eng* (2020) 361:112737. doi:10.1016/j.cma.2019.112737

52. Puente-Baliarda C, Romeu J, Pous R, Cardama A. On the behavior of the Sierpinski multiband fractal antenna. *IEEE Trans Antennas Propag* (1998) 46(4):517–24. doi:10.1109/8.664115

53. Castiñeira-Ibáñez S, Rubio C, Redondo J, Sánchez-Pérez JV. Quantitative characterization of bandgap properties of sets of isolated acoustic scatterers arranged using fractal geometries. *Appl Phys Express* (2014) 7(4):042201. doi:10.7567/apex.7.042201

54. Huang Y, Zhang C, Chen W. Tuning band structures of two-dimensional phononic crystals with biasing fields. *J Appl Mech* (2014) 81(9). doi:10.1115/1.4027915

55. Wang Y-Z, Li F-M, Wang Y-S. Active feedback control of elastic wave metamaterials. *J Intell Mater Syst Structures* (2017) 28(15):2110–6. doi:10.1177/1045389x16682851

frontiers | Frontiers in Physics

TYPE Mini Review
PUBLISHED 22 November 2022
DOI 10.3389/fphy.2022.1069722

OPEN ACCESS

EDITED BY
Hui Chen,
Ningbo University, China

REVIEWED BY
Qiujiao Du,
China University of Geosciences Wuhan, China
Xiaodong Zhang,
Huaqiao University, China

*CORRESPONDENCE
Huajie Dai,
qinlongcrcc@foxmail.com
Chuanping Zhou,
zhoucp@hdu.edu.cn
Zhiwen Wang,
wzw3049972460@hdu.edu.cn
Rougang Zhou,
42141@hdu.edu.cn

SPECIALTY SECTION
This article was submitted to Physical Acoustics and Ultrasonics, a section of the journal Frontiers in Physics

RECEIVED 14 October 2022
ACCEPTED 07 November 2022
PUBLISHED 22 November 2022

CITATION
Zheng Y, Dai H, Wu J, Zhou C, Wang Z, Zhou R and Li W (2022), Research progress and development trend of smart metamaterials.
Front. Phys. 10:1069722.
doi: 10.3389/fphy.2022.1069722

Research progress and development trend of smart metamaterials

Yongju Zheng[1,2], Huajie Dai[1]*, Junyi Wu[3], Chuanping Zhou[1]*, Zhiwen Wang[1]*, Rougang Zhou[1,4]* and Wenxin Li[1]

[1]School of Mechanical Engineering, Hangzhou Dianzi University, Hangzhou, China, [2]College of Environmental Science and Engineering, Tongji University, Shanghai, China, [3]Sanmen Sanyou Technology Co., Ltd., Taizhou, China, [4]Wenzhou Institute of Hangzhou Dianzi University, Wenzhou, China

The development of smart metamaterials has brought changes to human society, and various new products based on smart metamaterials are emerging endlessly. In recent years, smart electromagnetic metamaterials, smart acoustic metamaterials, smart mechanical metamaterials, smart thermal metamaterials and machine learning have attracted much attention in metamaterials. These fields share similar theories, such as multiphysics coupling fields, novel artificial cells and programmability. Through theoretical and technical research, smart metamaterials will show exquisite applications in many fields, such as antenna and optical communication systems, microwave imaging, acoustic stealth, thermal camouflage, etc. In particular, the characteristics of the personalized microstructure design of smart metamaterials perfectly match the characteristics of 3D printing. The combination of them leads the development of metamaterials, which are undoubtedly of great value. In this paper, focusing on the representative key technologies, we review the development history, main research directions and latest applications of smart metamaterials. Finally, the possible development direction of metamaterials is predicted.

KEYWORDS

smart metamaterials, electromagnetic metamaterials, acoustic metamaterials, mechanical metamaterials, thermal metamaterials, machine learning

Introduction

Changing the properties of materials by changing their composition is the way in which materials science has been developed in the past. The physical properties of natural materials depend on the basic units and structures which make them up, such as atoms, molecules, lattices, etc. These basic units and structures are interrelated, and many complex factors need to be considered when designing materials. Unfortunately, these factors influence and restrict each other, and limit the upper limit of material properties. In 1968, Veselago first proposed the concept of "medium with negative refractive index" [1], which refers to the medium with negative permittivity and permeability. He also theoretically proved some physical phenomena that contradict common sense, such as the

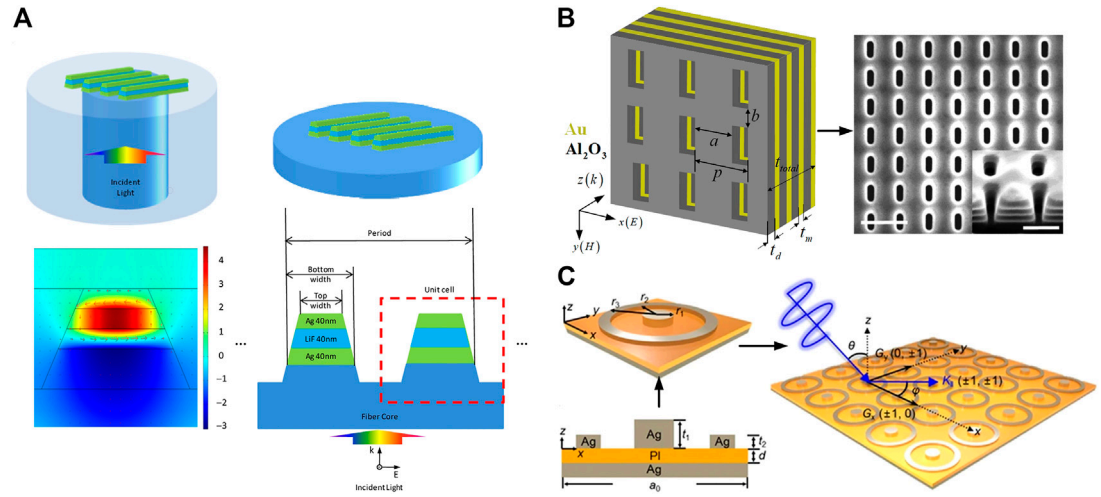

FIGURE 1
(A) A fiber-coupled magnetic metamaterial structure schematically [12]. **(B)** Schematic diagram of a fishnet metamaterial made of metal-dielectric multilayer stack and top scanning electron microscope image of its structure. The scale bars are 1 μm and 500 nm, respectively [13]. **(C)** Schematic diagram and surface plasmon polariton excitation of the dual-band perfect absorber. The Metal–insulator–metal structure is composed of Ag and polyimide (PI) layers having thicknesses of t_1, t_2, and d, and a unit cell period of a_0. Unit cell of the circular ring-disk structure, where the disk radius is r_1 and the inner and outer radii of the ring are r_2 and r_3, respectively. Incident light (red line) with polar angle θ encounters a 2D array consisting of circular metal disks and rings. The first Brillouin zone is defined by connecting the perpendicular bisectors of the reciprocal lattice, and a portion of the incident light propagates in the plane containing the periodic pattern with azimuthal angle φ [14].

inverse propagation of electromagnetic waves, inverse Doppler effect and inverse Cherenkov radiation in negative refractive index media. However, as there is no medium with negative permittivity and permeability in nature, Veselago's theory cannot be verified experimentally, so people do not pay enough attention to his discovery. It was not until 2001 that Smith et al. [2] from the University of California, San Diego, made media with negative permittivity and permeability in the microwave band with copper composite materials. They used the brilliant design method which id proposed by Professor John Pendry [3–5] from Imperial College London, United Kingdom. Thus, the phenomenon of negative refraction was experimentally confirmed for the first time. The result of this research has stimulated the research enthusiasm for metamaterials.

Smart materials are materials that respond to stimuli in the environment. Differing from traditional functional materials, smart metamaterials can not only possess the above characteristics but also control electromagnetic and elastic waves through special microstructure design, which enables the materials to display novel force, thermal, acoustic and optical properties. In the early days, the design of metamaterials was mainly based on the equivalent medium theory. The core idea is to break through the limitations of natural laws through the well-designed microstructures, so as to obtain extraordinary physical properties that natural materials do not have [6], such as negative refractive index, negative mass density, negative Poisson ratio, negative dielectric constant, negative permeability, negative bulk modulus, anti-sign thermal expansion coefficient, etc. [7, 8]. Compared with the physical properties of the constituent materials, these features are mainly determined by the topology and deformation of the artificial microstructures [9–11]. Although this concept has appeared in the electromagnetic field as early as the last century, it is only in the last decade that the research and development of electromagnetic wave control has been started to achieve novel functions. A Fiber-Metamaterials solution addresses the light in- and out-coupling issues and can provide fundamentally new solutions for photonic-on-a-chip systems for sensing, subwavelength imaging, image processing, and biomedical applications (Figure 1A). As shown in Figure 1B, the structure of a fishnet metamaterial is demonstrated. To be able to precise its effective parameters, an alternative optical vortex based interferometric approach for the characterization of the effective parameters of optical metamaterials (OMMs) is reported by directly measuring the transmission and reflection phase shifts from metamaterials according to the rotation of vortex spiral interference pattern. The results will pave the way for the advancement of new spectroscopic and interferometric techniques to characterize OMMs, metasurfaces, and nanostructured thin films in general. Electromagnetic stealth is also one of the hot research directions in recent years. By adjusting the physical parameters of the stealth material or changing the

structure, the resonance can be achieved and the frequency of the signal response can be changed, so as to reduce the signal detection and achieve low observability (Figure 1C).

With the advancement of advanced manufacturing technology, Metamaterials have also been extended to other control fields. Acoustic metamaterials have the ability to control the acoustic energy flow. With this unique ability, acoustic metamaterials have been used in many applications, such as acoustical absorption [15], acoustical holography [16], acoustical switching [17], energy harvesting [18], and hyperlens [19]. The basic concepts for these applications often rely on subwavelength resonance structures in the form of spatial helices, Helmholtz resonators, membrane resonators, and porous metamaterials. Although these common design methods have great acoustic manipulation capabilities, these methods are mainly passive, resulting in fixed spatial structures that can only yield limited performance and cannot adapt to changing environmental conditions. Therefore, tunable acoustic smart structures are desirable because their acoustic response can be actively controlled according to requirements. The block of mechanical metamaterial is a superatom, which deforms, bends, rotates and breaks under the action of external force, and its design enables the adjacent block to produce the desired collective behavior [7]. In recent years, with the continuous development of advanced manufacturing technologies such as 3D printing and laser selective melting, the research scope of mechanical metamaterials has expanded from dynamic properties to static elastic mechanical properties, such as elastic modulus, Poisson's ratio, stiffness, strength and other mechanical parameters. It is possible to prepare mechanical metamaterials with more complex microstructures [20]. Based on the microstructure design, mechanical metamaterials can achieve abnormal and singular mechanical properties such as negative Poisson's ratio [20], lightweight [21], and negative stiffness [22]. The invention of locally resonant acoustic materials has created the field of acoustic metamaterials [23]. Their work has directly inspired metamaterial research beyond electromagnetic wave systems, including acoustic, elastic, or mechanical studies. In 2008, Fan et al. extended the concept of transform optics from wave systems to diffusion systems [24]. In the past decade, thermal metamaterials have been rapidly developed and applied in human daily life, such as thermal stealth [25], thermal camouflage [26] and thermal concentration [27].

This review investigates applications of smart metamaterials in different fields with similar theoretical foundations, such as multiphysics coupling mechanisms, novel artificial cell design, and programmability research. We summarize the fields of technology that have received priority attention from scientists and scholars to achieve smart metamaterials. These fields are smart electromagnetic metamaterials (SEMs), smart acoustic metamaterials (SAMs), smart mechanical metamaterials (SMMs), smart thermal metamaterials (STMs) and smart metamaterials and machine learning (SMML). After summarizing the key technologies and development of these smart metamaterials, we briefly discuss the development trend of smart metamaterials in recent years. Due to limited space, this review cannot cover all aspects, and relevant excellent work can be read from other reviews in recent years.

Development and research of smart metamaterials

Smart electromagnetic metamaterialss

SEMs, also known as information metamaterials, can be classified into digitally programmable metamaterials [28], computing metamaterials [29], and optically switchable metamaterials [30]. Among many research directions, digital coding and programmable metamaterials have become an important research direction. In 2014, Giovampaola and Engheta proposed a method to construct "metamaterial bytes" by spatially mixing "metamaterial bits" [31]. The "metamaterial bits" that they used are made up of particles of materials with different electromagnetic properties, such as silicon with positive permittivity and silver with negative permittivity. However, these metamaterial bytes are still constructed from the equivalent medium. As shown in Figure 2, the concepts of digital metamaterials, programmable metamaterials and metasurfaces were first proposed by Cui et al. in 2014 [28]. The programmable properties of metamaterials mean that they can achieve different functions through digital control and realize real-time regulation of electromagnetic waves. Inspired by the binary representation of digital circuits, digital metamaterials first found a way to design metamaterials from binary. By encoding the phase response of the meta-atom as "0" and "1," the electromagnetic parameters are simply related to the digital expression [32]. In fact, the method of constructing digital expressions using opposed phase before coding digital metamaterials has been widely used in antenna and optical communication fields. For example, combine a thin artificial magnetic conductor with perfect electric conductor cells into a chessboard like configuration. Around the operational frequency of the artificial magnetic conductor elements, the reflection of the artificial magnetic conductor and perfect electric conductor have opposite phase, so for any normal incident plane wave the reflections cancel out, thus reducing the radar cross-section. The same applies to specular reflections for off-normal incidence angles [33]. Similarly, by designing metamaterial resonant cells, spatial light modulators based on metamaterial absorbers can also be realized in the terahertz-band [34–36].

Traditional metasurface patterns have been completely replaced by digital coded patterns. Digital metamaterials introduce ideas from information science to simplify the design process and create more functionality. At present,

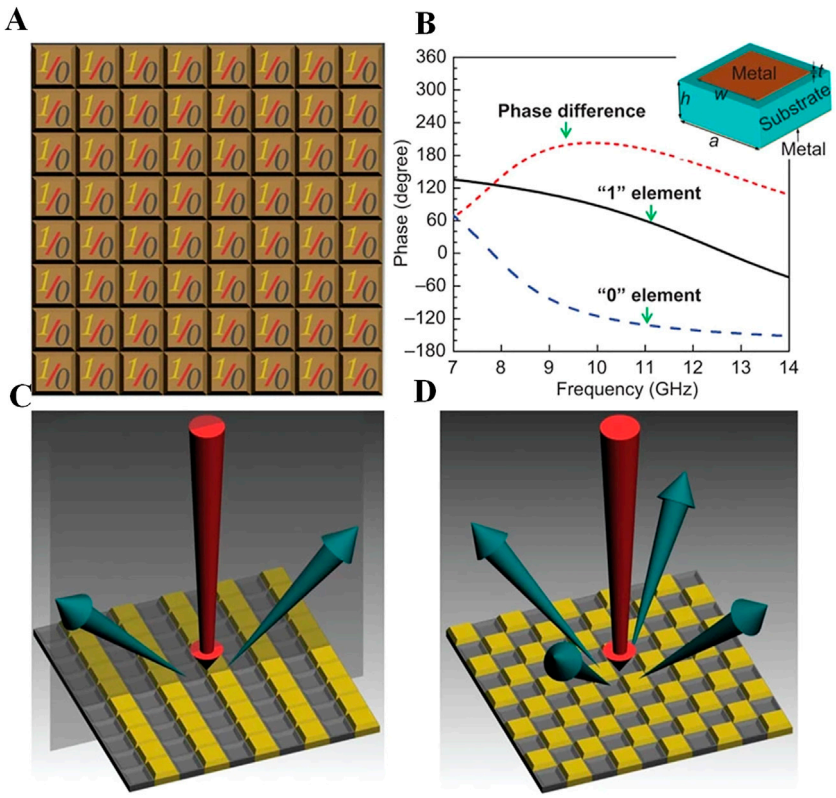

FIGURE 2
The 1-bit digital metasurface and coding metasurface. **(A)** The 1-bit digital metasurface is composed of only two types of elements: "0"and "1." **(B)** A square metallic patch unit structure (inset) to realize the "0" and "1" elements and the corresponding phase responses in a range of frequencies. **(C,D)** Two 1-bit periodic coding metasurfaces to control the scattering of beams by designing the coding sequences of "0" and "1" elements: **(C)** the 010101 . . . /010101... code and **(D)** 010101 . . . /101010... code.

digital metamaterials and programmable metasurfaces have been widely used in microwave imaging [37], information processing [38], and wireless communication [39]. More importantly, programmable metasurfaces build a bridge between the physical and digital world, which enables researchers to explore metasurfaces from the perspective of information science, forming a research system for information metasurfaces [40].

Smart acoustic metamaterials

Since both electromagnetic wave and acoustic wave meet the wave equation and have common parameters, such as wave vector, wave impedance and energy flow density, researchers have extended the design idea of electromagnetic metamaterials to the acoustic field and designed acoustic metamaterials that can have various strange effects on acoustic waves [41]. In 2000, Liu first proposed the construction of acoustic metamaterials by using structural cells of the locally resonant type [23], which opened a new way for the research of acoustic metamaterials. Similar to electromagnetic metamaterials, acoustic metamaterials are constructed by artificial design of two or more materials to form periodic/aperiodic geometric structures. The cell size of the structure is much smaller than the wavelength. Corresponding effective elastic parameters of the artificial structural functional materials can be obtained through the long-wave limit. As shown in Figure 3, in addition to local resonance acoustic metamaterials, there are tunable acoustic hypersurfaces [42], labyrinth or space coiled acoustic metamaterials [43] based on the generalized Snell's law, and porous acoustic metamaterials [44] that use different apertures and subwavelength holes of arbitrary shape to obtain high refractive index.

Over the past decade, various acoustic structures have been successfully developed to control acoustic waves, bringing new strategies for noise reduction and energy harvesting. Although these common design methods have great acoustic manipulation capability, they are mainly passive. Most acoustic metamaterials with subwavelength scale show good performance around certain frequency bands. Once the structure is established, it cannot adapt to changing circumstances. Using smart materials to design

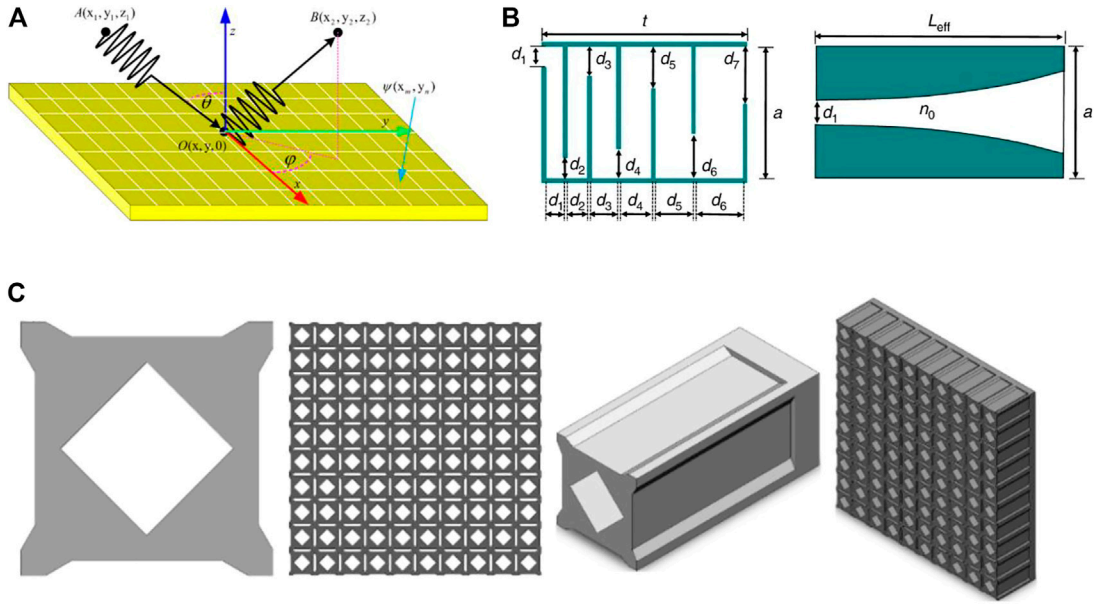

FIGURE 3
(A) Acoustic wave impinges a surface with nonzero phase gradient [42]. **(B)** Horn-like space-coiling metamaterial unit cell and its equivalent model [43]. **(C)** Composition of three-dimensional honeycomb porous frequency modulation acoustic metamaterial [44].

structures has proved to be an effective and promising approach. Smart materials are materials that change shape or properties when exposed to changes in external physical fields, such as light, electric, magnetic, and pressure. Smart materials include electroactive polymers, piezoelectric materials, shape memory materials and magnetic sensitive materials. Due to their inherent advantages such as sensitivity and biocompatibility, smart materials have been widely used in soft robots, actuators, sensors and biomedicine. Modulating external stimuli to manipulate physical properties has attracted increasing interest in the study of smart materials in tunable acoustic structures. Among the currently available works, electrically tuned [45] and magnetically tuned [46] acoustic absorbing smart metamaterials have attractive properties and good design potential.

The fusion of smart materials with acoustic metamaterials offers the opportunity for anomalously effective material properties at tunable frequencies and has great potential. Potential applications that have been identified include acoustic manipulation [47], acoustic absorption [48], acoustic focusing [49], and acoustic stealth [50], which are well beyond traditional materials. A SAM consisting of a mechanical resonator and a piezoelectric element can generate a local resonant band gap near a mechanical or electrical resonance [51]. The main advantage of these electromechanical hybrid resonators over ordinary acoustic metamaterials is that they allow tunable effective mass and stiffness characteristics. Akl has carried out pioneering research on piezoelectric SAMs, especially the analysis and experiments on the composite acoustic resonator with piezoelectric membrane as sensor and actuator [52–55].

Smart mechanical metamaterials

The research of mechanical metamaterials includes design and manufacturing. And structural design is the core of mechanical metamaterials. In recent years, machine learning has developed rapidly. It provides a powerful tool for the automated design of mechanical metamaterials, especially with diverse objective functions [56]. Increasingly complex geometries of mechanical metamaterials pose serious challenges to the material manufacturing technology. And the traditional material reduction manufacturing method is no longer applicable, especially for the structures at the micro or nano scale. So the researchers used additive manufacturing to achieve special complex geometries. Recent developments in additive manufacturing also allow for the manufacture of stimuli-responsive materials, creating structures that can change their geometry, properties, or function. This is often referred to as 4D printing, and the fourth dimension is time.

4D printing is based on 3D printing, but the object is no longer static. Under the external stimulus, the shape, property or function of the object will change with time. Stimulus-responsive shape memory materials based on 4D printing have the advantages of simple manufacturing process, large

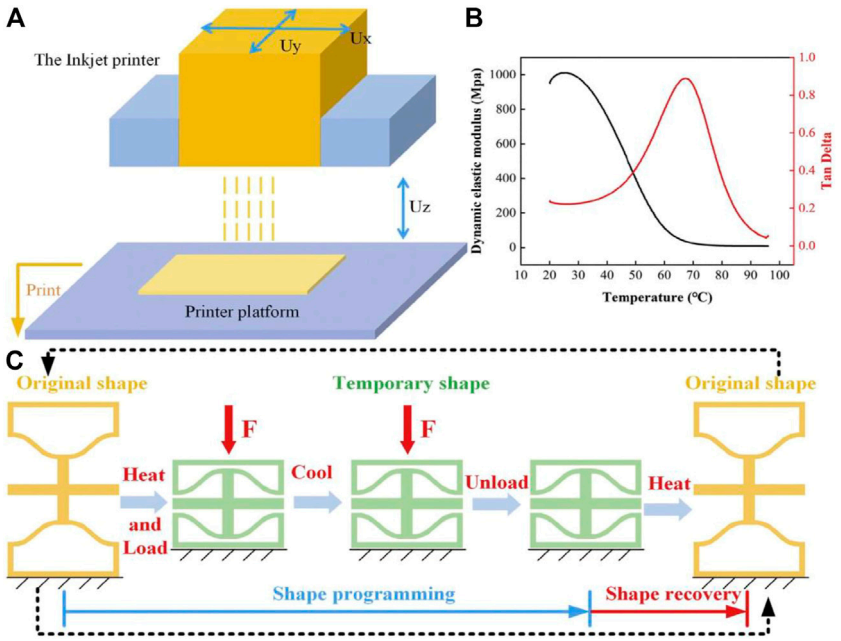

FIGURE 4
(A) 3D printer principle. **(B)** Dynamic mechanical analysis result of shape memory polymer. **(C)** Schematic of shape memory effect [64].

deformation capacity and various stimulus forms. Common 4D printing stimulus-responsive shape memory materials include shape memory alloys [57], shape memory polymers [58] and shape memory hydrogels [59]. SMMs is an emerging discipline with the continuous development of mechanical design and materials science, and has great application prospects in the fields of engineering and science. 4D printing technology is an optimized rapid prototyping technology. Its integration with SMMs provides new vitality for the development of SMMs. If mechanical metamaterials are reconfigured by replacing traditional materials with stimuli-responsive materials, they will be able to automatically deform, move and change their structural properties or functions in response to external stimulus, such as photothermal effect [60], thermal effect [61], electro mechanical effect [62] and compressive response [63]. To take full advantage of the unique advantages of different material systems, researchers will select appropriate stimuli-responsive materials according to different and application needs. Therefore, SMMs can also be called active mechanical metamaterials. The metamaterial shown in Figure 4 can adaptively switch mechanical properties and shapes without continuous external excitation of the physical field [64].

SMMs have gradually become a new protagonist in the field of materials and have been endowed with richer functional properties, including reconfigurable [65, 66], programmable [67], elastic wave propagation control [68, 69] and mechanical computing [70, 71]. et al. In the future, the functional properties of natural materials will gradually diminish. In more cases, they will be used as components of functional metamaterials in the form of raw materials. Combined with machine learning and advanced manufacturing processes of 4D printing, SMMs can take full advantage of their flexible design.

Smart thermal metamaterials

Thermal metamaterials are thermal materials with artificial structures, and their novel structures enable them to possess thermal properties or functions that natural materials do not have. It belongs to the emerging Frontier cross-research direction of thermodynamics and statistical physics, thermophysical properties and heat transfer [72]. Since the 21st century, metamaterials have made vigorous progress in the fields of acoustics, optics, elastic wave control and mechanics, which is mainly caused by the huge application demand in these fields. Metamaterials did not make great progress in thermal field until the Fan et al. first introduced the concept of electromagnetic invisibility cloak into thermal field in 2008 [24]. Drawing on the theory of transformation optics, they put forward the theory of transformation heat and predicted the cloak of thermal stealth. At the same time, the phenomenon of heat flow

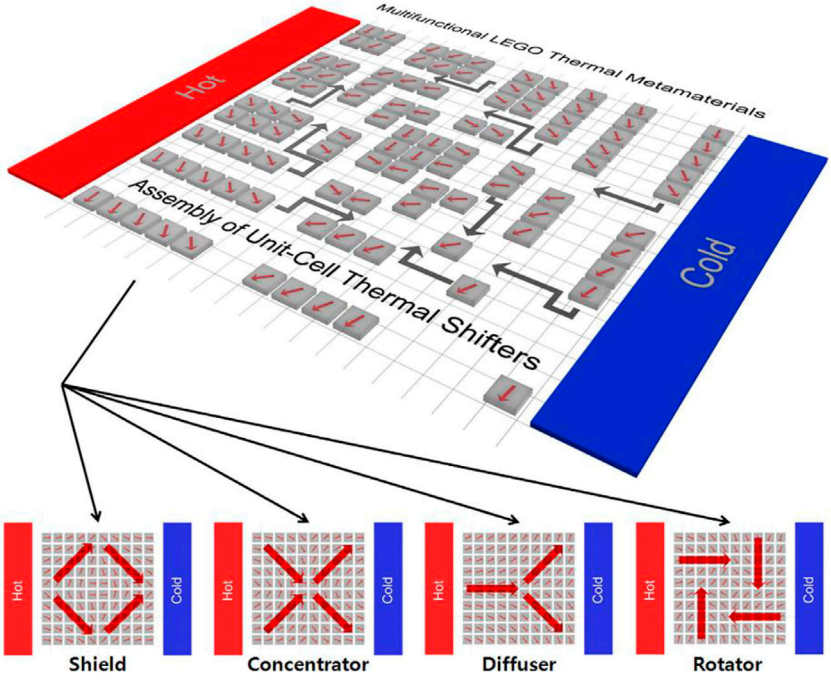

FIGURE 5
Scheme of tunable multifunctional thermal metamaterials [77].

inversion in the system is predicted, which is completely different from the traditional view of "heat flowing to low temperature," and the concept of negative thermal conductivity is proposed. After more than 10 years of development, thermal metamaterials have achieved various functions, such as thermal stealth [73], thermal transparency [74, 75], thermal camouflage [26], and macroscopic diodes and temperature capture [76], etc.

STMs are artificial composite materials that can sense external heat sources and respond actively, and have the potential to be applied to thermoelectric conversion of micro-nano structures. So far, the basic theories of STMs can be classified into two categories [72]: macroscopic phenomenology theory and microscopic phonon/thermal photon theory. The former controls heat flow and utilizes thermal energy, while the latter utilizes thermal photons for information transmission. Therefore, the application of thermal metamaterials has been developed in a macroscopic and microscopic manner, respectively. The emergence of nonlinear transform thermology makes thermal metamaterials develop towards smart. In addition to linear devices, the effect of this STM is dynamic and changes with the environment. Therefore, following this philosophy, it is crucial to find materials that can change their properties when the external environment changes. Park et al. introduced tunable thermal metamaterials that use the assembly of unit-cell thermal shifters for a remarkable enhancement in multifunctionality as well as manufacturability as show in Figure 5 [77]. In addition, Shen et al. designed and manufactured a thermal cloak concentrator device [78] and a non-energy thermostat [76]. Some of the attractive operations can be achieved by combining nonlinear transformation theory with multi-physical function design. Yang et al. researched the nonlinear responses of thermal metamaterials with 2D or 3D core-shell structures. By calculating the effective thermal conductivity, the nonlinear modulation of the nonlinear magnetic core is derived. Using this theory, a smart thermo-transparent device that can respond to the direction of the thermal field is designed [79]. Wang et al. designed a thermoelectric thermostat cloak with double-layer structure, confirmed the effect predicted by theory with finite element method, and discussed the possibility of experimental demonstration with natural materials [80].

Thermal camouflage or illusion is another important application that has direct military applications. Yang et al proposed simulation and experimental results of thermal invisibility and illusion in single-particle structured materials. By appropriately adjusting the shape factors of individual particles, thermal invisibility and illusion can be achieved simultaneously with a single device. This work not only opens a way for the design of thermal materials based on single-particle structures, but also applies to other physical fields such as

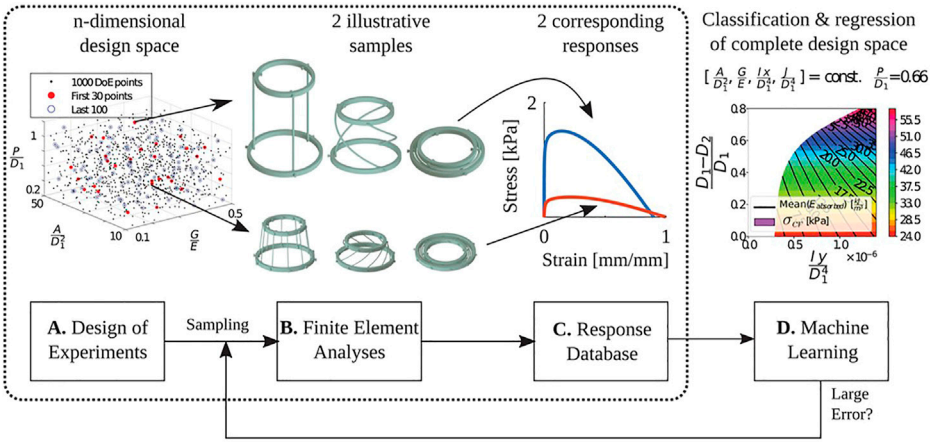

FIGURE 6
Data-driven design of supercompressible metamaterial building block using seven design variables [86].

electrostatics, magnetostatics and particle dynamics [81]. Compared with static thermal camouflage, dynamic thermal camouflage has greater practicability and prospect in future military applications. For this purpose, the required dynamic thermal camouflage requires an adaptive material that can be initiated in response to external stimuli such as electricity, light, temperature, moisture, machinery, steam, etc. [82].

Smart metamaterials and machine learning

With the development of computer science, computer-aided design and computer-aided engineering are playing an important role in the development of metamaterials [83]. Machine learning has debuted in material and structure studies as the symbol method since the 1990s, such as high-throughput screening approaches enable both simulation and experimental databases to be compiled, with the data used to build models that enable property prediction, determine feature importance, and guide experimental design between the material and structure parameters and the mechanical performance for the fibre/matrix interfaces in ceramic-matrix composites [84]. In order to capture subtle knowledge among the existing data, machine learning performs superior to the traditional statistical methods in terms of the computational efficiency for a significant class of computationally hard problems in materials science, which, therefore, has been extensively used to address different problems in new materials discovery and material property prediction.

When designing metamaterials, numerical simulation can effectively predict the feasibility of the scheme. The design of materials can use data-driven artificial intelligence and other methods to shorten the development cycle and improve the efficiency by training the computational model through experimental data. Both genetic algorithm and neural networks model are adopted to execute the designing process. The method starts from selection of the structural bases based on the existing studies and then combines performance evaluation together with structural evolution to construct meta-atoms with specified properties [85]. Data-driven design of the metamaterial concept is then summarized in Figure 6. A computational data-driven approach is followed for exploring a new metamaterial concept and adapting it to different target properties, choice of base materials, length scales, and manufacturing processes [86]. Training convolutional neural networks to predict the electromagnetic response of metal-dielectric-metal metamaterials, including complex freeform designs, can be explained to reveal deeper insights into the underlying physics of nanophotonic structures [87].

Machine learning uses computers to mine potential value from data, and learns patterns and characteristics of targets. But it is important to note that whether a machine learned model remains accurate outside of the dataset is always known after validation. Therefore, the independent variables should be kept in the training data space to ensure the correctness of the model.

Summary and prospect

To sum up, this review briefly makes a systematic classification and scientific review of smart metamaterials, but there are many kinds of smart metamaterials and many excellent works that cannot be mentioned. Possible directions for smart metamaterials are listed below. This discussion is intended to be the beginning of a conversation, not the final word.

(1) SEMs can realize real-time regulation of electromagnetic waves, opening up a new way for beam scanning, and can be applied to new field programmable radars in the future.

Compared with traditional phased array antennas, it has the advantages of simplicity, efficiency and low cost. We believe that SEMs will have broad development prospects and huge application potential in signal processing, digital communication, information theory, electromagnetic imaging and other fields in the future.

(2) SAMs possess extraordinary physical properties not found in natural materials. Lightweight, low frequency, broadband, small size and strong attenuation are still the goals which are constantly pursued in the research of SAMs.

(3) SMMs regulate elastic waves based on complex topologies. A lot of basic research work remains to be carried out, especially how to transform the traditional theory in the field of condensed matter physical crystallography into the design and characterization of artificial microstructure.

(4) Most of the existing device functions are presented at the macroscopic scale. In order to improve the application value of STMs, nanoscale-based thermal metamaterials need to be designed. Thus, the existing functions of thermal metamaterials will be realized at the micro-nano scale.

(5) One of the most important problems in predicting metamaterial responses. The next step in smart metamaterials and machine learning is to obtain the ideal structures by directly considering the desired response.

Author contributions

Conceptualization, CZ and HD; investigation, HD and JW; data curation, RZ and WL; writing—original draft preparation, YZ and HD; writing—review and editing, YZ, CZ, and ZW; funding acquisition, YZ and RZ.

Funding

This research was funded by the Sichuan Science and Technology Program (No. 2022YFG0274), the Key Research and Development Program of Zhejiang Province (Grant No. 2022C01199), National Natural Science Foundation of China (Grant No. 51875146).

Conflict of interest

JW is employed by the Sanmen Sanyou Technology Co., Ltd.

The remaining authors declare that the research was conducted in the absence of any commercial or financial relationships that could be construed as a potential conflict of interest.

Publisher's note

All claims expressed in this article are solely those of the authors and do not necessarily represent those of their affiliated organizations, or those of the publisher, the editors and the reviewers. Any product that may be evaluated in this article, or claim that may be made by its manufacturer, is not guaranteed or endorsed by the publisher.

References

1. Vesselago V THE ELECTRODYNAMICS OF SUBSTANCES WITH SIMULTANEOUSLY NEGATIVE VALUES OF ϵ AND μ. *Sov Phys Usp* (1968) 10(4):509–14. doi:10.1070/pu1968v010n04abeh003699

2. Pendry H., Stewart Y. I., Stewart W. J. Extremely low frequency plasmons in metallic mesostructures. *Phys Rev Lett* (1996) 76(25):4773–6. doi:10.1103/PhysRevLett.76.4773

3. Pendry J. B., Holden A. J., Robbins D. J., Stewart W. Magnetism from conductors and enhanced nonlinear phenomena. *IEEE Trans Microw Theor Tech* (1999) 47(11):2075–84. doi:10.1109/22.798002

4. Pendry J. B. Negative refraction makes a perfect lens. *Phys Rev Lett* (2000) 85(18):3966–9. doi:10.1103/PhysRevLett.85.3966

5. Shelby R. A, Smith D. R, Schultz S, 292. New York NY (2001). American Association for the Advancement of Sciencep. 77–9. doi:10.1126/science.1058847*Experimental verification of a negative index of refractionScience5514*

6. Srivastava A Elastic metamaterials and dynamic homogenization: A review. *Int J Smart Nano Mater* (2015) 6(1):41–60. doi:10.1080/19475411.2015.1017779

7. Bertoldi K., Vitelli V., Christensen J., van Hecke M. Flexible mechanical metamaterials. *Nat Rev Mater* (2017) 2(11):17066. doi:10.1038/natrevmats.2017.66

8. Wu W., Hu W., Qian G., Liao H., Xu X., Berto F. Mechanical design and multifunctional applications of chiral mechanical metamaterials: A review. *Mater Des* (2019) 180:107950. doi:10.1016/j.matdes.2019.107950

9. Chaturvedi P., Hsu K., Zhang S., Fang N. New frontiers of metamaterials: Design and fabrication. *MRS Bull* (2008) 33(10):915–20. doi:10.1557/mrs2008.199

10. Kadic M., Milton G. W., van Hecke M., Wegener M. 3d metamaterials. *Nat Rev Phys* (2019) 1(3):198–210. doi:10.1038/s42254-018-0018-y

11. Zheludev N. I The road ahead for metamaterials. *Science* (2010) 328(5978):582–3. doi:10.1126/science.1186756

12. Wang X., Venugopal G., Zeng J., Chen Y., Lee D. H., Litchinitser N. M., et al. Optical fiber metamagnetics. *Opt Express* (2011) 19(21):19813–21. doi:10.1364/oe.19.019813

13. Cao W., Gao J., Yang X. Determination of effective parameters of fishnet metamaterials with vortex based interferometry. *Opt Express* (2020) 28(14):20051–61. doi:10.1364/oe.391873

14. Kim J., Han K., Hahn J. W. Selective dual-band metamaterial perfect absorber for infrared stealth technology. *Sci Rep* (2017) 7(1):6740. doi:10.1038/s41598-017-06749-0

15. Yang M., Sheng P. An integration strategy for acoustic metamaterials to achieve absorption by design. *Appl Sci* (2018) 8(8):1247. doi:10.3390/app8081247

16. Fan S. W., Zhu Y., Cao L., Wang Y. F., Li Chen A., Merkel A., et al. Broadband tunable lossy metasurface with independent amplitude and phase modulations for acoustic holography. *Smart Mater Struct* (2020) 29(10):105038. doi:10.1088/1361-665X/abaa98

17. Lee K. H., Yu K., Al Ba'ba'a H., Xin A., Feng Z., Wang Q. Sharkskin-inspired magnetoactive reconfigurable acoustic metamaterials. *Research* (2020) 2020:1–13. doi:10.34133/2020/4825185

18. Ma K. J., Tan T., Liu F. R., Zhao L. C., Liao W. H., Zhang W. M. Acoustic energy harvesting enhanced by locally resonant metamaterials. *Smart Mater Struct* (2020) 29(7):075025. doi:10.1088/1361-665X/ab8fcc

19. Chiang T. Y., Wu L. Y., Tsai C. N., Chen L. W. A multilayered acoustic hyperlens with acoustic metamaterials. *Appl Phys A* (2011) 103(2):355–9. doi:10.1007/s00339-011-6306-3

20. Mercer C., Speck T., Lee J., Balint D. S., Thielen M. Effects of geometry and boundary constraint on the stiffness and negative Poisson's ratio behaviour of auxetic metamaterials under quasi-static and impact loading. *Int J Impact Eng* (2022) 169:104315. doi:10.1016/j.ijimpeng.2022.104315

21. Chen J., Xu W., Wei Z., Wei K., Yang X. Stiffness characteristics for a series of lightweight mechanical metamaterials with programmable thermal expansion. *Int J Mech Sci* (2021) 202-203:106527. doi:10.1016/j.ijmecsci.2021.106527

22. Zhu S., Tan X., Chen S., Wang B., Ma L., Wu L. Quasi-all-directional negative stiffness metamaterials based on negative rotation stiffness elements. *Phys Status Solidi B* (2020) 257(6):1900538. doi:10.1002/pssb.201900538

23. Liu Z., Zhang X., Mao Y., Zhu Y. Y., Yang Z., Chan C. T., et al. Locally resonant sonic materials. *Science* (2000) 289(5485):1734–6. doi:10.1126/science.289.5485.1734

24. Fan C. Z., Gao Y., Huang J. P. Shaped graded materials with an apparent negative thermal conductivity. *Appl Phys Lett* (2008) 92(25):251907. doi:10.1063/1.2951600

25. Duan J, Liu R, Xu H, Zhang R, Zhang B, Kim B. S Emt conversion of composite broadband Absorbent metamaterials for stealth application over X-bands. *IEEE Access* (2020) 8:153787–98. doi:10.1109/ACCESS.2020.3018018

26. Zhang J., Huang S., Hu R. Adaptive radiative thermal camouflage via synchronous heat conduction. *Chin Phys Lett* (2021) 38(1):010502. doi:10.1088/0256-307x/38/1/010502

27. Zhang Q., Zhu W., Feng J., Zhou J., Deng Y. High-efficient heat flux manipulation of micro-scale thermal metamaterials with facile functional unit design. *Mater Des* (2021) 204:109657. doi:10.1016/j.matdes.2021.109657

28. Cui T. J., Qi M. Q., Wan X., Zhao J., Cheng Q. Coding metamaterials, digital metamaterials and programmable metamaterials. *Light Sci Appl* (2014) 3(10):e218. doi:10.1038/lsa.2014.99

29. Zangeneh-Nejad F., Sounas D. L., Alù A., Fleury R. Analogue computing with metamaterials. *Nat Rev Mater* (2021) 6(3):207–25. doi:10.1038/s41578-020-00243-2

30. Kafesaki M., Shen N. H., Tzortzakis S., Soukoulis C. M. Optically switchable and tunable terahertz metamaterials through photoconductivity. *J Opt* (2012) 14(11):114008. doi:10.1088/2040-8978/14/11/114008

31. Della Giovampaola C., Engheta N. Digital metamaterials. *Nat Mater* (2014) 13(12):1115–21. doi:10.1038/nmat4082

32. Ma Q., Cui T. J. Information metamaterials: Bridging the physical world and digital world. *PhotoniX* (2020) 1(1):1. doi:10.1186/s43074-020-00006-w

33. Paquay M., Iriarte J. C., Ederra I., Gonzalo R., de Maagt P. Thin AMC structure for radar cross-section reduction. *IEEE Trans Antennas Propag* (2007) 55(12):3630–8. doi:10.1109/TAP.2007.910306

34. Chan W. L., Chen H. T., Taylor A. J., Brener I., Cich M. J., Mittleman D. M. A spatial light modulator for terahertz beams. *Appl Phys Lett* (2009) 94(21):213511. doi:10.1063/1.3147221

35. Savo S., Shrekenhamer D., Padilla W. J. Liquid crystal metamaterial absorber spatial light modulator for thz applications. *Adv Opt Mater* (2014) 2(3):275–9. doi:10.1002/adom.201300384

36. Watts C. M., Shrekenhamer D., Montoya J., Lipworth G., Hunt J., Sleasman T., et al. Terahertz compressive imaging with metamaterial spatial light modulators. *Nat Photon* (2014) 8(8):605–9. doi:10.1038/nphoton.2014.139

37. Lv Z., Li Z., Xu W., Pei Y. Implementing fractional order fourier transformation and confocal imaging with microwave computational metamaterials. *EPL (Europhysics Letters)* (2020) 131(2):24001. doi:10.1209/0295-5075/131/24001

38. Li L., Cui T. J. Information metamaterials – from effective media to real-time information processing systems. *Nanophotonics* (2019) 8(5):703–24. doi:10.1515/nanoph-2019-0006

39. Tian S., Zhang X., Wang X., Han J., Li L. Recent advances in metamaterials for simultaneous wireless information and power transmission. *Nanophotonics* (2022) 11(9):1697–723. doi:10.1515/nanoph-2021-0657

40. Cui TJ, Li L, Liu S, Ma Q, Zhang L, Wan X, et al. Information metamaterial systems. *iScience* (2020) 23(8):101403. doi:10.1016/j.isci.2020.101403

41. Song H., Ding X., Cui Z., Hu H. Research progress and development trends of acoustic metamaterials. *Molecules* (2021) 26(13):4018. doi:10.3390/molecules26134018

42. Esfahlani H., Karkar S., Lissek H., Mosig J. R. Acoustic carpet cloak based on an ultrathin metasurface. *Phys Rev B* (2016) 94(1):014302. doi:10.1103/PhysRevB.94.014302

43. Ghaffarivardavagh R., Nikolajczyk J., Glynn Holt R., Anderson S., Zhang X. Horn-like space-coiling metamaterials toward simultaneous phase and amplitude modulation. *Nat Commun* (2018) 9(1):1349. doi:10.1038/s41467-018-03839-z

44. Zhou Y., Li H., Ye M., Shi Y., Gao L. Novel design scheme for structural fundamental frequency of porous acoustic metamaterials. *Materials* (2022) 15(19):6569. doi:10.3390/ma15196569

45. Bacigalupo A., De Bellis M. L., Misseroni D. Design of tunable acoustic metamaterials with periodic piezoelectric microstructure. *Extreme Mech Lett* (2020) 40:100977. doi:10.1016/j.eml.2020.100977

46. Zhao J., Li X., Wang W., Wang Y., Zhu L., Liu Y. Membrane-type Acoustic metamaterials with tunable frequency by a compact magnet. *The J Acoust Soc America* (2019) 145(5):EL400–EL4. doi:10.1121/1.5107431

47. Tian Z., Shen C., Li J., Reit E., Gu Y., Fu H., et al. Programmable acoustic metasurfaces. *Adv Funct Mater* (2019) 29(13):1808489. doi:10.1002/adfm.201808489

48. Koutserimpas T. T., Rivet E., Lissek H., Fleury R. Active acoustic resonators with reconfigurable resonance frequency, absorption, and bandwidth. *Phys Rev Appl* (2019) 12(5):054064. doi:10.1103/PhysRevApplied.12.054064

49. Liao G., Wang Z., Luan C., Liu J., Yao X., Fu J. Broadband controllable acoustic focusing and asymmetric focusing by acoustic metamaterials. *Smart Mater Struct* (2021) 30(4):045021. doi:10.1088/1361-665X/abeb2e

50. Yu G., Qiu Y., Li Y., Wang X., Wang N. Underwater acoustic stealth by a broadband 2-bit coding metasurface. *Phys Rev Appl* (2021) 15(6):064064. doi:10.1103/PhysRevApplied.15.064064

51. Xiao H., Li T., Zhang L., Liao W. H., Tan T., Yan Z. Metamaterial based piezoelectric acoustic energy harvesting: Electromechanical coupled modeling and experimental validation. *Mech Syst Signal Process* (2023) 185:109808. doi:10.1016/j.ymssp.2022.109808

52. Akl W., Baz A. Multi-cell active acoustic metamaterial with programmable bulk modulus. *J Intell Mater Syst Structures* (2010) 21(5):541–56. doi:10.1177/1045389X09359434

53. Akl W., Baz A. Analysis and experimental demonstration of an active acoustic metamaterial cell. *J Appl Phys* (2012) 111(4):044505. doi:10.1063/1.3686210

54. Allam A., Elsabbagh A., Akl W. Experimental demonstration of one-dimensional active plate-type Acoustic metamaterial with adaptive programmable density. *J Appl Phys* (2017) 121(12):125106. doi:10.1063/1.4979020

55. Allam A., Elsabbagh A., Akl W. Modeling and design of two-dimensional membrane-type Active acoustic metamaterials with tunable anisotropic density. *J Acoust Soc America* (2016) 140(5):3607–18. doi:10.1121/1.4966627

56. Wu L., Liu L., Wang Y., Zhai Z., Zhuang H., Krishnaraju D., et al. A machine learning -based method to design modular metamaterials. *Extreme Mech Lett* (2020) 36:100657. doi:10.1016/j.eml.2020.100657

57. Milleret A. 4d printing of Ni–Mn–Ga magnetic shape memory alloys: A review. *Mater Sci Tech* (2022) 38(10):593–606. doi:10.1080/02670836.2022.2062655

58. Chan B. Q. Y., Low Z. W. K., Heng S. J. W., Chan S. Y., Owh C., Loh X. J. Recent advances in shape memory soft materials for biomedical applications. *ACS Appl Mater Inter* (2016) 8(16):10070–87. doi:10.1021/acsami.6b01295

59. Chen Z., Li Y., Li Q. M. Hydrogel-driven origami metamaterials for tunable swelling behavior. *Mater Des* (2021) 207:109819. doi:10.1016/j.matdes.2021.109819

60. Wang L. C., Song W. L., Fang D. Twistable origami and kirigami: From structure-guided smartness to mechanical energy storage. *ACS Appl Mater Inter* (2019) 11(3):3450–8. doi:10.1021/acsami.8b17776

61. Zhang Y. J., Wang L. C., Song W. L., Chen M., Fang D. Hexagon-twist frequency reconfigurable antennas via multi-material printed thermo-responsive origami structures. *Front Mater* (2020) 7:7. doi:10.3389/fmats.2020.600863

62. Wang Y., Cheng X. D., Song W. L., Ma C. J., Bian X. M., Chen M. Hydro-sensitive sandwich structures for self-tunable smart electromagnetic shielding. *Chem Eng J* (2018) 344:342–52. doi:10.1016/j.cej.2018.03.097

63. Korpas L. M., Yin R., Yasuda H., Raney J. R. Temperature-responsive multistable metamaterials. *ACS Appl Mater Inter* (2021) 13(26):31163–70. doi:10.1021/acsami.1c07327

64. Hu W., Ren Z., Wan Z., Qi D., Cao X., Li Z., et al. Deformation behavior and band gap switching function of 4d printed multi-stable metamaterials. *Mater Des* (2021) 200:109481. doi:10.1016/j.matdes.2021.109481

65. Wu Y., Guo G., Wei Z., Qian J. Programming soft shape-morphing systems by harnessing strain mismatch and snap-through bistability: A review. *Materials* (2022) 15(7):2397. doi:10.3390/ma15072397

66. Xin X., Liu L., Liu Y., Leng J. 4d printing auxetic metamaterials with tunable, programmable, and reconfigurable mechanical properties. *Adv Funct Mater* (2020) 30(43):2004226. doi:10.1002/adfm.202004226

67. Bai Y., Liu C., Li Y., Li J., Qiao L., Zhou J., et al. Programmable mechanical metamaterials with tailorable negative Poisson's ratio and arbitrary thermal

expansion in multiple thermal deformation modes. *ACS Appl Mater Inter* (2022) 14(31):35905–16. doi:10.1021/acsami.2c08270

68. Chen Y., Hu J., Huang G. A design of active elastic metamaterials for control of flexural waves using the transformation method. *J Intell Mater Syst Structures* (2016) 27(10):1337–47. doi:10.1177/1045389X15590273

69. Chen Y. Y., Huang G. L. Active elastic metamaterials for subwavelength wave propagation control. *Acta Mech Sin* (2015) 31(3):349–63. doi:10.1007/s10409-015-0402-0

70. Zheng B., Xu J. Mechanical logic switches based on DNA-inspired acoustic metamaterials with ultrabroad low-frequency band gaps. *J Phys D Appl Phys* (2017) 50(46):465601. doi:10.1088/1361-6463/aa8b08

71. Zhang H., Wu J., Fang D., Zhang Y. Hierarchical mechanical metamaterials built with scalable tristable elements for ternary logic operation and amplitude modulation. *Sci Adv* (2021) 7(9):eabf1966. doi:10.1126/sciadv.abf1966

72. Wang J., Dai G., Huang J. Thermal metamaterial: Fundamental, application, and outlook. *iScience* (2020) 23(10):101637. doi:10.1016/j.isci.2020.101637

73. Yang C., Niu S., Chang H., Wang Y., Feng Y., Zhang Y., et al. Thermal infrared and broadband microwave stealth glass windows based on multi-band optimization. *Opt Express* (2021) 29(9):13610–23. doi:10.1364/oe.424226

74. He X., Wu L. Thermal transparency with the concept of neutral inclusion. *Phys Rev E* (2013) 88(3):033201. doi:10.1103/PhysRevE.88.033201

75. Zeng L., Song R. Experimental observation of heat transparency. *Appl Phys Lett* (2014) 104(20):201905. doi:10.1063/1.4878738

76. Shen X., Li Y., Jiang C., Huang J. Temperature trapping: Energy-free maintenance of constant temperatures as ambient temperature gradients change. *Phys Rev Lett* (2016) 117(5):055501. doi:10.1103/PhysRevLett.117.055501

77. Park G., Kang S., Lee H., Choi W. Tunable multifunctional thermal metamaterials: Manipulation of local heat flux via assembly of unit-cell thermal shifters. *Sci Rep* (2017) 7(1):41000. doi:10.1038/srep41000

78. Shen X., Li Y., Jiang C., Ni Y., Huang J. Thermal cloak-concentrator. *Appl Phys Lett* (2016) 109(3):031907. doi:10.1063/1.4959251

79. Yang S., Xu L., Huang J. Metathermotics: Nonlinear thermal responses of core-shell metamaterials. *Phys Rev E* (2019) 99(4):042144. doi:10.1103/PhysRevE.99.042144

80. Wang J., Shang J., Huang J. P. Negative energy consumption of thermostats at ambient temperature: Electricity generation with zero energy maintenance. *Phys Rev Appl* (2019) 11(2):024053. doi:10.1103/PhysRevApplied.11.024053

81. Yang S., Xu L. J., Wang R. Z., Huang J. P. Full control of heat transfer in single-particle structural materials. *Appl Phys Lett* (2017) 111(12):121908. doi:10.1063/1.4994729

82. Mandal J., Jia M., Overvig A., Fu Y., Che E., Yu N., et al. Porous polymers with switchable optical transmittance for optical and thermal regulation. *Joule* (2019) 3(12):3088–99. doi:10.1016/j.joule.2019.09.016

83. Bishara D., Xie Y., Liu W. K., Li S. *A state-of-the-art review on machine learning-based multiscale modeling, simulation, homogenization and design of materials*.Netherlands Archives of Computational Methods in Engineering (2022). doi:10.1007/s11831-022-09795-8

84. Vasudevan R. K., Choudhary K., Mehta A., Smith R., Kusne G., Tavazza F., et al. Materials science in the artificial intelligence age: High-throughput library generation, machine learning, and a pathway from correlations to the underpinning physics. *Mrs Commun* (2019) 9(3):821–38. doi:10.1557/mrc.2019.95

85. Wu L., Liu L., Wang Y., Zhai Z., Zhuang H., Krishnaraju D., et al. A machine learning -based method to design modular metamaterials. *Extreme Mech Lett* (2020) 36:100657. doi:10.1016/j.eml.2020.100657

86. Bessa M. A, Glowacki P., Houlder M. Bayesian machine learning in metamaterial design: Fragile becomes supercompressible. *Adv Mater* (2019) 31(48):1904845. doi:10.1002/adma.201904845

87. Yeung C., Tsai J. M., King B., Kawagoe Y., Ho D., Knight M. W., et al. Elucidating the behavior of nanophotonic structures through explainable machine learning algorithms. *ACS Photon* (2020) 7(8):2309–18. doi:10.1021/acsphotonics.0c01067

frontiers | Frontiers in Physics

TYPE Mini Review
PUBLISHED 22 November 2022
DOI 10.3389/fphy.2022.1068838

OPEN ACCESS

EDITED BY
Lingyun Yao,
Southwest University, China

REVIEWED BY
Fuyin Ma,
Xi'an Jiaotong University, China

*CORRESPONDENCE
Ning Hu,
hooning@hdu.edu.cn
Zhenjing Zhu,
shockpig@hdu.edu.cn
Maofa Wang,
wangmfl600@163.com
Yongju Zheng,
joany0204@163.com
Huajie Dai,
qinlongcrcc@foxmail.com

SPECIALTY SECTION
This article was submitted to Physical Acoustics and Ultrasonics, a section of the journal Frontiers in Physics

RECEIVED 13 October 2022
ACCEPTED 03 November 2022
PUBLISHED 22 November 2022

CITATION
Zhao J, Hu N, Wu J, Li W, Zhu Z, Wang M, Zheng Y and Dai H (2022), A review of piezoelectric metamaterials for underwater equipment.
Front. Phys. 10:1068838.
doi: 10.3389/fphy.2022.1068838

A review of piezoelectric metamaterials for underwater equipment

Jiabao Zhao[1,2], Ning Hu[2,4]*, Junyi Wu[3], Wenxin Li[2], Zhenjing Zhu[2,4]*, Maofa Wang[2,4]*, Yongju Zheng[2]* and Huajie Dai[2]*

[1]College of Electronic Information, Hangzhou Dianzi University, Hangzhou, China, [2]College of Mechanical Engineering, Hangzhou Dianzi University, Hangzhou, China, [3]Sanmen Sanyou Technology Inc, Taizhou, China, [4]Marine Technology and Equipment Research Center, Hangzhou Dianzi University, Hangzhou, China

As an important tool for monitoring the marine environment, safeguarding maritime rights and interests and building a smart ocean, underwater equipment has developed rapidly in recent years. Due to the problems of seawater corrosion, excessive deep-sea static pressure and noise interference in the marine environment and economy, the applicability of manufacturing materials must be considered at the beginning of the design of underwater equipment. Piezoelectric metamaterial is widely used in underwater equipment instead of traditional materials because the traditional materials can not meet the application requirements. In this paper, according to the application range of piezoelectric metamaterials in underwater equipment, the current application of piezoelectric metamaterials is reviewed from the aspects of sound insulation and energy conversion. On this basis, the future development prospect of piezoelectric metamaterials in underwater equipment is introduced.

KEYWORDS

piezoelectric metamaterials, underwater equipment, band gap, sound insulation, piezoelectric conversion

1 Introduction

In recent years, with the rapid development of the world economy, land resources are becoming more and more scarce. Researchers have turned their attention to the ocean for resource exploitation. The development of marine resource exploration has become more and more rapid. Many marine technologies and underwater equipment (UE) have been rapidly developed. As UE continues to operate in the ocean for longer periods, researchers have found that a large number of equipment cannot meet the requirements because the equipment is made of traditional materials. The emergence of piezoelectric metamaterials (PMs) has solved many problems with their unique properties, so it has been rapidly applied to UE.

Metamaterial is a kind of artificially designed material with special structure, which can achieve singular or anomalous properties that ordinary materials do not have through

a certain spatial arrangement. Metamaterials generally have such characteristics as band gap, waveguide, negative refraction, negative modulus, negative density, hyperlens, acoustic focusing, acoustic stealth and topological states [1, 2]. In the past few decades, left-handed materials [3], photonic crystals, phononic crystals [4], time crystals and even metasurfaces [5] can be classified as metamaterials. They have a very promising future in many fields such as communication, medicine, defense and military, aerospace and remote sensing. Metamaterials generally select existing materials and design new microstructures to achieve superior and anomalous functions. The selection of materials should follow the following rules. High modulus generally corresponds to high operating frequency, low modulus generally corresponds to low operating frequency and the large impedance difference between different component phases generally corresponds to a wider bandwidth gap. In order to carry out active control, intelligent materials such as piezoelectric material and shape memory alloy are generally selected. Compared with other smart materials, piezoelectric materials have outstanding advantages such as fast response speed, high control precision, small size and large market. The excellent electro-mechanical coupling effect of piezoelectric materials makes it possible to use different external circuits to change the mechanical properties of piezoelectric materials and then regulate and control various aspects of metamaterials [6].

The structure of PM is a kind of intelligent structure and its local resonance band gap has the characteristics of active tunability, which can meet the requirements of structural vibration frequency changing with the environment. The structure of PM has the characteristics of small additional mass and intelligently tunable band gap, which makes it have obvious advantages compared with other types of materials [7]. PM is a kind of acoustic metamaterial, and acoustic metamaterial is a medium composed of multiple materials with negative mass density, negative bulk modulus and other properties designed based on the principle of local resonance [8]. When the elastic wave in a specific frequency range propagates in the structure, it will cause the resonance phenomenon in the local resonance unit [9], which hinders the propagation of the elastic wave and generates a band gap. The band gap properties of PMs can be used to make sound insulation materials for UE. At the same time, the band gap characteristic is used to collect the vibration energy of elastic waves within a specific frequency range, and the vibration energy is confined to the local resonance unit and converted into electric energy by piezoelectric materials. The piezoelectric conversion properties of this PM can be used for piezoelectric sensors, underwater transducers, hydrophones and other equipment.

This paper is organized as follows. Section 2 introduces the band gap properties and piezoelectric conversion properties of PMs; Section 3 presents the research on the use of PMs as sound insulation and energy conversion functions in UE; Section 4 concludes and discusses the future directions of PMs in UE.

2 Piezoelectric metamaterials

Acoustic metamaterial is a kind of artificial composite structure material, which is obtained by combining a variety of materials with different elastic modulus. It is a new functional material. When the elastic wave in a specific frequency range propagates in the structure, the elastic wave band gap will be generated as shown in Figure 1 [10]. The band gap can inhibit and absorb the elastic wave propagation in the relevant frequency range. The elastic band gap of acoustic metamaterial is generated by two main mechanisms, Bragg scattering mechanism and local resonance mechanism respectively. According to the different principles of band gap generation, acoustic metamaterial can be divided into Bragg scattering phononic crystals and local resonance acoustic metamaterial. Bragg scattering phononic crystals due to the Bragg reflection of the structure. When the wavelength of the propagating elastic wave is close to the lattice coefficient of the structure, the band gap will be generated, which has a strong inhibition and absorption effect on the elastic wave. For the local resonance metamaterial, the band gap is mainly generated by the local resonance element inside it. When the frequency of the elastic wave propagating in the local resonance element is close to its resonance frequency, the local resonance element will resonate under the action of the vibration energy of the elastic wave. Resonance will absorb vibration energy, so that elastic waves cannot continue to propagate forward and form band gap [11–15].

2.1 Band gap properties of PMs

The PM is a type of acoustic metamaterial, so it has the properties of an acoustic metamaterial. This will cause resonance phenomenon in its local resonance unit, resulting in band gap that hinder the propagation of elastic waves. PMs are smart materials with excellent electro-mechanical coupling effect that allow the band gap of PMs to be regulated by changing the mechanical properties of the PM with different external circuits [6].

The tunable band gap of PMs allows them to better adapt to environmental changes, broaden the operating frequency range and overcome the serious drawbacks of passive metamaterials working at a single frequency or narrow band [16]. According to the material and structural characteristics, the bandgap performance of metamaterial structures can be generally classified into fixed bandgap characteristics and tunable bandgap characteristics [17]. Fixed bandgap metamaterial structures have been studied

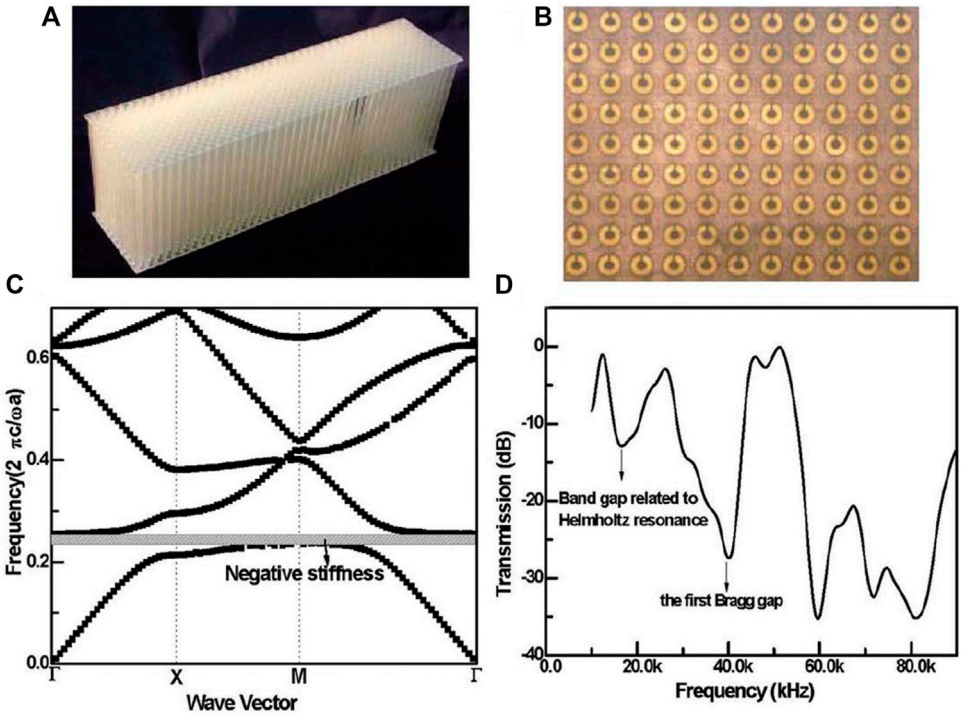

FIGURE 1
(A) phononic crystal **(B)** The contour of the phononic crystal is composed of Helmholtz resonator **(C)** Low resonant frequency band gap showing negative stiffness **(D)** Frequency position corresponding to band gap.

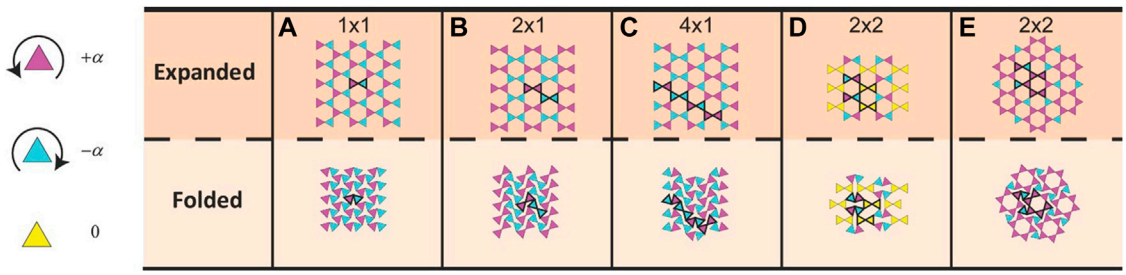

FIGURE 2
Schematic of the basic folding mechanisms in a rigid kagome network. The basic unit cell for each folding mechanism is outlined in black. The color of the triangles corresponds to their rotation. **(A)** Mode with a basic cell of size 1 × 1; **(B)** Mode with a basic cell of size 2 × 1; **(C)** Mode with a basic cell of size 4 × 1; **(D)** Mode with a basic cell of size 2 × 2; **(E)** Mode with a basic cell of size 2 × 2 [36].

for many years [18–22]. The materials and structures required are some common ones, such as beam-plate composite metamaterial structures [23] and rod-beam composite metamaterial structures [24]. However, once the structure and model parameters of the metamaterial are determined, the position and width of the band gap are determined, which greatly limits its application in UE. Therefore, the metamaterial structure must have band gap tunability and this property is also very useful in practice.

Tunable band gap of metamaterial structures has been studied. Generally, the stiffness or inertia of the metamaterial structure is adjusted by special technical means and thus the position and width of the band gap can be adjusted. The first studies on tunable metamaterials started by Goffaux and

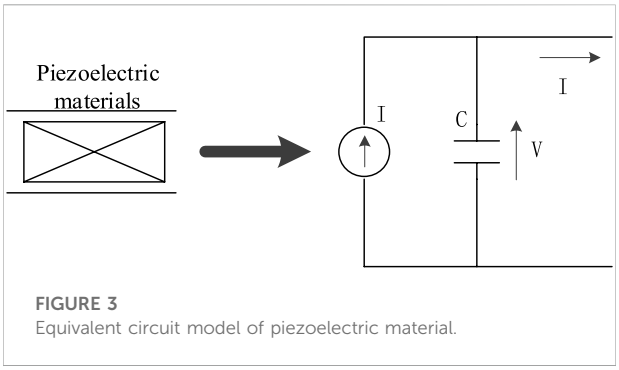

FIGURE 3
Equivalent circuit model of piezoelectric material.

Vigneron [25], who proposed to rotate a non-axisymmetric solid scatterer by a certain angle to change the band gap width for fluid-solid phonon crystals. In addition to adjusting the mechanical properties of metamaterials by rotating scatterers [26–28], changing the stiffness or shape of structures by applying external loads is also an effective method [29–32]. For example, Wang et al. [33] used post-buckling deformation to realize the regulation of the local resonance type band gap. Bertoldi et al. [34, 35] increased the bandgap width by compression of porous soft material structures with negative Poisson's ratio. As shown in Figure 2, Shan et al. [36] studied the porous structure of triangular circular hole array and effectively tuned the elastic wave propagation in the structure by controlling the loading direction to enhance the tunability of the system's dynamic response. Meaud [37] studied the propagation of elastic waves in a lattice with alternating linear and nonlinear springs.

The band gap can also be controlled indirectly through the properties of the piezoelectric material. Active control of the band gap of a nonlinear piezoelectric spring model using positive and negative proportional control strategies is proposed. Nimmagadda proposed a composite structure composed of periodic lattice and local resonators. The two element structures have different dependence on temperature. The opening and closing of the band gap can be controlled by controlling the temperature, because the elastic modulus of the two element structures will change with temperature. Xia et al. [38] studied the effect of water temperature on the local resonance band gap and negative bulk modulus of acoustic metamaterials, and the local resonance band gap and negative bulk modulus were regulated by adjusting the water temperature.

PMs are metamaterials that use piezoelectric materials to design metamaterial structures. Metamaterials with the desired bandgap position and width can be obtained by an active control strategy. Piezoelectric materials not only give metamaterials intelligence but also expand the functional scope of metamaterials, so that related equipment has a variety of superior properties at the same time, which can effectively promote the multi-functionalization of equipment.

2.2 Piezoelectric regulation of PMs

Among many intelligent materials, piezoelectric materials have a special electro-mechanical coupling effect and the equivalent circuit of piezoelectric materials is shown in Figure 3. They can be found in alloys or piezoelectric ceramics, soft polymers and conductors or semiconductors. There is no doubt that it is the most well-researched, the most mature and the most widely used intelligent material [39]. Common piezoelectric materials can be divided into three categories: piezoelectric crystals (such as quartz crystals), piezoelectric ceramics and piezoelectric polymers. They are used in different fields and play different values according to their different properties and states. The electro-mechanical coupling effect of piezoelectric materials is that under the action of mechanical pressure, surface charges will appear and form an electric field in the body, which is called the positive piezoelectric effect. Piezoelectric materials can also deform in response to an electric field, which is called the inverse piezoelectric effect. The electro-mechanical coupling effect of piezoelectric materials is that surface charges will appear under the action of mechanical pressure and an electric field will be formed in the body, which is called the positive piezoelectric effect and it can also deform under the action of the electric field, which is called the inverse piezoelectric effect. The mechano-electric coupling characteristics give piezoelectric materials the ability to convert electrical energy and mechanical energy, which can be used in applications such as transducers, sensors and actuators [6].

The excellent electro-mechanical coupling effect of piezoelectric materials makes it possible to use different external circuits to modify the mechanical properties of the piezoelectric material and thus modulate various aspects of the metamaterial. The key is to find a way to control the vibration of the structure. Piezoelectric shunt technology is an important means of vibration suppression, especially in the vibration control of smart structures. Because of the advantages of relatively low added mass, it is widely used in the field of vibration and noise control. According to the operating characteristics, piezoelectric shunt circuits can be divided into linear circuits and nonlinear circuits [7].

For linear circuits, the piezoelectric shunt damping technique was first proposed in 1979 and this technique [40] uses a resistive-inductive (RL) shunt circuit for vibration damping. If the resonance of the circuit is equal to the resonance of the mechanical system, the circuit is in the resonant state and will generate a considerable control force against the vibration of the mechanical system. The simplicity and ease of implementation of RL-based piezoelectric shunt damping techniques have attracted more and more attention [41–43]. The circuit control effect mainly depends on RL resonance. The traditional RL resonant shunt circuit has the following problems. For example, the vibration attenuation capability of the circuit under the

condition of multi-modal vibration is not ideal [44], the realization of low-frequency vibration requires a hundred Henry-level inductance [45] and the circuit control effect is very sensitive to the change of circuit parameters [46]. In addition to the RL piezoelectric shunt damping circuit, the negative capacitive damping technology can also effectively avoid the narrow band gap and achieve the effect of broadband vibration control. On the one hand, the negative capacitance shunt circuit can effectively change the equivalent stiffness of piezoelectric materials [47], and on the other hand, it can produce a good damping effect [48, 49]. In particular, changes in the environment may cause dramatic changes in the structural resonance frequency. At the same time, the temperature will also change the capacitance in the control circuit, which will affect the performance of the shunt circuit. Based on the proposal of an accurate model for constructing piezoelectric materials, the problem of how to reduce or avoid the instability of the negative capacitance piezoelectric shunt damping circuit is solved [50].

In terms of nonlinear circuits, the most representative one is the synchronous switch damping (SSD) shunt circuit [51–54]. The synchronous switch damping shunt circuit is a semi-active control method, which is equivalent to providing a nonlinear impact load. The voltage of the piezoelectric material will continuously flip with the change of the structural displacement under the action of the nonlinear switch of the SSD circuit. Among SSD circuits, synchronous switched inductive damping circuit (SSDI) has attracted wide attention because of its excellent stability and good low-frequency vibration suppression effect without very large inductors [55, 56]. However, the manufacturing process and other factors will affect the quality factor of the inductor, which will affect the vibration suppression effect of SSDI circuit. To reduce this detrimental effect, Xu et al. [57] improved the vibration suppression effect of the circuit by adding negative capacitance to the circuit to improve the electromechanical coupling coefficient of the piezoelectric element. In addition, a voltage source is connected in series in the SSDI circuit to form the enhanced SSDV, which can also effectively improve the vibration suppression of the circuit. However, this method tends to cause circuit instability and a synchronous switching damping circuit based on a negative capacitance (SSDNC) structure has also been developed. This circuit can counteract the equivalent capacitance value of piezoelectric material by adjusting the value of negative capacitance, so as to improve the electromechanical coupling coefficient of piezoelectric material, increase the flipping voltage of piezoelectric material, and achieve better vibration suppression effect. This shunt circuit does not require precise system identification of the controlled structure. The vibration control effect is better and more stable. Changes in the external environment have a low impact on the control system. Most importantly, the control system is simple and can be implemented with only a few electronic components [58].

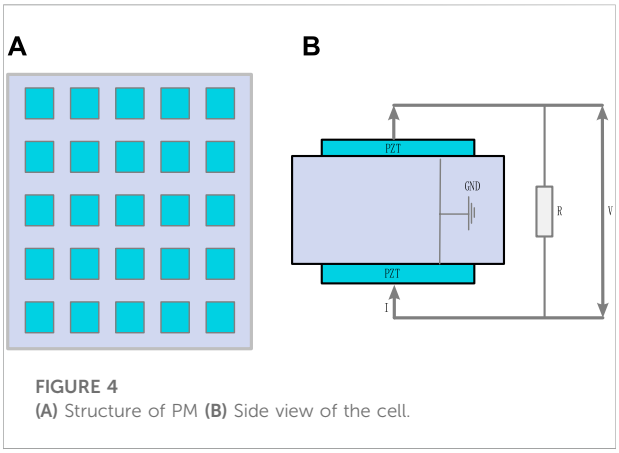

FIGURE 4
(A) Structure of PM **(B)** Side view of the cell.

3 Research progress of PMs used in UE

At present, PMs has been widely used in UE, including underwater gliders, hydrophones, underwater robots, offshore drilling platforms, submarines and underwater communication equipment [59–61]. It is also used to improve ultrasonic sensors and special equipment for detecting underwater explosives and underwater pollution [62, 63]. PMs has a very broad application prospect. For underwater equipment, the most prominent feature is that the hard boundary of sound field meets the need for hydrostatic pressure. The sound wave in the underwater equipment flows from the seawater environment to the underwater equipment. The water to equipment here is the hard boundary. The hard boundary condition is that the normal sound pressure is zero. Hydrostatic pressure refers to the pressure exerted by static liquid on adjacent contact. The band gap characteristics of PMs can be used for sound insulation of UE. To sum up, the application of piezoelectric metamaterial in underwater equipment can be developed in two directions. First, the band gap characteristics are used for sound insulation of underwater equipment. Second, piezoelectric conversion characteristics are used for energy harvesting in underwater devices. The application prospect of PMs in UE will be very broad.

The following describes the research content and research progress of PMs in terms of sound insulation and piezoelectric conversion of UE.

3.1 Sound insulation

PM structures have good applications in the field of sound insulation and vibration damping due to their unique elastic wave band gap properties, i.e., elastic waves cannot propagate in their band gap frequency range [64, 65].

Zhou et al. [66] used a new method to verify and deduce a new type of piezoelectric composite metamaterial, which has both viscoelastic and piezoelectric properties. The viscosity of the viscoelastic material dissipates the mechanical energy of vibration and absorbs the sound waves to achieve passive noise reduction. The properties of piezoelectric materials can achieve the effect of active noise cancellation, by emitting the opposite phase of the sound wave to a known sound source to cancel out the sound wave. This material is applied to the coating of submarines. The reflection is eliminated by applying a controlled periodic voltage to the piezoelectric material layer to create a corresponding stress, which in turn emits sound waves that are in the opposite phase of the vibration. The concealment of submarine is improved, and the feasibility of using this new material for UE sound insulation is discussed theoretically. Yi et al. [67] proposed a general method for designing multi-resonant PMs, as shown in Figure 4. This metamaterial contains periodically distributed piezoelectric patches bonded to the surface of the main structure, the shunt circuit works with the patches in a self-inductive mode. By studying the effective bending stiffness of the multi-resonance metamaterial plate, the mechanism of multi-band gap generated by the transfer function is explained. When the effective bending stiffness becomes negative, the transfer function induces multiple frequency ranges, resulting in multiple band gaps The characteristics of these bandgaps can be studied, and their coupling and merging phenomena can be observed and analyzed. The elastic wave isolation effect of the material in multiple frequency bands is verified by numerical results in the frequency domain, which proves the functionality of the material and provides a new choice for sound insulation and vibration reduction of underwater equipment.

He et al. [68] designed a tunable thin-film metamaterial based on piezoelectric materials for the isolation of low-frequency noise. The material is made of a piezoelectric mass embedded in an elastic film, and it is verified by experiments that the material has good sound insulation performance in the frequency range of 20–1,200 Hz. Moreover, the external circuit of the piezoelectric mass block is explored to form an LC oscillating circuit, and the resonant frequency of the circuit can be adjusted by changing the parameters of the external circuit to realize the adjustability of the sound insulation performance. The results of this study provide a reference for the design of sound-insulating tunable PMs and support for the material to be used in UE.

To realize the sound insulation and vibration reduction of UE, Wang et al. [7] overcome the shortcoming of the relatively narrow band gap of PM structures by externally connecting different shunt circuits, and realized the adjustment of the band gap of metamaterials. The synthetic impedance technology is proposed, and the synthetic impedance equivalent control loop is designed. Through simulation research, it is shown that the method can flexibly adjust the band gap range of PMs using software programming, which provides a new way for the vibration and sound insulation of PMs in UE. With its unique piezoelectric properties, the PM is used in the sound insulation of UE, overcoming the problem of poor isolation of low-frequency sound by traditional materials, reducing the impact of underwater noise on UE and improving the data accuracy of the equipment.

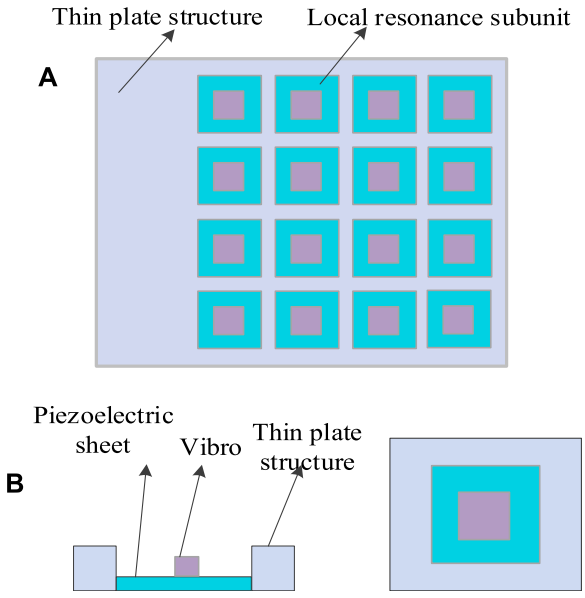

FIGURE 5
(A) Schematic diagram of the structural plane of the local resonance type PM sheet **(B)** Schematic diagram of the structure of the local resonance type PM resonant subunit.

3.2 Piezoelectric conversion

Vibration energy in water mostly exists in the form of low frequency and broadband sound waves, and the vibration energy in water can be converted into electric energy through piezoelectric conversion characteristics.

The PM structure is designed to capture the underwater vibration energy of broadband and low frequency. The model of elastic wave propagation in PM structure is established, and then the characteristics of elastic wave propagation are solved by simulation. The band gap of the PM structure is solved and analyzed, and the energy output of PMs using different piezoelectric materials is simulated and experimentally analyzed to demonstrate the effectiveness of the material structure [8]. Experiments show that the PM structure can effectively absorb elastic wave vibration energy in a specific frequency range and convert it into electrical energy, which can realize energy storage and power supply for underwater robots and other equipment. Khan et al. [69] studied and

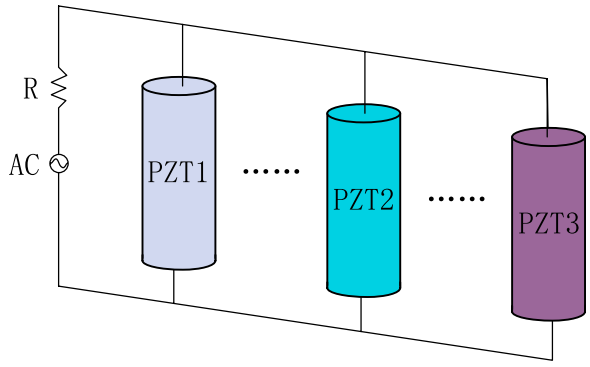

FIGURE 6
Material structure of PM mechanical antenna.

proposed a modeling framework based on micromechanical finite element, which was used to calculate the electromechanical characteristics of 3–3 PMs based on honeycomb structural variants. The hydrostatic quality factor of the longitudinal polarization network is increased by four orders of magnitude and the acoustic impedance is reduced by one order of magnitude, which is very suitable for the design of hydrophones. Hydrophones are made of new PMs with higher hydrostatic quality factors. An active gradient metamaterial based on the composite structure of conventional piezoelectric materials was proposed to achieve acoustic impedance matching and underwater acoustic focusing [70]. The active focusing and broadband focusing behaviors of this PM are demonstrated by simulation and experiments, which can replace acoustic metamaterials used in UE.

To solve the power problem of underwater low-power wireless sensors, Zhang et al. [71] organically combined elastic wave fluctuation characteristics with piezoelectric energy-harvesting structures to improve the vibration energy capture efficiency of broadband low-frequency environments. As shown in Figure 5, a local resonant piezoelectric metamaterial thin sheet is designed and manufactured for test verification. The test results show that the optimized circuit can effectively improve the energy harvesting efficiency and provide a choice for long-term uninterrupted power supply of underwater low-power equipment. Sayed Saad Afzal et al. [72] proposed to create a completely battery-free and scalable underwater sensor network. By developing a backscattering underwater sensor using PMs, backscattering sensors can simply collect energy from environmental signals in the environment and then reflect them to communicate with near-zero power consumption, which is called piezoelectric acoustic backscattering. It is an underwater backscatter network system that uses underwater transducers to provide energy for communication and has made great progress in power-free underwater communication.

Figure 6 is a structural diagram of a PM, which is used to fabricate a mechanical antenna that can be used for UE communication. The antenna has high radiation efficiency, multiple frequency bands and small size [73]. Through the structural parameters and materials of the piezoelectric radiation unit, the three operating frequency bands of 22, 24, and 26 kHz can be independently adjusted and the modulation range exceeds 15 kHz. The experimental results show that the proposed piezoelectric metamaterial antenna has great application potential in underwater communication equipment.

Xiao et al. proposed a two-dimensional local resonance metamaterial acoustic energy collector for the problem of sound energy harvesting. The acoustic energy density and conversion efficiency are improved by studying and utilizing piezoelectric energy harvesting technology of acoustic metamaterials. The sound energy conversion and sound insulation performance of the plate are studied from the acoustic point of view, so that the utilization rate of sound energy into electric energy can reach the highest [74]. Ma et al. designed a single cavity underwater acoustic metasurface unit with subwavelength thickness that simultaneously achieves high refractive index in underwater environment. By arranging several metasurface elements with gradient refractive index distribution along the radial direction, a 3D planar underwater acoustic lens with gradient refractive index is constructed. In addition, a lens-based acoustic concentrator is proposed to greatly increase the acoustic energy gain over a wide frequency range. It has potential application value in acoustic energy harvesting [75]. Kim et al. designed spherical and ellipsoidal metamaterial lenses based on Luneburg lenses and transform optics for underwater ultrasound imaging. It can enhance the signal over a wide frequency range and detect objects at wide angles. The lens has a wide frequency characteristic and can achieve the half maximum of focal length and full width in the frequency range of 60–160 kHz.These lenses can be used in sound-guided ranging, offering the possibility of detecting underwater at higher resolution at broadband and wide angles [15].

The emergence of PMs improves the efficiency of underwater elastic wave vibration energy harvesting, so they are mostly used to improve the traditional underwater energy harvesting equipment. The emergence of PMs provides a new option for the fabrication of UE, thus improving the performance of UE. In conclusion, the emergence of PMs has greatly promoted the development of UEs.

4 Summary and outlook

PMs can be widely used in UE due to their bandgap characteristics and piezoelectric conversion characteristics. The band gap characteristics are mainly related to the absorption of elastic waves. Under water, PMs are mainly used to absorb sound

waves, play the role of sound insulation, noise reduction, vibration reduction and so on. The vibrational energy of elastic waves can be converted into electric energy by piezoelectric conversion. Under water, PMs can convert the vibrational energy to electricity to power UE. In addition, PM has excellent electro-mechanical coupling effect. The external shunt circuit is easy to be adjusted and designed in various ways, so that the PM has controllable characteristics, which can meet the different requirements of the functional design and application of acoustic equipment. In practical engineering, the application of PM can reduce noise and vibration of UE, which is helpful to improve the accuracy of hydrophones. The energy conversion efficiency of PM can be improved by changing its piezoelectric structure through the design of external shunt circuit. In general, the application of PM in UE extends the application range of UE.

So far, few piezoelectric metamaterial have been used underwater, or even acoustic metamaterial for underwater equipment. In recent years, the research of piezoelectric metamaterials has attracted great interest and attention of many researchers. At the same time, a lot of scientific research achievements have been made, but there is still a big gap with the actual demand and application. In the future, researchers still need to strengthen the corresponding theoretical, numerical and experimental research. Most of the existing related research is still based on basic research, and there is still a great lack of corresponding applied research. The research results of piezoelectric metamaterial are transformed into practical technology to make structures, components and equipment suitable for practical application. This requires the cooperation and efforts of theoretical researchers and technicians engaged in the field of applied research and technology development.

Based on the current research status, there is still room for future development as follows: 1) The mature application of PMs in UE is relatively small, and most of them are still in the theoretical and simulation stage. Experimental research on PMs should be accelerated, and more applications should be applied to UE. 2) Piezoelectric materials with better performance should be developed to power energy storage for larger UEs. 3) With the rapid development of artificial intelligence, the structure of PM can be designed by artificial intelligence algorithm. For example, it can be intelligently designed according to the range and function of use. 4) The properties of piezoelectric materials are fully exploited by UE, and researchers also need to develop equipment that can accurately process mechanical signals and design better external control circuits.

Author contributions

JZ, the author of the article, was responsible for the design and writing of the article. NH provided valuable advice on the design and writing of the article. JW offered advice on the use of metamaterials in underwater devices. WL was in charge of literature research. ZZ provided valuable advice on the design and writing of the article. MW, YZ and HD are coordinating the authors

Funding

This research was supported by the Zhejiang Science and Technology Plan Project (No. 2022C01199), and the Zhejiang science and technology project (No. GK219909299001-021). The funders had no role in the design of the study; in the collection, analyses, or interpretation of data; in the writing of the manuscript, or in the decision to publish the results.

Conflict of interest

Author JW was employed by Sanmen Sanyou Technology Inc.

The remaining authors declare that the research was conducted in the absence of any commercial or financial relationships that could be construed as a potential conflict of interest.

Publisher's note

References

1. Liu J, Guo H, Wang T. A review of acoustic metamaterials and phononic crystals. *Crystals* (2020) 10(4):305. doi:10.3390/cryst10040305

2. Liao G, Luan C, Wang Z, Liu J, Yao X, Fu J. Acoustic metamaterials: A review of theories, structures, fabrication approaches, and applications. *Adv Mater Technol* (2021) 6(5):2000787. doi:10.1002/admt.202000787

3. Grzegorczyk TM, Kong JA. Review of left-handed metamaterials: Evolution from theoretical and numerical studies to potential applications. *J Electromagn Waves Appl* (2012) 20(14):2053–64. doi:10.1163/156939306779322620

4. Kushwaha MS, Halevi P, Dobrzynski L, Djafari-Rouhani B. Acoustic band structure of periodic elastic composites. *Phys Rev Lett* (1993) 71(13):2022–5. doi:10.1103/PhysRevLett.71.2022

5. He Q, Sun S, Xiao S, Zhou L. High-efficiency metasurfaces: Principles, realizations, and applications. *Adv Opt Mater* (2018) 6(19):1800415. doi:10.1002/adom.201800415

6. Yuan Y, You Z, Chen W. PMs and wave control: Status quo and prospects. *Chin J Theor Appl Mech* (2021) 53(08):2101–16. doi:10.6052/0459-1879-21-198

7. Bo WL. *Research on vibration control based on PMs northwestern*. London: Polytechnical University (2019).

8. Dong C. *Vibration energy collection system based on one-dimensional PMs master of engineering*. China: Harbin Engineering University (2021).

9. Li Z, Wang Y, Ma T, Zhang C. Smart piezoelectric phononic crystals and metamaterials:state-of-the-art review and outlook. *Chin Sci Bull* (2022) 67(12): 1305–25. doi:10.1360/TB-2021-1265

10. Lu M-H, Feng L, Chen Y-F. Phononic crystals and acoustic metamaterials. *Mater Today* (2019) 12(12):34–42. doi:10.1016/S1369-7021(09)70315-3

11. Ma F, Huang Z, Liu C, Wu JH. Acoustic focusing and imaging via phononic crystal and acoustic metamaterials. *J Appl Phys* (2022) 131(1):011103. doi:10.1063/5.0074503

12. Ji Y, Luan C, Yao X, Fu J, He Y. Recent progress in 3d printing of smart structures: Classification, challenges, and trends. *Adv Intell Syst* (2021) 3(12): 2000271. doi:10.1002/aisy.202000271

13. Maldovan M. Sound and heat revolutions in phononics. *Nature* (2013) 503(7475):209–17. doi:10.1038/nature12608

14. Ma F, Wang C, Liu C, Wu JH. Structural designs, principles, and applications of thin-walled membrane and plate-type Acoustic/elastic metamaterials. *J Appl Phys* (2021) 129(23):231103. doi:10.1063/5.0042132

15. Kim J-W, Hwang G, Lee S-J, Kim S-H, Wang S. Three-dimensional acoustic metamaterial Luneburg lenses for broadband and wide-angle underwater ultrasound imaging. *Mech Syst Signal Process* (2022) 179:109374. doi:10.1016/j.ymssp.2022.109374

16. Tian Y, Ge H, Lu M-H, Chen Y-F. Research advances in acoustic metamaterials. *Acta Phys Sin* (2019) 68(19):194301. doi:10.7498/aps.68.20190850

17. Ren T. *Investigations on bandgap tuning and sound insulation characteristics of metamaterial structures doctor of engineering*. China: Harbin Engineering University (2021).

18. Guo Z, Li F. Advances in active tuning of elastic wave band gaps in metamaterial structures. *Chin Sci Bull* (2021) 67(12):1249–63. doi:10.1360/tb-2021-0483

19. Martínez J, Coves Á, Bronchalo E, San Blas ÁA, Bozzi M. Band-pass filters based on periodic structures in siw technology. *AEU - Int J Elect Commun* (2019) 112:152942. doi:10.1016/j.aeue.2019.152942

20. Taniker S, Yilmaz C. Phononic gaps induced by inertial amplification in bcc and fcc lattices. *Phys Lett A* (2013) 377(31-33):1930–6. doi:10.1016/j.physleta.2013.05.022

21. Hajhosseini M, Rafeeyan M, Ebrahimi S. Vibration band gap analysis of a new periodic beam model using gdqr method. *Mech Res Commun* (2017) 79:43–50. doi:10.1016/j.mechrescom.2017.01.002

22. Abueidda DW, Jasiuk I, Sobh NA. Acoustic band gaps and elastic stiffness of pmma cellular solids based on triply periodic minimal surfaces. *Mater Des* (2018) 145:20–7. doi:10.1016/j.matdes.2018.02.032

23. Li Y, Chen T, Wang X, Xi Y, Liang Q. Enlargement of locally resonant sonic band gap by using composite plate-type Acoustic metamaterial. *Phys Lett A* (2015) 379(5):412–6. doi:10.1016/j.physleta.2014.11.028

24. Al Ba'ba'a HB, Nouh M. Mechanics of longitudinal and flexural locally resonant elastic metamaterials using a structural power flow approach. *Int J Mech Sci* (2017) 122:341–54. doi:10.1016/j.ijmecsci.2017.01.034

25. Goffaux C, Vigneron JP. Theoretical study of a tunable phononic band gap system. *Phys Rev B* (2001) 64(7):075118. doi:10.1103/PhysRevB.64.075118

26. Tian Y, Tan Z, Han X, Li W. Phononic crystal lens with an asymmetric scatterer. *J Phys D Appl Phys* (2019) 52(2):025102. doi:10.1088/1361-6463/aae679

27. Lin S-CS, Huang TJ. Tunable phononic crystals with anisotropic inclusions. *Phys Rev B* (2011) 83(17):174303. doi:10.1103/PhysRevB.83.174303

28. Wu F, Liu Z, Liu Y. Acoustic band gaps created by rotating square rods in a two-dimensional lattice. *Phys Rev E* (2002) 66(4):046628. doi:10.1103/PhysRevE.66.046628

29. Ning S, Yang F, Luo C, Liu Z, Zhuang Z. Low-frequency tunable locally resonant band gaps in acoustic metamaterials through large deformation. *Extreme Mech Lett* (2020) 35:100623. doi:10.1016/j.eml.2019.100623

30. Chen Y, Wu B, Li J, Rudykh S, Chen W. Low-frequency tunable topological interface states in soft phononic crystal cylinders. *Int J Mech Sci* (2021) 191:106098. doi:10.1016/j.ijmecsci.2020.106098

31. Huang Y, Shen XD, Zhang CL, Chen WQ. Mechanically tunable band gaps in compressible soft phononic laminated composites with finite deformation. *Phys Lett A* (2014) 378(30-31):2285–9. doi:10.1016/j.physleta.2014.05.032

32. Huang Y, Li J, Chen W, Bao R. Tunable bandgaps in soft phononic plates with spring-mass-like resonators. *Int J Mech Sci* (2019) 151:300–13. doi:10.1016/j.ijmecsci.2018.11.029

33. Wang P, Casadei F, Shan S, Weaver JC, Bertoldi K. Harnessing buckling to design tunable locally resonant acoustic metamaterials. *Phys Rev Lett* (2014) 113(1): 014301. doi:10.1103/PhysRevLett.113.014301

34. Bertoldi K, Boyce MC. Mechanically triggered transformations of phononic band gaps in periodic elastomeric structures. *Phys Rev B* (2008) 77(5):052105. doi:10.1103/PhysRevB.77.052105

35. Bertoldi K, Boyce MC, Deschanel S, Prange SM, Mullin T. Mechanics of deformation-triggered pattern transformations and superelastic behavior in periodic elastomeric structures. *J Mech Phys Sol* (2008) 56(8):2642–68. doi:10.1016/j.jmps.2008.03.006

36. Shan S, Kang SH, Wang P, Qu C, Shian S, Chen ER, et al. Harnessing multiple folding mechanisms in soft periodic structures for tunable control of elastic waves. *Adv Funct Mater* (2014) 24(31):4935–42. doi:10.1002/adfm.201400665

37. Nimmagadda C, Matlack KH. Thermally tunable band gaps in architected metamaterial structures. *J Sound Vibration* (2019) 439:29–42. doi:10.1016/j.jsv.2018.09.053

38. Xia B, Chen N, Xie L, Qin Y, Yu D. Temperature-controlled tunable acoustic metamaterial with active band gap and negative bulk modulus. *Appl Acoust* (2016) 112:1–9. doi:10.1016/j.apacoust.2016.05.005

39. Katzir S. *The discovery of the piezoelectric effect the beginnings of piezoelectricity*. Berlin, Germany: Springer (2006). p. 15–64.

40. Forward RL. Electronic damping of vibrations in optical structures. *Appl Opt* (1979) 18(5):690–7. doi:10.1364/ao.18.000690

41. Hollkamp JJ. Multimodal passive vibration suppression with piezoelectric materials and resonant shunts. *J Intell Mater Syst Structures* (2016) 5(1):49–57. doi:10.1177/1045389x9400500106

42. Behrens S, Moheimani SOR, Fleming AJ. Multiple Mode current flowing passive piezoelectric shunt controller. *J Sound Vibration* (2003) 266(5):929–42. doi:10.1016/s0022-460x(02)01380-9

43. Thomas O, Ducarne J, Deü JF. Performance of piezoelectric shunts for vibration reduction. *Smart Mater Struct* (2012) 21(1):015008. doi:10.1088/0964-1726/21/1/015008

44. Wu S-y. Method for multiple-mode shunt damping of structural vibration using a single pzt transducer. In: Conference of Smart structures and materials 1998: passive damping and isolation; 16 June 1998; San Diego, CA, United States. Bellingham, Washington, United States: SPIE (1998). p. 1–5.

45. Moheimani SR, Fleming AJ. *Piezoelectric transducers for vibration control and damping*. Berlin, Germany: Springer (2006).

46. Berardengo M, Manzoni S, Vanali M. The behaviour of mistuned piezoelectric shunt systems and its estimation. *Shock and Vibration* (2016) 2016:1–18. doi:10.1155/2016/9739217

47. Date M, Kutani M, Sakai S. Electrically controlled elasticity utilizing piezoelectric coupling. *J Appl Phys* (2000) 87(2):863–8. doi:10.1063/1.371954

48. Imoto K, Nishiura M, Yamamoto K, Date M, Fukada E, Tajitsu Y. Elasticity control of piezoelectric lead zirconate titanate (pzt) materials using negative-capacitance circuits. *Jpn J Appl Phys* (2005) 44(9):7019–23. doi:10.1143/jjap.44.7019

49. Beck BS, Cunefare KA, Ruzzene M, Collet M. Experimental analysis of a cantilever beam with a shunted piezoelectric periodic array. *J Intell Mater Syst Structures* (2011) 22(11):1177–87. doi:10.1177/1045389x11411119

50. Richard C, Guyomar D, Audigier D, Ching G. Semi-passive damping using continuous switching of a piezoelectric device. In: Conference of Smart Structures and Materials 1999: Passive Damping and Isolation; 12 July 1999; San Diego, CA, United States. Bellingham, Washington, United States: SPIE (1999). p. 1–8.

51. Lin Q, Ermanni P. Semi-active damping of a clamped plate using pzt. *Int J Sol Structures* (2004) 41(7):1741–52. doi:10.1016/j.ijsolstr.2003.11.023

52. Lefeuvre E, Badel A, Petit L, Richard C, Guyomar D. Semi-passive piezoelectric structural damping by synchronized switching on voltage sources. *J Intell Mater Syst Structures* (2006) 17(8-9):653–60. doi:10.1177/1045389x06055810

53. Muhammad BB, Wan M, Feng J, Zhang W-H. Dynamic damping of machining vibration: A review. *Int J Adv Manuf Technol* (2016) 89(9-12): 2935–52. doi:10.1007/s00170-016-9862-z

54. Neubauer M, Han X, Schwarzendahl SM. Enhanced switching law for synchronized switch damping on inductor with bimodal excitation. *J Sound Vibration* (2011) 330(12):2707–20. doi:10.1016/j.jsv.2011.01.003

55. Faiz A, Guyomar D, Petit L, Buttay C. Wave transmission reduction by a piezoelectric semi-passive technique. *Sensors Actuators A: Phys* (2006) 128(2): 230–7. doi:10.1016/j.sna.2006.02.021

56. Tang W, Wang B, Bao B, Cao JJ. Experimental comparisons of two detection methods for semi-passive piezoelectric structural damping. *J Vib Eng Technol* (2017) 5(4):367–79.

57. Han X, Neubauer M, Wallaschek J. Improved piezoelectric switch shunt damping technique using negative capacitance. *J Sound Vibration* (2013) 332(1): 7–16. doi:10.1016/j.jsv.2012.08.001

58. Zhang S. *A study on semi-active noise control by using synchronized switch damping method master of engineering*. China: Nanjing University of Aeronautics and Astronautics (2016).

59. Hu G, Tang L, Banerjee A, Das R. Metastructure with piezoelectric element for simultaneous vibration suppression and energy harvesting. *J Vib Acoust* (2017) 139(1):4034770. doi:10.1115/1.4034770

60. Apaydin N, Sertel K, Volakis JL. Nonreciprocal leaky-wave antenna based on coupled microstrip lines on a non-uniformly biased ferrite substrate. *IEEE Trans Antennas Propag* (2013) 61(7):3458–65. doi:10.1109/tap.2013.2257646

61. Erb RM, Libanori R, Rothfuchs N, Studart AR. Composites reinforced in three dimensions by using low magnetic fields. *Science* (2012) 335(6065):199–204. doi:10.1126/science.1210822

62. Bisoffi M, Hjelle B, Brown DC, Branch DW, Edwards TL, Brozik SM, et al. Detection of viral bioagents using a shear horizontal surface acoustic wave biosensor. *Biosens Bioelectron X* (2008) 23(9):1397–403. doi:10.1016/j.bios.2007.12.016

63. Courjal N, Bernal MP, Ulliac G, Dahdah J, Benchabane S, Merolla JM. Linbo3 acousto-optical and electro-optical micromodulators. *J Eur Opt Soc Rapid Publications* (2009) 4:09018. doi:10.2971/jeos.2009.09018

64. Wang Y-Z, Li F-M, Kishimoto K, Wang Y-S, Huang W-H. Band gaps of elastic waves in three-dimensional piezoelectric phononic crystals with initial stress. *Eur J Mech - A/Solids* (2010) 29(2):182–9. doi:10.1016/j.euromechsol.2009.09.005

65. Lebon F, Rizzoni R. Higher order interfacial effects for elastic waves in one dimensional phononic crystals via the Lagrange-Hamilton's principle. *Eur J Mech - A/Solids* (2018) 67:58–70. doi:10.1016/j.euromechsol.2017.08.014

66. Zou S. *Analysis of the acoustic concealing from the underwater polymer matrix piezoelectric composites*. Beijing, China: Huazhong University of Science & Technology (2009).

67. Yi K, Liu Z, Zhu R. Multi-resonant metamaterials based on self-sensing piezoelectric patches and digital circuits for broadband isolation of elastic wave transmission. *Smart Mater Struct* (2021) 31(1):015042. doi:10.1088/1361-665X/ac3b1f

68. He Z-H, Zhao J-B, Yao H, Jiang J-N, Chen X. Sound insulation performance of thin-film AcousticMetamaterials based on piezoelectric materials. *Acta Phys Sin* (2019) 68(13):134302–90. doi:10.7498/aps.68.20190245

69. Khan KA, Khan MA. 3-3 piezoelectric metamaterial with negative and zero Poisson's ratio for hydrophones applications. *Mater Res Bull* (2019) 112:194–204. doi:10.1016/j.materresbull.2018.12.016

70. Li Z, Zhao J, Hou C, Fei C, Zheng C, Lou L, et al. High-frequency self-focusing ultrasonic transducer with piezoelectric metamaterial. *IEEE Electron Device Lett* (2022) 43(6):946–9. doi:10.1109/led.2022.3170613

71. Zhang F. *Study on coupling modeling and structural topology optimization method of local resonance PM vibration energy capture system master of engineering*. Changsha, China: National University of Defense Technology (2018).

72. Afzal SS. Battery-free subsea internet of things. *XRDS: Crossroads, ACM Mag Students* (2020) 27(2):62–5. doi:10.1145/3436203

73. Xu J, Cao J, Guo M, Yang S, Yao H, Lei M, et al. Metamaterial Mechanical Antenna for Very Low Frequency Wireless Communication. *Adv Compos Hybrid Mater* (2021) 4(3):761–7. doi:10.1007/s42114-021-00278-1

74. Xiao H, Li T, Zhang L, Liao W-H, Tan T, Yan Z. Metamaterial Based Piezoelectric Acoustic Energy Harvesting: Electromechanical Coupled Modeling and Experimental Validation. *Mechanical Systems and Signal Processing* (2023) 185: 109808. doi:10.1016/j.ymssp.2022.109808

75 Ma F, Zhang H, Du P, Wang C, Wu JH. An Underwater Planar Lens for broadband Acoustic concentrator. *Appl Phys Lett* (2022) 120(12):121701. doi:10.1063/5.0089288

frontiers | Frontiers in Physics

TYPE Original Research
PUBLISHED 13 December 2022
DOI 10.3389/fphy.2022.1054634

OPEN ACCESS

EDITED BY
Bing Li,
Northwestern Polytechnical University, China

REVIEWED BY
Anastasiia O. Krushynska,
University of Groningen, Netherlands
Kuo-Chih Chuang,
Zhejiang University, China

*CORRESPONDENCE
Xiaopeng Li,
xiaopeng.li@toyota.com

SPECIALTY SECTION
This article was submitted to Physical Acoustics and Ultrasonics, a section of the journal Frontiers in Physics

RECEIVED 27 September 2022
ACCEPTED 02 December 2022
PUBLISHED 13 December 2022

CITATION
Li X, Yu Z and Lee T (2022), Experimental study of a tunable perfect flexural wave absorber with a piezoelectric shunted resonator.
Front. Phys. 10:1054634.
doi: 10.3389/fphy.2022.1054634

Experimental study of a tunable perfect flexural wave absorber with a piezoelectric shunted resonator

Xiaopeng Li*, Ziqi Yu and Taehwa Lee

Toyota Research Institute of North America, Toyota Motor North America, Ann Arbor, MI, United States

Metamaterials and metasurfaces have been widely developed recently for extraordinary acoustic and elastic wave control at a deep subwavelength scale. Perfect wave absorption as an extreme case to totally absorb the impinged waves has gained great attention, whereas most existing designs based on local resonance lack tunabilities, making perfect absorption be observed at a single frequency. To overcome this drawback, in this work, we design and fabricate a tunable inductance-resistance (LR) shunted mechanical resonator *via* a bonded piezoelectric patch for perfect flexural wave absorption at low frequency. The LR shunted absorber could be reconfigured to a broad frequency range for perfect flexural wave absorption. The tunable perfect absorption performances are validated through experiments and unit absorption is achieved in experiments. In the end, to further highlight the advantages of shunted damping we numerically demonstrate that the absorption spectrum could be enhanced to broadband absorption with a negative capacitance and an inductance-resistance circuit (NC-LR) connected in parallel. The approach proposed provides an alternative solution to achieve perfect wave absorption in the low-frequency range and enables practical application in complex engineering structures.

KEYWORDS

perfect absorber, metasurface, metamaterial, tunable absorber, programmable absorber, flexural wave absorber, piezoelectric

1 Introduction

Recently, elastic metamaterials have gained lots of attention thanks to their extraordinary dynamic properties [1–3], such as effective negative mass density and/or stiffness [4–7], that are not directly available in natural materials. By artificially designing the microstructures at the deep subwavelength scale, elastic metamaterials have been proven to be good candidates for remarkable wave manipulation [7–12], wave attenuation [1, 13], *etc.* Most recently, efforts are more paid to the design of elastic metasurfaces [14–19], which are a new kind of planar metamaterials, to manipulate wavefronts *via* a suitable arrangement of discontinuities on a material interface or boundary. Perfect wave absorption, an exceptional wave control ability to totally

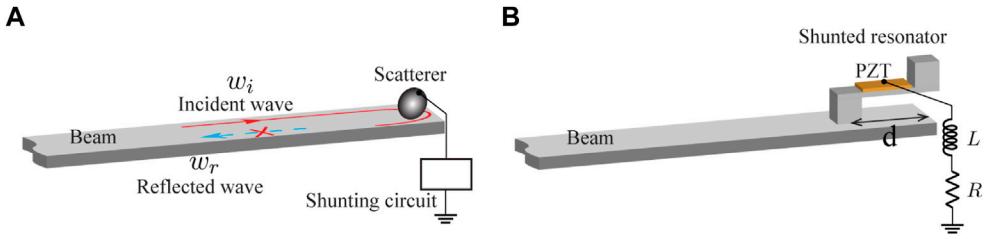

FIGURE 1
Design of an LR-shunted tunable perfect flexural wave absorber. **(A)** Concept of a shunted scatterer for perfect flexural wave absorption. **(B)** Schematic of an LR-shunted tunable perfect flexural wave absorber.

absorb incoming waves, has been demonstrated in 1-dimensional (1D) or 2-dimensional (2D) acoustic and elastic metamaterials/metasurfaces using passive [20–28] or active [18, 29] approaches. Examples of the perfect absorption demonstrated in optics, acoustics, as well as elastic waves, were achieved by satisfying the critical coupling condition [23–27, 30, 31], in which the balance between the energy leakage and the inherent losses of the resonator was fulfilled. Similar to optics [31], by placing a scatterer at or near a waveguide boundary, i.e., a perfect reflecting mirror, in a one-port system, the perfect absorption is observed, through the tuning of loss. The one-port and two-port near perfect flexural wave absorbers on 1D structures have also been reported using acoustic black hole (ABH) [30], Willis coupling [27, 29, 32], coated strip-like beam [26, 28], *etc.* However, most of the existing passive perfect absorbers achieve perfect absorption only at a single frequency point, which hinders their practical applications. Precisely controlling the amount of damping in the scatterers also makes it difficult to design and fabricate the absorbers in experiments. To tune or broaden the absorption frequency, actively shunted piezoelectric patches [18, 29] and thermally controlled shape memory polymer resonators [33] have made it possible, whereas there are still limitations in the existing designs, such as degraded low-frequency performance and inconvenient control strategies.

Using a shunted damping concept proposed by Forward [34], one can not only accurately control the added damping but also tune the system parameters. In this work, we design and fabricate a tunable inductance-resistance (LR) shunted mechanical resonator *via* a bonded piezoelectric patch for the demonstration of perfect flexural wave absorption at the low-frequency range. By changing the electrical resonance, perfect absorption can be tuned to various frequencies for perfect absorption. The tunable perfect absorption performances are further validated through experiments. In the end, we further numerically demonstrate that the absorption spectrum could be enhanced to broadband absorption with an additional negative capacitance connected in parallel. The approach proposed sheds light on designs of reconfigurable dynamic control devices and enables alternative solutions for ultrasonic sensing of complex engineering structures.

2 Materials and methods

2.1 Design

The concept and a schematic of our designed LR shunted absorber are shown in Figures 1A, B, respectively. The shunted resonator is designed with a cantilever-like beam bonded with a piezoelectric patch (PZT-5H) on its top surface. The piezoelectric patch with dimensions ($L_p \times w_p \times h_p = 10$ mm $\times$ 5 mm $\times$ 1 mm) is connected to an LR-shunted circuit. For low-frequency wave absorption, a large value of inductance is required, which will largely increase the added weight and size to the overall system. To avoid this bulky design, we implement a synthetic inductor described in more detail in the next. The LR-shunted resonator is attached near a free end of a semi-infinite beam with a cross-section area ($w \times h = 12.7$ mm $\times$ 3.1 mm) and material properties being Young's modulus ($E = 70$ GPa), mass density ($\rho = 2700$ kg/m^3), and Poisson's ratio ($\nu = 0.33$). A cube-shape tip mass made of stainless steel with Young's modulus ($E = 205$ GPa), mass density ($\rho = 7850$ kg/m^3), and Poisson's ratio ($\nu = 0.28$), is attached at the end of an aluminum strip. Another identical cube functions as a support connected to the other end but on the bottom surface of this beam strip. In our previously investigated coupled mechanical resonators on a two-port system [27], we demonstrated that the coupling distance and the mechanical damping played essential roles in achieving perfect absorption due to the scattering toward the two ports as well as the neighboring resonators. Here, in the one port system as shown in Figure 1, we consider a general case where the scatterer is placed at $x = d$ away from the free end. The scattered waves from the resonator will interfere with the waves reflected from the free boundary and the incident waves [18]. The effect of the location of the resonator on the absorption performance is analyzed through a systematic study. In this analysis, we evaluate the absorption performance as a

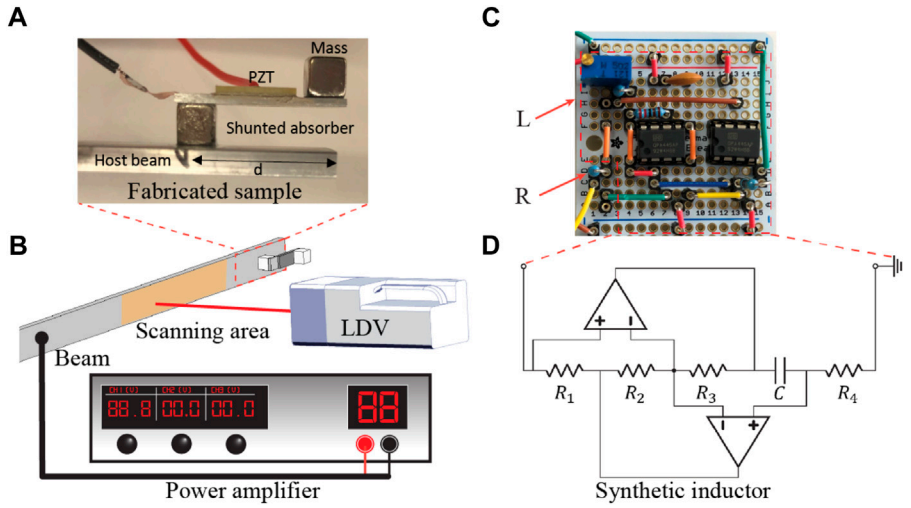

FIGURE 2
Fabricated samples and experimental setup. **(A)** A photo of the fabricated LR-shunted resonator attached near a free end of a beam end. **(B)** A schematic of the experimental setup. **(C)** A photo of the fabricated LR circuit. **(D)** Schematic of the synthetic inductor.

function of resonator location and resonator damping by considering the mechanical resonator as a damped resonator. We find that for the current chosen design the optimized location of the resonator is at $d = 17$ mm away from the free end of the beam, which is in the deep subwavelength of the working frequency. Other geometric parameters can be found in the Supplementary Material, and the material properties of the piezoelectric patch can be found in [19]. We use a commercially available Finite Element Method (FEM) package, COMSOL MultiPhysics, to validate our design. Both frequency domain and time domain simulations are performed and the simulation results are given in the next section.

2.2 Sample fabrication and experimental setup

In what follows we fabricate our LR-shunted resonator and characterize its absorption performance through experiments. The fabricated samples and the experimental setup are illustrated in Figure 2. To fabricate the mechanical resonator, a aluminum strip ($L_1 \times w_1 \times h_1 = 21$ mm $\times$ 5 mm $\times$ 1 mm) is bonded with two identical stainless-steel cubes with side length ($w_c = 5$ mm) on each side of the beam strip facing each other. One of the cubes functions as a tip mass, and the other one as a support to interact with the host beam. A piezoelectric patch is glued on the top surface of the beam strip with a 1 mm gap to the tip mass. A photo of the fabricated absorber is shown in Figure 2A. The bottom electrode of the piezoelectric patch is grounded and the top one is connected to the external LR circuit. To realize a large value of inductance without adding too much weight to the system, we implement a synthetic inductor, Antoniou's Circuit. A photo of the fabricated circuit and a schematic of the Antoniou's circuit are shown in Figures 2C, D, respectively. The synthetic inductor consists of two operational amplifiers (OPA445), four resistors (R_1–R_4), and a capacitor (C). The inductance of the synthetic inductor is calculated as, $L = R_1R_3R_4C/R_2$. One can see that by simply adjusting one of the circuit parameters the inductance can be tuned. In the experiment, we use a trimmer to tune the resistor, R_1, while keeping other parameters fixed. In practical application, this trimmer could be replaced with a digital resistor programmed by a control system to realize perfect absorption at the required frequency.

To test the absorption performance of the fabricated LR-shunted absorber, we carry out the experiments with the setup as demonstrated in Figure 2B. An additional piezoelectric patch attached at 0.5 m away from the right free end of the host beam functions as an actuator to generate incident waves. This distance could effectively reduce the evanescent waves generated by the actuator without affecting the measurement results. A sine-signal sweeping from 1.0 kHz to 2.5 kHz generated from a function generator is fed to the actuator *via* a power amplifier. An artificial absorbing layer made with high damping materials is carefully placed on the surface of the left end of the host beam to suppress the reflected waves from that boundary. A laser vibrometer is used to scan the pointwise velocity responses of the host beam in the highlighted orange region with 21 points and a point distance of 5 mm [27]. The measured responses are processed to calculate the wave reflection (r) and absorption ($\alpha = 1 - r$) coefficients.

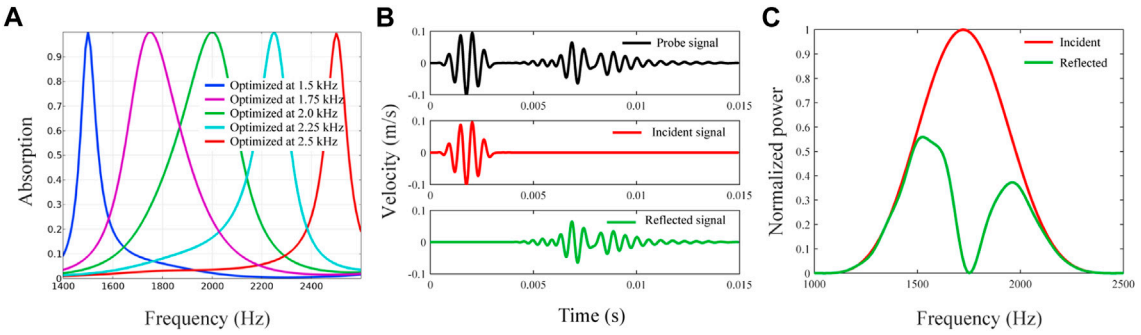

FIGURE 3
Numerical simulation results for the tunable perfect flexural wave absorber. **(A)** Illustration of perfect flexural wave absorption tuned to different frequencies. **(B)** Time domain simulation for perfect absorption at 1.75 kHz. **(C)** Normalized powers of the incident and reflected signals.

3 Results

3.1 Simulation results

3.1.1 Frequency domain simulation

To demonstrate the robustness of our tunable absorber to achieve perfect absorption at multiple frequencies, we optimize the circuit parameters, L and R, at each interested frequency. In the optimization, the Nelder-Mead method [35] is used by minimizing the wave reflection coefficient, r, as the objective function with two optimization variables, L and R. Perfect absorption peaks could be achieved from 1.5 kHz to 2.5 kHz. Here, we only plot the absorption spectra optimized at 1.5 kHz–2.5 kHz with an increment of 0.25 kHz, as illustrated in Figure 3A. Still, one could understand that perfect absorption could be achieved at other frequencies in this range, as well, by optimizing the circuit parameters. Optimized circuit parameters are listed in Supplementary Table S1. One can see that as the electrical resonances increase by decreasing the inductor values the peaks of the absorption spectra are shifted to higher frequencies.

The simulated absorption spectra clearly show that perfect absorption could be achieved from a broadband frequency range. Note that in the simulation no damping is added to the mechanical resonator and the perfect absorption is mainly due to the strong interaction between the mechanical and electrical resonances as well as the destructive interference due to the terminal end of the host beam. Also, we notice that when the electrical and mechanical resonances are strongly coupled the absorption spectra (purple and green lines) are wider, whereas as the electric resonance is shifted away from the mechanical resonance the absorption spectra (blue and red lines) are much narrower. Here, the mechanical resonance is at about 2.0 kHz. Nevertheless, perfect absorption can be achieved at various frequencies by tuning the circuit parameters along, which demonstrates the robustness of our proposed tunable perfect absorber.

3.1.2 Transient simulation

To further show the effectiveness of our proposed absorber in flexural wave mitigation, transient analysis is performed. In the simulation, we choose the target frequency at 1.75 kHz for perfect absorption by adopting the circuit parameters listed in Supplementary Table S2. A 5-peak tone-burst signal centered at f_c = 1.75 kHz is excited at the host beam. A displacement probe is placed on the host beam to capture the out-of-plane response. The position of the probe is chosen at 1 m away from the shunted resonator so that the incident and reflected signals can be separated from each other in the time domain. The recorded signal is shown in the top panel of Figure 3B, which contains two main wave packets, the incident response from the incident waves (middle panel of Figure 3B) and the reflected response corresponding to the reflected waves (bottom panel of Figure 3B). The overall amplitude of the reflected signal is largely reduced and the largest amplitude reduction is observed near the center of the reflected wave packet, which is corresponding to the perfect absorption frequency. To further verify this, we calculate the reflected and incident powers normalized to the maximum power of the incident wave, as illustrated in Figure 3C. We can see that almost zero reflected energy is found located near the optimized frequency, f = 1.75 kHz, in the power spectra, thanks to the perfect absorption from the LR-shunted resonator.

3.2 Experimental results

Next, we carry out our experiment to characterize the absorption performance of this proposed tunable absorber. Before we evaluate the shunting circuit performance, we first test the absorption performance with an open circuit.

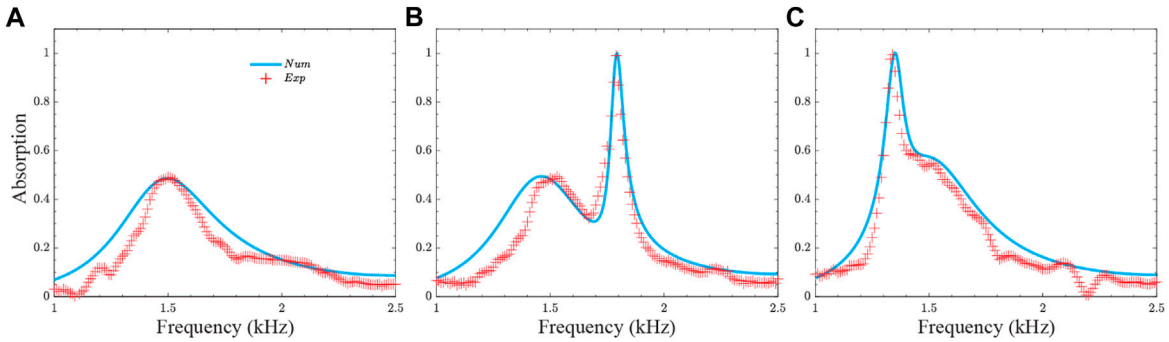

FIGURE 4
Experimentally measured absorption spectra (read plus symbols) compared to numerical simulations (blue solid lines). The absorption spectra with **(A)** an open circuit and an LR-shunted circuit with **(B)** L =5.8 H and R =1.0 kΩ **(C)** L =9.7 H and R =2.9 kΩ.

3.2.1 Open circuit performance

Due to the intrinsic loss in the fabricated resonator, the mechanical resonator with an open circuit might be able to dissipate part of the incident energy. Therefore, before evaluating the absorption performance, we perform a vibration test from Frequency Response Function (FRF) by exciting the fabricated mechanical resonator alone on a shaker. The loss factor is characterized as $\eta = 0.057$ from a half-power bandwidth method [27]. To quantify the absorption due to this passive damping from the resonator, the measured absorption coefficient is illustrated by red plus symbols in Figure 4A. Peak absorption of about 50% can be observed in the experiment at around 1.5 kHz. To further validate our experimental results, a 3-D numerical model is built by adopting the same loss factor measured from the experiment for the resonator. In this simulation, a 0.1 mm thin layer is also added between the supporting cube and the beam strip to consider the effect of the supper glue with material properties being Young's modulus $E = 1.1$ GPa, Poisson's ratio $\nu = 0.35$, and mass density $\rho = 1050\ \mathrm{kg/m^3}$. A solid blue line denotes the simulated absorption spectrum shown in Figure 4A. The experimentally measured absorption spectrum matches well with the simulated spectrum.

3.2.2 LR-shunted circuit performance

Our proposed tunable flexural wave perfect absorber is experimentally tested for its performance. For illustration purposes, we show two perfect absorption spectra in Figures 4B, C, respectively. Two absorption peaks can be observed in both of the absorption spectra. The peak at around 1.5 kHz with a wider bandwidth but a lower absorption coefficient is due to the intrinsic mechanical damping, which has a similar shape as the open circuit case. However, the second peak at about 1.8 kHz (1.32 kHz for Figure 4C) induced by the coupling between the mechanical and electrical resonances can almost reach to unit absorption. Interestingly, by varying the electrical resonance, i.e., re-programming the circuit inductance and resistance, the unit absorption peaks can be tuned to different frequencies, which can make our proposed absorber much more robust for overcoming some uncertainties in a time-varying environment. For example, by adjusting the inductance from $L = 5.8$ H to $L = 9.7$ H, and the resistance from $R = 1$ kΩ to $R = 2.9$ kΩ, the absorption peak is tuned from 1.8 kHz to 1.32 kHz. The absorption performance of the tunable absorber is compared with numerical simulations. A very good agreement can be found, as well. The tunable perfect absorber can achieve almost perfect absorption in a broad frequency range, from 1.5 kHz to 2.5 kHz, and more than 99.8% absorption is experimentally obtained at various frequencies.

4 Discussion

Negative capacitance shunting circuits have been demonstrated in acoustic and elastic metamaterials for broadband damping performance [36–38]. Here, we use a simple negative capacitor ($C_{NC} = -C$) connected with a resistor (R') in series hybrid with an LR-shunted (NC-LR) circuit to investigate broadband absorption performance through numerical simulation. Figure 5A shows the schematic of the design of enhanced absorption with the hybrid shunting circuit. In the simulation, we optimize the inductor value (L) and two resistor values (R and R'), while keeping the value of the negative capacitor as $\beta = C_{NC}/C_p = -0.8$, where C_p is the capacitance of the piezoelectric patch. A color map of the absorption spectra optimized from 1.5 kHz to 2.5 kHz with a step of 0.1 kHz is shown in Figure 5B. Due to the presence of the negative capacitor, broadband absorption can be observed. The negative capacitor functions as broadband shunted damping to

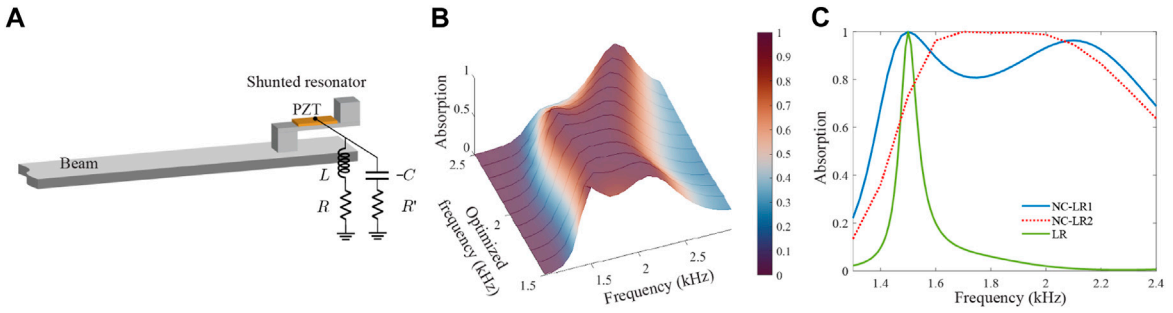

FIGURE 5
Enhanced flexural wave absorption with a hybrid shunting circuit. **(A)** Schematic of the enhanced flexural wave absorption with an NC-LR shunted circuit. **(B)** Color map of the absorption spectra optimized from 1.5 kHz to 2.5 kHz. **(C)** Comparison of the absorption spectra with the NC-LR shunted circuit to the LR shunted circuit.

the mechanical resonator. Due to the compensation of the damping from the negative capacitor to the mechanical resonator, the absorption spectrum originating from the mechanical resonator starts to approach to the unit absorption. Note that by using a negative capacitor one can achieve perfect absorption as well, but the absorption spectrum is equivalent to a damped mechanical resonator showing a single absorption peak. Here, in order to show the advantage of the NC-LR shunted circuit, we combine the NC circuit with the LR-shunted circuit so that the absorption peaks are merged together to form a broadband absorption spectrum as the electrical resonance is close to the mechanical resonance. To better illustrate the effect of the hybrid circuit, two of the optimization results optimized at 1.5 kHz (blue solid line) and 1.7 kHz (red dotted line), respectively, are shown in Figure 5C compared with the absorption spectrum from an LR-shunted circuit alone (green solid line). The absorption spectrum is largely enhanced to a broad frequency range. Two absorption peaks can be seen in the case with NC-LR1, whereas the two peaks are merged into a single broadband peak by properly choosing the optimization parameters. The circuit parameters for the NC-LR1 and NC-LR2 circuits used in the simulations are provided in the Supplementary Material.

5 Conclusion

We have designed and experimentally demonstrated a tunable absorber for perfect flexural wave absorption at a broad frequency range. The tunable absorber is composed of a mechanical resonator with a bonded piezoelectric patch and a shunted circuit. The critical coupling conditions are fulfilled through the shunted circuit damping at various frequencies by varying the circuit parameters. Therefore, unit absorption peaks are achieved at a broad frequency range, which is validated through numerical simulations and experiments. In the end, we numerically demonstrate an enhanced absorption spectrum with a hybrid NC-LR circuit for broadband absorption. Thanks to the flexible tunability and enhanced low-frequency performance, the proposed tunable absorber could set forth the basis of a markedly distinct approach toward perfect absorbers of subwavelength wave and elastic wave cloaking.

Data availability statement

The raw data supporting the conclusion of this article will be made available by the authors, without undue reservation.

Author contributions

XL: conceptualization, methodology, software, investigation, writing–original draft, writing–review and editing. ZY: conceptualization, investigation, validation, writing–review and editing. TL: conceptualization, investigation, validation, writing–review and editing. All authors contributed to manuscript revision, read, and approved the submitted version.

Conflict of interest

Authors XL, ZY and TL were employed by company Toyota Motor North America.

Publisher's note

All claims expressed in this article are solely those of the authors and do not necessarily represent those of their

affiliated organizations, or those of the publisher, the editors and the reviewers. Any product that may be evaluated in this article, or claim that may be made by its manufacturer, is not guaranteed or endorsed by the publisher.

Supplementary material

The Supplementary Material for this article can be found online at: https://www.frontiersin.org/articles/10.3389/fphy.2022.1054634/full#supplementary-material

References

1. Liu Z, Zhang X, Mao Y, Zhu Y, Yang Z, Chan CT, et al. Locally resonant sonic materials. *science* (2000) 289:1734–6. doi:10.1126/science.289.5485.1734

2. Kadic M, Milton GW, van Hecke M, Wegener M. 3D metamaterials. *Nat Rev Phys* (2019) 1:198–210. doi:10.1038/s42254-018-0018-y

3. Bertoldi K, Vitelli V, Christensen J, Van Hecke M. Flexible mechanical metamaterials. *Nat Rev Mater* (2017) 2:17066–11. doi:10.1038/natrevmats.2017.66

4. Wu Y, Lai Y, Zhang ZQ. Elastic metamaterials with simultaneously negative effective shear modulus and mass density. *Phys Rev Lett* (2011) 107:105506. doi:10.1103/physrevlett.107.105506

5. Huang H, Sun C, Huang G. On the negative effective mass density in acoustic metamaterials. *Int J Eng Sci* (2009) 47:610–7. doi:10.1016/j.ijengsci.2008.12.007

6. Liu XN, Hu GK, Huang GL, Sun CT. An elastic metamaterial with simultaneously negative mass density and bulk modulus. *Appl Phys Lett* (2011) 98:251907. doi:10.1063/1.3597651

7. Zhu R, Liu X, Hu G, Sun C, Huang G. Negative refraction of elastic waves at the deep-subwavelength scale in a single-phase metamaterial. *Nat Commun* (2014) 5:5510–8. doi:10.1038/ncomms6510

8. Yan X, Zhu R, Huang G, Yuan FG. Focusing guided waves using surface bonded elastic metamaterials. *Appl Phys Lett* (2013) 103:121901. doi:10.1063/1.4821258

9. Chen Y, Huang G. Active elastic metamaterials for subwavelength wave propagation control. *Acta Mech Sin* (2015) 31:349–63. doi:10.1007/s10409-015-0402-0

10. Mousavi SH, Khanikaev AB, Wang Z. Topologically protected elastic waves in phononic metamaterials. *Nat Commun* (2015) 6:8682–7. doi:10.1038/ncomms9682

11. Cha J, Kim KW, Daraio C. Experimental realization of on-chip topological nanoelectromechanical metamaterials. *Nature* (2018) 564:229–33. doi:10.1038/s41586-018-0764-0

12. Chen H, Nassar H, Huang G. A study of topological effects in 1d and 2d mechanical lattices. *J Mech Phys Sol* (2018) 117:22–36. doi:10.1016/j.jmps.2018.04.013

13. Huang H, Sun C. Wave attenuation mechanism in an acoustic metamaterial with negative effective mass density. *New J Phys* (2009) 11:013003. doi:10.1088/1367-2630/11/1/013003

14. Assouar B, Liang B, Wu Y, Li Y, Cheng JC, Jing Y. Acoustic metasurfaces. *Nat Rev Mater* (2018) 3:460–72. doi:10.1038/s41578-018-0061-4

15. Zhu H, Semperlotti F. Anomalous refraction of acoustic guided waves in solids with geometrically tapered metasurfaces. *Phys Rev Lett* (2016) 117:034302. doi:10.1103/physrevlett.117.034302

16. Chen Y, Li X, Nassar H, Hu G, Huang G. A programmable metasurface for real time control of broadband elastic rays. *Smart Mater Struct* (2018) 27:115011. doi:10.1088/1361-665x/aae27b

17. Zhu H, Patnaik S, Walsh TF, Jared BH, Semperlotti F. Nonlocal elastic metasurfaces: Enabling broadband wave control via intentional nonlocality. *Proc Natl Acad Sci U S A* (2020) 117:26099–108. doi:10.1073/pnas.2004753117

18. Li X, Chen Y, Zhu R, Huang G. An active meta-layer for optimal flexural wave absorption and cloaking. *Mech Syst Signal Process* (2021) 149:107324. doi:10.1016/j.ymssp.2020.107324

19. Li X, Chen Y, Zhang X, Huang G. Shaping elastic wave mode conversion with a piezoelectric-based programmable meta-boundary. *Extreme Mech Lett* (2020) 39:100837. doi:10.1016/j.eml.2020.100837

20. Zhang C, Hu X. Three-dimensional single-port labyrinthine acoustic metamaterial: Perfect absorption with large bandwidth and tunability. *Phys Rev Appl* (2016) 6:064025. doi:10.1103/physrevapplied.6.064025

21. Wei P, Croënne C, Tak Chu S, Li J. Symmetrical and anti-symmetrical coherent perfect absorption for acoustic waves. *Appl Phys Lett* (2014) 104:121902. doi:10.1063/1.4869462

22. Long H, Shao C, Liu C, Cheng Y, Liu X. Broadband near-perfect absorption of low-frequency sound by subwavelength metasurface. *Appl Phys Lett* (2019) 115:103503. doi:10.1063/1.5109826

23. Lee T, Nomura T, Dede EM, Iizuka H. Asymmetric loss-induced perfect sound absorption in duct silencers. *Appl Phys Lett* (2020) 116:214101. doi:10.1063/5.0009631

24. Lee T, Iizuka H. Heavily overdamped resonance structurally engineered in a grating metasurface for ultra-broadband acoustic absorption. *Appl Phys Lett* (2018) 113:101903. doi:10.1063/1.5047798

25. Huang S, Fang X, Wang X, Assouar B, Cheng Q, Li Y. Acoustic perfect absorbers via spiral metasurfaces with embedded apertures. *Appl Phys Lett* (2018) 113:233501. doi:10.1063/1.5063289

26. Leng J, Gautier F, Pelat A, Picó R, Groby JP, Romero-Garcia V. Limits of flexural wave absorption by open lossy resonators: Reflection and transmission problems. *New J Phys* (2019) 21:053003. doi:10.1088/1367-2630/ab1761

27. Li X, Yu Z, Iizuka H, Lee T. Experimental demonstration of extremely asymmetric flexural wave absorption at the exceptional point. *Extreme Mech Lett* (2022) 52:101649. doi:10.1016/j.eml.2022.101649

28. Cao L, Yang Z, Xu Y, Fan SW, Zhu Y, Chen Z, et al. Flexural wave absorption by lossy gradient elastic metasurface. *J Mech Phys Sol* (2020) 143:104052. doi:10.1016/j.jmps.2020.104052

29. Chen Y, Li X, Hu G, Haberman MR, Huang G. An active mechanical willis meta-layer with asymmetric polarizabilities. *Nat Commun* (2020) 11:3681–8. doi:10.1038/s41467-020-17529-2

30. Leng J, Romero-García V, Pelat A, Pico R, Groby JP, Gautier F. Interpretation of the acoustic black hole effect based on the concept of critical coupling. *J Sound Vibration* (2020) 471:115199. doi:10.1016/j.jsv.2020.115199

31. Piper JR, Fan S. Total absorption in a graphene monolayer in the optical regime by critical coupling with a photonic crystal guided resonance. *Acs Photon* (2014) 1:347–53. doi:10.1021/ph400090p

32. Norris AN, Packo P. Non-symmetric flexural wave scattering and one-way extreme absorption. *The J Acoust Soc America* (2019) 146:873–83. doi:10.1121/1.5087133

33. Raybaud G, Ouisse M, Leng J, Pelat A, Groby JP, Romero-García V, et al. Control of bending wave reflection at beam terminations by thermally tunable subwavelength resonators. *J Sound Vibration* (2022) 530:116918. doi:10.1016/j.jsv.2022.116918

34. Forward RL. Electronic damping of vibrations in optical structures. *Appl Opt* (1979) 18:690–7. doi:10.1364/ao.18.000690

35. Conn AR, Scheinberg K, Vicente LN. *Introduction to derivative-free optimization*. Thailand: SIAM (2009).

36. Fukada E, Date M, Kimura K, Okubo T, Kodama H, Mokry P, et al. Sound isolation by piezoelectric polymer films connected to negative capacitance circuits. *IEEE Trans Dielectr Electr Insul* (2004) 11:328–33. doi:10.1109/tdei.2004.1285904

37. Beck BS, Cunefare KA, Collet M. The power output and efficiency of a negative capacitance shunt for vibration control of a flexural system. *Smart Mater Struct* (2013) 22:065009. doi:10.1088/0964-1726/22/6/065009

38. Beck B, Cunefare KA, Ruzzene M. Broadband vibration suppression assessment of negative impedance shunts. *Smart Mater Adaptive Structures Intell Syst* (2008) 43314:491–500.

frontiers | Frontiers in Physics

TYPE Mini Review
PUBLISHED 15 December 2022
DOI 10.3389/fphy.2022.1068833

OPEN ACCESS

EDITED BY
Han Zhang,
Institute of Acoustics (CAS), China

REVIEWED BY
Chen Shen,
Rowan University, United States

*CORRESPONDENCE
Ning Hu,
hooning@hdu.edu.cn
Jiabao Zhao,
212040208@hdu.edu.cn
Maofa Wang,
wangmfl600@163.com
Fanzong Zeng,
202243010060@hdu.edu.cn
Huajie Dai,
qinlongcrcc@foxmail.com
Yongju Zheng,
joany0204@163.com

SPECIALTY SECTION
This article was submitted to Physical Acoustics and Ultrasonics, a section of the journal Frontiers in Physics

RECEIVED 13 October 2022
ACCEPTED 29 November 2022
PUBLISHED 15 December 2022

CITATION
Zhu Z, Hu N, Wu J, Li W, Zhao J, Wang M, Zeng F, Dai H and Zheng Y (2022), A review of underwater acoustic metamaterials for underwater acoustic equipment.
Front. Phys. 10:1068833.
doi: 10.3389/fphy.2022.1068833

A review of underwater acoustic metamaterials for underwater acoustic equipment

Zhenjing Zhu[1,2], Ning Hu[1,2]*, Junyi Wu[3], Wenxin Li[1,2], Jiabao Zhao[2,4]*, Maofa Wang[1,2,4]*, Fanzong Zeng[1,2]*, Huajie Dai[1,2]* and Yongju Zheng[1,2]*

[1]School of Mechanical Engineering, Hangzhou Dianzi University, Hangzhou, China, [2]Marine Technology and Equipment Research Center, Hangzhou Dianzi University, Hangzhou, China, [3]Sanmen Sanyou Technology Inc, Taizhou, China, [4]School of Electronic Information, Hangzhou Dianzi University, Hangzhou, China

Researchers use underwater acoustic equipment to explore the unknown ocean environment, which is one of the important means to understand and utilize the ocean. For underwater acoustic equipment, the application of underwater acoustic metamaterials is the premise to ensure and improve the performance of underwater acoustic communication, acoustic stealth, and sonar detection. Due to the limitations of mass density law and high hydrostatic pressure, traditional underwater acoustic materials cannot effectively absorb low-frequency sound waves and have low efficiency of elastic energy conversion. The sound absorption effect is poor under low frequency and high hydrostatic pressure. In recent years, with the development of acoustic metamaterials technology, all kinds of underwater acoustic metamaterials have also been proposed. Compared with sound waves propagating in the air, underwater sound is more difficult to control than air sound with the same frequency, so the design of underwater acoustic metamaterials is more complicated. This paper reviews the basic characteristics, development history of sound absorption, sound insulation decoupling, and underwater acoustic guided metamaterials, then the existing problems and the future development direction of underwater acoustic metamaterials are discussed.

KEYWORDS

absorption materials, metamaterials, underwater acoustic equipment, sound absorption, sound isolation

1 Introduction

For human beings, the ocean is a natural treasure house, which contains abundant natural resources. The marine ecosystem is closely related to human daily life [1, 2]. At present, human knowledge of the ocean is far less than that of the land. With the rapid development of underwater acoustic equipment (UAE) and underwater detection technology, higher requirements are put forward for acoustic performance of underwater target detection equipment, sea area information collection equipment

and underwater military equipment (UME) [3]. Therefore, the application of underwater acoustic metamaterials is the key to improve the performance index of UAE.

The performance indexes of UAE mainly include underwater acoustic detection and acoustic stealth. As UAE is often used in various sea conditions, it will inevitably produce some subtle irregular vibrations, which will lead to near field self noise [4], resulting in the degradation of underwater acoustic detection performance of the equipment. In addition, more and more UME began to pursue "stealth" characteristics to reduce the probability of being discovered by enemy sonar. To solve these problems, in recent years, scholars have been studying underwater acoustic materials [5–8], aiming at reducing self-noise interference, improving their underwater acoustic communication and sonar detection performance, and countering active and passive sonar detection.

There are many classification methods of underwater acoustic materials, which can be divided into coating type and structural underwater acoustic materials according to the different molding process and bearing capacity. According to the frequency characteristics of the incident wave or its special structure, it can be divided into low, medium and high frequency underwater acoustic materials and porous and resonant underwater acoustic materials. According to the specific functions to be realized, underwater acoustic materials can be divided into sound absorption type, sound insulation type, decoupling type and reflect sound type.

Underwater acoustic materials include a wide range, which can be natural materials in nature, or metamaterials designed artificially according to task requirements or working frequency band. Among them, traditional underwater acoustic materials mainly include polymer materials, porous materials, filler materials, cavity resonant materials and impedance gradient materials [9, 10].

In 1990s, Sigalas and Economou proposed the concept of an artificial material/structure with elastic band gap mass density and periodic distribution of elastic constant, that is, phononic crystal. In the early stage when the concept of phononic crystal was put forward, scholars focused on the generation and modulation mechanism of band gap. The formation of phononic crystal band gap is mainly based on Bragg scattering mechanism. To control low-frequency waves, a large cell size is needed, which limits the engineering application of phononic crystals to a certain extent. In 2000, Liu et al. of Hong Kong University of Science and Technology found that the material had a low frequency band gap far lower than the Bragg band gap frequency by periodically arranging the local resonance unit composed of rubber coated shot in the elastic medium, and attributed the reason of this band gap to the resonance effect, so the concept of local resonance phononic crystal was put forward. At the same time, in the field of electromagnetism, researchers have designed "double negative materials" whose dielectric constant and permeability are negative at the same time, and called this kind of materials metamaterials. In 2004, Li and Chan of Hong Kong University of Science and Technology discovered that their designed composite artificial structure also showed "double negative" acoustic characteristics, so they proposed the concept of acoustic metamaterial by analogy with electromagnetic metamaterial. The development of acoustic metamaterials is shown in Figure 1.

Underwater acoustic metamaterial is also an artificial periodic structure [11] with microstructure as its basic building unit. This kind of structure can suppress waves in certain frequency ranges, which is called the so-called propagation "band gap" phenomenon. The frequency range of band gap can be adjusted by changing the configuration and spatial distribution of metamaterial microstructure units. This feature can be used to improve the signal to noise ratio of sonar system and reduce the near field self noise [12].

On the basis of acoustic metamaterials, underwater acoustic metamaterials transfer the research object from air to underwater, and the sound wave changes from air sound to underwater sound. Underwater acoustic metamaterials for underwater acoustic equipment are mainly divided into three categories according to different functions: (1) Sound absorption metamaterials (SAM): The absorption of sound waves is achieved by small surface reflection and high loss factor. It is mainly used to absorb near field self noise generated by the equipment body and active sonar detection sound waves. (2) Sound insulation decoupling metamaterials (SIDM): Through the impedance mismatch between the structure and the water, the self-noise caused by the vibration of the internal structure is blocked from transmitting into the water. (3) Underwater acoustic guided metamaterials (UAGM): Stealth is achieved by directing sound waves to travel along a specific path and thus changing their reflection path. The functional schematic diagram of three different types of underwater acoustic metamaterials is shown in Figure 2. In this paper, the basic characteristics, development history and future development direction of these three kinds of metamaterials are summarized, in order to point out the direction for the follow up researchers.

This paper is organized as follows. *Introduction* introduces the SAM. *Introduction* introduces the SIDM. *Introduction* introduces the UAGM. *Introduction* summarizes and discusses the future development direction of underwater sound absorption metamaterials.

2 Sound absorption metamaterials

Rubber polymer is usually used as the traditional acoustic absorbing material (TSAM), which is designed according to the two basic principles of impedance matching and damping dissipation [13, 14]. However, for the traditional sound absorbing materials, the reflection coefficient of the material

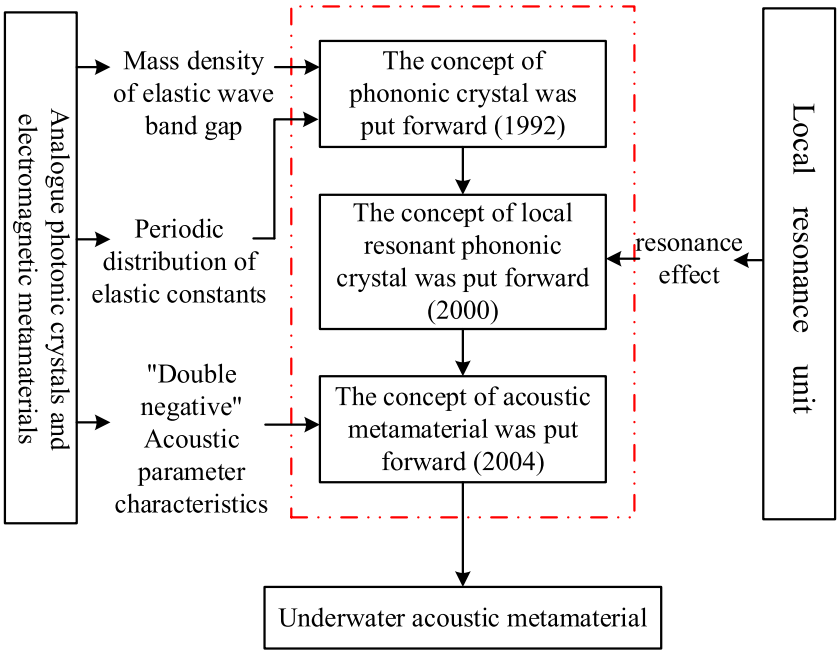

FIGURE 1
Sketch of development history of acoustic metamaterials.

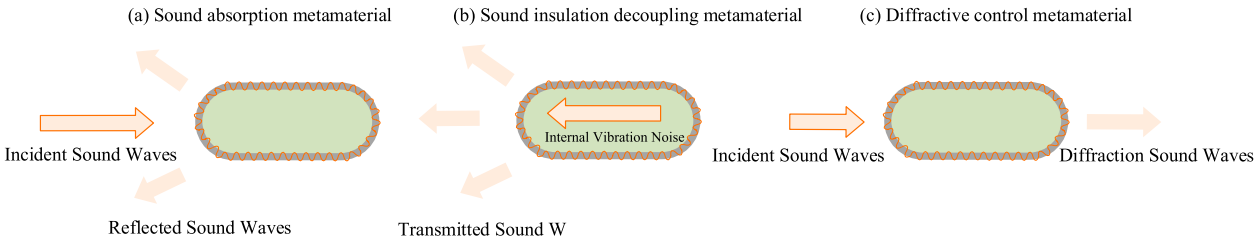

FIGURE 2
Schematic diagram of regulation function of three kinds of underwater acoustic metamaterials.

surface is proportional to its loss factor, that is, there is a contradiction between the impedance matching requirement of the material and the high loss. Therefore, in order to promote acoustic damping dissipation, the internal acoustic structure of traditional materials needs to be changed. At present, the commonly used methods to change the acoustic structure of materials are the pore cavity resonance method, particle filling method, sandwich composite method, *etc.* At the same time, the TSAM also faces the two major problems of poor low frequency sound absorption capacity and poor sound absorption capacity under hydrostatic pressure.

Therefore, the development and design of low frequency (below 2 kHz), broadband, water pressure resistant SAM are the main challenges currently faced.

According to different sound absorption mechanisms, SAM can be divided into local resonance metamaterials (LRM) and non-resonance metamaterials (NRM).

In 2006, Zhao [15, 16] et al. introduced the local resonance theory into the design of sound-absorbing metamaterials for the first time, and systematically studied the absorption characteristics caused by local resonance. By filling the metal core covered by soft rubber layer in viscoelastic polymer as the local resonator, the underwater acoustic absorption effect at the local resonance frequency was verified. The cross section of metal steel ball array coated in viscoelastic polymer matrix is shown in Figure 3.

The experimental results show that the designed local resonance metamaterial has low-frequency underwater sound

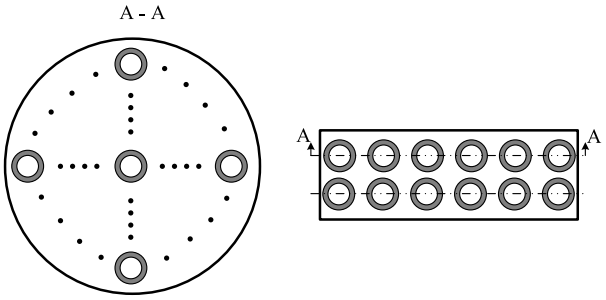

FIGURE 3
Cross sections of the array of coated steel spheres embedded in a viscoelastic polymer matrix.

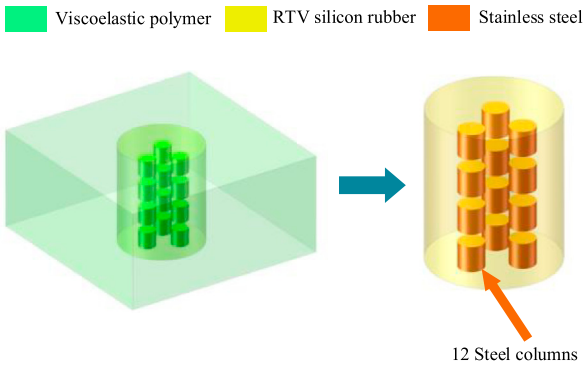

FIGURE 4
Schematic diagram of SAM with multiple resonance units.

absorption characteristics, and the underwater sound absorption effect at the local resonance frequency is obvious. Although the LRM has good sound absorption effect in low frequency band, the effective frequency range of sound absorption performance is relatively narrow. Therefore, Zhao, Wen et al. [17–20] further investigated the problem that the band gap width of LRM is too narrow by using finite element method and multiple scattering method. The results show that metamaterials with different local resonance frequencies can be superimposed to improve the sound absorption effect of metamaterials at low frequencies. Shi et al. [21] similarly designed a multilayer composite local resonance metamaterial, which widened or generated multiple band gaps by embedding multilayer local resonance couplings inside the matrix.

As shown in Figure 4, in order to explore the influence of coupling of multiple resonance units on sound absorption, Gu [22] et al. designed a sound-absorbing metamaterial with 12 resonance units in each basic unit. Under the action of this specific structure and multiple scattering, this material can absorb broadband low-frequency underwater sound in the frequency range of 600–2000 Hz and the high hydrostatic pressure of 0.5Mpa.

Zhong et al. [23] develops an underwater acoustic metamaterial plate with potential advantages of low-frequency broadband sound absorption and high hydrostatic pressure resistance. The proposed metamaterial is composed of particle-filled polyurethane damping materials and a square lattice of spiral resonators. The formation mechanisms of the locally resonant band gaps are investigated based on the modal analysis of plate modes and local resonances. Results show that In the frequency domain (0.8 kHz, 6 kHz), the average sound absorption coefficient of the proposed metamaterial plate under normal atmospheric pressure is 0.54. Furthermore, the sound absorption coefficient of the proposed structure is experimentally studied under different hydrostatic pressure conditions. Specifically, the proposed metamaterial structure achieves average sound absorption coefficient of 0.51 in the frequency range (1.5 kHz, 6 kHz) under 0.5 MPa.

At present, due to the limitation of the inherent characteristics of the local resonance theory, the sound absorption frequency band is narrow, and the sound absorption capacity needs to be improved in underwater use scenes. How to enhance the sound absorption band of metamaterials by using the multiple scattering effect generated by resonant coupling elements is a key issue in this field in the future.

NRM mainly includes porous foam metamaterials, gradient index metamaterials and other new sound absorption metamaterials.

A recent publication on broadband underwater metamaterial, Qu et al [24]. Present a novel metamaterial absorber with structured impedance-matched composite, which can realized an underwater acoustic absorber exhibiting high absorption from 4 to 20 kHz. And the structured composite represents a new type of acoustic metamaterials that has high acoustic energy density and promises broad underwater applications.

Xu et al. [25, 26] designed an open-cell SiC foam to solve the impedance mismatch problem of the existing underwater porous foam at low frequency. The experiment shows that the underwater sound absorption performance of the material can be improved by filling the holes with silicone oil, and the sound absorption coefficient is close to one in 750–4000 Hz. When the holes are filled with water, the sound absorption performance of the material can also be enhanced. However, it is worth noting that this material needs to rely on the rigid backing behind it. Wang et al. [27] developed a kind of gradient exponential metamaterial with acoustic black hole effect based on multiple scattering theory. The simulation results show that the metamaterial has an omnidirectional sound absorption effect in underwater broadband, which provides a new idea for the design of underwater acoustic coating.

In addition, Yuan et al. [14] proposed a kind of NRM based on the composite of graphene microchip and rubber material. The experimental results show that this material can enhance the absorption effect of 2–30 Hz underwater sound. Gao and Zhang et al. [28] put forward a kind of NRM with a spiral metal ring embedded in the viscoelastic layer. Results show that this metastructure can achieve the low frequency and broadband acoustic absorption below 1,000 Hz.

3 Sound insulation decoupling metamaterials

SIMD are mainly used to reduce the near-field self-noise caused by flow-induced vibration, so as to improve the sound detection and stealth performance of equipment.

At present, SIDM is mainly faced with two problems. First, if the soft rubber material is applied directly to the surface of the underwater acoustic equipment, the impedance mismatch can be formed. In this case, the structure of the device will become heavy and not conducive to use. Second, most of SIDMs are structural forms with embedded cavities, and the cavity volume is directly proportional to the impedance mismatch effect [3] and inversely proportional to the material pressure resistance [29]. The relationship between the two is difficult to balance. Therefore, how to improve the sound absorption performance while ensuring the pressure resistance of materials is the research focus of SIDM at present.

Previously, some researchers [30, 31] have studied the decoupling mechanism of traditional porous metamaterials and pointed out that its sound absorption mainly comes from the vibration isolation of the decoupling layer. Porous metamaterials has light weight and effective medium and high frequency decoupling ability, but its low frequency vibration suppression and isolation ability is still very weak, so it is difficult to play a decoupling role. Huang et al. [32] designed a complex axisymmetric pass based on the traditional cylindrical and conical pass and established an equivalent fluid model for simulation analysis. The simulation results show that the complex axisymmetric pass has better decoupling performance than the traditional pass.

Due to the design characteristics of a single local resonance unit, the sound insulation metamaterial also has the problem of the narrow sound insulation frequency band. However, the researchers found that the local resonators are also suitable for SIDM. In 2016, Huang et al. [33] introduced single-degree-of-freedom periodic local resonators into SIDM for the first time and established a computational model for local resonant scatterers based on effective medium theory and elastic dynamics theory. It is demonstrated that the effective density of the acoustic metamaterial decoupling layer has a great influence on the mechanical impedance of the system, and the low frequency noise reduction near the local resonance frequency is more obvious. Yang et al. [8] designed a kind of SIDM for UAE, which broadened the sound absorption band of metamaterials by coupling the local resonance and Bragg sound insulation band.

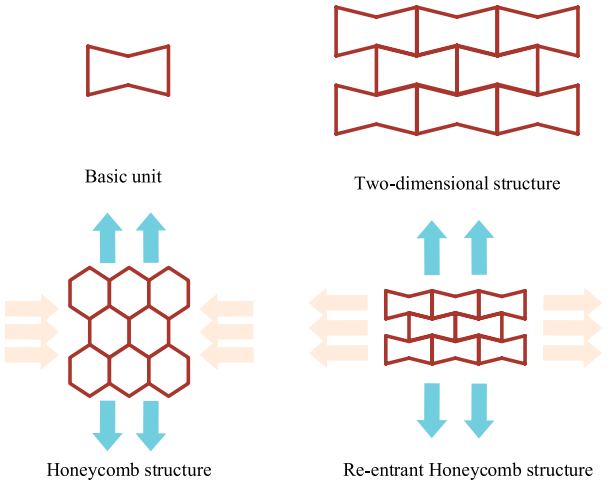

FIGURE 5
Schematic diagram of negative Poisson's ratio metamaterial.

Zhong et al. [34] proposes a new type of composite underwater honeycomb-type acoustic metamaterial (AM) plate with the advantages of low-frequency broadband sound insulation and high hydrostatic pressure resistance. The underwater sound insulation performance and mechanisms of the new type of AM were investigated numerically and experimentally. The results show that the honeycomb-type AM has good underwater sound insulation performance at low frequencies and the proposed AM structure can still achieve an average sound transmission loss of 10 dB in the frequency range (2kHz, 10 kHz) under the hydrostatic pressure of 3 Mpa.

The chiral structure is a kind of porous structure with high shear stiffness, negative Poisson's ratio and negative equivalent mass density. Wang et al. [35] studied the suppression effect of different frequency regions on acoustic radiation noise by adding a metal core local harmonic oscillator to chiral structural materials. The results show that not only chiral materials can also be used in SIDM, but also the coupling relationship between the local harmonic oscillator and chiral structure can inhibit the vibration of materials. Spadoni and Ruzzene et al. [36, 37] have analyzed the sound radiation characteristics of chiral beams, and the results show that chiral structures have an important influence on the vibration and sound isolation of beams. Zhu et al. [38] designed three groups of control tests (solid coating, chiral metamaterial coating and chiral coating filled with polystyrene foam) to verify the influence of different materials on the sound insulation effect of chiral metamaterials. The

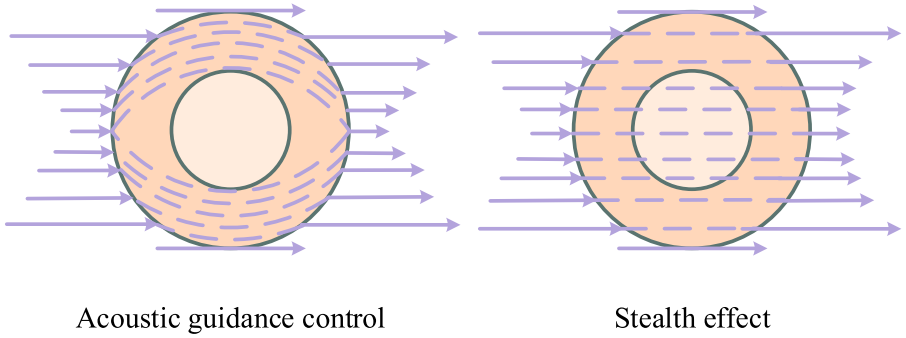

FIGURE 6
Acoustic guidance model of invisibility cloak.

experimental results show that polystyrene foam is helpful to enhance the sound insulation effect of chiral metamaterials.

In addition, mechanical metamaterials with negative Poisson's ratio are also widely used in the field of sound insulation and decoupling. The negative Poisson's ratio property means that when a material is axially compressed, it will contract longitudinally, and when it is axially stretched, it will expand longitudinally. When the transverse strain of the material is equal to the longitudinal strain, the Poisson's ratio is -1. Its basic unit body, tension and compression schematic are shown in Figure 5. Zhang et al. [39] designed a honeycomb vibration isolator for ships by using the characteristic of negative Poisson's ratio. The metamaterial has a good vibration isolation effect below 50 Hz.

4 Underwater acoustic guided metamaterials

In recent years, with the increasingly wide application of UAE, not only the requirements for detection and communication accuracy are getting higher and higher, but also how to realize "stealth" detection has gradually become a research hotspot. Underwater acoustic control based on the principle of sound absorption and sound insulation will inevitably leave a "sound shadow area", which is difficult to resist multi-directional stereo detection technologies such as multi-base sonar detection. Through the structural design of metamaterials, guiding sound waves to propagate along a specific path is the basic idea to realize stealth function.

In 2006, based on the theory of electromagnetic wave regulation, Pendry et al. [40] predicted the wave's propagation trajectory to deduce the required material structure and designed an invisibility cloak that could control the wave to bypass the target without scattering, and provides a general theory for the design of uniform materials to guide sound waves to propagate along a specific curved path. As shown in Figure 6, the acoustic guidance control model and stealth effect diagram of stealth cloak can control acoustic waves to bypass the target object without scattering. Based on this idea, Cummer and Schuring et al. [41] developed the theory of transformation acoustics. In 2007, Chen et al. [42] demonstrated the possibility of transforming acoustic theory and designed a theoretical model of an invisibility cloak, which achieved the ideal invisibility effect. In 2018, Bi et al. [43] designed a three-dimensional underwater acoustic stealth cloak based on the theory of transformation acoustics. Its structural shape is an octahedral pyramid. When used, it is placed above the target, and the scattered wave is manipulated to imitate the plane scattered wave, so as to achieve the effect of hiding the target. However, these metamaterials are made up of anisotropic and heterogeneous media, and there are still great challenges in physical realization and engineering application.

In 2008, Norris et al. [12] Based on the transformation acoustic theory of anisotropic elastic modulus, the design idea of acoustic invisibility cloak using Pentamode metamaterials is proposed. Pentamode metamaterials have the characteristics of shear modulus far less than compression modulus, all-solid medium, and wide frequency band [44], so it has more application value in engineering. In 2013, On the basis of previous studies, Norris et al. [45] conducted experiments on the underwater acoustic refraction principle of pentamode metamaterials, and verified the feasibility of pentamode metamaterials in the field of underwater acoustic control. The variable model, solid characteristics, and anisotropic heterogeneous media make the pentamode metamaterials supplement the deficiency of UAGM, so it shows Pentamode metamaterials have gradually become the main way to realize underwater acoustic guided metamaterials.

Sun et al. [46] obtained the parameters needed for cloaks in impedance matching by inverse Laplace equation and designed cloaks based on pentamode metamaterials. The simulation results show that the cloak has a good broadband stealth effect. Chen et al. [47] designed a practical pentamode metamaterials cloak. The proposed cloak is assembled by

pentamode lattice made of a single-phase solid material. During the simulation process, it was found that the pentamode metamaterials cloak could not achieve the ideal broadband characteristics because of its low shear modulus. Therefore, the pentamode metamaterials cloak could only hide the target within the segmented frequency range. Chen et al. found that the shear resonance can be improved by introducing material damping, and then the broadband performance can be improved.

Zhao et al. [48] prepared a two-dimensional pentamode metamaterials sample using a single metal material and verified its acoustic characteristics. The experimental results prove the correctness of the design idea. The above work shows that the pentamode metamaterials have gradually become the main way to realize UAGM.

Due to the limitation of material characteristics, at the beginning of the design of UAGM, its operating frequency band is set to a fixed value, which can only play the effect of diffraction regulation on the incident wave of a specific frequency. In the future, how to flexibly adjust the working frequency band of UAGM with the change of incident wave frequency and realize adaptive control is the main challenge before it is applied to underwater engineering.

5 Summary and prospect

This paper reviews the sound absorption mechanism and structural design process of SAM, SIDM, and UAGM from three perspectives: basic properties of metamaterials, development history, and future development directions. This paper also summarizes the sound absorption effect and underwater sound absorption performance of underwater acoustic metamaterials to provide a reference for subsequent researchers. The conclusions of this paper are as follows:

(1) Due to the limitation of the inherent characteristics of the local resonance theory, the sound absorption band of SAM is narrow and the sound absorption capacity for underwater use scenarios still needs to be improved. How to use the multiple scattering effects generated by the resonant coupling unit to enhance the sound absorption band of metamaterials is a key issue in this field in the future.
(2) In the environment of high hydrostatic pressure, SIDM is usually designed to be thicker and heavier. How to apply it in UAE under the premise of light weight is a major engineering problem for future sound insulation decoupling metamaterials.
(3) How to adjust the working frequency band of UAGM flexibly with the change of incident wave frequency and realize the active guidance of incident sound waves is a difficult problem to be solved in UAGM.

Generally speaking, compared with the traditional underwater acoustic materials, the performance of underwater acoustic metamaterials has great advantages, but the practical engineering application effect needs further demonstration. In the future, underwater acoustic metamaterials will develop in the direction of broadband, low frequency, and pressure resistance.

Author contributions

ZZ is the general manager of the article, responsible for the design and writing of this article. NH provided valuable suggestions for the design and writing of this article. JW provided opinions on the application of metamaterials in underwater equipment. WL is in charge of literature research. JZ provided valuable suggestions for the design and writing of this article. MW provided valuable suggestions for revision. FZ, HD, and YZ is responsible for coordinating the authors.

Funding

This research was supported by the Zhejiang Science and Technology Plan Project (No. 2022C01199), and Fundamental Research Funds for the Provincial Universities of Zhejiang (GK219909299001-021). The funders had no role in the design of the study; in the collection, analyses, or interpretation of data; in the writing of the manuscript, or in the decision to publish the results.

Conflict of interest

Author JW was employed by the Sanmen Sanyou Technology Inc.

The remaining authors declare that the research was conducted in the absence of any commercial or financial relationships that could be construed as a potential conflict of interest.

Publisher's note

References

1. Wang J, Sun J, Xie W, Chen H, Wang C, Yu Y, et al. Simulation and analysis of multiphase flow in a novel deepwater closed-cycle riserless drilling method with a subsea Pump+Gas combined lift. *Front Phys* (2022) 10:10. doi:10.3389/fphy.2022.946516

2. Hu Y, Xu D, Zhou Z, Zhao T, Shi Y, Tian Y, et al. Research on the influence of metamaterials on single photon lidar. *Front Phys* (2020) 8:8. doi:10.3389/fphy.2020.585881

3. Zhang Y, Chen K, Hao X, Cheng Y. A review of underwater acoustic metamaterials. *Chin Sci Bull* (2020) 65(15):1396–410. doi:10.1360/tb-2019-0690

4. Yin J, Cai L, Fang X, Xiao Y, Yang H, Zhang H, et al. Review on research progress of mechanical metamaterials and their applications on vibration and noise control. *Adv Mechanics(in Chinese)* (2022) 2022:1–64. doi:10.6052/1000-0992-12-345

5. Ko SH. Reduction of structure-borne noise using an air-voided elastomer. *J Acoust Soc Am* (1997) 101(6):3306–12. doi:10.1121/1.418292

6. Tao M, Tang W, Hua H. Noise reduction analysis of an underwater decoupling layer. *J Vib Acoust* (2010) 132:061006. doi:10.1115/1.4002126

7. Hao H. Gain influence for a reflection baffle. *Appl Acoust(in Chinese)* (2011) 20:187–92. doi:10.3969/.issn.1000-310X.2011.03.004

8. Yang H, Xiao Y, Zhao H, Zhong J, Wen J. On wave propagation and attenuation properties of underwater acoustic screens consisting of periodically perforated rubber layers with metal plates. *J Sound Vibration* (2019) 444:21–34. doi:10.1016/j.jsv.2018.12.031

9. Mei J, Ma G, Yang M, Yang Z, Wen W, Sheng P. Dark acoustic metamaterials as super absorbers for low-frequency sound. *Nat Commun* (2012) 3:756. Epub 2012/03/29. doi:10.1038/ncomms1758

10. Yang M, Ma G, Yang Z, Sheng P. Coupled membranes with doubly negative mass density and bulk modulus. *Phys Rev Lett* (2013) 110(13):134301. Epub 2013/04/16. doi:10.1103/PhysRevLett.110.134301

11. Kushwaha MS, Halevi P, Dobrzynski L, Djafari-Rouhani B. Acoustic band structure of periodic elastic composites. *Phys Rev Lett* (1993) 71(13):2022–5. Epub 1993/09/27. doi:10.1103/PhysRevLett.71.2022

12. Norris AN. Acoustic cloaking theory. *Proc R Soc A* (2008) 464(2097):2411–34. doi:10.1098/rspa.2008.0076

13. Mei J, Zhang X, Wu Y. Ultrathin metasurface with high absorptance for waterborne sound. *J Appl Phys* (2018) 123(9):091710. doi:10.1063/1.5009382

14. Yuan B, Jiang W, Jiang H, Chen M, Liu Y. Underwater acoustic properties of graphene nanoplatelet-modified rubber. *J Reinforced Plastics Composites* (2018) 37(9):609–16. doi:10.1177/0731684418754411

15. Zhao H, Wen J, Yu D, Wen X. Low-frequency acoustic absorption of localized resonances: Experiment and theory. *J Appl Phys* (2010) 107(2):023519. doi:10.1063/1.3284943

16. Zhao H, Liu Y, Wen J, Yu D, Wen X. Tri-component phononic crystals for underwater anechoic coatings. *Phys Lett A* (2007) 367(3):224–32. doi:10.1016/j.physleta.2007.02.048

17. Wen J, Zhao H, Lv L, Yuan B, Wang G, Wen X. Effects of locally resonant modes on underwater sound absorption in viscoelastic materials. *J Acoust Soc Am* (2011) 130(3):1201–8. Epub 2011/09/08. doi:10.1121/1.3621074

18. Zhong J, Wen J-H, Zhao H-G, Yin J-F, Yang H-B. Effects of core position of locally resonant scatterers on low-frequency acoustic absorption in viscoelastic panel. *Chin Phys B* (2015) 24(8):084301. doi:10.1088/1674-1056/24/8/084301

19. Zhao H, Wen J, Yang H, Lv L, Wen X. Backing effects on the underwater acoustic absorption of a viscoelastic slab with locally resonant scatterers. *Appl Acoust* (2014) 76:48–51. doi:10.1016/j.apacoust.2013.07.022

20. Meng H, Wen J, Zhao H, Wen X. Optimization of locally resonant acoustic metamaterials on underwater sound absorption characteristics. *J Sound Vibration* (2012) 331(20):4406–16. doi:10.1016/j.jsv.2012.05.027

21. Shi K, Jin G, Liu R, Ye T, Xue Y. Underwater sound absorption performance of acoustic metamaterials with multilayered locally resonant scatterers. *Results Phys* (2019) 12:132–42. doi:10.1016/j.rinp.2018.11.060

22. Gu Y, Zhong H, Bao B, Wang Q, Wu J. Experimental investigation of underwater locally multi-resonant metamaterials under high hydrostatic pressure for low frequency sound absorption. *Appl Acoust* (2021) 172:107605. doi:10.1016/j.apacoust.2020.107605

23. Zhong HB, Gu YH, Wu JH, Wang Q. 2D underwater acoustic metamaterials incorporating a combination of particle-filled polyurethane and spiral-based local resonance mechanisms. *Compos Structures* (2019) 220:1–10. doi:10.1016/j.compstruct.2019.03.091

24. Qu SC, Gao N, Tinel A, Morvan B, Romero-Garcia V, Groby JP, et al. Underwater metamaterial absorber withimpedance-matched composite. *Sci Adv* (2022) 8:eabm4206. doi:10.1126/sciadv.abm4206

25. Xu W, Jiang C, Zhang J. Underwater acoustic absorption of air-saturated open-celled silicon carbide foam. *Colloids Surf A: Physicochemical Eng Aspects* (2015) 471:153–8. doi:10.1016/j.colsurfa.2015.01.091

26. Xu W, Jiang C, Zhang J. Improvement in underwater acoustic absorption performance of open-celled sic foam. *Colloids Surf A: Physicochemical Eng Aspects* (2015) 482:568–74. doi:10.1016/j.colsurfa.2015.06.046

27. Wang C, Li S-D, Zheng W-G, Huang Q-B. Acoustic absorption characteristics of new underwater omnidirectional absorber. *Chin Phys Lett* (2019) 36(4):044301. doi:10.1088/0256-307x/36/4/044301

28. Gao N, Zhang Y. A low frequency underwater metastructure composed by helix metal and viscoelastic damping rubber. *J Vibration Control* (2018) 25(3):538–48. doi:10.1177/1077546318788446

29. Huang L, Xiao Y, Wen J, Yang H, Wen X. Analysis of decoupling mechanism of an acoustic coating layer with horizontal cylindrical cavities. *Acta Phys Sin* (2015) 64(15):154301. doi:10.7498/aps.64.154301

30. Ko S, Seong W, Pyo S. Structure-borne noise reduction for an infinite, elastic cylindrical shell. *J Acoust Soc Am* (2001) 109(4):1483–95. doi:10.1121/1.1349540

31. Laulagnet B, Guyader JL. Sound radiation from finite cylindrical coated shells, by means of asymptotic expansion of three-dimensional equations for coating. *J Acoust Soc Am* (1994) 96(1):277–86. doi:10.1121/1.410480

32. Huang L, Xiao Y, Wen J, Zhang H, Wen X. Optimization of decoupling performance of underwater acoustic coating with cavities via equivalent fluid model. *J Sound Vibration* (2018) 426:244–57. doi:10.1016/j.jsv.2018.04.024

33. Huang LZ, Xiao Y, Wen JH, Yang HB, Wen XS. Analysis of underwater decoupling properties of a locally resonant acoustic metamaterial coating. *Chin Phys B* (2016) 25(2):024302. doi:10.1088/1674-1056/25/2/024302

34. Wang D, Zhu D, Huang X. Influences of internal resonances on the vibration and sound reduction of chiral layer coating. *Noise Vibr Contrl (in Chinese)* (2015) 35:22–5. doi:10.3969/j.issn.1006-1335.2015.06.005

35. Zhong HB, Tian YJ, Gao NS, Lu K, Wu J. Ultra-thin composite underwater honeycomb-type acoustic metamaterial with broadband sound insulation and high hydrostatic pressure resistance. *Compos Structures* (2021) 277:114603. doi:10.1016/j.compstruct.2021.114603

36. Spadoni A, Ruzzene M. Structural and acoustic behavior of chiral truss-core beams. *J Vib Acoust* (2007) 5:616–26. doi:10.1115/1.2202161

37. Spadoni A, Ruzzene M, Gonella S, Scarpa F. Phononic properties of hexagonal chiral lattices. *Wave Motion* (2009) 46(7):435–50. doi:10.1016/j.wavemoti.2009.04.002

38. Zhu D, Huang X, wang Y, Xiao F, Hua H. Experimental and numerical research on the underwater sound radiation of floating structures with covering layers. *Proc Inst Mech Eng C: J Mech Eng Sci* (2014) 229(3):447–64. doi:10.1177/0954406214536719

39. Zhang G, Yang D, Zhu J. Performance analysis of a novel marine honeycomb vibration isolator. *Chin J Ship Res* (2013) 8:52–8. doi:10.3969/j.issn.1673-3185.2013.04.009

40. Pendry BJ, Schurig D, Smith DR. Controlling electromagnetic fields. *science* (2006) 312:5781–2. doi:10.1126/science.1125907

41. Cummer SA, Schurig D. One path to acoustic cloaking. *New J Phys* (2007) 9(3):45. doi:10.1088/1367-2630/9/3/045

42. Chen H, Chan CT. Acoustic cloaking in three dimensions using acoustic metamaterials. *Appl Phys Lett* (2007) 91(18):183518. doi:10.1063/1.2803315

43. Bi Y, Jia H, Sun Z, Yang Y, Zhao H, Yang J. Experimental demonstration of three-dimensional broadband underwater acoustic carpet cloak. *Appl Phys Lett* (2018) 112(22):223502. doi:10.1063/1.5026199

44. Su X, Norris AN, Cushing CW, Haberman MR, Wilson PS. Broadband focusing of underwater sound using a transparent pentamode lens. *J Acoust Soc Am* (2017) 141(6):4408–17. Epub 2017/06/18. doi:10.1121/1.4985195

45. Hladky-Hennion AC, Vasseur JO, Haw G, Croënne C, Haumesser L, Norris AN. Negative refraction of acoustic waves using a foam-like metallic structure. *Appl Phys Lett* (2013) 102(14):144103. doi:10.1063/1.4801642

46. Sun Z, Sun X, Jia H, Bi Y, Yang J. Quasi-isotropic underwater acoustic carpet cloak based on latticed pentamode metafluid. *Appl Phys Lett* (2019) 114(9):094101. doi:10.1063/1.5085568

47. Chen Y, Liu X, Hu G. Latticed pentamode acoustic cloak. *Sci Rep* (2015) 5:15745. Epub 2015/10/28. doi:10.1038/srep15745

48. Zhao A, Zhao Z, Zhang X, Cai X, Wang L, Wu T, et al. Design and experimental verification of a water-like pentamode material. *Appl Phys Lett* (2017) 110(1):011907. doi:10.1063/1.4973924

frontiers | Frontiers in Physics

TYPE Original Research
PUBLISHED 22 December 2022
DOI 10.3389/fphy.2022.1094077

OPEN ACCESS

EDITED BY
Xiaopeng Li,
Toyota Research Institute of North America, United States

REVIEWED BY
Qian Wu,
University of Missouri, United States
Menglong Liu,
Harbin Institute of Technology, Shenzhen, China

*CORRESPONDENCE
Zheng Li,
lizheng@pku.edu.cn

SPECIALTY SECTION
This article was submitted to Physical Acoustics and Ultrasonics, a section of the journal Frontiers in Physics

RECEIVED 09 November 2022
ACCEPTED 05 December 2022
PUBLISHED 22 December 2022

CITATION
Zhang Y, Xia R, Huang K and Li Z (2022), Theoretical analysis of guided waves propagation in periodic piezoelectric plates with shunting circuits.
Front. Phys. 10:1094077.
doi: 10.3389/fphy.2022.1094077

Theoretical analysis of guided waves propagation in periodic piezoelectric plates with shunting circuits

Youqi Zhang[1], Rongyu Xia[1], Kefu Huang[2] and Zheng Li[1]*

[1]Department of Mechanics and Engineering Science, State Key Laboratory for Turbulence and Complex Systems, Peking University, Beijing, China, [2]Department of Mechanics and Aerospace Engineering, Southern University of Science and Technology, Shenzhen, China

The tunable manipulation of guided waves in plates brings out great potential applications in engineering practices, and the electromechanical coupling effects of piezoelectric material with shunting circuits have exhibited powerful tunability and flexibility for guided wave propagation. In this paper, a theoretical model is established to analyze the guided wave propagation in one-dimensional periodic piezoelectric plate constructed from a periodic array of anisotropic piezoelectric materials under periodic electrical boundary conditions. The extended Stroh formalism incorporating with the plane wave expansion method is developed to transform the wave motion equations of the periodic piezoelectric plate into a linear eigenvalue system, and a more concise and elegant solution of generalized displacement and generalized stress can be derived. There are various dispersion relations in terms of the altering electrical boundary conditions to be acquired, if the thin electrodes with shunting circuits are attached periodically to both surfaces of the piezoelectric plate. Analytical results show that the coupling of the local electric resonant mode and propagating elastic wave modes can induce hybridization bandgaps, and the bandgaps of Lamb waves and SH waves in the piezoelectric plate can be tuned by designing appropriate material polarization orientations and shunting circuits. In addition, the Bragg bandgaps can also be influenced by the external circuits. Results indicate that the proposed theoretical model can effectively analyze the performances of guided waves in periodic piezoelectric plate and provide useful theoretical guidance for designing smart wave control devices.

KEYWORDS

metamaterials, phononic crystals, guided waves, piezoelectricity, electromechanical coupling, Stroh formalism

1 Introduction

Phononic crystals/metamaterials as kinds of artificial composite materials can achieve various fantastic performances [1–5] and have been attracting more and more attention for a wide variety of potential applications [6–11]. Especially, phononic crystals/metamaterials with anomalous dynamic characteristics can fulfill special functions, like wave resistance [12], vibration reduction [13, 14], vibration and wave motion control [15–17], which are significant for maintaining safety and stability of engineering structures. Phononic crystals are based on the Bragg scattering in periodic structures to reduce vibration and manipulate wave propagation by adjusting their band structures [18, 19], and the most concern is the Bragg bandgaps. The wavelength corresponding to the Bragg bandgap is of the same order as the lattice constant. However, metamaterials mainly focus on the locally resonant bandgaps at lower frequency range by changing the local mechanical properties, and the vibration reduction and wave propagation can be controlled at a deeply subwavelength scale [20]. Nowadays, many bandgap-based dynamic behavior altering design combine the characteristics of both phononic crystals and metamaterials [21], so there is no rigorous distinction between them.

The Bragg bandgaps of phononic crystals depend on the periodicity of the structure and are normally fixed and invariable. However, it is meaningful to design phononic crystals with tunable and controllable band structures in practical applications [22]. Consequently, multi-physics coupling phononic crystals have been introduced to manipulate the performances of guided waves propagation by adjusting the multi-physics coupling effects. For one-dimensional piezoelectric or piezomagnetic phononic crystals, Guo et al. investigated the influences of initial stresses [23], mechanically and dielectrically imperfect interfaces [24], and functionally graded interlayers [25] on the dispersion relations of elastic waves. For nanoscale periodic layered piezoelectric composites [26, 27] or piezoelectric/piezomagnetic laminates [28], the influences of nanoscale size and multi-physics coupling on elastic waves were discussed based on the non-local theory. For the piezoelectric plate with a periodic arrangement of electrodes on both surfaces, its electrical Bragg bandgaps can be optimized by changing the crystallographic orientation of the piezoelectric plate [29], and the Bragg gaps of guided wave modes can be controlled by the electrical boundary conditions *via* either floating potential or short circuit [30, 31]. However, most researches lack discussion on how to control the dynamic behaviors of the piezoelectric plate by using the electromechanical coupling effect, but it is vital for designing phononic crystals with the tunability of band structures.

Since 1979 Forward [32] introduced electric damping to control the vibration of the structure, the design of piezoelectric transducers with shunting circuits has been applied to actively attenuate noise and vibration in structures [33, 34]. In most cases, the periodic piezoelectric patches with shunting circuits are attached to the surfaces of elastic structures as metamaterials to change the equivalent properties of elastic materials, and the band structures of guided waves can be relatively manipulated by external circuits. For an elastic beam with periodic piezoelectric patches, its band structures can be altered by different external circuits to induce local resonances, such as inductance circuits [35], an inductor in series with a positive or negative resistor [36], in series or in parallel negative capacitance and negative inductance circuits [37] or digital circuits with feedback control loops [38]. Sugino et al. [39] proposed a piezoelectric bimorph beam with mechanical and electromechanical resonators, and two resonant bandgaps could be merged to form a broaden bandgap of flexural wave by altering the mechanical resonator and shunting circuit. For an elastic plate with periodic piezoelectric patches, different external circuits such as inductance-capacitance circuits [40] or negative capacitance circuits [41, 42] have also been used to design the tunable band structures of Lamb waves and SH waves. However, for the multi-mode guided waves in piezoelectric plate, the interactions between mechanical and electric resonant modes are too difficult to analyze, so that the researches on the mechanism of manipulating guided wave propagation in piezoelectric plate with shunting circuits are relatively limited. For a homogeneous piezoelectric plate periodically covered electrodes with external circuits, spectral element method was applied to reveal the electromechanical coupling effect on the resonance bandgaps of symmetric mode Lamb waves by shunting inductance-capacitance circuits [43]. Kherraz et al. found the external inductance circuits could cause an electric resonant mode to form a hybridization bandgap by coupling with both symmetric and antisymmetric mode Lamb waves [44–46]. Nevertheless, there is no theoretical analysis of all guided wave modes in composite plates with alternative arrangements of different piezoelectric materials for a broad tunability range of guided waves, because it is too complicated to describe the electromechanical coupling effect on bandgaps induced by the coupling of shunting circuits and all guided wave modes. The very challenging task is how to study the wave motion in periodic piezoelectric plate by considering the anisotropic property of piezoelectric material and the electromechanical coupling effect of external circuits simultaneously.

As a representative theory of anisotropic elasticity, the Stroh formalism was established by Stroh [47, 48] in 1958 and systematically reconstructed by Ting [49] and Tanuma [50], and it has been developed to solve the static problems about piezoelectric and magneto-electro-elastic solids [51], magneto-electro-elastic composite laminates [52, 53] and homogenized piezoelectric plates [54]. For dynamic problems, the pseudo-Stroh formalism was proposed by solving the eigenvalue problem to conduct forced vibrations analysis [55, 56] and study the dynamic responses of piezoelectric plates [57] and magneto-

electro-elastic plates [58]. Furthermore, based on the elegant mathematical form of Stroh formalism, the wave motion and dispersion relations of plates have been studied, such as SH waves in multilayered piezoelectric semiconductor plates [59], Lamb waves in piezoelectric and elastic multilayered plates [60], both Lamb waves and SH wave in a magneto-electro-elastic laminate [61] or in a single piezoelectric semiconductor plate [62]. Due to the unique piezoelectric effects of piezoelectric materials which can achieve energy conversion between electric fields and mechanical deformations, there are many smart devices to be made of piezoelectric materials. Although Stroh Formalism has been developed to be an efficient way for theoretically solving multi-physics coupling problems, it still needs to be improved to solve the wave propagation problems in anisotropic periodic piezoelectric plates, especially with external circuits. In fact, the periodic piezoelectric plate with shunting circuits can be treated as a perfect combination of phononic crystal with periodic structure and metamaterial with varying external circuits, and it can reveal more fascinating performances by periodic arrangement of piezoelectric materials and altering electrical boundary conditions.

In this paper, for a one-dimensional periodic piezoelectric plate, which consists of periodically alternating two piezoelectric materials with thin electrodes shunted electric circuits to be attached on both surfaces, a novel theoretical model based on Stroh formalism is proposed for investigating the propagation features of elastic waves in the periodic piezoelectric plate. The rest of the paper is organized as follows. In Section 2, the extended Stroh formalism is derived for the theoretical model of wave motion in a periodic piezoelectric plate, and the solutions of generalized displacement and generalized stress are provided based on the plane wave expansion method for calculating the dispersion relations by a linear superposition of the corresponding eigenvalues and eigenvectors. After that, the effects of electrical boundary conditions on the dispersion relations are discussed in Section 3, and the corresponding dispersion relations of guided waves are derived for revealing the electromechanical effects. There are some typical examples to discuss the electromechanical coupling effects on guided waves by changing the polarizations of piezoelectric materials and the external circuits in Section 4. Finally, the conclusions of this paper are addressed in Section 5.

2 Theoretical model of wave motion in periodic piezoelectric plate

2.1 Wave equations of piezoelectric medium

For an anisotropic piezoelectric plate, if the 3D Cartesian coordinate system is coincident with its three material principal axes, the mechanical stress tensor $\boldsymbol{\sigma}$ and the electric displacement vector $\mathbf{D}$ are related to the strain tensor $\boldsymbol{\varepsilon}$ and electric field vector $\mathbf{E}$ by the following constitutive equations,

$$\begin{aligned} \sigma_{ij} &= \sum_{k,l=1}^{3} C_{ijkl}\varepsilon_{kl} - \sum_{k=1}^{3} e_{kij}E_k, \\ D_j &= \sum_{k,l=1}^{3} e_{jkl}\varepsilon_{kl} + \sum_{k=1}^{3} \epsilon_{jk}E_k, \end{aligned} \qquad i,j = 1,2,3, \tag{1}$$

where $E_k = -\frac{\partial\phi}{\partial x_k}$, $\varepsilon_{kl} = \frac{1}{2}\left(\frac{\partial u_k}{\partial x_l} + \frac{\partial u_l}{\partial x_k}\right)$, $\mathbf{u}$ and ϕ are the displacement vector and electric potential, and $\mathbf{C}$, $\mathbf{e}$, $\boldsymbol{\epsilon}$ are the elasticity tensor, piezoelectric tensor and dielectric tensor, respectively.

Because of the symmetry of piezoelectric material, there are $C_{ijkl} = C_{jikl} = C_{ijlk} = C_{klij}$, $e_{lij} = e_{lji}$, $\varepsilon_{jk} = \varepsilon_{kj}$, and then Eq. 1 can be rewritten as

$$\begin{aligned} \sigma_{ij} &= \sum_{k,l=1}^{3} C_{ijkl}\frac{\partial u_k}{\partial x_l} + \sum_{k=1}^{3} e_{kij}\frac{\partial\phi}{\partial x_k}, \\ D_j &= \sum_{k,l=1}^{3} e_{jkl}\frac{\partial u_k}{\partial x_l} - \sum_{k=1}^{3} \epsilon_{jk}\frac{\partial\phi}{\partial x_k}, \end{aligned} \qquad i,j = 1,2,3. \tag{2}$$

In order to unify the variables in Eq. 2, the generalized displacement vector and generalized stress tensor are defined by

$$\tilde{u}_K = \begin{cases} u_K, & K = 1,2,3, \\ \phi, & K = 4, \end{cases}$$
$$\tilde{\sigma}_{Ij} = \begin{cases} \sigma_{Ij}, & I,j = 1,2,3, \\ D_j, & I = 4, \quad j = 1,2,3, \end{cases}$$

and a new material parameter tensor $\mathbf{B}$ is introduced as

$$B_{IjKl} = \begin{cases} C_{IjKl}, & I,j,K,l = 1,2,3, \\ e_{lIj}, & I,j,l = 1,2,3, \ K = 4, \\ e_{jKl}, & j,K,l = 1,2,3, \ I = 4, \\ -\epsilon_{jl}, & j,l = 1,2,3, \ I = K = 4, \end{cases}$$

so that Eq. 2 can be written equivalently by

$$\tilde{\sigma}_{Ij} = \sum_{K=1}^{4}\sum_{l=1}^{3} B_{IjKl}\frac{\partial\tilde{u}_K}{\partial x_l}, \quad I = 1,2,3,4, \ j = 1,2,3. \tag{3}$$

For the piezoelectric plate without body force and free charge, the dynamic governing equation and the electric equilibrium equation are given by

$$\begin{aligned} \sum_{j=1}^{3}\frac{\partial\sigma_{ij}}{\partial x_j} &= \rho\frac{\partial^2 u_I}{\partial t^2}, \quad i = 1,2,3, \\ \sum_{j=1}^{3}\frac{\partial D_j}{\partial x_j} &= 0. \end{aligned} \tag{4}$$

Based on the notations of generalized displacement vector and generalized stress tensor, Eq. 4 can be simplified as

$$\sum_{j=1}^{3}\frac{\partial\tilde{\sigma}_{Ij}}{\partial x_j} = \rho\frac{\partial^2\tilde{u}_I}{\partial t^2}\left(\sum_{\alpha=1}^{3}\delta_{I\alpha}\right), \quad I = 1,2,3,4. \tag{5}$$

Combining Eqs 3, 5, the wave equation of anisotropic piezoelectric plate can be derived as

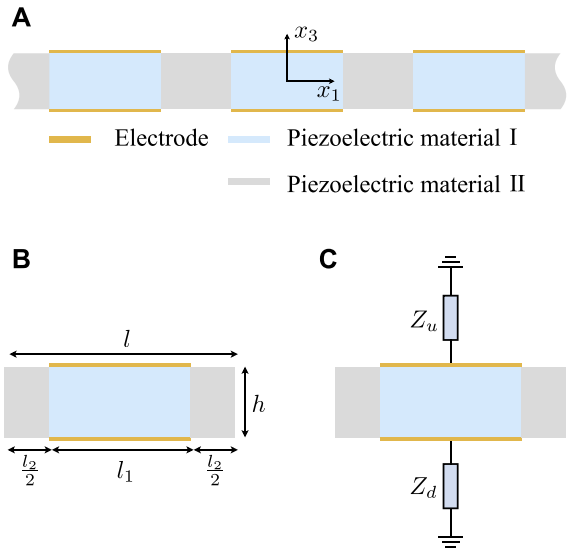

FIGURE 1
(A) Schematic of the periodic piezoelectric plate covered by periodic electrodes on both sides, **(B)** its corresponding unit cell, and **(C)** the considering electrical boundary conditions.

$$\sum_{j=1}^{3}\sum_{K=1}^{4}\sum_{l=1}^{3}\frac{\partial}{\partial x_j}\left(B_{IjKl}\frac{\partial \tilde{u}_K}{\partial x_l}\right)=\rho\frac{\partial^2\tilde{u}_I}{\partial t^2}\left(\sum_{\alpha=1}^{3}\delta_{I\alpha}\right),\quad I=1,2,3,4. \tag{6}$$

Therefore, the wave motion in piezoelectric plate can be obtained by solving Eq. 6 under initial and boundary conditions.

2.2 Periodic piezoelectric plate

Considering a piezoelectric composite plate with periodically alternating two piezoelectric materials in one dimensional series as shown in Figure 1A, the Cartesian coordinate system with the original point lying at the center is used, and the plate has a finite thickness h along x_3 axis and infinite size in x_2 axis. The unit cell as shown in Figure 1B consists of two piezoelectric materials marked as part I (blue) and part II (gray) with segment lengths l_1 and $2\times\frac{l_2}{2}$ to form a symmetric structure along x_1 axis with the lattice constant $l = l_1+l_2$. Their material parameter tensors are $\mathbf{B}_\mathrm{I}$ and $\mathbf{B}_\mathrm{II}$, and densities are ρ_I and ρ_II. It needs to emphasize that the material parameter tensors $\mathbf{B}_\mathrm{I}$ and $\mathbf{B}_\mathrm{II}$ have to be transformed from their material coordinate system to Cartesian coordinate system before substituting into Eq. 6. Set the center of each unit cell as its location, the unit cells along the positive direction of x_1 axis are listed as the 1st, 2nd, $\cdots$, J^{th} unit cell in sequence, and the J^{th} unit cell is located along the x_1 coordinate axis in the range $\mathrm{O} = [Jl-\frac{l}{2}, Jl+\frac{l}{2}]$ with the corresponding ranges of part I $\mathrm{O_I} = [Jl-\frac{l_1}{2}, Jl+\frac{l_1}{2}]$ and part II $\mathrm{O_{II}} = [Jl-\frac{l}{2}, Jl-\frac{l_1}{2}]\cup[Jl+\frac{l_1}{2}, Jl+\frac{l}{2}]$, separately.

Due to the spatial periodicity of piezoelectric plate, the material parameter tensor $\mathbf{B}$ can be expanded into Fourier series in the x_1 direction as

$$\mathbf{B}(x_1)=\sum_{m=-\infty}^{m=+\infty}\mathbf{B}_m\,\mathrm{e}^{\mathrm{i}\frac{2\pi m}{l}x_1}, \tag{7}$$

where $\mathrm{i}=\sqrt{-1}$ is the unit imaginary number, and m is integer. $\mathbf{B}_m$ is the Fourier expansion coefficient matrix for each unit cell, and it can be calculated for the J^{th} unit cell by

$$\mathbf{B}_m=\frac{1}{l}\int_{Jl-\frac{l}{2}}^{Jl+\frac{l}{2}}\mathbf{B}(x_1)\mathrm{e}^{-\mathrm{i}\frac{2\pi m}{l}x_1}\mathrm{d}x_1,$$

so,

$$\mathbf{B}_m=\begin{cases}\mathbf{B}_\mathrm{I}\dfrac{l_1}{l}+\mathbf{B}_\mathrm{II}\dfrac{l_2}{l}, & m=0,\\ \dfrac{1}{m\pi}(\mathbf{B}_\mathrm{I}-\mathbf{B}_\mathrm{II})\sin\left(m\pi\dfrac{l_1}{l}\right), & m\neq 0.\end{cases}$$

In addition, the density of the periodic plate can be silimlarly expanded into Fourier series as the material parameter tensor. For the spatial periodicity of piezoelectric plate along x_1 axis, the Fourier expansion coefficient matrix is the same for all the unit cells.

Here, we only consider the wave propagation along x_1 direction, and the plane strain condition is adopted [63] to simplify Eq. 6, i.e., $\partial/\partial x_2 = 0$. Therefore, the basic form of generalized displacement vector is

$$\tilde{\mathbf{u}}(x_1,x_3,t)=\mathbf{a}\mathrm{e}^{\mathrm{i}k_3x_3}\mathrm{e}^{\mathrm{i}k_1x_1}\mathrm{e}^{-\mathrm{i}\omega t}, \tag{8}$$

where k_1 and k_3 are the wave vector components along x_1 and x_3 axes, respectively, ω is the angular frequency, $\mathbf{a}$ is the unknown coefficient vector. The periodicity along x_1 indicates that the solution of the generalized displacement vector can be expanded by the form of Fourier series based on the Bloch theorem as

$$\mathbf{a}=\sum_{n=-\infty}^{+\infty}\mathbf{a}_n\mathrm{e}^{\mathrm{i}\frac{2\pi n}{l}x_1}. \tag{9}$$

Substituting Eq. 9 into Eq. 8, we obtain the generalized displacement vector in one-dimensional periodic structure as

$$\tilde{\mathbf{u}}(x_1,x_3,t)=\mathrm{e}^{-\mathrm{i}\omega t}\mathrm{e}^{\mathrm{i}k_3x_3}\sum_{n=-\infty}^{+\infty}\mathbf{a}_n\mathrm{e}^{\mathrm{i}\left(k_1+\frac{2\pi n}{l}\right)x_1}. \tag{10}$$

In order to get the solution of generalized displacement, the main attention is focused on solving the wave vector component k_3 and coefficient vectors $\mathbf{a}_n$.

2.3 The extended Stroh formalism for elastic dynamics

For simplicity, several matrices related to are introduced as

$$Q_{IK} = B_{I1K1},\ R_{IK} = B_{I1K3},\ T_{IK} = B_{I3K3},\quad I, K = 1, 2, 3, 4. \tag{11}$$

Because the material parameters are functions of x_1, then, Eq. 6 is rewritten as

$$\frac{\partial \mathbf{Q}}{\partial x_1}\frac{\partial \tilde{\mathbf{u}}}{\partial x_1} + \frac{\partial \mathbf{R}}{\partial x_1}\frac{\partial \tilde{\mathbf{u}}}{\partial x_3} + \mathbf{Q}\frac{\partial^2 \tilde{\mathbf{u}}}{\partial x_1^2} + \left(\mathbf{R} + \mathbf{R}^{\mathrm{T}}\right)\frac{\partial^2 \tilde{\mathbf{u}}}{\partial x_1 \partial x_3} + \mathbf{T}\frac{\partial^2 \tilde{\mathbf{u}}}{\partial x_3^2} = \rho \mathbf{Y}\frac{\partial^2 \tilde{\mathbf{u}}}{\partial t^2}, \tag{12}$$

where $\mathbf{Y} = \mathrm{diag}(1, 1, 1, 0)$. Substituting Eqs 7, 10 into Eq. 12, and set $p = m + n$, we obtain

$$\sum_{p=-\infty}^{+\infty}\sum_{n=-\infty}^{+\infty} \mathbf{F}_{p-n}^{n}\mathbf{a}_n \mathrm{e}^{\mathrm{i}\left(k_1 + \frac{2\pi p}{l}\right)x_1}\mathrm{e}^{\mathrm{i}(k_3 x_3 - \omega t)} = \mathbf{0}, \tag{13}$$

where

$$\mathbf{F}_{p-n}^{n} = \mathbf{Q}_{p-n}\left(k_1 + \frac{2\pi n}{l}\right)\left(k_1 + \frac{2\pi p}{l}\right) + \mathbf{R}_{p-n}k_3\left(k_1 + \frac{2\pi p}{l}\right) + \mathbf{R}_{p-n}^{\mathrm{T}}k_3\left(k_1 + \frac{2\pi n}{l}\right) + \mathbf{T}_{p-n}k_3^2 - \rho_{p-n}\mathbf{Y}\omega^2. \tag{14}$$

If the elementary solution is set by

$$H\left(k_1, p, x_1\right) = \mathrm{e}^{\mathrm{i}\left(k_1 + \frac{2\pi p}{l}\right)x_1},$$

the orthogonality condition can be satisfied, i.e.

$$\int_a^{a+l} H\left(k_1, p, x_1\right)H\left(-k_1, -q, x_1\right)\mathrm{d}x_1 = l\delta_{pq}, \tag{15}$$

where a is an arbitrary real number. In practice, the infinite sums in Eq. 13 are truncated by a finite value N, and only $2N + 1$ terms are considered. Taking advantage of the orthogonality relation in Eq. 15, the finite expansion of Eq. 13 can be equivalently expressed into a system of $2N + 1$ linear equations, and it is

$$\sum_{n=-N}^{N}\mathbf{F}_{q-n}^{n}\mathbf{a}_n = \mathbf{0} \tag{16}$$

for any integer $q \in [-N, N]$.

The generalized stress on the plane perpendicular to x_3 axis is

$$\tilde{\mathbf{t}} = \tilde{\sigma}_{I3} = \mathbf{R}^{\mathrm{T}}\frac{\partial \tilde{\mathbf{u}}}{\partial x_1} + \mathbf{T}\frac{\partial \tilde{\mathbf{u}}}{\partial x_3}. \tag{17}$$

Substituting Eqs 7, 10 into Eq. 17, and defining

$$\mathbf{b}_p = \sum_{n=-N}^{N}\mathbf{G}_{p-n}^{n}\mathbf{a}_n, \tag{18}$$

where

$$\mathbf{G}_{p-n}^{n} = \mathbf{R}_{p-n}^{\mathrm{T}}\left(k_1 + \frac{2\pi n}{l}\right) + k_3\mathbf{T}_{p-n}. \tag{19}$$

It derives

$$\tilde{\mathbf{t}} = \sum_{p=-N}^{p=N}\mathrm{i}\mathbf{b}_p \mathrm{e}^{\mathrm{i}\left(k_1 + \frac{2\pi p}{l}\right)x_1}\mathrm{e}^{\mathrm{i}(k_3 x_3 - \omega t)}.$$

Setting all the $2N + 1$ vectors of $\mathbf{a}_n$ as a new column vector $\tilde{\mathbf{a}}$ and the $2N + 1$ vectors of $\mathbf{b}_p$ as a new column vector $\tilde{\mathbf{b}}$ in Eq. 18, they have the relation as

$$\tilde{\mathbf{b}} = \tilde{\mathbf{S}}\tilde{\mathbf{a}} + k_3\tilde{\mathbf{T}}\tilde{\mathbf{a}}, \tag{20}$$

where the matrices of $\tilde{\mathbf{S}}$ and $\tilde{\mathbf{T}}$ are

$$\tilde{\mathbf{S}} = \begin{bmatrix} \mathbf{R}_0^{\mathrm{T}}\left(k_1 + \frac{2\pi(-N)}{l}\right) & \cdots & \mathbf{R}_{-N}^{\mathrm{T}}\left(k_1 + \frac{2\pi 0}{l}\right) & \cdots & \mathbf{R}_{-2N}^{\mathrm{T}}\left(k_1 + \frac{2\pi N}{l}\right) \\ \vdots & & \vdots & & \vdots \\ \mathbf{R}_N^{\mathrm{T}}\left(k_1 + \frac{2\pi(-N)}{l}\right) & \cdots & \mathbf{R}_0^{\mathrm{T}}\left(k_1 + \frac{2\pi 0}{l}\right) & \cdots & \mathbf{R}_{-N}^{\mathrm{T}}\left(k_1 + \frac{2\pi N}{l}\right) \\ \vdots & & \vdots & & \vdots \\ \mathbf{R}_{2N}^{\mathrm{T}}\left(k_1 + \frac{2\pi(-N)}{l}\right) & \cdots & \mathbf{R}_N^{\mathrm{T}}\left(k_1 + \frac{2\pi 0}{l}\right) & \cdots & \mathbf{R}_0^{\mathrm{T}}\left(k_1 + \frac{2\pi N}{l}\right) \end{bmatrix},$$

$$\tilde{\mathbf{T}} = \begin{bmatrix} \mathbf{T}_0 & \cdots & \mathbf{T}_{-N} & \cdots & \mathbf{T}_{-2N} \\ \vdots & & \vdots & & \vdots \\ \mathbf{T}_N & \cdots & \mathbf{T}_0 & \cdots & \mathbf{T}_{-N} \\ \vdots & & \vdots & & \vdots \\ \mathbf{T}_{2N} & \cdots & \mathbf{T}_N & \cdots & \mathbf{T}_0 \end{bmatrix}.$$

Because the matrix $\tilde{\mathbf{T}}$ is symmetric and invertible, $\tilde{\mathbf{T}}^{-1}$ exists [50]. Hence, from Eq. 20, we get

$$k_3\tilde{\mathbf{a}} = -\tilde{\mathbf{T}}^{-1}\tilde{\mathbf{S}}\tilde{\mathbf{a}} + \tilde{\mathbf{T}}^{-1}\tilde{\mathbf{b}}. \tag{21}$$

From Eqs. 14, 19, the matrix $\mathbf{F}$ can be expressed by $\mathbf{G}$ as

$$\mathbf{F}_{p-n}^{n} = \mathbf{Q}_{p-n}\left(k_1 + \frac{2\pi n}{l}\right)\left(k_1 + \frac{2\pi p}{l}\right) + \mathbf{R}_{p-n}k_3\left(k_1 + \frac{2\pi p}{l}\right) + k_3\mathbf{G}_{p-n}^{n} - \rho_{p-n}\mathbf{Y}\omega^2. \tag{22}$$

Combining Eq. 22 and the q^{th} linear equation in Eq. 16, when q takes all the integers from $-N$ to N, the linear system of $2N + 1$ equations can be rearranged as

$$\tilde{\mathbf{Q}}\tilde{\mathbf{a}} + k_3\tilde{\mathbf{R}}\tilde{\mathbf{a}} + k_3\tilde{\mathbf{b}} - \tilde{\boldsymbol{\rho}}\omega^2\tilde{\mathbf{a}} = \mathbf{0}, \tag{23}$$

where $\tilde{\mathbf{Q}}$, $\tilde{\mathbf{R}}$ and $\tilde{\boldsymbol{\rho}}$ are

$$\tilde{\mathbf{Q}} = \begin{bmatrix} \mathbf{Q}_0\left(k_1 + \frac{2\pi(-N)}{l}\right)\left(k_1 + \frac{2\pi(-N)}{l}\right) & \cdots & \mathbf{Q}_{-N}\left(k_1 + \frac{2\pi(-N)}{l}\right)\left(k_1 + \frac{2\pi 0}{l}\right) & \cdots & \mathbf{Q}_{-2N}\left(k_1 + \frac{2\pi(-N)}{l}\right)\left(k_1 + \frac{2\pi N}{l}\right) \\ \vdots & & \vdots & & \vdots \\ \mathbf{Q}_N\left(k_1 + \frac{2\pi 0}{l}\right)\left(k_1 + \frac{2\pi(-N)}{l}\right) & \cdots & \mathbf{Q}_0\left(k_1 + \frac{2\pi 0}{l}\right)\left(k_1 + \frac{2\pi 0}{l}\right) & \cdots & \mathbf{Q}_{-N}\left(k_1 + \frac{2\pi 0}{l}\right)\left(k_1 + \frac{2\pi N}{l}\right) \\ \vdots & & \vdots & & \vdots \\ \mathbf{Q}_{2N}\left(k_1 + \frac{2\pi N}{l}\right)\left(k_1 + \frac{2\pi(-N)}{l}\right) & \cdots & \mathbf{Q}_N\left(k_1 + \frac{2\pi N}{l}\right)\left(k_1 + \frac{2\pi 0}{l}\right) & \cdots & \mathbf{Q}_0\left(k_1 + \frac{2\pi N}{l}\right)\left(k_1 + \frac{2\pi N}{l}\right) \end{bmatrix},$$

$$\tilde{\mathbf{R}} = \begin{bmatrix} \mathbf{R}_0\left(k_1 + \frac{2\pi(-N)}{l}\right) & \cdots & \mathbf{R}_{-N}\left(k_1 + \frac{2\pi(-N)}{l}\right) & \cdots & \mathbf{R}_{-2N}\left(k_1 + \frac{2\pi(-N)}{l}\right) \\ \vdots & & \vdots & & \vdots \\ \mathbf{R}_N\left(k_1 + \frac{2\pi 0}{l}\right) & \cdots & \mathbf{R}_0\left(k_1 + \frac{2\pi 0}{l}\right) & \cdots & \mathbf{R}_{-N}\left(k_1 + \frac{2\pi 0}{l}\right) \\ \vdots & & \vdots & & \vdots \\ \mathbf{R}_{2N}\left(k_1 + \frac{2\pi N}{l}\right) & \cdots & \mathbf{R}_N\left(k_1 + \frac{2\pi N}{l}\right) & \cdots & \mathbf{R}_0\left(k_1 + \frac{2\pi N}{l}\right) \end{bmatrix},$$

$$\tilde{\boldsymbol{\rho}} = \begin{bmatrix} \rho_0\mathbf{Y} & \cdots & \rho_{-N}\mathbf{Y} & \cdots & \rho_{-2N}\mathbf{Y} \\ \vdots & & \vdots & & \vdots \\ \rho_N\mathbf{Y} & \cdots & \rho_0\mathbf{Y} & \cdots & \rho_{-N}\mathbf{Y} \\ \vdots & & \vdots & & \vdots \\ \rho_{2N}\mathbf{Y} & \cdots & \rho_N\mathbf{Y} & \cdots & \rho_0\mathbf{Y} \end{bmatrix}.$$

Therefore, from Eqs. 21, 23, we obtain the following eigen relation as

$$\mathbf{N}\boldsymbol{\xi} = k_3\boldsymbol{\xi},$$

where

$$\mathbf{N} = \begin{bmatrix} -\tilde{\mathbf{T}}^{-1}\tilde{\mathbf{S}} & \tilde{\mathbf{T}}^{-1} \\ -\tilde{\mathbf{Q}} + \tilde{\boldsymbol{\rho}}\omega^2 + \tilde{\mathbf{R}}\tilde{\mathbf{T}}^{-1}\tilde{\mathbf{S}} & -\tilde{\mathbf{R}}\tilde{\mathbf{T}}^{-1} \end{bmatrix}, \quad \boldsymbol{\xi} = \begin{bmatrix} \tilde{\mathbf{a}} \\ \tilde{\mathbf{b}} \end{bmatrix}.$$

The solution $\boldsymbol{\xi}$ is called Stroh eigenvector, where $\tilde{\mathbf{a}}$ and $\tilde{\mathbf{b}}$ represent generalized displacement vector part and generalized stress vector part, respectively. Because the size of the matrix $\mathbf{N}$ is $8(2N + 1) \times 8(2N + 1)$, there are $8(2N + 1)$ eigenvalues k_3 of complex conjugate pairs and corresponding eigenvectors $\boldsymbol{\xi}$, and the solutions of generalized displacement and stress vectors are (omitting the ranges of $p \in [-N, N]$ and $r \in [1, 8(2N + 1)]$ for notation simplicity below)

$$\tilde{\mathbf{u}}(x_1, x_3, t) = \mathrm{e}^{-\mathrm{i}\omega t}\sum_p\left(\sum_r c^r \mathrm{e}^{\mathrm{i}k_3^r x_3}\mathbf{a}_p^r\right)\mathrm{e}^{\mathrm{i}\left(k_1+\frac{2\pi p}{l}\right)x_1}, \tag{24}$$

and

$$\tilde{\mathbf{t}}(x_1, x_3, t) = \mathrm{i}\mathrm{e}^{-\mathrm{i}\omega t}\sum_p\left(\sum_r c^r \mathrm{e}^{\mathrm{i}k_3^r x_3}\mathbf{b}_p^r\right)\mathrm{e}^{\mathrm{i}\left(k_1+\frac{2\pi p}{l}\right)x_1}. \tag{25}$$

where the unknown coefficients c^r can be determined by different given boundary conditions on the surfaces of plate.

In order to study the propagations of elastic waves in periodic piezoelectric plate, the electromechanical coupling effect needs to be considered by the mechanical and electrical boundary conditions on the surfaces. The dispersion properties can be changed by various electrical boundary conditions, so that the tunable band structures can be achieved.

The traction free boundary conditions on the surfaces of periodic piezoelectric plate can be expressed by

$$\sigma_{31} = 0, \ \sigma_{32} = 0, \ \sigma_{33} = 0, \quad x_3 = \pm h/2. \tag{26}$$

No matter what kinds of external circuits are shunted *via* the electrodes whose thickness is negligible, the electrical boundary conditions can be expressed as functions of electric potential ϕ and normal component of electric displacement vector D_3 on surfaces, that is

$$f_e^{\pm}(\phi, D_3) = 0, \quad x_3 = \pm h/2. \tag{27}$$

By considering the orthogonality condition in Eqs. 15, a combination of the mechanical and electrical boundary conditions in Eqs. 26, 27 can be conducted by multiplying $H(-k_1, -q, x_1)$ and integrating them along x_1 axis from $Jl - \frac{l}{2}$ to $Jl + \frac{l}{2}$ for each unit cell, and the boundary conditions can be equivalently transformed into a system of $8 \times (2N + 1)$ linear equations as

$$\mathbf{M}(k_1, \omega)\mathbf{c} = \mathbf{0}, \tag{28}$$

where $\mathbf{c}$ is a column vector consisting of unknown coefficients c^r. In order to get the non-trivial solution, the determinant of coefficient matrix must be equal to zero. Then, the dispersion relation between wave number k_1 and angular frequency ω can be obtained by

$$\det\ \mathbf{M}(k_1, \omega) = 0. \tag{29}$$

Therefore, the dispersion relations of periodic piezoelectric plate can be obtained by solving Eq. 29 to explore the characteristics of guided wave motion.

3 Piezoelectric plate with periodic shunting circuit

3.1 Electrical boundary conditions

When the periodic piezoelectric plate is located in a vacuum, the normal components of electric displacement in the vacuum are $D_3^+(x_3 \geq \frac{h}{2})$, $D_3^-(x_3 \leq -\frac{h}{2})$, respectively. For the unit cell with shunting circuits as shown in Figure 1C, the thin electrodes cover the entire surfaces of part I and connect external circuits. If $\varphi_{J\mathrm{I}}^{\pm}$ indicates the external electric potentials on electrodes of the J^{th} unit cell, the electrical boundary conditions can be written as

$$\begin{cases} \phi|_{x_3=\pm\frac{h}{2}} = \varphi_{J\mathrm{I}}^{\pm}, & x_1 \in \mathrm{O_I}, \\ (D_3 - D_3^{\pm})|_{x_3=\pm\frac{h}{2}} = 0, & x_1 \in \mathrm{O_{II}}. \end{cases} \tag{30}$$

The electric potentials in the vacuum are $\phi^{\pm}$ and satisfy the Laplace equation, i.e. $\nabla^2\phi^{\pm} = 0$. Because the electric potentials gradually decrease in the vacuum and vanish at infinite, they can be expressed as

$$\begin{aligned} \phi^+ &= \sum_p C_p^+ \mathrm{e}^{\mathrm{i}\left(k_1+\frac{2\pi p}{l}\right)\left(x_1+\mathrm{i}s_p x_3\right)}\mathrm{e}^{-\mathrm{i}\omega t}, \quad x_3 \geq \frac{h}{2}, \\ \phi^- &= \sum_p C_p^- \mathrm{e}^{\mathrm{i}\left(k_1+\frac{2\pi p}{l}\right)\left(x_1-\mathrm{i}s_p x_3\right)}\mathrm{e}^{-\mathrm{i}\omega t}, \quad x_3 \leq -\frac{h}{2}, \end{aligned} \tag{31}$$

where

$$s_p = \begin{cases} 1, & \mathrm{Re}\left(k_1 + \dfrac{2\pi p}{l}\right) \geq 0, \\ -1, & \mathrm{Re}\left(k_1 + \dfrac{2\pi p}{l}\right) < 0. \end{cases}$$

From Eq. 24, the electric potential in the plate is

$$\phi = \mathrm{e}^{-\mathrm{i}\omega t}\sum_p\left[\sum_r c^r \mathrm{e}^{\mathrm{i}k_3^r x_3}\nu_p^r\right]\mathrm{e}^{\mathrm{i}\left(k_1+\frac{2\pi p}{l}\right)x_1}, \tag{32}$$

where ν_p^r is the corresponding component ϕ in $\mathbf{a}_p^r$. Using the continuity of electric potential on surfaces, $\phi^{\pm}|_{x_3=\pm\frac{h}{2}} = \phi|_{x_3=\pm\frac{h}{2}}$, the

normal components of electric displacement in the vacuum $D_3^{\pm}$ can be expressed by the electric potential in plate ϕ as

$$\begin{aligned} D_3^{+} &= -\epsilon_0\phi_{,3}^{+} = \epsilon_0 k_1\phi + \epsilon_0\sum_p\sum_r c^r\nu_p^r \mathrm{e}^{\mathrm{i}k_{32}^r\frac{h}{2}}\mathrm{e}^{\mathrm{i}\left(k_1+\frac{2\pi p}{l}\right)x_1} \\ &\quad \left(k_1\left(s_p-1\right)+\frac{2\pi p}{l}s_p\right)\mathrm{e}^{-\mathrm{i}\omega t},\ x_3=\frac{h}{2}, \\ D_3^{-} &= -\epsilon_0\phi_{,3}^{-} = -\epsilon_0 k_1\phi - \epsilon_0\sum_p\sum_r c^r\nu_p^r \mathrm{e}^{-\mathrm{i}k_{32}^r\frac{h}{2}}\mathrm{e}^{\mathrm{i}\left(k_1+\frac{2\pi p}{l}\right)x_1} \\ &\quad \left(k_1\left(s_p-1\right)+\frac{2\pi p}{l}s_p\right)\mathrm{e}^{-\mathrm{i}\omega t},\ x_3=-\frac{h}{2}. \end{aligned} \tag{33}$$

where $\epsilon_0 = 8.854\times10^{-12}$ F/m is the dielectric constant in the vacuum.

Using Eq. 25, the normal component of electric displacement of the plate can be expressed as

$$D_3 = \mathrm{i}\sum_p\left[\sum_r c^r\mathrm{e}^{\mathrm{i}k_3^r x_3}w_p^r\right]\mathrm{e}^{\mathrm{i}\left(k_1+\frac{2\pi p}{l}\right)x_1}\mathrm{e}^{-\mathrm{i}\omega t}, \tag{34}$$

where w_p^r is the corresponding component D_3 in $\mathbf{b}_p^r$. Moreover, by Eqs. 33, 34, we can get

$$\begin{aligned} \left(D_3-D_3^{+}\right) &= -\epsilon_0 k_1\phi + \sum_p\sum_r\left(f_p^r\right)^{+}c^r\mathrm{e}^{\mathrm{i}k_{32}^r\frac{h}{2}}\mathrm{e}^{\mathrm{i}\left(k_1+\frac{2\pi p}{l}\right)x_1}\mathrm{e}^{-\mathrm{i}\omega t},\ x_3=\frac{h}{2}, \\ \left(D_3-D_3^{-}\right) &= \epsilon_0 k_1\phi + \sum_p\sum_r\left(f_p^r\right)^{-}c^r\mathrm{e}^{-\mathrm{i}k_{32}^r\frac{h}{2}}\mathrm{e}^{\mathrm{i}\left(k_1+\frac{2\pi p}{l}\right)x_1}\mathrm{e}^{-\mathrm{i}\omega t},\ x_3=-\frac{h}{2}, \end{aligned} \tag{35}$$

where $\left(f_p^r\right)^{\pm} = \mathrm{i}w_p^r \mp \epsilon_0\nu_p^r\left(k_1\left(s_p-1\right)+\frac{2\pi p}{l}s_p\right)$. As a consequence, the electrical boundary conditions in Eq. 30 can be rewritten by electric potentials as

$$\phi|_{x_3=\pm\frac{h}{2}} = \begin{cases} \varphi_{J\mathrm{I}}^{\pm}, & x_1\in \mathrm{O_I}, \\ \varphi_{J\mathrm{II}}^{\pm}, & x_1\in \mathrm{O_{II}}, \end{cases} \tag{36}$$

where the electric potential $\varphi_{J\mathrm{II}}^{\pm}$ on the surfaces of part II is the same for each unit cell and can be calculated by Eq. 35 as

$$\varphi_{\mathrm{II}}^{\pm} = \varphi_{J\mathrm{II}}^{\pm} = \pm\frac{1}{\epsilon_0 k_1}\sum_p\sum_r\left(f_p^r\right)^{\pm}c^r\mathrm{e}^{\pm\mathrm{i}k_{32}^r\frac{h}{2}}\mathrm{e}^{\mathrm{i}\left(k_1+\frac{2\pi p}{l}\right)x_1}\mathrm{e}^{-\mathrm{i}\omega t}.$$

In addition, the charge densities on surfaces are $\theta^{\pm} = \pm\left(D_3 - D_3^{\pm}\right)$ and combining them with Eqs. 30, 35, the total charges on the electrodes of the J^{th} unit cell per unit length in x_2 direction can be calculated by

$$\begin{aligned} Q_J^{+} &= -\epsilon_0 k_1 l_1\varphi_{J\mathrm{I}}^{+} + \sum_p\sum_r\left(f_p^r\right)^{+}c^r\mathrm{e}^{\mathrm{i}k_{32}^r\frac{h}{2}}g\left(k_1,p,J\right)\mathrm{e}^{-\mathrm{i}\omega t}, \\ Q_J^{-} &= -\epsilon_0 k_1 l_1\varphi_{J\mathrm{I}}^{-} - \sum_p\sum_r\left(f_p^r\right)^{-}c^r\mathrm{e}^{-\mathrm{i}k_{32}^r\frac{h}{2}}g\left(k_1,p,J\right)\mathrm{e}^{-\mathrm{i}\omega t}, \end{aligned} \tag{37}$$

where

$$\begin{aligned} g\left(k_1,p,J\right) &= \int_{Jl-\frac{l_1}{2}}^{Jl+\frac{l_1}{2}}H\left(k_1,p,x_1\right)\mathrm{d}x_1 \\ &= \frac{2l}{k_1 l+2\pi p}\mathrm{e}^{\mathrm{i}k_1 Jl}\sin\left[\left(k_1+\frac{2\pi p}{l}\right)\frac{l_1}{2}\right]. \end{aligned}$$

Therefore the electric potential $\varphi_{J\mathrm{I}}^{\pm}$ on the electrodes of part I can be obtained from Eq. 37 by the electric charge $Q_J^{\pm}$ determined under different external circuits on the J^{th} unit cell. Substituting $\varphi_{J\mathrm{I}}^{\pm}$ and $\varphi_{\mathrm{II}}^{\pm}$ into Eq. 36 and performing the orthogonal integration in the range of O, the electrical boundary conditions of Eq. 27 can be provided by a system made of $2(2N+1)$ linear equations as $F_e(q)^{\pm} = 0$, $q = 0, \pm1, \cdots \pm N$, with

$$\begin{aligned} F_e\left(q\right)^{+} &= \sum_p\sum_r c^r\mathrm{e}^{\mathrm{i}k_{32}^r\frac{h}{2}}\mathrm{e}^{-\mathrm{i}\omega t}\left[\nu_p^r l\delta_{pq}-\frac{1}{\epsilon_0 k_1}\left(f_p^r\right)^{+}\left(l\delta_{pq}-g\left(0,p-q,J\right)\right)\right] \\ &\quad -g\left(-k_1,-q,J\right)\varphi_{J\mathrm{I}}^{+}, \\ F_e\left(q\right)^{-} &= \sum_p\sum_r c^r\mathrm{e}^{-\mathrm{i}k_{32}^r\frac{h}{2}}\mathrm{e}^{-\mathrm{i}\omega t}\left[\nu_p^r l\delta_{pq}+\frac{1}{\epsilon_0 k_1}\left(f_p^r\right)^{-}\left(l\delta_{pq}-g\left(0,p-q,J\right)\right)\right] \\ &\quad -g\left(-k_1,-q,J\right)\varphi_{J\mathrm{I}}^{-}. \end{aligned} \tag{38}$$

Correspondingly, the influences of electrical boundary conditions on dispersion relations of periodic piezoelectric plate can be analyzed to investigate the manipulating mechanism.

3.2 Loaded with shunting circuit

3.2.1 Electrically open circuit

When the J^{th} unit cell is electrically isolated, each electrode is recognized as an equipotential body and satisfies the condition of charge conservation to make the total charge of Eq. 37 equal to zero, so that the electric potentials $\varphi_{J\mathrm{I}}^{\pm}$ on the electrodes of part I can be derived as

$$\begin{aligned} \varphi_{J\mathrm{I}}^{+} &= \frac{1}{\epsilon_0 k_1 l_1}\sum_p\sum_r\left(f_p^r\right)^{+}c^r\mathrm{e}^{\mathrm{i}k_{32}^r\frac{h}{2}}g\left(k_1,p,J\right)\mathrm{e}^{-\mathrm{i}\omega t}, \\ \varphi_{J\mathrm{I}}^{-} &= -\frac{1}{\epsilon_0 k_1 l_1}\sum_p\sum_r\left(f_p^r\right)^{-}c^r\mathrm{e}^{-\mathrm{i}k_{32}^r\frac{h}{2}}g\left(k_1,p,J\right)\mathrm{e}^{-\mathrm{i}\omega t}. \end{aligned} \tag{39}$$

Substituting Eq. 39 into Eq. 38, the electrical boundary conditions of electrically open circuit on both surfaces can be expressed by

$$\begin{aligned} F_e\left(q\right)^{+} &= \sum_p\sum_r c^r\mathrm{e}^{\mathrm{i}k_{32}^r\frac{h}{2}}\mathrm{e}^{-\mathrm{i}\omega t} \\ &\quad \left[\nu_p^r l\delta_{pq}-\frac{1}{\epsilon_0 k_1}\left(f_p^r\right)^{+}\left(\left(l\delta_{pq}-g\left(0,p-q,J\right)\right)-\frac{1}{l_1}g\left(k_1,p,J\right)g\left(-k_1,-q,J\right)\right)\right], \\ F_e\left(q\right)^{-} &= \sum_p\sum_r c^r\mathrm{e}^{-\mathrm{i}k_{32}^r\frac{h}{2}}\mathrm{e}^{-\mathrm{i}\omega t} \\ &\quad \left[\nu_p^r l\delta_{pq}+\frac{1}{\epsilon_0 k_1}\left(f_p^r\right)^{-}\left(\left(l\delta_{pq}-g\left(0,p-q,J\right)\right)-\frac{1}{l_1}g\left(k_1,p,J\right)g\left(-k_1,-q,J\right)\right)\right]. \end{aligned} \tag{40}$$

3.2.2 Electrically short circuit

If the electrodes of the J^{th} unit cell are connected to the ground, their electrical potentials are forced to zero, that is $\varphi_{J\mathrm{I}}^{\pm} = 0$. Taking advantage of Eq. 38, the electrical boundary conditions of electrically short circuits on both surfaces are

$$F_e(q)^+ = \sum_p \sum_r c^r e^{ik_{32}^r h} e^{-i\omega t}\left[v_p^r l\delta_{pq} - \frac{1}{\epsilon_0 k_1}\left(f_p^r\right)^+\left(l\delta_{pq} - g(0,p-q,J)\right)\right],$$
$$F_e(q)^- = \sum_p \sum_r c^r e^{-ik_{32}^r h} e^{-i\omega t}\left[v_p^r l\delta_{pq} + \frac{1}{\epsilon_0 k_1}\left(f_p^r\right)^-\left(l\delta_{pq} - g(0,p-q,J)\right)\right]. \quad (41)$$

3.2.3 Loaded external circuit

If the impedances on the upper and lower electrodes of the J^{th} unit cell are Z_u, Z_d, separately, as shown in Figure 1C, the charges on the electrodes of the J^{th} unit cell can be derived as

$$Q_J^+ = \frac{1}{i\omega Z_u}\varphi_{J1}^+, \qquad Q_J^- = \frac{1}{i\omega Z_d}\varphi_{J1}^-. \quad (42)$$

Combining Eqs. 42, 37, the electric potentials on the electrodes of the J^{th} unit cell can be expressed as

$$\varphi_{J1}^+ = \left(\frac{1}{i\omega Z_u} + \epsilon_0 k_1 l_1\right)^{-1} \sum_p \sum_r \left(f_p^r\right)^+ c^r e^{ik_{32}^r h} g(k_1,p,J) e^{-i\omega t},$$
$$\varphi_{J1}^- = -\left(\frac{1}{i\omega Z_d} + \epsilon_0 k_1 l_1\right)^{-1} \sum_p \sum_r \left(f_p^r\right)^- c^r e^{-ik_{32}^r h} g(k_1,p,J) e^{-i\omega t}. \quad (43)$$

Substituting Eq. 43 into Eq. 38, it leads to

$$F(q)^+ = \sum_p \sum_r c^r e^{ik_{32}^r h} e^{-i\omega t}\left[v_p^r l\delta_{pq} - \frac{1}{\epsilon_0 k_1}\left(f_p^r\right)^+\left(l\delta_{pq} - g(0,p-q,J)\right) - \left(\frac{1}{i\omega Z_u} + \epsilon_0 k_1 l_1\right)^{-1}\left(f_p^r\right)^+ g(k_1,p,J) g(-k_1,-q,J)\right],$$
$$F(q)^- = \sum_p \sum_r c^r e^{-ik_{32}^r h} e^{-i\omega t}\left[v_p^r l\delta_{pq} + \frac{1}{\epsilon_0 k_1}\left(f_p^r\right)^-\left(l\delta_{pq} - g(0,p-q,J)\right) + \left(\frac{1}{i\omega Z_d} + \epsilon_0 k_1 l_1\right)^{-1}\left(f_p^r\right)^- g(k_1,p,J) g(-k_1,-q,J)\right]. \quad (44)$$

Obviously, when the impedances Z_u or $Z_d \to \infty$, the circuit becomes electrically open case, and Eq. 44 can be degenerated to Eq. 40. When the impedances Z_u or $Z_d = 0$, the circuit can also be equivalently transformed into electrically short case with Eq. 44 degenerated to Eq. 41. Otherwise, for different values of impedances Z_u or Z_d, there are various electrical boundary conditions to be provided.

The different kinds of electrical boundary conditions are converted into a set of linear homogeneous equations. Combining the wave motion equation in Eq. 6 and boundary conditions in Eqs. 26, 27, the eigenvalues and eigenvectors in Eqs. 28, 29 can be determined, and the generalized solutions Eqs. 24, 25 can be obtained in an accurate form with infinite N or an approximate form with the truncating finite terms of N.

4 Electromechanical coupling effects on guided waves

In order to discuss the electromechanical coupling effects on the guided wave propagation in the periodic structure, a periodic piezoelectric plate made of PZT-5H is considered and the material parameters based on its three material principal axes are listed in Table 1 with the Voigt notation. Each unit cell of the periodic piezoelectric plate is constructed by two PZT segments with separately polarized directions and shunted external circuits. Based on the theoretical model, the dispersion curves of both Lamb waves and SH waves in the periodic piezoelectric plate can be calculated under different electrical boundary conditions. By changing the polarization directions of PZT segments in a unit cell or shunting different types of external circuits, the dispersion properties of periodic piezoelectric plates can be easily altered to control the performances of guided waves propagations.

If the sizes of unit cell in Figure 1B are set $l = 5$ mm, $h = 3$ mm the dimensionless wave number $k_1 l$ and dimensionless frequency $\Omega = \frac{\omega l}{\sqrt{C_{44}/\rho}}$ are introduced, and the dispersion curves are calculated in the range $k_1 l = [0, \pi]$ for the symmetry of the periodic piezoelectric plate. Finite element method is also conducted by COMSOL Multiphysics for comparison. In COMSOL Multiphysics calculations, the Floquet periodicity is applied to unit cell boundaries perpendicular to x_1 direction. Providing the wave number k_1 by parametric sweep, the corresponding eigenfrequencies can be obtained.

4.1 Polarized along the x_2 axis

If the unit cell in Figure 1B is designed by a combination of part I with $l_1 = 0.8\ L$ and part II with $l_2 = 0.2\ L$, both parts are made of PZT-5H with the polarization directions along x_2 axis as illustrated in Figure 2 with red crosses, and only the surfaces of part I are fully covered with thin electrodes. It means that there is no difference between the piezoelectric materials in part I and part II except part I can connect external circuits. For discussing the influences of external circuits on the dispersion properties of the periodic piezoelectric plate, the shunting inductance circuit is considered. Compared to the electrically open case in Figure 2A, the external inductance circuit is set by connecting inductance L on the upper electrode, and the lower electrode is connected to the ground as shown in Figure 2B, i.e. $Z_u = i\omega L$, $Z_d = 0$. If the inductor in Figure 2B is chosen by $L = 50\ \mu$H and $L = 30\ \mu$H, separately, the corresponding dispersion curves of Figures 2A,B can be calculated by Eq. 29 and results are shown in Figure 3. For the case without external circuits in Figure 2A, the dispersion curves of Lamb waves and SH wave are the same as homogeneous plate as shown in Figure 3A, and the corresponding finite element results are obtained by the commercial software COMSOL Multiphysics and illustrated by gray rhombus marks. In Figure 3A, these two results are in complete agreement, so that the effectiveness and reliability of Eq. 29 is verified.

If the external circuits are involved, the dispersion curves of Lamb waves and SH wave are also calculated by Eq. 29 and shown in Figures 3B,C, and there is an extra electric mode (red lines) to couple with the guided waves compared to Figure 3A.

TABLE 1 Material parameters of PZT-5H [31].

Elastic constants (GPa)					
$C_{11} = C_{22}$	C_{12}	$C_{13} = C_{23}$	C_{33}	$C_{44} = C_{55}$	C_{66}
127.21	80.21	84.67	117.44	22.99	23.47
Piezoelectric constants (C/m^2)			Relative dielectric constants		Density (kg/m^3)
$e_{15} = e_{24}$	$e_{31} = e_{32}$	e_{33}	$\epsilon_{11}/\epsilon_0 = \epsilon_{22}/\epsilon_0$	ϵ_{33}/ϵ_0	ρ
17.03	−6.62	23.24	1704.4	1433.6	7500

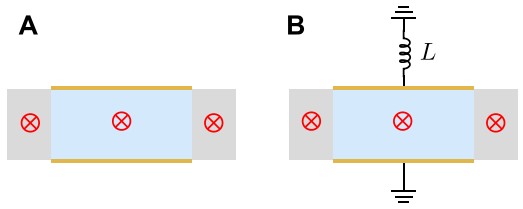

FIGURE 2
The periodic unit cell made of x_2 direction polarized PZT with different electrical boundary conditions: **(A)** electrically open, **(B)** shunting inductance.

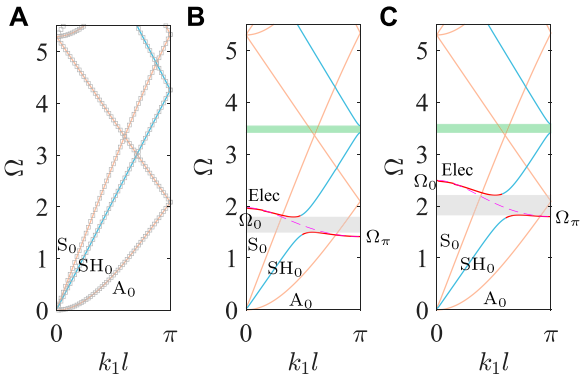

FIGURE 3
Dispersion curves of periodic plates with unit cells of **(A)** Figure 2A, **(B)** Figure 2B with L = 50 μH and **(C)** Figure 2B with L = 30 μH.

The corresponding finite element results calculated by COMMOL Multiphysics are not presented here because the "Electrical Circuit" interface of COMSOL is unstably supported for eigenvalue problem. Therefore, the reliability of Eq. 29 when the shunting circuits are involved is verified by the dispersion relation of the electric mode before coupling with guided waves, which can be derived from the equivalent-circuit model [44] as

$$\omega = [(2C_{\mathrm{II}}(1 - \cos kl) + C_{\mathrm{I}})L]^{-\frac{1}{2}}, \tag{45}$$

and illustrated by rose dashed curves in Figures 3B,C.

In this model, the unit cell in Figure 2B can be equivalent represented by a capacitor C_{I} whose surfaces are perpendicular to x_3 axis, and form a inductance-capacitance resonant circuit with the shunting inductance. In addition, the electrodes on the upper surfaces of adjacent unit cells are connected by an equivalent capacitor C_{II} whose surfaces are perpendicular to x_1 due to the electrical potential differences on these two electrodes. The values of C_{I} and C_{II} can be determined by the cutoff frequency ω_0 and ω_π denoted as the dimensionless Ω_0 and Ω_π in Figures 3B,C at the edges of Brillouin zone $k_1 l = 0$ and $k_1 l \to \pi$.

In Figures 3B,C, the shunted inductance circuit has no effect on Lamb waves due to their displacement vectors are perpendicular to the polarization orientation of piezoelectric material. By contrast, there is a strong interaction between the electric mode and SH_0 wave for the same directions of displacement vector and polarization orientation, and opening up the hybridization bandgaps as shown by gray shadow areas. According to Eq. 45, the lower inductance L can induce the electric mode at higher frequency range, and can result in the hybridization bandgaps at higher frequency range too, as shown in Figures 3B,C. The width of the hybridization bandgap increases to 1.3 times when the inductances decrease from 50 μH to 30 μH. Compared to Figure 3A, besides the hybridization bandgaps caused by electric mode, there is an extra narrow Bragg scattering bandgap (green shadow region) to be generated in Figures 3B,C for the periodicity of piezoelectric plate.

4.2 Polarized along the x_3 axis

The design of unit cell in Figure 4 is the same as that in Figure 2, except the polarization directions are all along x_3 axis as shown in Figure 4 with red arrows, and for Figure 4B the same electrical boundary conditions are considered as described in Section 4.1. The corresponding dispersion curves are calculated by Eq. 29 and results are illustrated in Figure 5. For the case of

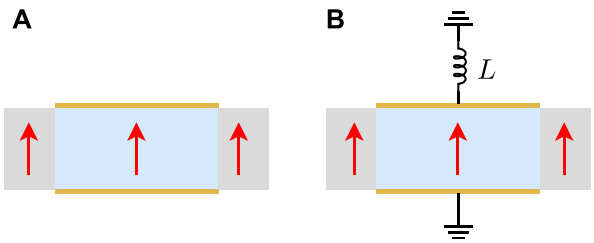

FIGURE 4
The periodic unit cell made of x_3 direction polarized PZT with different electrical boundary conditions: **(A)** electrically open, **(B)** shunting inductance.

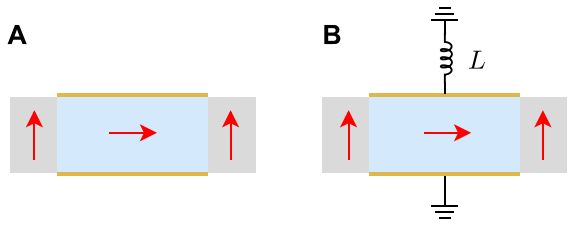

FIGURE 6
The periodic unit cell made of x_1 direction and x_3 direction polarized PZT with different electrical boundary conditions: **(A)** electrically open, **(B)** shunting inductance.

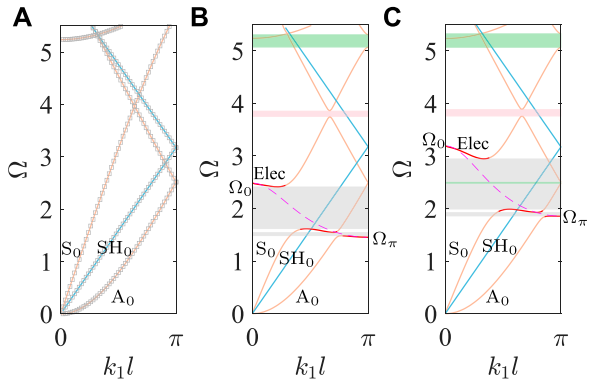

FIGURE 5
Dispersion curves of periodic plates with unit cells of **(A)** Figure 4A, **(B)** Figure 4B with L = 50 μH and **(C)** Figure 4B with L = 30 μH.

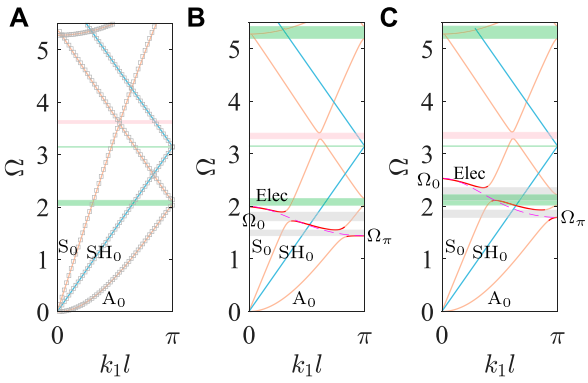

FIGURE 7
Dispersion curves of periodic plates with unit cells of **(A)** Figure 6A, **(B)** Figure 6B with L = 50 μH and **(C)** Figure 6B with L = 30 μH.

electrically open in Figure 4A, the finite element results are provided by the commercial software COMSOL Multiphysics and plotted in Figure 5A by gray rhombus symbols to show the good consistence with the theoretical model.

Compared to the dispersion curves in Figure 3, the big difference is that the shunting inductance circuit of Figure 4B has no influence on SH wave and the hybridization bandgaps emerge only from the coupling of the electric mode with the Lamb waves as gray shadow regions in Figures 5B,C. In Figures 5B,C, there is a stronger interaction with S_0-like mode to form a broader hybridization bandgap than that with A_0-like mode. It indicates that the electromechanical coupling effect on the guided waves can be effectively selected by the polarization direction of piezoelectric material. For the same shunting inductor with L = 50 μH, the electric mode calculated by Eq. 45 can cover a wider frequency range with lower Ω_π and higher Ω_0 in Figure 5B than that in Figure 3B, and leads to a nearly three times wider hybridization bandgap of S_0-like mode than that of SH_0 mode in Figure 3B. Similarly, the difference of the dispersion relations between Figure 5C and Figure 3C can be observed when the shunting inductor is L = 30 μH. Besides, there is another hybridization bandgap by the interaction between S_0-like mode and the folded negative-slope A_0-like mode denoted as the pink shadow regions in Figures 5B,C. The Bragg scattering bandgaps emerge when A_0-like and S_0-like waves are folded at the edge of the Brillouin zone, as denoted the green shadow areas in Figures 5B,C, and they are only related to the periodicity of piezoelectric plate but little influence by the shunting inductance circuit.

4.3 Polarized along the x_1 axis in part I and x_3 axis in part II

If two parts of unit cell are designed by the same PZT with different polarization directions, which are along x_1 axis in part I and x_3 axis in part II as illustrated in Figure 6, the dispersion curves of guided waves under the electrical boundary conditions of electrically open, shunting inductance with L = 50 μH and L =

30 μH, separately, can be calculated by Eq. 29 and shown in Figure 7. The differences of electromechanical coupling effects caused by the polarization directions and the shunting inductance circuits can be figured out in the dispersion curves of guided waves in Figure 7.

Similar to the dispersion curves in Figure 5, the external circuits have no influence on the propagation of SH waves in Figure 7, because the unit cell has no PZT part with the polarization direction along x_2 axis, i.e. the direction of SH wave motion, and the hybridization bandgaps shaded in gray in Figures 7B,C are only generated by the coupling of electric mode with A_0-like and S_0-like modes. However, there are some differences to be observed between Figures 5, 7. First, the Bragg bandgaps appear in Figure 7 when the guided waves fold at the edges of Brillouin zones for the periodicity of plate, but Bragg bandgaps of SH_0 branch cannot be observed in Figure 5 for the homogeneity of plate. In Figure 7, the bandgap of SH_0 branch is very narrow, and the bandgaps of A_0-like branch in Figures 7B,C are wider than that in Figures 5B,C while the bandgaps of S_0-like branch are thinner. Second, because the normal component of the dielectric tensor of PZT-5H after coordinate transformation increases when the polarization direction changes from x_3 to x_1 axis, and correspondingly the equivalent capacitance C_I increases, in consequence, the corresponding electric modes can cover a narrower frequency range in Figures 7B,C than that in Figures 5B,C. This is because the upper limits of electric modes decrease for the higher C_I based on Eq. 45, while the lower limits almost remain the same, so that the hybridization bandgaps open up at lower frequencies. Furthermore, the hybridization bandgaps are also influenced by the polarization directions, especially when the electric mode couples with S_0-like mode, the hybridization bandgaps in Figures 7B,C are narrower to be about 20% of that in Figures 5B,C.

4.4 Polarized along the x_2 axis in part I and x_3 axis in part II

The two parts of unit cell are designed in series with the same length $l_1 = l_2 = 0.5\,l$, and the electrodes are centered on both surfaces of these two parts with the length of $a_1 = 0.8\,l_1$, $a_2 = 0.8\,l_2$, respectively. The polarization directions of PZT are along x_2 axis in part I and x_3 axis in part II, as illustrated in Figure 8 with red crosses and arrows. The unit cell in Figure 8 is a combination of that in Figures 2, 4 with a half length. There are three different electrical boundary conditions to be considered as shown in Figure 8, the electrically open condition in Figure 8A, inductance shunting circuit loaded on the upper electrodes of part I in Figure 8B or part II in Figure 8C with the opposite lower electrodes connected to the ground. The dispersion curves of these three cases are calculated and shown in Figure 9, and the finite element results are obtained and drawn with gray rhombus marks to illustrate the good consistence in Figure 9A.

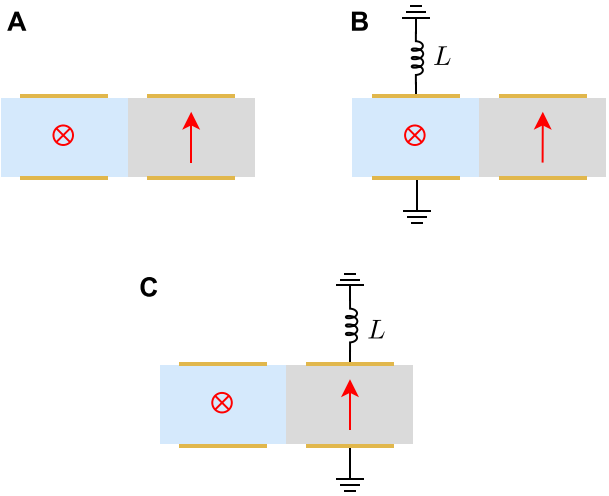

FIGURE 8
The periodic unit cell made of x_2 direction and x_3 direction polarized PZT with different electrical boundary conditions: **(A)** electrically open, **(B)** inductance shunting on part I and **(C)** inductance shunting on part II.

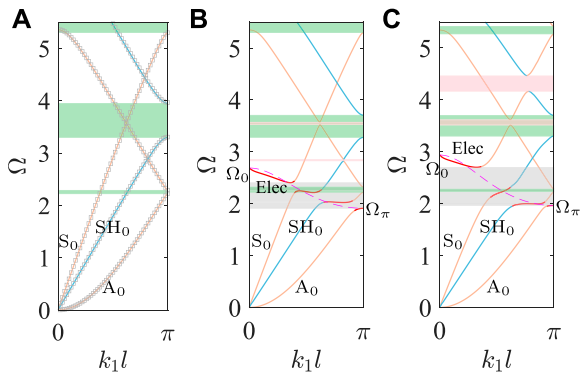

FIGURE 9
Dispersion curves of periodic plates with unit cells of **(A)** Figure 8A, **(B)** Figure 8B with L = 50 μH and **(C)** Figure 8C with L = 50 μH.

The big difference between Figure 7A and Figure 9A is the much wider Bragg bandgap (shaded in green) of SH_0 wave in Figure 9A for the part I polarized along the direction of SH_0 wave, and the broader length of part II polarized along axis in Figure 9A than the part II with the same polarization direction in Figure 7A cause a lower Bragg bandgap of S_0-like mode and a higher Bragg bandgap of A_0-like mode. Compared to Figure 3B with the same polarized PZT part shunted inductance circuit, the electric mode is located at a higher frequency range as rose dashed line in Figure 9B, and the electromechanical effect not only induces the

hybridization bandgap (shaded in gray) of SH_0 mode, but also causes the hybridization bandgaps for both A_0-like and S_0-like modes. The similar conclusion can be addressed from the comparison of Figure 5B and Figure 9C for the same polarized PZT part shunted inductance circuit, but the frequency range of electric mode is narrower in Figure 9C. It indicates that the hybridization bandgap caused by electromechanical effect strongly depends on the polarization direction of PZT, but the external circuit can influence the frequency range of electric mode. For a comparison of three Bragg bandgaps in Figure 9, the shunting inductance circuit can strongly decrease the frequency range of SH_0 mode no matter which part is shunted, but only slightly influences on both A_0-like and S_0-like modes. However, if the shunting inductance circuit is connected to the upper electrode of part I as shown in Figure 9B, the interactions between different wave modes are slight and hard to observe, while for the shunting inductance circuit connected to the upper electrode of part II as shown in Figure 9C, the S_0-like mode is strongly interacted with the folded negative-slope SH_0 mode and A_0-like mode to result in the opening up locally resonant bandgaps shaded in pink.

From Figures 3, 5, 7, 9, it is noteworthy that the obvious Bragg bandgaps can be observed for the heterogeneous plate with periodicity, and the heterogeneity can be induced by locally shunting circuits for homogeneous plate or by different polarization directions of two PZT segments. The external inductance circuits can introduce the electric mode to form the hybridization bandgaps after its interaction with guided waves. In addition, the coupling effect of electric mode only acts on the specific mode guided waves that have non-zero motion component along the polarization direction of PZT. It should be noticed in Figures 9B,C that the hybridization bandgap depends on the polarization direction of PZT even though the external circuit is connected to other PZT segments with different polarization directions.

5 Conslusion

Based on the extended Stroh formalism, a theoretical model is proposed for solving the guided wave propagation in periodic piezoelectric plate, and the dispersion relations of multi-modes guided waves in the periodic piezoelectric plate shunted with external circuits are theoretically investigated in this paper. Based on the theoretical analysis, the dispersion properties of the periodic piezoelectric plate can be manipulated by altering the polarization direction of piezoelectric material in a unit cell and the impedance parameters of shunting circuit, and the main points can be addressed as follows.

1. The periodic piezoelectric structure behaves as a combination of phononic crystal plate and metamaterial with shunting circuits. Consequently, both the Bragg bandgaps and the hybridization bandgaps emerge in different frequency ranges due to the electromechanical coupling effects. Compared to the Bragg bandgaps, the hybridization bandgaps locate at lower frequencies, hence, the manipulation of wave propagation can be achieved at subwavelength scale.
2. The shunting circuits connected to homogeneous unit cell can induce obvious bandgaps of guided wave when its motion direction is not perpendicular to the polarization direction of piezoelectric material. For the unit cell composed of piezoelectric materials with different polarization directions, the Bragg bandgap will appear no matter whether the shunting circuits exist or not.
3. The hybridization bandgaps originate from the coupling between electric mode and guided wave modes whose motion direction is the same as the polarization direction of the piezoelectric material in a unit cell. Hence, the manipulation of specific wave propagation can be achieved *via* the requested arrangement of polarization directions in a unit cell with shunting circuits.
4. The frequency range of the electric mode in the dispersion curves is modulated with the various inductance values and polarization orientations of the piezoelectric material in a unit cell, leading to the hybridization bandgaps opening at variable frequencies. Therefore, a tunable band structure of the periodic piezoelectric plate can be realized with the help of various electrical boundary conditions and different polarization orientation permutations of the segments in a unit cell.

In summary, the proposed theoretical model in this paper can be successfully applied to the wave motion problem of periodic piezoelectric plate with shunting circuits. Results predict that the periodic plate has a good ability to manipulate guided wave propagation and provide broad applications in wave guiding and controlling, non-destructive testing, and other engineering fields. Furthermore, the theoretical model can be developed to investigate the dispersion characters of guided waves in the periodic plate made of various materials with more multi-physics properties, such as piezomagnetic effect, and plate with more complex structures, such as multiple-layers, can also be studied by the modification of the theoretical approach.

Data availability statement

The original contributions presented in the study are included in the article/Supplementary Material, further inquiries can be directed to the corresponding author.

Author contributions

YZ: Conceptualization, methodology, software and data analysis, writing-original draft; RX: Conceptualization, validation, data analysis, reviewing and editing; KH: Supervision, reviewing; ZL: Supervision, writing-review and editing, funding acquisition. All authors listed have made a substantial contribution to the proposed work and approved the submitted version.

Funding

This work was supported by the National Natural Science Foundation of China under Grants No. 12172008 and No. 11991033.

Conflict of interest

The authors declare that the research was conducted in the absence of any commercial or financial relationships that could be construed as a potential conflict of interest.

Publisher's note

All claims expressed in this article are solely those of the authors and do not necessarily represent those of their affiliated organizations, or those of the publisher, the editors and the reviewers. Any product that may be evaluated in this article, or claim that may be made by its manufacturer, is not guaranteed or endorsed by the publisher.

References

1. Ji G, Huber J. Recent progress in acoustic metamaterials and active piezoelectric acoustic metamaterials - a review. *Appl Mater Today* (2021) 26:101260. doi:10.1016/j.apmt.2021.101260

2. Vasileiadis T, Varghese J, Babacic V, Gomis-Bresco J, Navarro Urrios D, Graczykowski B. Progress and perspectives on phononic crystals. *J Appl Phys* (2021) 129:160901. doi:10.1063/5.0042337

3. Xia R, Nassar H, Chen H, Li Z, Huang G. Microtwist homogenization of three-dimensional Pyrochlore lattices on zero modes and mechanical polarization. *J Mech Phys Sol* (2021) 155:104564. doi:10.1016/j.jmps.2021.104564

4. Chen H, Wang S, Li X, Huang G. Two-dimensional microtwist modeling of topological polarization in hinged Kagome lattices and its experimental validation. *Int J Sol Structures* (2022) 254-255:111891. doi:10.1016/j.ijsolstr.2022.111891

5. Yi J, Li Z, Negahban M, Xia R, Zhu J. Asymmetric viscoelastic metamaterials for broad bandgap design and unidirectional zero reflection. *Mech Syst Signal Process* (2022) 162:108101. doi:10.1016/j.ymssp.2021.108101

6. Valipour A, Kargozarfard MH, Rakhshi M, Yaghootian A, Sedighi HM. Metamaterials and their applications: An overview. *Proc Inst Mech Eng L: J Mater Des Appl* (2021) 236:2171–210. doi:10.1177/1464420721995858

7. Chiou MJ, Lin YC, Ono T, Esashi M, Yeh SL, Wu TT. Focusing and waveguiding of Lamb waves in micro-fabricated piezoelectric phononic plates. *Ultrasonics* (2014) 54:1984–90. doi:10.1016/j.ultras.2014.05.007

8. Wang Y, Zhao W, Rimoli JJ, Zhu R, Hu G. Prestress-controlled asymmetric wave propagation and reciprocity-breaking in tensegrity metastructure. *Extreme Mech Lett* (2020) 37:100724. doi:10.1016/j.eml.2020.100724

9. Miniaci M, Gliozzi A, Morvan B, Krushynska A, Bosia F, Scalerandi M, et al. Proof of concept for an ultrasensitive technique to detect and localize sources of elastic nonlinearity using phononic crystals. *Phys Rev Lett* (2017) 118:214301. doi:10.1103/PhysRevLett.118.214301

10. Yi J, Negahban M, Li Z, Su X, Xia R. Conditionally extraordinary transmission in periodic parity-time symmetric phononic crystals. *Int J Mech Sci* (2019) 163:105134. doi:10.1016/j.ijmecsci.2019.105134

11. Wu Q, Zhang X, Shivashankar P, Chen Y, Huang G. Independent flexural wave frequency conversion by a linear active metalayer. *Phys Rev Lett* (2022) 128:244301. doi:10.1103/PhysRevLett.128.244301

12. Cui R, Zhou J, Gong D. Wave-resistance sleeper with locally resonant phononic crystals: Bandgap property and vibration reduction mechanism. *AIP Adv* (2021) 11:035043. doi:10.1063/5.0027591

13. Zhang B, Chen P, Chen H, Feng T, Cai C, Zhang J. Application of phononic crystals for vibration reduction and noise reduction of wheel-driven electric buses based on neural networks. *Proc Inst Mech Eng D: J Automobile Eng* (2022) 236:1619–27. doi:10.1177/09544070211035906

14. Liu L, Lee HP. A review: Elastic metamaterials and inverse design methods for shock and vibration mitigation. *Int J Appl Mech* (2021) 13:2150102. doi:10.1142/S1758825121501027

15. Arretche I, Matlack KH. Locally resonant effective phononic crystals for subwavelength vibration control of torsional cylindrical waves. *J Vib Acoust* (2021) 144:031007. doi:10.1115/1.4052748

16. Dalela S, Balaji PS, Jena DP. A review on application of mechanical metamaterials for vibration control. *Mech Adv Mater Structures* (2022) 29:3237–62. doi:10.1080/15376494.2021.1892244

17. Arretche I, Matlack K. Effective phononic crystals for non-Cartesian elastic wave propagation. *Phys Rev B* (2020) 102:134308. doi:10.1103/PhysRevB.102.134308

18. Kushwaha M, Djafari-Rouhani B, Dobrzynski L. Sound isolation from cubic arrays of air bubbles in water. *Phys Lett A* (1998) 248:252–6. doi:10.1016/S0375-9601(98)00640-9

19. Tamura S, Hurley DC, Wolfe JP. Acoustic-phonon propagation in superlattices. *Phys Rev B* (1988) 38:1427–49. doi:10.1103/PhysRevB.38.1427

20. Oudich M, Gerard NJ, Deng Y, Jing Y. Tailoring structure-borne sound through bandgap engineering in phononic crystals and metamaterials: A comprehensive review. *Adv Funct Mater* (2022) 2022:2206309. doi:10.1002/adfm.202206309

21. Wu Q, Chen H, Nassar H, Huang G. Non-reciprocal Rayleigh wave propagation in space–time modulated surface. *J Mech Phys Sol* (2021) 146:104196. doi:10.1016/j.jmps.2020.104196

22. Wang YF, Wang YZ, Wu B, Chen W, Wang YS. Tunable and active phononic crystals and metamaterials. *Appl Mech Rev* (2020) 72:040801. doi:10.1115/1.4046222

23. Guo X, Wei P, Lan M, Li L. Dispersion relations of elastic waves in one-dimensional piezoelectric/piezomagnetic phononic crystal with functionally graded interlayers. *Ultrasonics* (2016) 70:158–71. doi:10.1016/j.ultras.2016.04.025

24. Guo X, Wei P, Li L. Dispersion relations of elastic waves in one-dimensional piezoelectric phononic crystal with mechanically and dielectrically imperfect interfaces. *Mech Mater* (2016) 93:168–83. doi:10.1016/j.mechmat.2015.11.004

25. Guo X, Wei P. Dispersion relations of elastic waves in one-dimensional piezoelectric phononic crystal with initial stresses. *Int J Mech Sci* (2016) 106:231–44. doi:10.1016/j.ijmecsci.2015.12.020

26. Yan DJ, Chen AL, Wang YS, Zhang C, Golub M. In-plane elastic wave propagation in nanoscale periodic layered piezoelectric structures. *Int J Mech Sci* (2018) 142–143:276–88. doi:10.1016/j.ijmecsci.2018.04.054

27. Yan DJ, Chen AL, Wang YS, Zhang C, Golub M. Propagation of guided elastic waves in nanoscale layered periodic piezoelectric composites. *Eur J Mech - A/Solids* (2017) 66:158–67. doi:10.1016/j.euromechsol.2017.07.003

28. Chen AL, Yan DJ, Wang YS, Zhang C. In-plane elastic wave propagation in nanoscale periodic piezoelectric/piezomagnetic laminates. *Int J Mech Sci* (2019) 153–154:416–29. doi:10.1016/j.ijmecsci.2019.02.017

29. Vasseur C, Croënne C, Vasseur JO, Dubus B, Thi MP, Prévot C, et al. Electrical evidence of the tunable electrical Bragg bandgaps in piezoelectric plates. *IEEE Trans Ultrason Ferroelectr Freq Control* (2018) 65:1552–62. doi:10.1109/TUFFC.2018.2847246

30. Kherraz N, Haumesser L, Levassort F, Benard P, Morvan B. Controlling Bragg gaps induced by electric boundary conditions in phononic piezoelectric plates. *Appl Phys Lett* (2016) 108:093503. doi:10.1063/1.4943138

31. Xia R, Zhu J, Yi J, Shao S, Li Z. Guided wave propagation in multilayered periodic piezoelectric plate with a mirror plane. *Int J Mech Sci* (2021) 204:106539. doi:10.1016/j.ijmecsci.2021.106539

32. Forward RL. Electronic damping of vibrations in optical structures. *Appl Opt* (1979) 18:690–7. doi:10.1364/AO.18.000690

33. Gripp JAB, Rade DA. Vibration and noise control using shunted piezoelectric transducers: A review. *Mech Syst Signal Process* (2018) 112:359–83. doi:10.1016/j.ymssp.2018.04.041

34. Wu Q, Chen Y, Huang G. Asymmetric scattering of flexural waves in a parity-time symmetric metamaterial beam. *The J Acoust Soc America* (2019) 146:850–62. doi:10.1121/1.5116561

35. Flores Parra E, Bergamini A, Van Damme B, Ermanni P. Controllable wave propagation of hybrid dispersive media with LC high-pass and band-pass networks. *Appl Phys Lett* (2017) 110:184103. doi:10.1063/1.4983088

36. Yi J, Ma Z, Xia R, Negahban M, Chen C, Li Z. Structural periodicity dependent scattering behavior in parity-time symmetric elastic metamaterials. *Phys Rev B* (2022) 106:014303. doi:10.1103/PhysRevB.106.014303

37. Chen Y, Hu G, Huang G. An adaptive metamaterial beam with hybrid shunting circuits for extremely broadband control of flexural waves. *Smart Mater Struct* (2016) 25:105036. doi:10.1088/0964-1726/25/10/105036

38. Li X, Chen Y, Hu GK, Huang G. A self-adaptive metamaterial beam with digitally controlled resonators for subwavelength broadband flexural wave attenuation. *Smart Mater Struct* (2018) 27:045015. doi:10.1088/1361-665X/aab167

39. Sugino C, Ruzzene M, Erturk A. Merging mechanical and electromechanical bandgaps in locally resonant metamaterials and metastructures. *J Mech Phys Sol* (2018) 116:323–33. doi:10.1016/j.jmps.2018.04.005

40. Xia R, Shao S, Yi J, Zheng K, Negahban M, Li Z. Tunable asymmetric transmission of Lamb waves in piezoelectric bimorph plates by electric boundary design. *Compos Structures* (2022) 300:116111. doi:10.1016/j.compstruct.2022.116111

41. Shao S, Xia R, Li Z. Tunable piezoelectric metasurface for manipulating multi-mode guided waves in plate. *Eng Structures* (2022) 270:114917. doi:10.1016/j.engstruct.2022.114917

42. Xia R, Yi J, Chen Z, Li Z. *In situ* steering of shear horizontal waves in a plate by a tunable electromechanical resonant elastic metasurface. *J Phys D Appl Phys* (2020) 53:095302. doi:10.1088/1361-6463/ab5cbc

43. Wang Y, Zhang C, Chen W, Li Z, Golub MV, Fomenko SI. Precise and target-oriented control of the low-frequency Lamb wave bandgaps. *J Sound Vibration* (2021) 511:116367. doi:10.1016/j.jsv.2021.116367

44. Kherraz N, Haumesser L, Levassort F, Benard P, Morvan B. Hybridization bandgap induced by an electrical resonance in piezoelectric metamaterial plates. *J Appl Phys* (2018) 123:094901. doi:10.1063/1.5016496

45. Chikh-Bled FH, Kherraz N, Sainidou R, Rembert P, Morvan B. Piezoelectric phononic plates: Retrieving the frequency band structure via all-electric experiments. *Smart Mater Struct* (2019) 28:115046. doi:10.1088/1361-665X/ab4aac

46. Kherraz N, Chikh-Bled FH, Sainidou R, Morvan B, Rembert P. Tunable phononic structures using Lamb waves in a piezoceramic plate. *Phys Rev B* (2019) 99:094302. doi:10.1103/PhysRevB.99.094302

47. Stroh AN. Dislocations and cracks in anisotropic elasticity. *Philos Mag* (1958) 3:625–46. doi:10.1080/14786435808565804

48. Stroh AN. Steady state problems in anisotropic elasticity. *J Maths Phys* (1962) 41:77–103. doi:10.1002/sapm196241177

49. Ting TTC. *Anisotropic elasticity: Theory and applications*. Oxford, UK: Oxford University Press (1996). doi:10.1093/oso/9780195074475.001.0001

50. Tanuma K. Stroh formalism and Rayleigh waves. *J Elast* (2007) 89:5–154. doi:10.1007/s10659-007-9117-1

51. Hsu CL, Hwu C, Shiah YC. Three-dimensional boundary element analysis for anisotropic elastic solids and its extension to piezoelectric and magnetoelectroelastic solids. *Eng Anal Boundary Elem* (2019) 98:265–80. doi:10.1016/j.enganabound.2018.10.022

52. Kuo HY, Shih CL, Pan E. Enhancing magnetoelectric effect in magneto-electro-elastic laminated composites via interface modulus and stress. *Int J Sol Structures* (2020) 195:66–73. doi:10.1016/j.ijsolstr.2020.03.014

53. Hsu CW, Hwu C. Holes/cracks/inclusions in magneto-electro-elastic composite laminates under coupled stretching-bending deformation. *Compos Structures* (2022) 297:115960. doi:10.1016/j.compstruct.2022.115960

54. Tassi N, Magouh N, Azrar L. 3D static analysis of homogenized piezoelectric plates based on the Mori-Tanaka and the Stroh approach. In: 2020 IEEE 7th International Conference on Engineering Technologies and Applied Sciences (ICETAS). Kuala Lumpur, Malaysia: IEEE (2020). p. 1–6. doi:10.1109/ICETAS51660.2020.9484313

55. Manyo Manyo JA, Ntamack GE, Azrar L. 3D-dynamic modeling of cross-ply magneto-electro-elastic laminates based on the pseudo-Stroh formalism. *Mech Adv Mater Structures* (2021) 28:1337–54. doi:10.1080/15376494.2019.1668094

56. Manyo Manyo JA, Ntamack GE, Azrar L. Time and frequency 3D-dynamic analyses of multilayered magnetoelectroelastic plates with imperfect interfaces. *Arch Appl Mech* (2022) 92:2273–301. doi:10.1007/s00419-022-02177-3

57. Magouh N, Lahcen A. Mathematical modeling of linear dynamic response of piezoelectric single Pz52 plates based on Stroh-like Formalism. In: 2021 7th International Conference on Optimization and Applications (ICOA). Wolfenbüttel, Germany: IEEE (2021). p. 1–6. doi:10.1109/ICOA51614.2021.9442670

58. Ewolo Ngak FP, Ntamack GE, Azrar L. Dynamic analysis of multilayered magnetoelectroelastic plates based on a pseudo-Stroh formalism and Lagrange polynomials. *J Intell Mater Syst Structures* (2019) 30:939–62. doi:10.1177/1045389X19828505

59. Tian R, Liu J, Pan E, Wang Y. SH waves in multilayered piezoelectric semiconductor plates with imperfect interfaces. *Eur J Mech - A/Solids* (2020) 81:103961. doi:10.1016/j.euromechsol.2020.103961

60. Huang H, Zhu F, Zhu J, Wang B, Qian Z. A general approach for dispersion relations in multilayered structures with an arbitrary number of piezoelectric layers and elastic layers. *Acta Mech* (2020) 231:489–502. doi:10.1007/s00707-019-02540-6

61. Kuo HY, Wang YH. Wave motion of magneto-electro-elastic laminated plates with membrane-type interfacial imperfections. *Compos Structures* (2022) 293:115661. doi:10.1016/j.compstruct.2022.115661

62. Tian R, Liu J, Pan E, Wang Y, Soh AK. Some characteristics of elastic waves in a piezoelectric semiconductor plate. *J Appl Phys* (2019) 126:125701. doi:10.1063/1.5116662

63. Graff KF. *Wave motion in elastic solids*. Chelmsford, MA, USA: Courier Corporation (2012).

frontiers | Frontiers in Physics

TYPE Brief Research Report
PUBLISHED 21 March 2023
DOI 10.3389/fphy.2023.1133586

OPEN ACCESS

EDITED BY
Yangyang Chen,
Hong Kong University of Science and Technology, Hong Kong SAR, China

REVIEWED BY
Hui Chen,
Ningbo University, China
Zongliang Du,
Dalian University of Technology, China

*CORRESPONDENCE
Lingyun Yao,
lingyunyao@swu.edu.cn

SPECIALTY SECTION
This article was submitted to Physical Acoustics and Ultrasonics, a section of the journal Frontiers in Physics

RECEIVED 29 December 2022
ACCEPTED 09 March 2023
PUBLISHED 21 March 2023

CITATION
Yao J, Xu K, Yao D and Yao L (2023), A metamaterial cylindrical shell with multiple graded resonators for broadband longitudinal wave attenuation
.
Front. Phys. 11:1133586.
doi: 10.3389/fphy.2023.1133586

A metamaterial cylindrical shell with multiple graded resonators for broadband longitudinal wave attenuation

Jingyi Yao, Ke Xu, Dunhui Yao and Lingyun Yao*

College of Engineering and Technology, Southwest University, Chongqing, China

This paper investigates a metamaterial cylindrical shell with local resonators for broadband longitudinal wave attenuation. A three-component phononic crystal metamaterial cylindrical shell that opens local resonant bandgaps at low frequencies is formed by periodically inserting a lead column coated with soft rubber into an ordinary cylindrical shell. First, the governing equations of elastic wave propagation in cylindrical shell structures are derived through coordinate transformation. Subsequently, numerical models of the metamaterial cylindrical shell are established, and the dispersion relation and vibration transmission characteristics of this structure are calculated using the Finite Element Method (FEM). Finally, in order to further broaden the bandgaps and the strong suppression range of the structure, a multiple-graded-resonator metamaterial cylindrical shell with three different local resonators is also proposed. These local resonators have different start frequencies and locations of their longitudinal wave bandgaps, so they can be combined to produce a wider overall bandgap. Numerical results show that this kind of multiple-graded-resonator metamaterial cylindrical shell has a good vibration suppression effect on longitudinal waves in the range of approximately 180–710 Hz and the vibration suppression effect can reach −40 dB at best. In addition, experimental results on vibration transmission characteristics show good agreement with the numerical results. This work provides a new idea and method for the development of acoustic metamaterials to obtain broadband and low-frequency bandgaps for cylindrical shell structures.

KEYWORDS

longitudinal wave mitigation, vibration suppression, multiple-graded-resonators, vibration transmission, metamaterial cylindrical shell

1 Introduction

In recent years, the issue of mechanical system noise control has attracted an increasing amount of attention in a bid to improve the quality of the environment for people due to stringent legal regulations on noise. Vibration and noise control devices may affect the performance of mechanical systems. Therefore, novel solutions that are simple and easy to apply in engineering problems are needed in order to achieve excellent performance while meeting low noise requirements [1]. Phononic crystal (PC) structures are becoming increasingly interesting as an innovative and efficient noise control solution.

A phononic crystal is an artificial periodic elastic composite structure consisting of two or more materials with elastic wave bandgaps [2]. A periodic arrangement of scatters can prevent the propagation of elastic waves in certain frequency ranges, thus forming

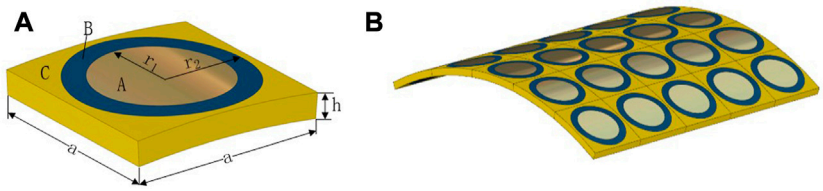

FIGURE 1
Metamaterial cylindrical shell: **(A)** unit cell; **(B)** 5 × 5 metamaterial cylindrical shell.

directional or complete bandgaps. The bandgaps in PCs can be used for sound insulation and environmental noise control [3–5]. The propagation of acoustic and elastic waves in PCs has attracted considerable attention over the past two decades [6–8]. Wu *et al.* [9] validated the existence of complete bandgaps and resonance in PC plates with periodic stubbed surfaces using numerical and experimental methods. Badreddine et al. [10] presented hybrid PCs composed of periodic stepped pillars and holes in order to obtain lower and wider bandgaps.

An original and impressive piece of work demonstrated the fact of spectral gaps with a lattice constant two orders of magnitude smaller than the relevant wavelength and presented the concept of a local resonance phononic crystal (LRPC) [11]. LRPC structures have shown particularly great potential in efficiently insulating noise and vibration [12, 13]. In LRPC structures, the existence of the stopband phenomenon is due to the distribution of resonance cells in the host structure at the sub-wavelength scale (i.e., the size is smaller than the wavelength of host structure at the frequency of interest) [14]. The stopbands of LRPCs are almost fully independent of the spatial arrangement of scatters, and the widths of the stopbands are closely related to the filling ratio [15].

In acoustic metamaterial design, a flat host structure is a common type of structure in engineering applications. Many researchers focus on metamaterials with a flat host structure, such as acoustic metamaterial beams [16–18] and plates [19, 20]. However, the range of applications of complete beams and plates in engineering is narrower than that of cylindrical shell structures. Cylindrical shells form the basic structure used in various aircrafts, ships, rockets, and precision instruments, and are widely used in the chemical industry, aerospace, and national defense, among other domains. Therefore, researchers have extensively studied wave propagation in cylindrical shells using analytical and numerical methods. The propagation of axis waves in cylindrically curved panels of infinite length was studied by Pany et al., and their natural frequencies of bending vibration were determined [21]. Recently, the Wave Finite Element Method was utilized by Manconi et al. to analyze wave dispersion in isotropic and orthotropic cylindrical panels and closed cylindrical shells [22]. The stopband behavior of cylindrically curved metamaterial panels in different directions was studied by Nateghi et al., who also discuss the influence of the radius of the cylindrical shell on the bandgaps [23].

The studies mentioned above have mainly focused on the fundamental mechanism of wave propagation in acoustic metamaterials, while other researchers have attempted to adjust the width and location of the bandgaps of acoustic metamaterials by theoretical and experimental methods. In many engineering

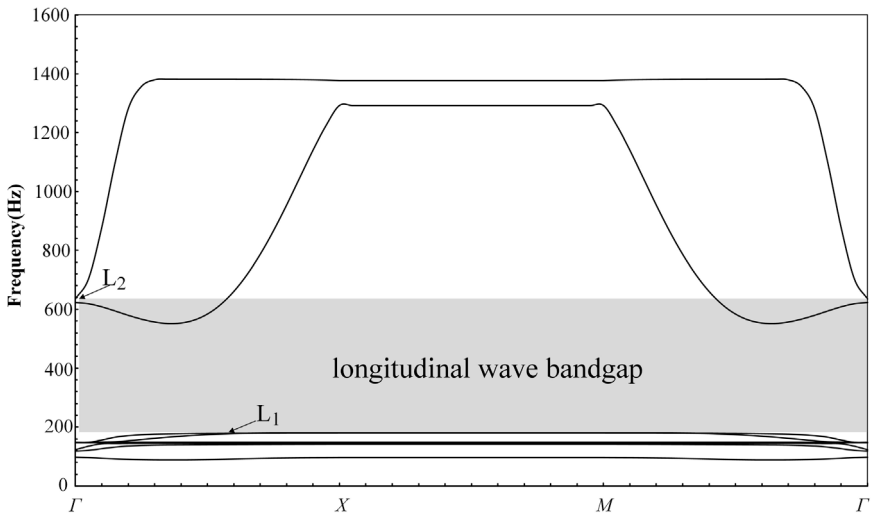

FIGURE 2
Dispersion curves of the unit cell with r_1 = 10 mm.

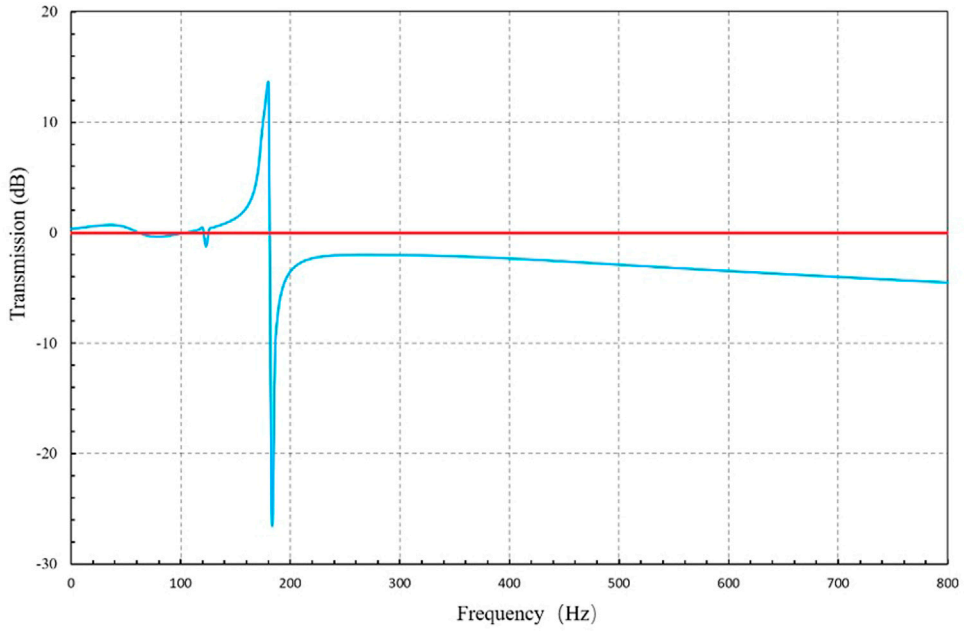

FIGURE 3
Longitudinal transmission coefficient of the cylindrical shell model with r_1 = 10 mm.

applications, a broadband resonant metamaterial is more appealing than conventional linear narrow-band metamaterials. Banerjee et al. [24] studied the graded parametrical arrangements of resonating units to modify the ranges of the stopband and transmission band. In addition, Ding et al. [25] proposed a broadband acoustic metamaterial with a space-coiling structure including an impedance-matching layer introduced between the air and the metamaterial. The impedance-matching layer was achieved by specifically designing the parameters of the space-coiling structure to form a gradient index. A hierarchical structure was also constructed to work in broadband, in which the shock wave was resisted in multiple bands, and the relationship between these bands and the hierarchy was thoroughly demonstrated. There is also another way to design multi-resonator metamaterials [26], namely by increasing the number of internal masses arranged in parallel in each metamaterial unit. An acoustic metamaterial plate was designed by integrating mass–spring subsystems with two degrees of freedom with an isotropic plate to act as vibration absorbers. A theoretical model of one-dimensional (1D) periodic graded metacomposites has been studied to investigate and enlarge the bandgaps in which wave propagation is prevented [27].

To the authors' knowledge, the propagation of longitudinal waves in three-component PC metamaterial cylindrical shells has never been studied in previous work. Motivated by the objective of understanding stopband behavior in PCs for wave propagation, this paper presents a study of the propagation of longitudinal waves in three-component PC metamaterial cylindrical shells based on the local resonance mechanism. First, the finite periodic condition along the circumferential direction of the cylindrical shell is transformed into an infinite periodic condition by coordinate transformation. Subsequently, numerical models for cylindrical shells are established by deriving the dynamic equation and the Bloch periodic condition, the dispersion relation of the unit cell is calculated using the Finite Element Method, and the effects of scatterer radius on stopband behavior are studied. Finally, the suppression of longitudinal waves in a finite periodic metamaterial cylindrical shell structure is further studied to verify the stopband behavior through numerical simulation and experimentation investigating the vibration transmission characteristics.

The paper is structured as follows. Section 2 briefly introduces the cylindrical shell model and presents a derivation of the governing equations of elastic waves. Section 3 presents a calculation of the dispersion relation of the unit cell and the vibration transmission characteristics of the finite structure using the FEM. The multiple-graded-resonator structure is presented and its vibration transmission characteristics are studied *via* experimentation and simulation in Section 4. Several conclusion are presented in the final section.

2 Theoretical foundation

This section briefly introduces the unit cell for metamaterial cylindrical shells and illustrates the rule of coordinate transformation. Subsequently, the numerical model for the unit cell is established through derivation of the governing equations of elastic waves.

2.1 Coordinate transformation

The unit cell of the metamaterial cylindrical shell investigated is as shown in Figure 1A. The lattice constant is *a*, and the shell

thickness is $h = 0.1 \times a$. The radii of the cylindrical shell, the scatterer A, and the connector B are R, r_1, and r_2, respectively. The unit cell is composed of a lead cylinder coated with a silicone rubber layer, arranged periodically in the epoxy resin matrix C. Figure 1B shows the 5 × 5 metamaterial cylindrical shell.

To better describe the unit cell of the metamaterial cylindrical shell, it is necessary to convert from the Cartesian coordinate system to the cylindrical coordinate system, in which points are represented by ring coordinate s, axis coordinate y, and transverse coordinate z representing distance from the cylinder center.

The transformation equation is as follows:

$$R\theta \to s, z \to y, r \to z \tag{1}$$

and the corresponding displacement is given by:

$$u_\theta \to u, u_z \to v, u_r \to w \tag{2}$$

At a given moment, the non-zero strains are therefore:

$$\begin{aligned} \varepsilon_{ss} &= -\frac{w}{R} + \frac{\partial u}{\partial s} - z\left(\frac{\partial^2 w}{\partial s^2} + \frac{1}{R}\frac{\partial u}{\partial s}\right) \varepsilon_{yy} = \frac{\partial v}{\partial y} - z\frac{\partial^2 w}{\partial y^2} \\ \varepsilon_{sy} &= \frac{1}{2}\left[\frac{\partial v}{\partial s} + \frac{\partial u}{\partial y} - z\left(2\frac{\partial^2 w}{\partial s \partial y} + \frac{1}{R}\frac{\partial u}{\partial y}\right)\right] \end{aligned} \tag{3}$$

2.2 Derivation of governing equations

In order to obtain the governing equation for the time-harmonic vibration of the cylindrical shell with multiple graded resonators shown in Figure 1B, it is assumed that the shell is very thin. Given this assumption, we can obtain the kinetic energy δT, elastic energy δU, and non-conservative work done δW by the external loads:

$$\delta T = -\int_s \int_y \rho h \ddot{u} \delta u ds dy - \int_s \int_y \rho h \ddot{v} \delta v ds dy - \int_s \int_y \rho h \ddot{w} \delta w ds dy \tag{4}$$

$$\delta W = 0 \tag{5}$$

$$\delta U = \int_{-s_0/2}^{+s_0/2} \int_{-y_0}^{+y_0} \int_{-h/2}^{+h/2} \left[\left(\varepsilon_{ss} \cdot \delta\varepsilon_{ss} + \varepsilon_{yy} \cdot \delta\varepsilon_{yy} + 2\varepsilon_{ss} \cdot \delta\varepsilon_{yy}\right) \cdot E^* + G\varepsilon_{sy} \cdot \delta\varepsilon_{sy}\right] ds dy dh \tag{6}$$

where Poisson's ratio is denoted by ν, Young's modulus is denoted by E, $E^* \equiv \frac{E}{(1-\nu^2)}$, and $G = \frac{E}{2(1+\nu)}$. By substituting Eq. 3 into Eq. 6 and integrating along the thickness direction, the total strain energy is obtained:

$$\delta U = \int_{-s_0/2}^{+s_0/2} \int_{-y_0}^{+y_0} \left(\hat{E}U_1 + DU_2\right) ds dy \tag{7}$$

where $D \equiv \frac{Eh^3}{12(1-\nu^2)}$, $\hat{E} \equiv \frac{Eh}{1-\nu^2}$.

$$\begin{aligned} U_1 = &\left(\frac{\partial u}{\partial s} + \frac{\partial v}{\partial y} - \frac{w}{R}\right)^2 \\ &+ \frac{1}{2}(1-\nu)\left[-4\left(\frac{\partial u}{\partial s} - \frac{w}{R}\right)\frac{\partial v}{\partial y} + \left(\frac{\partial u}{\partial y} + \frac{\partial v}{\partial s}\right)^2\right] \end{aligned} \tag{8}$$

$$\begin{aligned} U_2 = &\left(\frac{\partial^2 w}{\partial s^2} + \frac{\partial^2 w}{\partial y^2} + \frac{1}{R}\frac{\partial u}{\partial s}\right)^2 - 2(1-\nu)\frac{\partial^2 w}{\partial y^2}\left(\frac{\partial^2 w}{\partial s^2} + \frac{1}{R}\frac{\partial u}{\partial s}\right) \\ &+ \frac{1}{2}(1-\nu)\left(2\frac{\partial^2 w}{\partial s \partial y} + \frac{1}{R}\frac{\partial u}{\partial y}\right)^2 \end{aligned} \tag{9}$$

Using Hamilton's principle, we obtain:

$$\int_0^t (\delta T - (\delta U + \delta W))dt = 0 \tag{10}$$

Setting δw, δu, and δv to zero yields the governing equations of an infinitely long cylindrical shell with multiple graded resonators:

$$\hat{E}\begin{bmatrix} \frac{\partial^2 u}{\partial s^2} + \frac{1}{2}(1-\nu)\frac{\partial^2 u}{\partial y^2} \\ +\frac{1}{2}(1+\nu)\frac{\partial^2 v}{\partial s \partial y} - \frac{1}{R}\frac{\partial w}{\partial s} \end{bmatrix} + \frac{D}{R^2}\begin{bmatrix} \frac{\partial^2 u}{\partial s^2} + \frac{1}{2}(1-\nu)\frac{\partial^2 u}{\partial y^2} \\ +R\frac{\partial^3 w}{\partial y^2 \partial s} + R\frac{\partial^3 w}{\partial s^3} \end{bmatrix} = \rho h \frac{\partial^2 u}{\partial t^2} \tag{11}$$

$$\hat{E}\left[\frac{1}{2}(1+\nu)\frac{\partial^2 u}{\partial s \partial y} + \frac{\partial^2 v}{\partial y^2} + \frac{1}{2}(1-\nu)\frac{\partial^2 v}{\partial s^2} - \frac{\nu}{R}\frac{\partial w}{\partial y}\right] = \rho h \frac{\partial^2 v}{\partial t^2} \tag{12}$$

$$\begin{aligned} &-\hat{E}\left[\frac{1}{R}\frac{\partial u}{\partial s} + \frac{\nu}{R}\frac{\partial v}{\partial s} - \frac{w}{R^2}\right] + D\left[\frac{\partial^4 w}{\partial s^4} + 2\frac{\partial^4 w}{\partial s^2 \partial y^2} + \frac{\partial^4 w}{\partial y^4}\right] \\ &+ \frac{D}{R}\left[\frac{\partial^3 u}{\partial y^2 \partial s} + \frac{\partial^3 u}{\partial s^3}\right] = -\rho h \frac{\partial^2 w}{\partial t^2} \end{aligned} \tag{13}$$

3 Numerical simulation

In this section, the dispersion relation of the unit cell is calculated using the FEM and the effects of scatterer radius on longitudinal wave stopband are discussed. In order to verify the attenuation effect on longitudinal vibration in the finite structure of metamaterial cylindrical shells, we also study the vibration transmission characteristics.

3.1 Calculation and discussion of dispersion relation

In the present work, the COMSOL Multiphysics software package was used to calculate the dispersion relation of metamaterial cylindrical shells by eigenvalue analysis in solid mechanics. The details of the FEM model are as follows: the unit cell is divided into 1,855 nodes, and the number of degrees of freedom is 37,449. In addition, the geometrical and material parameters identified in Figure 1 are given: $a = 30$ mm, $h = 3$ mm, $r_1 = 10$ mm, $r_2 = 12$ mm, $R = 50$ mm. The density(ρ) of the scatterer A (made of lead) is 11,600 kg m^{-3}, Poisson's ratio (ν) is 0.369, and Young's modulus (E) is 40.8 GP. The connector B is made of silicone rubber, $\rho = 1{,}300$ kg m^{-3}, $\nu = 0.469$, $E = 1.175e^{-4}$GP. The cylindrical shell C is made of epoxy resin, $\rho = 1{,}180$ kg m^{-3}, $\nu = 0.368$, $E = 4.35$ GP.

Figure 2 shows the numerical simulation results for the dispersion curves. The dispersion curves exhibit several different propagation waves. The bandgap for longitudinal waves ranges from 188 to 635 Hz because there are no freely propagating solutions in the longitudinal mode.

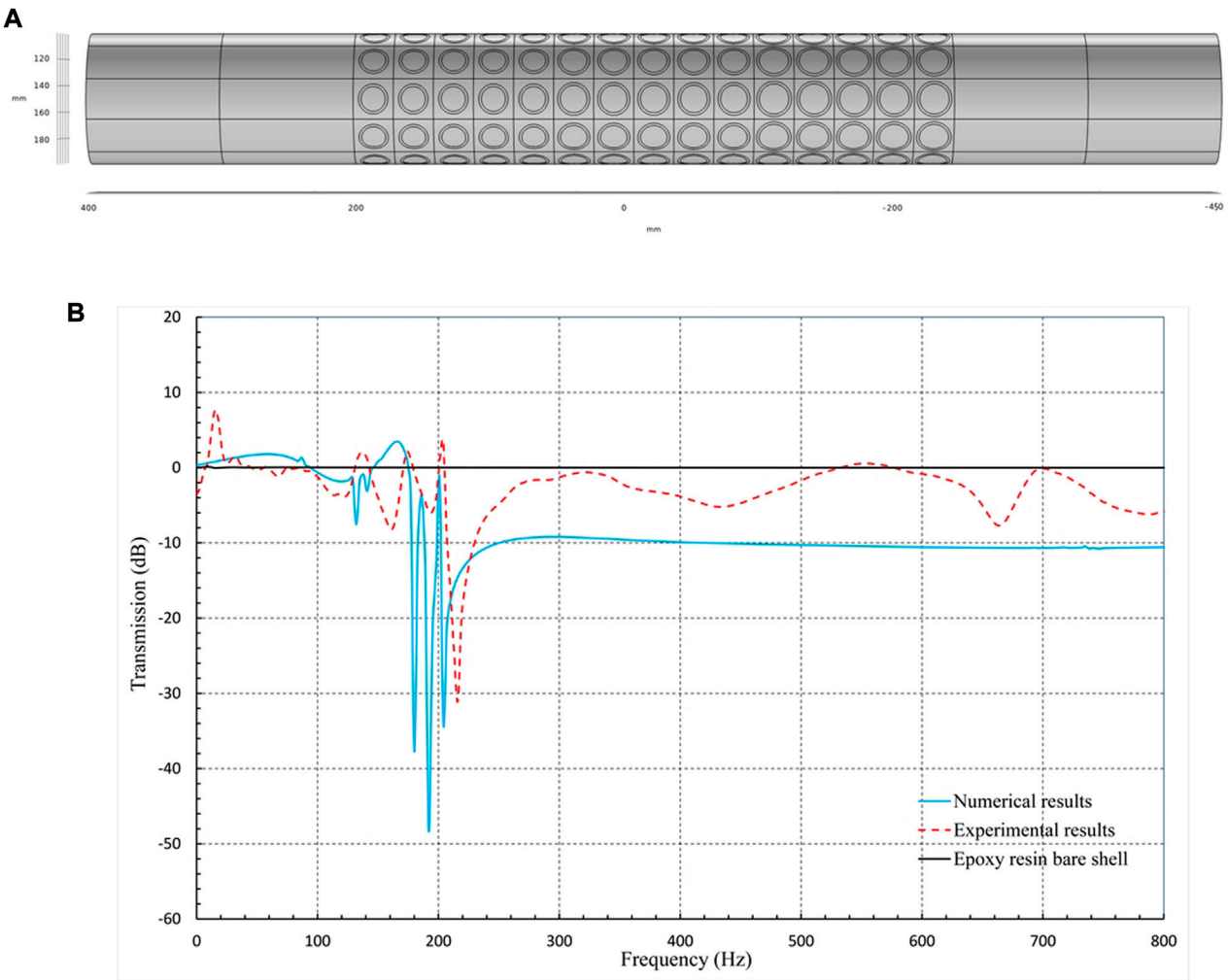

FIGURE 4
Cylindrical shell with multiple graded resonators: **(A)** the numerical model; **(B)** longitudinal transmission coefficient.

3.2 Effect of the scatterer radius

In order to obtain a wider longitudinal wave bandgap, we also studied the effect of scatterer radius on stopband behavior. For this purpose, we calculated the dispersion relation for unit cells with scatterer radii of 9, 10, and 11 mm. The bandgaps in the 9, 10, and 11 mm cases fell within the intervals (199,589), (188,635), and (178,711), respectively. It can be seen that with the increase in scatterer radius, the start frequency of the bandgap decreases slightly, while the stop frequency increases greatly. These shifts are caused by the increase in scatterer mass and filling rate, respectively.

3.3 Vibration transmission analysis for the finite periodic structure

The dispersion curves illustrate the frequency location and width of the bandgap. However, the dispersion curves cannot provide a full explanation of the vibration characteristics of the finite periodic structure. To further illustrate the vibration transmission characteristics and validate the accuracy of the bandgap, an analysis of vibration transmission for the finite periodic structure is presented in this section.

The finite periodic metamaterial cylindrical shell consists of 25 unit cells arranged periodically in a 5 × 5 layout along the *s* and *y* directions. To determine the transmission coefficient along the ΓX direction, incident longitudinal waves along this axis direction are modeled by applying harmonic displacements $Q_{inc} = q_{inc}e^{i\omega t}$ in the axis direction. The homogeneous parts are the transitional material connecting the periodic structure and the perfectly matched layers (PMLs). The PMLs are applied at both ends of the homogeneous part to prevent reflections by the scattering waves from the domain boundaries. Both the homogeneous parts and the PMLs have the same material parameters as the matrix. In addition, periodic boundary conditions are applied in the plane of the *s* direction.

The harmonic displacement response occurring along the interface between the homogeneous part and the periodic structure on the right side is represented by $Q_{res} = q_{res}e^{i\omega t}$. The transmission coefficient should be defined as:

$$T = 20lg\frac{Q_{res}}{Q_{inc}} \tag{14}$$

A frequency domain analysis sweeping from 0 to 800 Hz at intervals of 3 Hz was performed, and the simulated transmission coefficient as a function of frequency is plotted in Figure 3. The transmission coefficient agrees well with the corresponding dispersion curves of the unit cell, but the longitudinal wave transmission coefficient exhibits strong attenuation only at the start frequency of the bandgap, due to Fano-like interference phenomena. This shows that the metamaterial cylindrical shell structure has good vibration absorption characteristics.

4 The multiple-graded-resonator cylindrical shell

In this section, a cylindrical shell structure with multiple graded resonators, composed of scatterers with three different radii, is proposed in order to widen the longitudinal wave bandgaps. Additionally, the vibration transmission characteristics of this structure without a PML are verified *via* experiments.

As stated in the previous section, due to the presence of Fano-like interference in the metamaterial based on the local resonance mechanism, the longitudinal vibration transmission of the metamaterial only exhibits strong attenuation at the start frequency of the bandgaps. Therefore, we propose a multiple-graded-resonator cylindrical shell structure with a wider range of strong vibration attenuation, developed by combining three kind of metamaterial cylindrical shells with different start frequencies and locations, as shown in Figure 4A.

In order to verify the practical attenuation effect of the longitudinal vibration of this structure, we carried out a vibration attenuation experiment using a Siemens data acquisition instrument (type: LMS SCADAS Mobile). Two accelerometers (type: 356A16 SNLW180872; sensitivity: 98.3 mv/g) were used, with one placed at each end of the model. A hammer (type: PCB 086C01; sensitivity: 11.2 mv/N) was used to strike the model on one side.

The materials of the subject were consistent with those described in Section 3.1, and the components were connected to each other by adhesive bonding. In the experiment, vertical excitation was induced by the hammer hitting the outer surface of one end of the subject, which was freely positioned on a sponge, and the acceleration sensor was used to collect the stable response of the target point in the range 0–800 Hz. Subsequently, the transmission coefficient was obtained using Eq. 14.

Figure 4B shows the comparison between the experimental results and the simulation results on the vibration transmission characteristics of the multiple-graded-resonator structure.

As can be seen, the experimental results on the vibration transmission characteristics exhibit the same trend as the numerical results. In general, although the longitudinal vibration attenuation effect of the actual structure was slightly smaller than the effect in the simulation results, the bandwidth of the actual attenuation was wider. For the actual structure, there were three attenuation peaks at 162, 192, and 216 Hz. The first and third attenuation peaks differed by approximately 15 Hz from the simulation results, in which the corresponding peaks occurred at 178 and 201 Hz. Deviations in the material parameters and manufacturing process may be the main reason for the offset between experimental results and numerical results. In addition, the range of bandgaps of the multiple-graded-resonator cylindrical shell is the superposition of three single-resonator structures, and the strong attenuation range of this multiple-graded-resonator cylindrical shell (180–255 Hz) is approximately triple that of the single-resonator structure (178–199 Hz).

5 Conclusion

The present work investigated the property of longitudinal wave propagation in a metamaterial cylindrical shell. The dispersion curves of the proposed structure were used to analyze stopband behavior. Several numerical and experimental tests were also conducted and the results investigated in detail to study the effectiveness of the proposed structure. The following conclusions resulted from the work:

(1) The metamaterial cylindrical shell structure creates a longitudinal wave bandgap at 188–635 Hz, in which the propagation of longitudinal waves is impossible.
(2) As the scatterer radius is increased, the start frequency of the bandgap decreases slightly, while the stop frequency increases greatly; these shifts are caused by the increase in scatterer mass and filling rate, respectively.
(3) The bandgap range of the multiple-graded-resonator cylindrical shell is the superposition of that of three single-resonator structures, and the strong attenuation range of the multiple-graded-resonator cylindrical shell is triple that of the single-resonator structure. The development of this metamaterial cylindrical shell structure and the use of multiple graded resonators pave the way toward vibration reduction and noise control in the cylindrical shell structure.

Data availability statement

The raw data supporting the conclusion of this article will be made available by the authors, without undue reservation.

Author contributions

JY: Conceptualization, methodology, and writing; KX: Modeling and writing; DY: Modeling, methodology, and writing; LY: Conceptualization, discussions, and editing. All authors contributed to the article and approved the submitted version.

Funding

This work was supported by the National Natural Science Foundation of China (No. 52175121).

Conflict of interest

The authors declare that the research was conducted in the absence of any commercial or financial relationships that could be construed as a potential conflict of interest.

Publisher's note

References

1. Panza MA. A review of experimental techniques for NVH analysis on a commercial vehicle. *Energ Proced* (2015) 82:1017–23. doi:10.1016/j.egypro.2015.11.861

2. Deymier PA. *Acoustic Metamaterials and phononic crystals*. Berlin Heidelberg: Springer-Verlag (2013).

3. Li L, Gang X, Sun Z, Zhang X, Zhang F. Design of phononic crystals plate and application in vehicle sound insulation. *Adv Eng Softw* (2018) 1(125):19–26. doi:10.1016/j.advengsoft.2018.08.002

4. Charles C, Bonello B, Ganot F. Propagation of guided elastic waves in 2D phononic crystals. *Ultrasonics* (2006) 44(4):e1209–13. doi:10.1016/j.ultras.2006.05.096

5. Song Y, Wen J, Yu D, Liu Y, Wen X. Reduction of vibration and noise radiation of an underwater vehicle due to propeller forces using periodically layered isolators. *J Sound vibration* (2014) 333(14):3031–43. doi:10.1016/j.jsv.2014.02.002

6. Yao L, Huang G, Chen H, Barnhart MV. A modified smoothed finite element method (M-SFEM) for analyzing the band gap in phononic crystals. *Acta Mech* (2019) 230(6):2279–93. doi:10.1007/s00707-019-02396-w

7. Yao L, Jiang G, Wu F, Luo J. Band structure computation of two-dimensional and three-dimensional phononic crystals using a finite element-least square point interpolation method. *Appl Math Model* (2019) 76:591–606. doi:10.1016/j.apm.2019.05.052

8. Yao LY, Wu F, Wu G. Numerical study of exterior acoustic problems using a novel finite element-least square point interpolation method with perfectly matched layerfinite element-least square point interpolation method with perfectly matched layer. *Eng Anal Boundary Elem* (2019) 102:87–96. doi:10.1016/j.enganabound.2019.01.021

9. Wu TT, Huang ZG, Tsai TC, Wu TC. Evidence of complete band gap and resonances in a plate with periodic stubbed surface. *Appl Phys Lett* (2008) 93(11):111902. doi:10.1063/1.2970992

10. Badreddine Assouar M, Sun JH, Lin FS, Hsu JC. Hybrid phononic crystal plates for lowering and widening acoustic band gaps. *Ultrasonics* (2014) 54(8):2159–64. doi:10.1016/j.ultras.2014.06.008

11. Liu Z, Zhang X, Mao Y, Zhu YY, Yang Z, Chan CT, et al. Locally resonant sonic materials. *science* (2000) 289(5485):1734–6. doi:10.1126/science.289.5485.1734

12. Liu Z, Chan CT, Sheng P. Analytic model of phononic crystals with local resonances. *Phys Rev B* (2005) 71(1):014103. doi:10.1103/physrevb.71.014103

13. Goffaux C, Sánchez-Dehesa J. Two-dimensional phononic crystals studied using a variational method: Application to lattices of locally resonant materials. *Phys Rev B* (2003) 67(14):144301. doi:10.1103/physrevb.67.144301

14. Claeys CC, Sas P, Desmet W. On the acoustic radiation efficiency of local resonance based stop band materials. *J Sound Vibration* (2014) 333(14):3203–13. doi:10.1016/j.jsv.2014.03.019

15. Zhang X, Liu Y, Wu F, Liu Z. Large two-dimensional band gaps in three-component phononic crystals. *Phys Lett A* (2003) 317(1-2):144–9. doi:10.1016/j.physleta.2003.08.032

16. Chen H, Li XP, Chen YY, Huang G. Wave propagation and absorption of sandwich beams containing interior dissipative multi-resonators. *Ultrasonics* (2017) 76:99–108. doi:10.1016/j.ultras.2016.12.014

17. Sharma B, Sun CT. Impact load mitigation in sandwich beams using local resonators. *J sandwich structures Mater* (2016) 18:50–64. doi:10.1177/1099636215583171

18. Yao DH, Xiong MK, Luo JY, Yao L. Flexural wave mitigation in metamaterial cylindrical curved shells with periodic graded arrays of multi-resonator. *Mech Syst Signal Process* (2022) 168:108721. doi:10.1016/j.ymssp.2021.108721

19. Oudich M, Li Y. Tunable sub-wavelength acoustic energy harvesting with a metamaterial plate. *J Phys D: Appl Phys* (2017) 50(31):315104. doi:10.1088/1361-6463/aa779d

20. He ZC, Xiao X, Li E. Design for structural vibration suppression in laminate acoustic metamaterials. *Composites B: Eng* (2017) 131:237–52. doi:10.1016/j.compositesb.2017.07.076

21. Pany C, Parthan S. Axial wave propagation in infinitely long periodic curved panels. *J Vibration Acoust* (2003) 125(1):24–30. doi:10.1115/1.1526510

22. Manconi E, Mace B. Wave characterization of cylindrical and curved panels using a finite element method. *The J Acoust Soc America* (2009) 125(1):154–63. doi:10.1121/1.3021418

23. Nateghi A, Belle LV, Claeys C, Deckers E, Pluymers B, Desmet W. Wave propagation in locally resonant cylindrically curved metamaterial panels. *Int J Mech Sci* (2017) 127:73–90. doi:10.1016/j.ijmecsci.2016.07.003

24. Banerjee A, Das R, Calius EP. Frequency graded 1D metamaterials: A study on the attenuation bands. *J Appl Phys* (2017) 122(7):075101. doi:10.1063/1.4998446

25. Ding YH, Yi H, Statharas EC, Hong M. A broadband acoustic metamaterial with impedance matching layer of gradient index. *Appl Phys Lett* (2017) 110(24):241903. doi:10.1063/1.4986472

26. Yu X, Lu ZB, Cui FS, Cheng L, Cui Y. Tunable acoustic metamaterial with an array of resonators actuated by dielectric elastomer. *Extreme Mech Lett* (2017) 12:37–40. doi:10.1016/j.eml.2016.07.003

27. An X, Fan H, Zhang C. Wave dispersion in one-dimensional periodic graded metacomposites. *J Sound Vibration* (2017) 409:217–26. doi:10.1016/j.jsv.2017.08.002

frontiers | Frontiers in Physics

TYPE Original Research
PUBLISHED 26 April 2023
DOI 10.3389/fphy.2023.1191108

OPEN ACCESS

EDITED BY
Feng Zhou,
Toyota Research Institute of North America, United States

REVIEWED BY
Yabin Jin,
Tongji University, China
Yongyuan Jiang,
Harbin Institute of Technology, China

*CORRESPONDENCE
Rui Wang,
wangruinuc@163.com

RECEIVED 21 March 2023
ACCEPTED 13 April 2023
PUBLISHED 26 April 2023

CITATION
Han J and Wang R (2023), Switchable acoustic projection displays based on coding composite structures.
Front. Phys. 11:1191108.
doi: 10.3389/fphy.2023.1191108

Switchable acoustic projection displays based on coding composite structures

Jianning Han and Rui Wang*

School of Information and Communication Engineering, North University of China, Taiyuan, Shanxi, China

Projection display is of relevance for various applications, for example, information communication, encryption and storage. Although numerous optical projection devices have been reported in past years, the realization of switchable acoustic projection display without built-in circuits is a challenge. In this work, we propose a coding composite structure composed of a perforated plate and a coiling-up cavity with six interdigital rigid walls to achieve switchable acoustic projection displays. The configuration can be served as bits '0' and '1' by using forward and backward placements, respectively. The required projection can be displayed as long as the expected image regions are filled with bit '1' and other regions are filled with bit '0'. By switching control wave P_c, the projected image is able to be switched from 'Off state' to 'On state' accordingly. The underlying physical mechanism is the different scattering responses between two coding bits induced by coherent superposition. Our design provides an effective solution for the construction of acoustic projection displays with switchable feature, which may have potential applications in information encryption and storage.

KEYWORDS

composite structure, coiling-up cavity, switchable projection, coherent superposition, artificial structure

1 Introduction

As an effective approach to display required images or information, projection device plays important roles in many applications including light-emitting diode screens, electronic billboard signage and traffic light. Despite numerous achievements in optical projection displays [1–10], the similar devices in acoustic category have not been widely reported so far, especially for switchable fashion without built-in circuits. The realization of acoustic projection display is of great significant in information storage and communication. Given the advantages of subwavelength scale, flexibility and planer feature, the development of acoustic metasurface provides a possible solution for the design of acoustic projection device.

In past several years, acoustic metasurface (a composite structure with planer configuration) has been demonstrated to be good candidates to achieve various fascinating phenomena, such as beam deflection [11–13], beam focusing [14–19], vortex beam [20], splitting beam [21] and Airy beam [22] by utilizing Helmholtz resonators [23, 24], coiling-up cavities [25], or spiral particles [26]. Owing to the shifts of equivalent refractive index induced by resonance effect, arbitrary phase or amplitude response can be obtained by adopting ultrathin structural design, making it is suitable to be integrated in acoustic devices. To accurately fit the phase or amplitude profile, however, multiple discrete orders are required for designed units, which increases the complexity of the structure. In addition, some harsh parameters may be involved in discrete process, which are hardly to be

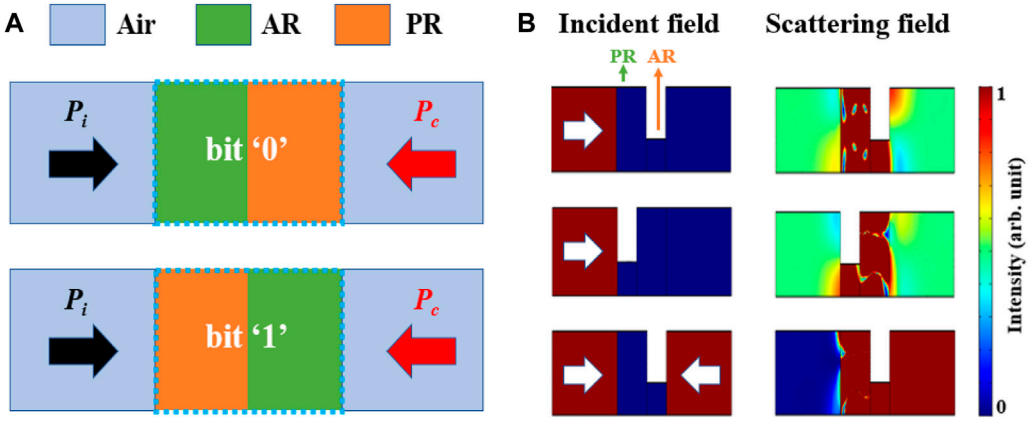

FIGURE 1
(A) Schematic diagrams of bits '0' and '1', where light blue region, green region and orange region are air background, AR and PR, respectively. The black and red arrows present the input wave P_i and control wave P_c. **(B)** The normalized incident and scattering fields of bits '0' and '1' for one side incidence and both sides incidence. The white arrows indicate the incident directions, and the operating frequency is 3,430 Hz.

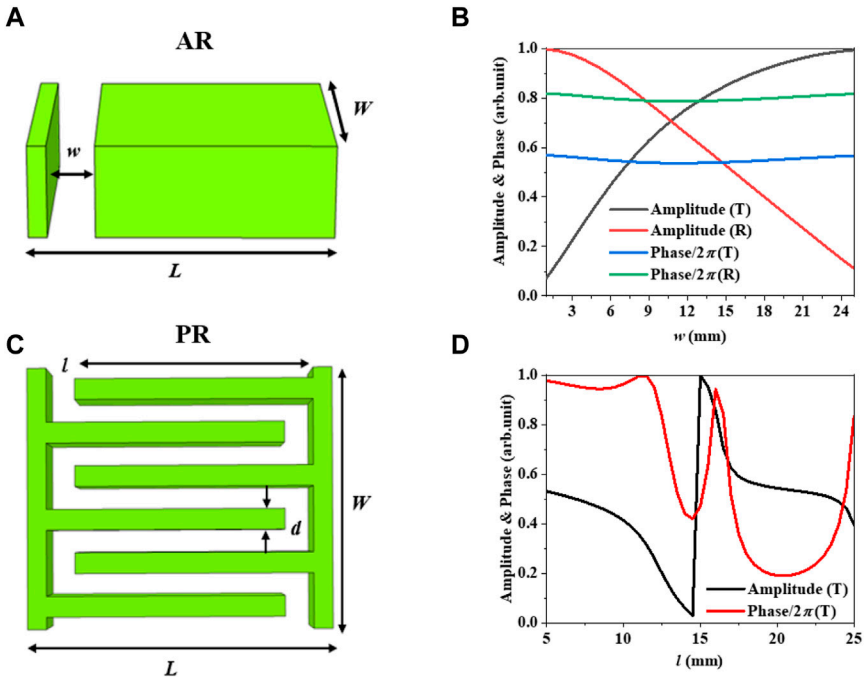

FIGURE 2
Schematic diagrams of **(A)** AR and **(C)** PR. AR is a perforated plate and PR is a coiling-up cavity with six interdigital rigid walls. The amplitude and phase responses of **(B)** AR and **(D)** PR with the change of w and l. The operating frequency is f = 3,430 Hz. The characters of 'T' and 'R' in legends of **(B)** and **(D)** present the transmission wave and reflection wave, respectively.

fabricated by 3D printing technology, and the thermal viscosity loss is non-negligible. Recently, the emergence of coding metasurface offers a simplified method for the realization of wavefront modulation [27–30]. Only two kinds of units with opposite phase responses (0 and π) are needed to serve as coding bit '0' and '1', and numerous beam-shaping behaviors can be achieved as well without complicated design philosophy. Hence, the combination between coding metasurface and acoustic projection displays is expected to be a valuable tool for advanced acoustic devices.

In this work, a composite structure composed of a phase regulator (PR) and an amplitude regulator (AR) is proposed to build switchable acoustic projection devices, through which arbitrary image can be projected by adopting corresponding coding sequences, and the 'On/Off states' are capable of switching by additional control wave P_c. To achieve desirable scattering responses for AR and PR, a perforated plate and a coiling-up cavity with six interdigital rigid walls are constructed to modulate the amplitudes and phases of scattering waves continuously. The composite structure can play the roles of bits '0' and '1' by using

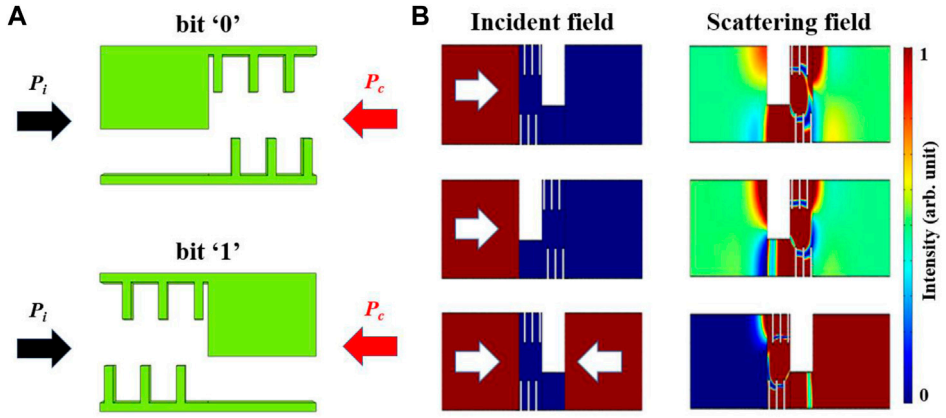

FIGURE 3
(A) Schematic diagram of the composite structure, which can be acted as bits '0' and '1' by using forward and backward placements, respectively. The black and red arrows present the input wave P_i and control wave P_c. **(B)** The incident and scattering fields of bits '0' and '1' for one side incidence and both sides incidence. The white arrows indicate the incident directions, and the operating frequency is 3,430 Hz.

forward and backward placements, respectively, due to their extremely asymmetric scattering responses induced by coherent superposition, greatly simplifying the design philosophy by using coding acoustic metasurface. The acoustic projection display illustrated in our work may have profound impact on exploring various acoustic information related devices.

2 Theory

To achieve switchable acoustic projection displays, we propose two kinds of unit and encode them as bits '0' and '1'. The transmission and reflection coefficients of bit '0' are assumed to be $T_0 = 1/\sqrt{2}$ and $R_0 = -1/\sqrt{2}$, respectively, while those of bit '1' are both desired to be $T_1 = R_1 = 1/\sqrt{2}$. In other words, bit '0' has the same transmission coefficient as bit '1', and the reflection coefficients between them have a phase difference of π. If two acoustic beams with opposite directions are incident on bits '0' and '1' simultaneously, the scattered acoustic pressures of 2 bits (S_0 and S_1) can be expressed as a matrix:

$$\begin{bmatrix} S_0 \\ S_1 \end{bmatrix} = \begin{bmatrix} T_0 & R_0 \\ T_1 & R_1 \end{bmatrix} \begin{bmatrix} P_i \\ P_c \end{bmatrix} = \frac{1}{\sqrt{2}} \begin{bmatrix} P_i - P_c \\ P_i + P_c \end{bmatrix} \tag{1}$$

where P_i and P_c represent input wave and control wave, respectively. Following Eq. 1, it can be deduced that the normalized amplitude of S_0 and S_1 are 0.5 in the case of only P_i incidence owing to the identical transmission response for bits '0' and '1'. When input wave and control wave are incident on them simultaneously, however, the normalized amplitude of S_0 and S_1 are 0 and 1 owing to the existence of destructive interference in bit '0' and constructive interference in bit '1'. Therefore, switchable acoustic projection displays are expected to be obtained by utilizing coherent incident waves with opposite propagating directions.

Here, we intend to construct a model with an asymmetric configuration to act as bits '0' and '1' by using forward and backward placements, respectively, which needs the scattered pressures on both sides of the model agree with those on right side of bits '0' and '1'. To achieve this goal, as shown in Figure 1A, we consider a composite structure composed of an AR and a PR. AR is placed on left and right sides of the PR for bits '0' and '1', respectively. Note that the phase (amplitude) response for AR (PR) is fixed when modulating the amplitude (phase) response continuously. For bit '0', the input wave P_i becomes $P_i{}^*t_A{}^*t_P$ after passing through AR and PR, and the control wave P_c becomes $P_c{}^*t_P{}^*r_A{}^*t_P$ because it first passes through PR, then is reflected by AR, and finally passes through PR again. t_P and t_A represent the transmittance of PR and AR, and r_A represent the reflection of AR. Therefore, the transmission and reflection coefficients of bits '0' and '1' can be expressed as follows:

$$\begin{bmatrix} T_0 & R_0 \\ T_1 & R_1 \end{bmatrix} = \begin{bmatrix} t_A t_P & t_P r_A t_P \\ t_P t_A & t_A \end{bmatrix} \tag{2}$$

From Eq. 2 it can be deduced that the phase difference between R_0 and R_1 is related to t_P, so the asymmetric phase response can be controlled by PR, and the exact values of scattering coefficients (T_0, T_1, R_0, R_1) are capable of modulating by AR accordingly. When input wave and control wave are incident on composite structure simultaneously, the scattered pressures on left side of the bits '0' and '1' can be expressed as:

$$\begin{bmatrix} S_{00} \\ S_{11} \end{bmatrix} = \begin{bmatrix} t_A t_P P_i + t_P r_A t_P P_C \\ t_P t_A P_i + r_A P_C \end{bmatrix} \tag{3}$$

According to Eq. 1, Eq. 3, the relation of $S_{00} = S_0$ and $S_{11} = S_1$ can be obtained when the requirements of $t_P = \exp(i\pi/2)$, $t_A = 1/\sqrt{2}\exp(-i\pi/2)$ and $r_A = 1/\sqrt{2}$ are satisfied, which indicates that the composite structure can serve as bits '0' and '1' simultaneously once the AR and PR with proper scattering coefficients are designed.

To verify above deductions, as shown in Figure 1B, an equivalent medium meeting the conditions of $t_P = \exp(i\pi/2)$, $t_A = 1/\sqrt{2}\exp(-i\pi/2)$ and $r_A = 1/\sqrt{2}$ is proposed to numerically simulate the incident and scattering fields of bits '0' and '1'. The module of pressure acoustic is adopted in *COMSOL Multiphysics* software. The condition of plane wave radiation is applied to the left and right boundaries of waveguide to suppress the unwanted

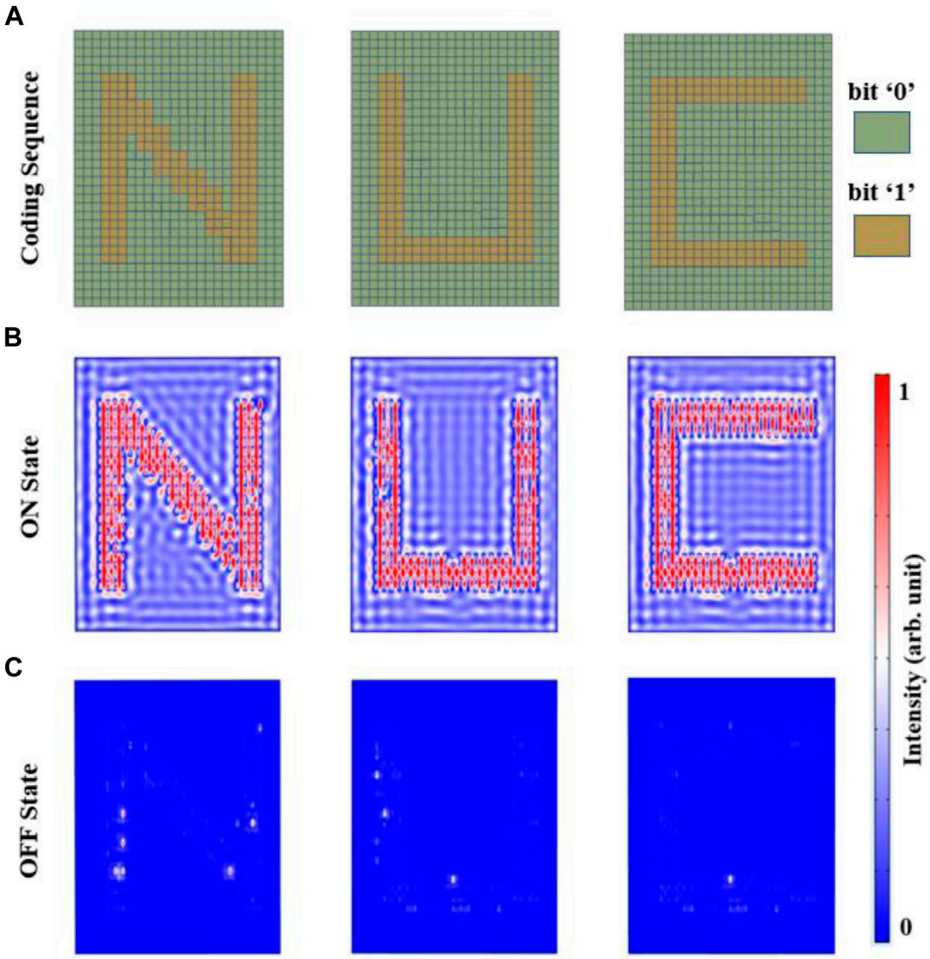

FIGURE 4
(A) Schematic diagrams of coding sequences adopted in projection acoustic devices for 'N', 'U', 'C'. The dark green region and dark yellow region represent bit '0' and bit '1', respectively. Acoustic scattering intensity fields of the projection devices with **(B)** input wave P_i incidence and **(C)** input wave P_i and control wave P_c incidence simultaneously.

reflection waves. The radiated acoustic pressure of the incident source is 1 Pa. Hard boundary condition is applied to the upper and lower boundaries of the waveguide to act as rigid material whose acoustic impedance is much larger than that of fluid background. In our simulations, the background medium is air (c_a = 343 m/s and ρ_a = 1.21 kg/m^3). To ensure the desirable phase delay and perfect transmittance, the equivalent acoustic velocity and density of the PR is set as c_e = 91.85 m/s and ρ_e = 4.8173 kg/m^3. The required amplitude response is achieved by adjusting the length of hard boundary between AR and scattering field. Three different incident cases, left side of bit '0' incidence, left side of bit '1' incidence, and both sides of composite structure incidence, are required to be considered. From the scattering fields of three incident cases, it can be observed that the intensity distributions in both sides of composite structure is almost identical for left side incident from bits '0' and '1', which shows that the normalized amplitude of S_0 and S_1 are 0.5 under this circumstance. For both sides of composite structure incidence, the intensity field in right side of bit '1' is strong, while that in left side of bit '1' is weak, illustrates an extremely asymmetric intensity response due to the coherent interference, and the normalized amplitude of S_0 and S_1 are 0 and 1 in this situation. The simulation results fully confirms that the amplitude of scattering wave for bit '0' is the same as that for bit '1' with only input wave P_i incidence, but the amplitude of scattering wave for bit '1' is larger than that for bit '0' with input wave P_i and control wave P_c incidence simultaneously, which agrees well with our theoretical prediction. Thus, the required projection can be displayed as long as the expected image regions are filled with bit '1' and other regions are filled with bit '0'. By switching control wave P_c, the projected image is able to be switched from dark state to bright state accordingly.

3 Structural design

To construct desirable composite structure, a practical configuration with phase and amplitude modulation capability is required. Note that the phase (amplitude) response needs to be fixed when the amplitude (phase) response is modulated continuously by AR (PR), and the transmittance of PR should be as high as possible to

guarantee the projection quality. As shown in Figures 2A,C, we propose a perforated plate and a coiling-up cavity with six interdigital rigid walls to serve as AR and PR, respectively. The length and width of AR and PR are L = 25 mm and W = 28 mm, which are much smaller than the operating wavelength λ_0 (L = 0.25λ_0, W = 0.28λ_0), and have the advantage of subwavelength scale. To obtain amplitude modulation, the opening size of the perforated plate is a variable from w = 5 mm to w = 25 mm. With the reduction of w, as shown in Figure 2B, the transmitted (reflected) amplitude decreases (increases) gradually owing to the impedance mismatch induced by small opening size, while the transmitted and reflected phase responses are nearly fixed, exhibiting an excellent ability for amplitude modulation independently. As a special case, when w = 10.8 mm the transmitted amplitude is the same as reflected amplitude ($T = R = 1/\sqrt{2}$), and the phase difference between transmission wave and reflection wave is $\pi/2$, which meets the requirement of scattering coefficients for AR.

On the other hand, to achieve phase modulation by PR, the length of interdigital rigid wall in a coiling-up cavity is set to a variable from l = 5 mm to l = 25 mm. The thickness of interdigital rigid wall is a constant of d = 2 mm. It can be seen from Figure 2D that the transmitted phase shifts cover a wide range of 0-2π with the change of parameter l, and the transmitted amplitude of PR is over 0.9 when l < 12 mm. The desirable phase delay is attributed to the length change of propagation path in PR induced by labyrinth configuration, and the high amplitude is owing to the impedance matching induced by resonance effect in PR. Note that the transmitted phase and amplitude is $\pi/2$ and 0.95, respectively, in the case of l = 8.6 mm, satisfying the requirement of scattering coefficients for PR.

Next, we splice the AR and PR to integrate an asymmetric composite structure. As shown in Figure 3A, the configuration can be served as bits '0' and '1' by using forward and backward placements, respectively. To obtain expected scattering feature, the parameters of w and l are selected as w = 10.8 mm and l = 8.6 mm. Figure 3B illustrates the incident fields and corresponding scattering fields for left side of bits '0' incidence, left side of bits '1' incidence, and both sides of bits '0' and '1' incidence. Compared with Figure 1B, Figure 3B, the results of intensity field (the square of acoustic pressure) for composite structure designed by a practical configuration are identical with those for composite structure designed by equivalent medium. For input acoustic wave P_i incidence, the transmitted amplitudes of bits '0' and '1' are 0.5, while those are 0 and 1, respectively, for input wave P_i and control wave P_c incidence simultaneously, fully confirming the feasibility of our approach to achieve switchable control of scattering field via two coherent incident acoustic waves.

4 Switchable projection displays

Given the scattering feature of the composite structure, as shown in Figure 4A, we construct three acoustic projection devices with different coding sequences. The metasurface is composed of 24 × 32 coding bits, where the expected image regions are filled with bit '1' and other regions are filled with bit '0'. To avoid the coupling actions between two coding bits, the distance between two adjacent coding bits is set as 2W. In addition, to observe the scattering fields conveniently, background pressure field is adopted in the incident field, and the plane acoustic waves are generated with a working frequency of 3,430 Hz. We define input wave P_i incidence as 'Off state' and input wave P_i and control wave P_c incidence simultaneously as 'On state'. For 'On state', as illustrated in Figure 4B, three different characters ('N', 'U', 'C') are projected clearly in the scattering fields of three proposed devices owing to the extremely asymmetric intensity responses between bits '0' and '1' in this case. For 'Off state', as shown in Figure 4C, the scattering field is a uniform field, and no obvious projection images are able to be observed in this case due to the identical intensity responses between bits '0' and '1'. Therefore, arbitrary image can be projected by adopting corresponding coding sequences, and the 'On/Off states' are capable of switching by control wave P_c.

5 Conclusion

An approach is exhibited in this work for switchable acoustic projection displays by using two identical coding units (bits '0' and '1') with different placements. To obtain desirable scattering coefficients for acoustic waves, an AR (a perforated plate) and a PR (a coiling-up cavity with six interdigital rigid walls) are constructed to decouple the phase and amplitude modulations. The composite structure composed of AR and PR shows an extremely asymmetric scattering feature when two coherent acoustic waves incident simultaneously. The required projection can be displayed as long as the expected image regions are filled with bit '1' and other regions are filled with bit '0' due to the coherent superposition. As examples, three distinct characters ('N', 'U', 'C') are projected clearly by adopting three different coding sequences, and the projected images are able to be switched from 'Off state' to 'On state' accordingly by switching control wave P_c, confirming the feasibility of our approach. Given the advantages of simplified and passive design, the acoustic projection device proposed in our work may have numerous acoustic related engineering applications.

Data availability statement

The original contributions presented in the study are included in the article/Supplementary Material, further inquiries can be directed to the corresponding author.

Author contributions

JH conceived the presented idea. RW performed the calculations and simulations and drafted the manuscript. All authors discussed the results and contributed to the final manuscript.

Funding

This work was supported by the Natural Science Foundation of Shanxi Province under Grant 202103021224201.

Conflict of interest

The authors declare that the research was conducted in the absence of any commercial or financial relationships that could be construed as a potential conflict of interest.

Publisher's note

References

1. Walter F, Li G, Meier C, Zhang S, Zentgraf T. Ultrathin nonlinear metasurface for optical image encoding. *Nano Lett* (2017) 17:3171–5. doi:10.1021/acs.nanolett.7b00676

2. Wintz D, Genevet P, Ambrosio A, Woolf A, Capasso F. Holographic metalens for switchable focusing of surface plasmons. *Nano Lett* (2015) 15:3585–9. doi:10.1021/acs.nanolett.5b01076

3. Wang Q, Zhang X, Plum E, Xu Q, Wei M, Xu Y, et al. Polarization and frequency multiplexed terahertz meta-holography. *Adv Opt Mater* (2017) 5:1700277. doi:10.1002/adom.201700277

4. Huang YW, Chen WT, Tsai WY, Wu PC, Wang CM, Sun G, et al. Aluminum plasmonic multicolor meta-hologram. *Nano Lett* (2015) 15:3122–7. doi:10.1021/acs.nanolett.5b00184

5. Ye WM, Zeuner F, Li X, Reineke B, He S, Qiu CW, et al. Spin and wavelength multiplexed nonlinear metasurface holography. *Nat Commun* (2016) 7:11930. doi:10.1038/ncomms11930

6. Zhang CM, Yue FY, Wen DD, Chen M, Zhang ZR, Wang W, et al. Multichannel metasurface for simultaneous control of holograms and twisted light beams. *ACS Photon* (2017) 4:1906–12. doi:10.1021/acsphotonics.7b00587

7. Li JX, Kamin S, Zheng GX, Neubrech F, Zhang S, Liu N. Addressable metasurfaces for dynamic holography and optical information encryption. *Sci Adv* (2018) 4:eaar6768. doi:10.1126/sciadv.aar6768

8. Li LL, Cui TJ, Ji W, Liu S, Ding J, Wan X, et al. Electromagnetic reprogrammable coding-metasurface holograms. *Nat Commun* (2017) 8:197. doi:10.1038/s41467-017-00164-9

9. Zang XF, Dong F, Yue F, Zhang C, Xu L, Song Z, et al. Polarization encoded color image embedded in a dielectric metasurface. *Adv Mater* (2018) 30:1707499. doi:10.1002/adma.201707499

10. Zhang XH, Pu MB, Li X, Gao P, Ma XL, Wang CT, et al. Helicity multiplexed spin-orbit interaction in metasurface for colorized and encrypted holographic display. *Ann Phys* (2017) 529:1700248. doi:10.1002/andp.201700248

11. Song GY, Cheng Q, Cui TJ, Jing Y. Acoustic planar surface retroreflector. *Phys Rev Mater* (2018) 2:065201. doi:10.1103/physrevmaterials.2.065201

12. Tang S, Wu J-L, Lü C, Song J, Jiang Y. Functional acoustic metamaterial using shortcut to adiabatic passage in acoustic waveguide couplers. *Phys Rev Appl* (2022) 18:014038. doi:10.1103/physrevapplied.18.014038

13. Xie Y, Wang W, Chen H, Konneker A, Popa B-I, Cummer SA. Wavefront modulation and subwavelength diffractive acoustics with an acoustic metasurface. *Nat Commun* (2014) 5:5553. doi:10.1038/ncomms6553

14. Tang S, Ren B, Feng Y, Song J, Jiang Y. Asymmetric acoustic beam shaping based on monolayer binary metasurfaces. *Appl Phys Express* (2021) 14:085504. doi:10.35848/1882-0786/ac15bf

15. Ge Y, S un HX, Liu C, Qian J, Yuan SQ, Xia JP, et al. Acoustic focusing by an array of heat sources in air. *Appl Phys Express* (2016) 9:066701. doi:10.7567/apex.9.066701

16. Liu C, Xia JP, Sun HX, Yuan SQ. Thermoacoustic focusing lens by symmetric Airy beams with phase manipulations. *J Phys D: Appl Phys* (2017) 50:505101. doi:10.1088/1361-6463/aa964a

17. Tang S, Wu J-L, Lü C, Wang X, Song J, Jiang Y. Acoustic wavelength-selected metamaterials designed by reversed fractional stimulated Raman adiabatic passage. *Phys Rev B* (2022) 105:104107. doi:10.1103/physrevb.105.104107

18. Wang WQ, Xie YB, Konneker A, Popa B-I, Cummer SA. Design and demonstration of broadband thin planar diffractive acoustic lenses. *Appl Phys Lett* (2014) 105:101904. doi:10.1063/1.4895619

19. Tang S, Lü C, Wu J-L, Song J, Jiang Y. Wavelength-selected bifunctional beam shaping for transmitted acoustic waves via coding metasurface. *Appl Acoust* (2022) 194:108786. doi:10.1016/j.apacoust.2022.108786

20. Jiang X, Li Y, Liang B, Cheng J-c., Zhang L. Convert acoustic resonances to orbital angular momentum. *Phys Rev Lett* (2016) 117:034301. doi:10.1103/physrevlett.117.034301

21. Tang S, Wu J-L, Lü C, Yao J, Wang X, Song J, et al. One-way acoustic beam splitting in spatial four-waveguide couplers designed by adiabatic passage. *New J Phys* (2023) 25:033032. doi:10.1088/1367-2630/acc609

22. Tang S, Ren B, Feng Y, Song J, Jiang Y. The generation of acoustic Airy beam with selective band based on binary metasurfaces: Customized on demand. *Appl Phys Lett* (2021) 119:071907. doi:10.1063/5.0060032

23. Zhang Y, Xie B, Liu W, Cheng H, Chen S, Tian J. Anomalous reflection and vortex beam generation by multibit coding acoustic metasurfaces. *Appl Phys Lett* (2019) 114:091905. doi:10.1063/1.5087636

24. Xie B, Cheng H, Tang K, Liu Z, Chen S, Tian J. Multiband asymmetric transmission of airborne sound by coded metasurfaces. *Phy Rev Appl* (2017) 7:024010. doi:10.1103/physrevapplied.7.024010

25. Ghaffarivardavagh R, Nikolajczyk J, Glynn Holt R, Anderson S, Zhang X. Horn-like space-coiling metamaterials toward simultaneous phase and amplitude modulation. *Nat Commun* (2018) 9:1349. doi:10.1038/s41467-018-03839-z

26. Zhu X, Li K, Zhang P, Zhu J, Zhang J, Tian C, et al. Implementation of dispersion-free slow acoustic wave propagation and phase engineering with helical-structured metamaterials. *Nat Commun* (2016) 7:11731. doi:10.1038/ncomms11731

27. Xie B, Tang K, Cheng H, Liu Z, Chen S, Tian J. Coding acoustic metasurfaces. *Adv Mater* (2017) 29:1603507. doi:10.1002/adma.201603507

28. Li K, Liang B, Yang J, Yang J, Cheng JC. Broadband transmission-type coding metamaterial for wavefront manipulation for airborne sound. *Appl Phys Express* (2018) 11:077301. doi:10.7567/apex.11.077301

29. Chen DC, Zhu X-F, Wu D-J, Liu X-J. Broadband Airy-like beams by coded acoustic metasurfaces. *Appl Phys Lett* (2019) 114:053504. doi:10.1063/1.5080202

30. Tang S, Ren B, Feng Y, Song J, Jiang Y. Broadband acoustic focusing via binary rectangular cavity/Helmholtz resonator metasurface. *J Appl Phys* (2021) 129:155307. doi:10.1063/5.0049407

Frontiers in Physics

Investigates complex questions in physics to understand the nature of the physical world

Addresses the biggest questions in physics, from macro to micro, and from theoretical to experimental and applied physics.

Discover the latest Research Topics

See more →

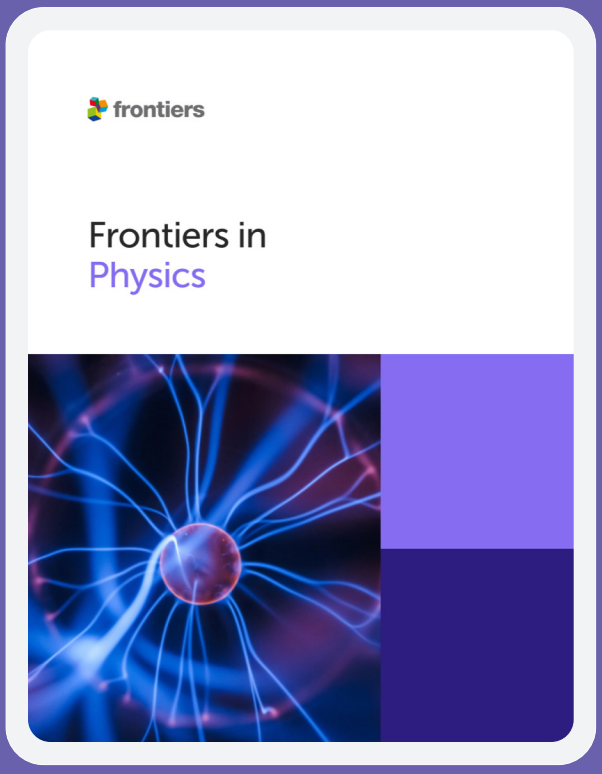

Frontiers

Avenue du Tribunal-Fédéral 34
1005 Lausanne, Switzerland
frontiersin.org

Contact us

+41 (0)21 510 17 00
frontiersin.org/about/contact